

DISSERTATION

AFRICAN EASTERLY WAVE ENERGETICS ON INTRASEASONAL TIMESCALES

Submitted by

Ghassan J. Alaka, Jr.

Department of Atmospheric Science

In partial fulfillment of the requirements

For the Degree of Doctor of Philosophy

Colorado State University

Fort Collins, Colorado

Fall 2014

Doctoral Committee:

Advisor: Eric D. Maloney

Wayne H. Schubert

Russ S. Schumacher

Subhas K. Venayagamoorthy

Copyright by Ghassan J. Alaka, Jr. 2014

All Rights Reserved

ABSTRACT

AFRICAN EASTERLY WAVE ENERGETICS ON INTRASEASONAL TIMESCALES

African easterly waves (AEWs) are synoptic-scale eddies that dominate North African weather in boreal summer. AEWs propagate westward with a maximum amplitude near 700 hPa and a period of 2.5-6-days. AEWs and associated perturbation kinetic energy (PKE) exhibit significant intraseasonal variability in tropical North Africa during boreal summer, which directly impacts local agriculture and tropical cyclogenesis. This study performs a comprehensive analysis of the 30-90-day variability of AEWs and associated energetics using both reanalysis data and model output. Specifically, the PKE and perturbation available potential energy (PAPE) budgets are used to understand the factors that contribute to PKE maxima in West Africa and the extent to which these surges of AEW activity are modulated by the Madden-Julian oscillation (MJO). The role of the MJO in the intraseasonal variability of AEWs is assessed by comparing PKE sources as a function of an MJO index and a local 30-90-day West African PKE index. Since East Africa is an initiation zone for AEW activity and is modulated by the MJO, the relationship between this region and West Africa is a primary focus in this study.

The intraseasonal variability of AEW energetics is first investigated in reanalysis products. While reanalysis data depicts a similar evolution of 30-90-day PKE anomalies in both the MJO and a local PKE index, the MJO index describes only a small (yet still significant) fraction of the local 30-90-day variance. In boreal summers with more significant MJO days, the correlation between the two indices is higher. Baroclinic energy conversions are important for the initiation of 30-90-day West African PKE events east of Lake Chad. In West Africa, both

barotropic and baroclinic energy conversions maintain positive PKE anomalies before they propagate into the Atlantic. The primary role of diabatic heating is to destroy PAPE in a negative feedback to baroclinic energy conversions in West Africa. More frequent East Atlantic tropical cyclone generation is associated with positive PKE events than with negative PKE events.

Easterly wave activity is then examined in a regional model. The Advanced Research Weather Research and Forecasting (WRF-ARW) simulates West African monsoon climatology more accurately than the WRF Nonhydrostatic Mesoscale Model (WRF-NMM). Although the WRF-NMM produces more realistic boreal summer rainfall than the WRF-ARW, it fails to accurately simulate the AEJ and other key West African monsoon features. Parameterizations within the WRF-ARW are scrutinized as well, with the WRF single-moment 6-class microphysics and the Noah land surface model outperforming Thompson microphysics and the RUC land surface model.

Three ten-year WRF-ARW experiments are performed to investigate the role of external forcing on intraseasonal variability in West Africa. In addition to a control simulation, two sensitivity experiments remove 30-90-day variability from the boundary conditions (for all zonal wavenumbers and just for eastward zonal wavenumbers 0-10). Overall, intraseasonal variability of AEWs shows only modest differences after the removal of all 30-90-day input into the model boundary conditions. PKE and PAPE budgets reveal that simulated positive PKE events in West Africa are preceded by extensions of the AEJ into East Africa, which enhance barotropic and baroclinic energy conversions in this region. This jet extension is associated with warm lower-tropospheric temperature anomalies in the eastern Sahara. In West Africa, the amplitude of PKE and PAPE budget terms exhibit a similar evolution (even in the sensitivity experiments) as in the reanalysis products.

ACKNOWLEDGEMENTS

First and foremost, I would like to express my deepest gratitude to my advisor, Dr. Eric D. Maloney, whose continuous guidance and wisdom helped mold several years worth of research into this dissertation. Dr. Maloney's expertise in tropical meteorology and his patience are second to none. I am especially grateful for the difficult questions he was always ready to ask and the different perspectives that he offered, since these have helped me grow as a scientist. I am very thankful for the helpful insight provided to this project by my committee members: Dr. Wayne S. Schubert, Dr. Russ S. Schumacher, and Dr. Karan Venayagamoorthy.

There are several groups and people who have helped make this research possible. This work was supported by the Climate and Large-Scale Dynamics Program of the National Science Foundation under grants AGS-0946911 and AGS-1347738. This project could not have been completed without the good people at the Mesoscale and Microscale Meteorology (MMM) Division, who maintain the WRF-ARW model and helped me troubleshoot numerous errors with it. I would like to express my thanks to Drs. Yongkang Xue and Fernando De Sales at the University of California Los Angeles, who provided me their version of the WRF-NMM and helped troubleshoot the model with ERA-Interim input. I am also thankful for my correspondence with Dr. Jen-Shan Hsieh at Texas A&M University, whose expertise in energetics helped the interpretation of many results. Many thanks are given to the ECMWF, NCEP, and NASA, especially the individuals responsible for producing quality-controlled, high-resolution reanalysis datasets. Special thanks go out to Dr. Matt Wheeler and Dr. Harry Hendon, whose MJO index is the basis for the one produced in this study.

I am indebted to William Stern of the Geophysical Fluid Dynamics Laboratory (GFDL), who presented work on the MJO that I had helped him with as an intern with a certain Dr. Eric Maloney in the audience. I am deeply appreciative of the continuous conversations about tropical cyclones and their formation with several individuals at the Cooperative Institute for Research in the Atmosphere (CIRA), especially John Knaff and Mark DeMaria. I am grateful for the insightful comments I received at group research meetings, namely from Dr. Thomas Birner, Dr. Elizabeth Barnes, Dr. Dave Thompson, and their respective graduate students. In addition, I would like to thank the following colleagues for helpful discussions about this dissertation: Walter Hannah, Adam Rydbeck, Brandon Wolding, Stephanie Henderson, Laura Paulik, Jeremiah Sjoberg, James Ruppert, Chris Slocum, Jim Benedict, Michael Ventrice, and Stephanie Leroux. From a technical support standpoint, Ammon Redman, Matt Bishop, and Kelley Wittmeyer deserve credit for helping me work through (or around) several issues at Colorado State University.

To finish, I would like to thank my friends and family for their constant support throughout this project. To my parents, Ghassan and Elaine, and my siblings, Armand, Noel, and Lila, you encouraged me to follow my dreams and have helped shape the person I am today. If this dissertation were a house, you would surely be the foundation upon which it has been built. To all of my friends, especially those with whom I have been close in Lynnfield, Ann Arbor, and Fort Collins, know that the happiness you have brought to my life has been a guiding force throughout my Ph.D. pursuit.

TABLE OF CONTENTS

ABSTRACT	ii
ACKNOWLEDGEMENTS	iv
TABLE OF CONTENTS.....	vi
CHAPTER 1 Introduction.....	1
1.1 Improving Prediction of African Easterly Wave Activity	1
1.2 African Easterly Waves: An Overview.....	3
1.3 The West African Monsoon.....	6
1.4 The Madden-Julian Oscillation.....	9
1.5 The Influence of the Madden-Julian Oscillation on African Easterly Waves	12
1.6 Energy Budgets.....	14
1.7 Study Overview	17
CHAPTER 2 The Intraseasonal Variability of African Easterly Wave Energetics in Observations	19
2.1 Introduction.....	19
2.2 Methodology	21
2.3 Remote and Local Intraseasonal Variability.....	22
2.3.1 MJO Index	23
2.2.2 700 hPa Perturbation Kinetic Energy Index	24
2.2.3 East African Indices	30
2.3 Boreal Summer Mean Energy Conversions in ERA-Interim	39
2.4 Boreal Summer Mean Energy Conversions in CFSR.....	45
2.5 Energy Budget Intraseasonal Variability in the Local PKE Index	46
2.5.1 PKE and PKE Tendency.....	47
2.5.2 Barotropic Energy Conversion	49
2.5.3 PKE/PAPE Conversion.....	53
2.5.4 Baroclinic Energy Conversion	53
2.5.5 Role of Diabatic Heating	54
2.5.6 Role of Other PKE Budget Terms	56
2.6 ISV of Energy Budgets for the MJO Index	57
2.7 Role of Meridional Gradients in PKE Sources	65
2.8 Intraseasonal Variability of Tropical Cyclogenesis in the East Atlantic	69
2.9 Discussion	70

CHAPTER 3 Simulation of the West African Monsoon in the WRF-ARW and WRF-NMM Dynamical Cores.....	76
3.1 Introduction.....	76
3.2 Models and Input Data	80
3.3 Running the WRF-NMM Dynamical Core with ERA-Interim Boundary Conditions	82
3.4 Sensitivity of Parameterization Options Using WRF-ARW	83
3.5 Simulation of the West African Monsoon in the WRF-ARW and WRF-NMM Dynamical Cores.....	90
3.6 Discussion	96
CHAPTER 4 The Intraseasonal Variability of African Easterly Wave Energetics in the WRF-ARW Model.....	98
4.1 Introduction.....	98
4.2 Methodology	100
4.2.1 Experimental Design.....	100
4.2.2 Conversion to Unformatted Binary.....	102
4.3 Simulated West African Monsoon in Boreal Summer	103
4.4 Boreal Summer Mean African Easterly Wave Energetics.....	105
4.5 Intraseasonal Variability of West African Perturbation Kinetic Energy	113
4.6 Intraseasonal Variability of African Easterly Wave Energetics in the Local PKE Index	118
4.6.1 PKE	118
4.6.2 Barotropic Energy Conversion	120
4.6.3 PKE/PAPE Conversion.....	124
4.6.4 Baroclinic Energy Conversion.....	125
4.6.5 Role of Diabatic Heating	129
4.7 Intraseasonal Variability of African Easterly Wave Energetics in the MJO Index	131
4.8 Intraseasonal Variability of AEW Trigger Mechanisms in East Africa	135
4.8.1 Eastward AEJ Extension.....	136
4.8.2 Static Stability Reduction	138
4.8.3 Moisture Budget.....	140
4.9 Discussion	143
CHAPTER 5 Conclusions.....	147
5.1 Main Findings	147
5.2 Outstanding Questions	151

5.3 Future Work	152
5.4 Final Remarks	154
REFERENCES	156
APPENDIX A Definitions for Perturbation Kinetic Energy and Perturbation Available Potential Energy Budget Terms	173
APPENDIX B The code for <i>unpack_netcdf.f90</i>	176

LIST OF FIGURES

<p>Fig. 1.1 MODIS satellite imagery from Aug. 20, 2012 patched together to show successive African easterly waves (marked by letters) that developed into Atlantic tropical cyclones. “G” stands for Gordon. “I” stands for Isaac. “J” stands for Joyce. “K” stands for Kirk. Image created in Google Earth.</p> <p>Fig. 1.2 Schematic of the West African monsoon system as viewed from the West adapted from Lafore et al. (2010). “TEJ” in the yellow tube stands for AEJ.....</p> <p>Fig. 1.3 June-September average plots for zonal wind (shading) and total wind (vectors) from 21 years (1990-2010) of ECMWF ERA-Interim data. Winds are plotted at <i>a</i>) 850 hPa and <i>b</i>) 650 hPa.....</p> <p>Fig. 1.4 a) Structure of an equatorial Rossby wave from Fig. 4c in Matsuno (1966). b) Structure of an equatorial Kelvin wave from Fig. 8 in Matsuno (1966).</p> <p>Fig. 1.5 A simple schematic of how equatorial waves propagate from MJO heating into tropical North Africa. The inset (from Heckley and Gill 1984) represents the circulation response to a heating along the equator.....</p> <p>Fig. 2.1 Boreal summer power spectra for 700 hPa PKE averaged between 5°N-15°N and 20°W-0° (see map) for 1990-2010. The associated red noise spectrum with 95% confidence bounds is given by the black curves. The gray shading represents the 30-90-day band.....</p> <p>Fig. 2.2 The 30-90-day 700 hPa PKE index lag correlated with (a) PC1 of the MJO index and (b) PC2 of the MJO index. The black line includes JJAS for all 21 years. The blue line includes JJAS with at least 60 significant MJO days (14 years). The green line includes JJAS with at least 70 significant MJO days (ten years). The red line includes JJAS with at least 80 significant MJO days (six years). Dashed lines represent the 95% significant threshold for each subset.....</p> <p>Fig. 2.3 Sample time series are shown for PC1 (black, dashed), PC2 (blue, dot-dashed), and 30-90-day 700 hPa PKE (red, solid) indices for a boreal summer with strong MJO activity (1 May 2002 and 31 October 2002). Each index is normalized by its standard deviation.....</p> <p>Fig. 2.4 Lead/Lag composites for a) Day -7 and b) Day 0 for ERA-Interim 400 hPa 30-90-day temperature anomalies. The shading interval is 0.1 K. Stippling represents 95% significance.....</p>	<p>2</p> <p>7</p> <p>8</p> <p>11</p> <p>13</p> <p>25</p> <p>26</p> <p>27</p> <p>28</p>
--	--

Fig. 2.5	Lead/Lag composites of a) Day -7 and b) Day 0 for ERA-Interim 30-90-day 200-400 hPa thickness anomalies. The shading interval is 10 m. Stippling represents 95% significance.....	29
Fig. 2.6	Boreal summer power spectra for CLAUS T_B averaged between 10°N-24°N and 16.5°E-27.5°E for 1989-2005. The associated red noise spectrum with 95% confidence bounds is given by the black curves. The gray shading represents the 30-90-day band.....	31
Fig. 2.7	Lead/Lag composites of 30-90-day T_B anomalies averaged for day -2 through day +2 with respect to a 30-90-day T_B index in the trigger region (marked by a black box). Composites are shown for a), significant positive 30-90-day T_B events, and b) significant negative 30-90-day T_B events. The shading interval is 0.6 K. Stippling represents 30-90-day T_B anomalies that are significant with 95% confidence.....	32
Fig. 2.8	As in 2.6, except for ERA-Interim OLR from 1990-2010.....	33
Fig. 2.9	The correlation of the PKE index with negative ERA-Interim OLR anomalies averaged in the trigger region. Negative lag days represent OLR leading PKE.....	34
Fig. 2.10	Lead/lag composites for positive PKE events in June-September (1990-2010) are averaged between 10°N and 20°N to create a Hovmöller diagram of 30-90-day OLR anomalies. The shading interval is 0.5 W m ⁻² . Stippling represents OLR ₃₀₋₉₀ anomalies that are significant with 95% confidence. The thick vertical dashed line marks the longitudinal center for the PKE index region, and the thick horizontal dashed line marks Day 0.....	34
Fig. 2.11	As in 2.10, except for 700 hPa PKE ₃₀₋₉₀ anomalies composited for significant OLR events in East Africa. The latitude range is changed to 10°N and 15°N.....	35
Fig. 2.12	As in 2.6, except for ERA-Interim TPW from 1990-2010.....	36
Fig. 2.13	The correlation of negative ERA-Interim OLR anomalies with ERA-Interim TPW anomalies, both averaged in the trigger region. Negative lag days represent TPW leading OLR.....	36
Fig. 2.14	The correlation of the PKE index with ERA-Interim TPW anomalies, averaged in the trigger region. Negative lag days represent TPW leading PKE.....	37
Fig. 2.15	As in 2.10, except for TPW ₃₀₋₉₀ anomalies composites for significant West African 700 hPa PKE ₃₀₋₉₀ events.....	38

Fig. 2.16	As in 2.10, except for PKE ₃₀₋₉₀ anomalies composites for significant East African TPW ₃₀₋₉₀ events.	38
Fig. 2.17	The vertically integrated PKE and PAPE budget terms and supporting fields are averaged in boreal summer (June-September). All budget terms are shaded and use the same color bar. Shown: (a) PKE advection (A_{TOT}) and 700 hPa PKE (contours; interval of $2 \text{ m}^2 \text{ s}^{-2}$), (b) barotropic energy conversion (B_T) and 650 hPa zonal wind (contours; interval of 1 m s^{-1} less than -7 m s^{-1}), (c) geopotential flux convergence (Φ_{FC}) and 850 hPa total wind (vectors), (d) baroclinic overturning (C_{pk}) and total precipitable water (contours; interval of 5 mm), (e) diabatic generation of PAPE (Q_T) and the mean apparent heating rate (contours; interval of 0.33 K day^{-1}), and (f) baroclinic energy conversion (B_C) and 850 hPa potential temperature (contours; interval of 2 K).	40
Fig. 2.18	The vertical structure of the PKE and PAPE budget terms and supporting fields are averaged between 10°W and 20°E during boreal summer (June-September). All budgets terms are shaded. Shown: (a) PKE advection (A_{TOT}) and PKE (contours; interval of $2 \text{ m}^2 \text{ s}^{-2}$), (b) barotropic energy conversion (B_T) and zonal wind (contours; interval of 1 m s^{-1} less than -7 m s^{-1}), (c) geopotential flux convergence (Φ_{FC}) and total wind (vectors), (d) baroclinic overturning (C_{pk}) and total wind (vectors), (e) diabatic generation of PAPE (Q_T) and the apparent heating rate (contours; interval of 1 K day^{-1}), and (f) baroclinic energy conversion (B_C) and potential temperature (contours; $\theta < 315$: interval of 2.5 K; $\theta > 315$: interval of 5 K).	41
Fig. 2.19	As in Fig. 2.18, except for the vertical structure of (a) the PKE residual term (D) and (b) the PAPE residual term (R).	44
Fig. 2.20	As in Fig. 2.17, except for boreal summer mean CFSR data (2000-2010).....	45
Fig. 2.21	Lead/lag composites are averaged between 10°N and 15°N to create Hovmöller diagrams. Shown: 30-90-day 700 hPa PKE anomalies (shading) and vertically averaged 30-90-day PKE tendency (contours) for June-September composited for significant events in a 30-90-day 700 hPa PKE index. The shading interval is $0.5 \text{ m}^2 \text{ s}^{-2}$. The contour interval is $4 \times 10^{-7} \text{ m}^2 \text{ s}^{-3}$. Stippling represents PKE anomalies that are significant with 95% confidence. The thick vertical dashed line marks the longitudinal center for the PKE index region. The thick horizontal dashed line marks Day 0.	47
Fig. 2.22	Lead/lag maps of 30-90-day 700 hPa PKE anomalies (shading) and vertically averaged 30-90-day PKE tendency (contours) for June-September composited for significant events in a 30-90-day 700 hPa PKE index. Shown: (a) day -10 and (b) day 0. The shading interval is $0.4 \text{ m}^2 \text{ s}^{-2}$.	

	The contour interval is $4 \times 10^{-7} \text{ m}^2 \text{ s}^{-3}$. Stippling represents PKE anomalies that are significant with 95% confidence. Coastlines are represented by a gray contour.....	48
Fig. 2.23	As in Fig. 2.21, except for vertically averaged, 30-90-day PKE creation terms south of the AEJ ($7.5^\circ\text{N} - 12.5^\circ\text{N}$). Shown: (a) barotropic energy conversion, (b) baroclinic overturning, (c) baroclinic energy conversion, and (d) PAPE generation by diabatic heating. Lead/lag composites are averaged between 7.5°N and 12.5°N to create Hovmöller diagrams. The shading interval is $2 \times 10^{-6} \text{ m}^2 \text{ s}^{-3}$	50
Fig. 2.24	As in Fig. 2.21, except for vertically averaged, 30-90-day PKE creation terms north of the AEJ ($12.5^\circ\text{N} - 17.5^\circ\text{N}$). Shown: (a) barotropic energy conversion, (b) baroclinic overturning, (c) baroclinic energy conversion, and (d) PAPE generation by diabatic heating. Lead/lag composites are averaged between 12.5°N and 17.5°N to create Hovmöller diagrams. The shading interval is $2 \times 10^{-6} \text{ m}^2 \text{ s}^{-3}$. If necessary, contours represent levels outside of the shading limits with an interval of $4 \times 10^{-6} \text{ m}^2 \text{ s}^{-3}$	51
Fig. 2.25	As in Fig. 2.22, except for vertically averaged, 30-90-day PKE creation terms on day -10. Shown: (a) barotropic energy conversion, (b) baroclinic overturning, (c) baroclinic energy conversion, and (d) PAPE generation by diabatic heating. The shading interval is $2 \times 10^{-6} \text{ m}^2 \text{ s}^{-3}$. If necessary, contours represent levels outside of the shading limits with an interval of $4 \times 10^{-6} \text{ m}^2 \text{ s}^{-3}$. Coastlines are represented by a gray contour.....	52
Fig. 2.26	As in Fig. 2.22, except for vertically averaged, 30-90-day PKE creation terms on day 0. Shown: (a) barotropic energy conversion, (b) baroclinic overturning, (c) baroclinic energy conversion, and (d) PAPE generation by diabatic heating. If necessary, contours represent levels outside of the shading limits with an interval of $4 \times 10^{-6} \text{ m}^2 \text{ s}^{-3}$. Coastlines are represented by a gray contour.....	52
Fig. 2.27	Day 0 regression of Q_I' (shading) and T' (contours) against 700 hPa eddy vorticity averaged in the shown black box. The shading interval is 0.04 K day^{-1} . The contour interval is 0.02 K . Stippling represents shading that is 95% significant. The gray contour represents that African coastline.....	55
Fig. 2.28	MJO phase composites for 30-90-day 700 hPa PKE anomalies (shading) and vertically averaged 30-90-day PKE tendency (contours) for June-September. The shading interval is $0.3 \text{ m}^2 \text{ s}^{-2}$. The contour interval is $4 \times 10^{-7} \text{ m}^2 \text{ s}^{-3}$. Stippling represents PKE anomalies that are significant with 95% confidence. Coastlines are represented by a gray contour.....	58
Fig. 2.29	As in Fig. 2.28, except for vertically-averaged 30-90-day B_T anomalies. The shading interval is $2 \times 10^{-6} \text{ m}^2 \text{ s}^{-3}$	60

Fig. 2.30	As in Fig. 2.28, except for vertically-averaged 30-90-day C_{pk} anomalies. The shading interval is $2 \times 10^{-6} \text{ m}^2 \text{ s}^{-3}$	61
Fig. 2.31	As in Fig. 2.28, except for vertically-averaged 30-90-day B_C anomalies. The shading interval is $2 \times 10^{-6} \text{ m}^2 \text{ s}^{-3}$	62
Fig. 2.32	As in Fig. 2.28, except for vertically-averaged 30-90-day Q_T anomalies. The shading interval is $2 \times 10^{-6} \text{ m}^2 \text{ s}^{-3}$	64
Fig. 2.33	As in Fig. 2.22, except for: (a) 30-90-day 700 hPa meridional zonal wind gradient anomalies (shading) and 30-90-day 700 hPa zonal wind $\leq -7 \text{ m s}^{-1}$ (contours) on day -10, (b) (a) on day 0, (c) 30-90-day 850 hPa meridional temperature gradient anomalies on day -10, and (d) (c) on day 0. Please note that the shading interval is $2 \times 10^{-7} \text{ s}^{-1}$ in (a), (c) and $1 \times 10^{-7} \text{ K m}^{-1}$ in (b), (d). The contour interval is 1 m s^{-1} in (a), (c). Coastlines are represented by a gray contour.....	66
Fig. 2.34	As in Fig. 2.21, except for: (a) 30-90-day 700 hPa barotropic energy conversion anomalies, (b) 30-90-day 850 hPa baroclinic energy conversion anomalies north of the AEJ, (c) B_{T1} anomalies, (d) B_{C1} anomalies, (e) B_{T2} anomalies, and (f) B_{C2} anomalies. (a), (c), and (e) have a shading interval of $2 \times 10^{-6} \text{ m}^2 \text{ s}^{-3}$ and are analyzed south of the AEJ. (b), (d), and (f) have a shading interval of $1 \times 10^{-5} \text{ m}^2 \text{ s}^{-3}$ and are analyzed north of the AEJ. If necessary, contours extend above/below the shading limits with an interval of $2 \times 10^{-6} \text{ m}^2 \text{ s}^{-3}$	67
Fig. 2.35	As in Fig. 2.21, except for: (a) 30-90-day 700 hPa PKE anomalies associated with positive PKE events over the East Atlantic and (b) 30-90-day 700 hPa PKE anomalies associated with negative PKE events over the East Atlantic. Hovmollers are averaged between 10°N and 15°N . Tropical cyclogenesis events (stars) are from the Revised Hurricane Database (HURDAT2). The shading interval is $0.3 \text{ m}^2 \text{ s}^{-2}$	70
Fig. 2.36	MJO phase composites for ERA-Interim 30-90-day 700 hPa PKE anomalies Tropical cyclogenesis events (stars) are from the Revised Hurricane Database (HURDAT2). The shading interval is $0.3 \text{ m}^2 \text{ s}^{-2}$	71
Fig. 2.37	MJO phase composites for ERA-Interim 30-90-day OLR anomalies. Tropical cyclogenesis events (stars) are from the Revised Hurricane Database (HURDAT2). The shading interval is 0.5 W m^{-2}	72
Fig. 3.1	A schematic showing how the root system of modeled vegetation penetrates into different layers for NCEP soil data (left) and ERA-Interim soil data (right).....	83

Fig. 3.2	Boreal summer mean (June-August) precipitation maps for a) TRMM 3B42, b) WSM6 microphysics and RUC land surface model, c) WSM6 microphysics and Noah land surface model, d) Thompson microphysics and RUC land surface model, and e) Thompson microphysics and NOAH land surface model. The shading interval is 0.5 mm day^{-1} . All plots are on the same scale.....	86
Fig. 3.3	Boreal summer mean (June-August) 650 hPa zonal wind maps for a) ERA-Interim, b) WSM6 microphysics and RUC land surface model, c) WSM6 microphysics and Noah land surface model, d) Thompson microphysics and RUC land surface model, and e) Thompson microphysics and NOAH land surface model.. The shading interval is 2 m s^{-1} . All plots are on the same scale.....	86
Fig. 3.4	As in Fig. 3.3, except for zonal wind cross-sections averaged between 20°W and 0°E . The shading interval is 2 m s^{-1} . All plots are on the same scale.....	87
Fig. 3.5	As in Fig. 3.3, except for zonal wind cross-sections averaged between 0°E and 20°E . The shading interval is 2 m s^{-1} . All plots are on the same scale.....	88
Fig. 3.6	Hovmöller diagrams of 700 hPa relative vorticity for a) ERA-Interim, b) WSM6 microphysics and RUC land surface model, c) WSM6 microphysics and NOAH land surface model, d) Thompson microphysics and RUC land surface model, and e) Thompson microphysics and NOAH land surface model.. The shading interval is $0.5 \times 10^{-5} \text{ m s}^{-1}$. All plots are on the same scale.....	89
Fig. 3.7	Boreal summer mean (June-August) precipitation maps for a) TRMM 3B42, b) WRF-ARW, and c) WRF-NMM. The shading interval is 0.5 mm day^{-1}	92
Fig. 3.8	Boreal summer mean (June-August) 650 hPa zonal wind maps for a) ERA-Interim, b) WRF-ARW, and c) WRF-NMM. The shading interval is 2 m s^{-1}	93
Fig. 3.9	Boreal summer mean (June-August) zonal wind cross-sections for a) ERA-Interim, b) WRF-ARW, and c) WRF-NMM. Plots are averaged between 20°W and 0°E . The shading interval is 2 m s^{-1}	93
Fig. 3.10	Boreal summer mean (June-August) zonal wind cross-sections for a) ERA-Interim, b) WRF-ARW, and c) WRF-NMM. Plots are averaged between 0°E and 20°E . The shading interval is 2 m s^{-1}	93
Fig. 3.11	Hovmöller diagrams of 700 hPa relative vorticity for a) ERA-Interim, b) WRF-ARW, and c) WRF-NMM. Plots are averaged between 5°N and	

15°N. The shading interval is $0.5 \times 10^{-5} \text{ m s}^{-1}$. The time axis is positive going down.....	95
Fig. 3.12 Boreal summer (June-August) meridional wind regressed against eddy 700 hPa vorticity for a) ERA-Interim, b) WRF-ARW, and c) WRF-NMM. In a), eddy vorticity at measured at the star. In b) and c), eddy vorticity is averaged in the black box. The shading interval is 0.2 m s^{-1}	95
Fig. 3.13 As in Fig. 3.11, except for 700 hPa PKE. The scales vary for each plot.	95
Fig. 4.1 Wavenumber-frequency filtering of the boundary conditions for the three proposed WRF experiments. In a), no filtering is applied. In b), all 30-90-day variability is removed. In c), only eastward-propagating wavenumbers 0 to 10 are removed from the 30-90-day band. Filtered parts of the wavenumber-frequency domain are represented by blue shading. Figure is adapted from Wheeler and Kiladis (1999).....	101
Fig 4.2 Boreal summer mean precipitation for three WRF-ARW experiments: a) C1, b) S1, and c) S2. The shading interval is 1 mm day^{-1}	103
Fig. 4.3 Boreal summer mean 650 hPa zonal wind for three WRF-ARW experiments: a) C1, b) S1, and c) S2. The shading interval is 2 m s^{-1} . 650 hPa total wind vectors are overlaid.....	104
Fig 4.4 Boreal summer mean zonal wind averaged between 10°W and 20°E for three WRF-ARW experiments: a) C1, b) S1, and c) S2. The shading interval is 2 m s^{-1}	104
Fig 4.5 Eddy 700 hPa meridional wind regressed against eddy 700 hPa vorticity averaged in the black box for three WRF-ARW experiments: a) C1, b) S1, and c) S2. The shading interval is 0.4 m s^{-1} . Stippling represents values that exceed the 95% confidence threshold.....	104
Fig 4.6 As in Fig. 2.17, except for C1.....	106
Fig 4.7 As in Fig. 2.18, except for C1.....	107
Fig 4.8 As in Fig. 2.17, except for S1.	109
Fig 4.9 As in Fig. 2.18, except for S1.	110
Fig 4.10 As in Fig. 2.17, except for S2.	111
Fig 4.11 As in Fig. 2.18, except for S2.	112

Fig 4.12	Boreal summer 30-90-day variance maps of 700 hPa PKE for three WRF-ARW experiments (C1, S1, S2).....	114
Fig 4.13	Boreal summer power spectra for 700 hPa PKE for different WRF simulations from 2001 to 2010 for: a) C1), b) S1, and c) S2. Maps show the area where spectra are computed. The associated red noise spectrum with 95% confidence bounds is given by the black curves. The gray shading represents the 30-90-day band.....	115
Fig 4.14	Correlation coefficients for West African 700 hPa PKE indices for observations (ERA-I) and three WRF-ARW experiments (C1, S1, S2). Correlations are performed for June-Sept from 2001-2010.....	116
Fig 4.15	As in Fig. 2.21, except for the three WRF-ARW experiments averaged over different latitudes: a) C1 (10°N - 20°N), b) S1 (11°N - 21°N), and c) S2 (13°N - 23°N). The shading interval is $1 \text{ m}^2 \text{ s}^{-2}$. Stippling represents significance at the 95% confidence level.....	119
Fig 4.16	As in Fig. 2.22, except for the three WRF-ARW experiments: a) C1 day -10, b) S1 day -10, c) S2 day -10, d), C1 day 0, e) S1 day 0, and f) S2 day 0. The shading interval is $1 \text{ m}^2 \text{ s}^{-2}$. Stippling represents significance at the 95% confidence level.....	119
Fig 4.17	As in Fig. 2.21, except for vertically averaged, 30-90-day PKE creation terms south of the AEJ (10°N – 15°N) in the C1 simulation. Shown: (a) barotropic energy conversion, (b) baroclinic overturning, (c) baroclinic energy conversion, and (d) PAPE generation by diabatic heating. Lead/lag composites are averaged between 10°N and 15°N to create Hovmöller diagrams. The shading interval is $2 \times 10^{-6} \text{ m}^2 \text{ s}^{-3}$. Contours represent levels outside of the shading limits with an interval of $4 \times 10^{-6} \text{ m}^2 \text{ s}^{-3}$	121
Fig 4.18	As in Fig. 2.21, except for vertically averaged, 30-90-day PKE creation terms north of the AEJ (15°N – 20°N) in the C1 simulation. Shown: (a) barotropic energy conversion, (b) baroclinic overturning, (c) baroclinic energy conversion, and (d) PAPE generation by diabatic heating. Lead/lag composites are averaged between 15°N and 20°N to create Hovmöller diagrams. The shading interval is $2 \times 10^{-6} \text{ m}^2 \text{ s}^{-3}$. Contours represent levels outside of the shading limits with an interval of $4 \times 10^{-6} \text{ m}^2 \text{ s}^{-3}$	122
Fig 4.19	As in Fig. 2.22, except for vertically averaged, 30-90-day PKE creation terms on day -10 in the C1 simulation. Shown: (a) barotropic energy conversion, (b) baroclinic overturning, (c) baroclinic energy conversion, and (d) PAPE generation by diabatic heating. The shading interval is $2 \times 10^{-6} \text{ m}^2 \text{ s}^{-3}$. Contours represent levels outside of the shading limits with an interval of $4 \times 10^{-6} \text{ m}^2 \text{ s}^{-3}$	123

Fig 4.20	As in Fig. 2.22, except for vertically averaged, 30-90-day PKE creation terms on day 0 in the C1 simulation. Shown: (a) barotropic energy conversion, (b) baroclinic overturning, (c) baroclinic energy conversion, and (d) PAPE generation by diabatic heating. The shading interval is $2 \times 10^{-6} \text{ m}^2 \text{ s}^{-3}$. Contours represent levels outside of the shading limits with an interval of $4 \times 10^{-6} \text{ m}^2 \text{ s}^{-3}$	123
Fig 4.21	As in Fig. 2.21, except for vertically averaged, 30-90-day PKE creation terms south of the AEJ ($13^\circ\text{N} - 18^\circ\text{N}$) in the S1 simulation. Shown: (a) barotropic energy conversion, (b) baroclinic overturning, (c) baroclinic energy conversion, and (d) PAPE generation by diabatic heating. Lead/lag composites are averaged between 13°N and 18°N to create Hovmöller diagrams. The shading interval is $2 \times 10^{-6} \text{ m}^2 \text{ s}^{-3}$. Contours represent levels outside of the shading limits with an interval of $4 \times 10^{-6} \text{ m}^2 \text{ s}^{-3}$	126
Fig 4.22	As in Fig. 2.21, except for vertically averaged, 30-90-day PKE creation terms north of the AEJ ($18^\circ\text{N} - 23^\circ\text{N}$) in the S1 simulation. Shown: (a) barotropic energy conversion, (b) baroclinic overturning, (c) baroclinic energy conversion, and (d) PAPE generation by diabatic heating. Lead/lag composites are averaged between 18°N and 23°N to create Hovmöller diagrams. The shading interval is $2 \times 10^{-6} \text{ m}^2 \text{ s}^{-3}$. Contours represent levels outside of the shading limits with an interval of $4 \times 10^{-6} \text{ m}^2 \text{ s}^{-3}$	127
Fig 4.23	As in Fig. 2.22, except for vertically averaged, 30-90-day PKE creation terms on day -10 in the S1 simulation. Shown: (a) barotropic energy conversion, (b) baroclinic overturning, (c) baroclinic energy conversion, and (d) PAPE generation by diabatic heating. The shading interval is $2 \times 10^{-6} \text{ m}^2 \text{ s}^{-3}$	128
Fig 4.24	As in Fig. 2.22, except for vertically averaged, 30-90-day PKE creation terms on day 0 in the S1 simulation. Shown: (a) barotropic energy conversion, (b) baroclinic overturning, (c) baroclinic energy conversion, and (d) PAPE generation by diabatic heating. The shading interval is $2 \times 10^{-6} \text{ m}^2 \text{ s}^{-3}$. Contours represent levels outside of the shading limits with an interval of $4 \times 10^{-6} \text{ m}^2 \text{ s}^{-3}$	128
Fig 4.25	As in Fig. 2.28, except for 700 hPa 30-90-day PKE anomalies in the C1 simulation. The shading interval is $0.5 \text{ m}^2 \text{ s}^{-2}$	132
Fig 4.26	As in Fig. 2.28, except for vertically-averaged 30-90-day B_T anomalies in the C1 simulation. The shading interval is $2 \times 10^{-6} \text{ m}^2 \text{ s}^{-3}$	133
Fig 4.27	As in Fig. 2.28, except for vertically-averaged 30-90-day B_C anomalies in the C1 simulation. The shading interval is $2 \times 10^{-6} \text{ m}^2 \text{ s}^{-3}$	134

Fig 4.28	As in Fig. 2.28, except for 700 hPa 30-90-day PKE anomalies in the S1 simulation. The shading interval is $0.5 \text{ m}^2 \text{ s}^{-2}$	135
Fig 4.29	As in Fig. 2.21, except for 30-90-day 650 hPa zonal wind anomalies from three WRF-ARW experiments averaged over different latitudes: a) C1 (12.5°N - 17.5°N), b) S1 (15.5°N - 20.5°N), and c) S2 (18°N - 23°N). The shading interval is 0.3 m s^{-1} . Stippling represents significance at the 95% confidence level.	137
Fig 4.30	As in Fig. 2.22, except for 30-90-day 650 hPa zonal wind anomalies from three WRF-ARW experiments: a) C1 day -10, b) S1 day -10, c) S2 day -10, d), C1 day 0, e) S1 day 0, and f) S2 day 0. The shading interval is 0.3 m s^{-1} . Stippling represents significance at the 95% confidence level.	137
Fig 4.31	As in Fig. 2.21, except for 30-90-day 400 hPa temperature anomalies from three WRF-ARW experiments averaged between 22.5°N - 27.5°N : a) C1, b) S1, and c) S2. The shading interval is 0.1 K . Stippling represents significance at the 95% confidence level.....	139
Fig 4.32	As in Fig. 2.22, except for 30-90-day 400 hPa temperature anomalies from three WRF-ARW experiments: a) C1 day -10, b) S1 day -10, c) S2 day -10, d), C1 day 0, e) S1 day 0, and f) S2 day 0. The shading interval is 0.3 m s^{-1} . Stippling represents significance at the 95% confidence level.	139
Fig 4.33	As in Fig. 2.21, vertically-integrated 30-90-day anomalies of the following moisture budget terms from the C1 simulation averaged over different latitudes: a) C1 (12.5°N - 17.5°N), b) S1 (15.5°N - 20.5°N), and c) S2 (18°N - 23°N). The shading interval is 0.1 mm day^{-1} . Stippling represents significance at the 95% confidence level.....	141
Fig 4.34	As in Fig. 2.22, except for vertically-integrated 30-90-day anomalies of the following moisture budget terms from the C1 simulation: a) moisture tendency day -10, b) meridional moisture advection day -10, c) precipitation day -10, d), moisture tendency day 0, e) meridional moisture advection day 0, and f) precipitation day 0. The shading interval is 0.1 mm day^{-1} . Stippling represents significance at the 95% confidence level.	141
Fig 4.35	As in Fig. 2.28, except for vertically-integrated 30-90-day moisture tendency anomalies in the C1 simulation. The shading interval is 0.5 mm day^{-1}	143

LIST OF TABLES

Table 3.1	Comparison of attributes within the WRF-ARW and WRF-NMM dynamical cores.	78
Table 3.2	Comparsion of the parameterizations used in the WRF-ARW and WRF-NMM dynamical cores.	91
Table 4.1	Correlation coefficients for West African 700 hPa PKE indices for observations (ERA-I) and three WRF-ARW experiments (C1, S1, S2). Correlations are performed for June-Sept from 2001-2010.....	117

CHAPTER 1 Introduction

1.1 Improving Prediction of African Easterly Wave Activity

African easterly waves (AEWs; see Section 1.2) are synoptic-scale disturbances that exhibit significant variations on intraseasonal timescales (i.e., 30-90-day) in West Africa (Leroux and Hall 2009; Alaka 2010; Alaka and Maloney 2012). Simply examining visible satellite imagery from the Moderate-resolution Imaging Spectroradiometer (MODIS) over the course of a boreal summer reveals several active and quiet periods of AEW activity (Fig. 1.1). For example, the period from August 15-30, 2012 featured several successive AEWs that developed into Atlantic tropical cyclones at some point in the basin: Hurricane Gordon, Tropical Storm Helene, Hurricane Isaac, Tropical Storm Joyce, Hurricane Kirk, and Hurricane Leslie. In September, 2012, which is the climatological height of the Atlantic hurricane season, only one Atlantic system formed from an AEW (Hurricane Nadine). Based on a wave tracking algorithm presented in Wang et al. (2012), AEW activity was stronger in August, 2012 than in September. Thus, an oscillation in AEW activity emerging from the West African coast could directly impact tropical cyclogenesis in the Atlantic. What factors contribute to this intraseasonal oscillation of AEW activity? Further, is 30-90-day AEW activity internally or externally forced? Given the dominance of the Madden-Julian oscillation (MJO; see Section 1.4) in the tropics on 30-90-day time scales, it is the leading candidate for an externally-forced modulation of AEW activity. If the slowly-evolving MJO and West African AEW activity are indeed highly-correlated, then the prediction of these synoptic-scale eddies would improve considerably. Models such as the monthly European Centre for Medium-Range Weather Forecasts (ECMWF) Ensemble Prediction System (EPS) exhibit strong sensitivity of Atlantic tropical cyclone activity to MJO

phasing and amplitude (Vitart 2009; Belanger et al. 2010), which has been partly attributed to the ISV of AEWs. The MJO is predicted with skill 3-4 weeks in advance (Waliser et al. 2006; Vitart and Molteni 2010), which could lead to a significant improvement in forecast skill for AEWs.

However, the West African monsoon (WAM) might also be influenced by several other atmospheric phenomena that project onto the 30-90-day band. In particular, the North Atlantic oscillation (NAO; Walker 1924) and the quasi-biweekly zonal dipole (QBZD; Mounier et al. 2008). might have a strong influence on intraseasonal activity in West Africa. Additionally, intraseasonal variability in this region could be internally-forced, associated with active/break cycles in the monsoon, movement of the Saharan heat low, and/or complex topography.

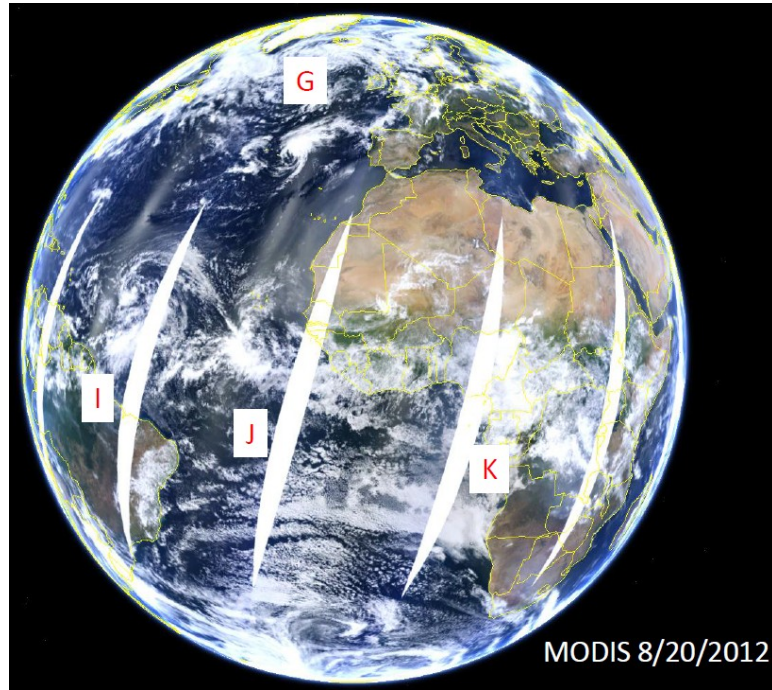


Fig. 1.1 MODIS satellite imagery from Aug. 20, 2012 patched together to show successive African easterly waves (marked by letters) that developed into Atlantic tropical cyclones. “G” stands for Gordon. “I” stands for Isaac. “J” stands for Joyce. “K” stands for Kirk. Image created in Google Earth.

Increasing the complexity, WAM and Saharan heat low variability could be modulated by external phenomena, providing an indirect pathway to AEW modulation.

Improving AEW forecasts is important for two primary reasons: 1) the rainfall associated with AEWs is vital to Sahelian agriculturalists (Sultan et al. 2005), and 2) AEWs seed Atlantic and eastern Pacific tropical cyclones (e.g., Hopsch et al. 2007), which cause significant damage to North American, Central American, and Caribbean communities (Avila 1991; Avila and Pasch 1992; Landsea et al. 1999; Pielke et al. 2008). The improvement of medium-range AEW forecasts in West Africa based on trends in 30-90-day anomalies is a fruitful avenue to explore due to the dominance of the quasi-predictable Madden-Julian oscillation in this frequency band. Such improved forecasts could increase lead time to distribute forecasts to self-sustaining Sahelian farmers and could allow the National Hurricane Center (NHC) to focus more resources on the East Atlantic when 30-90-day AEW activity trends upward. Given the relationship between the MJO and AEW precursors in East Africa (Alaka and Maloney 2012; see Section 1.5), this region will be studied as an initiation region for increases in downstream 30-90-day AEW activity. In this study, the growth, maintenance, and decay of AEWs on intraseasonal (i.e., 30-90-day) time scales are scrutinized using perturbation energy and moisture budgets. Thus, the evolution of 30-90-day AEW activity will be linked to dynamical and diabatic sources of kinetic energy.

1.2 African Easterly Waves: An Overview

African easterly waves (AEWs) are synoptic-scale eddies that initiate and grow via energy conversions over tropical North Africa during boreal summer (Carlson 1969a,b; Burpee 1972, 1974; Norquist et al. 1977; Reed et al. 1977). These eddies have wavelengths of 3000-4000 km (Kiladis et al. 2006) and are characterized by a 2.5-6-day regime that is symmetric

about the African easterly jet (AEJ; Diedhiou et al. 1999; Pytharoulis and Thorncroft 1999). The eddies to the south of the AEJ (i.e., AEWs) are typically characterized by strong fluctuations in deep convection and vorticity signatures at 700 hPa, while the eddies north of the AEJ are typically dry, are located near 900 hPa, and are generally unimportant for tropical cyclogenesis (Thorncroft and Hodges 2001; Zawislak and Zipser 2010). The northern and southern eddy tracks converge into a single track in the eastern Atlantic just north of the AEJ (Reed et al. 1988). Several studies have identified a 6-9-day regime that is asymmetric about the AEJ, but these disturbances appear to be dynamically different from AEWs (Diedhiou et al. 1998, 1999; Wu et al. 2013).

AEWs generally initiate somewhere east of 10°E in association with convection and topography (Carlson 1969a,b). Recent studies have focused on upstream convective disturbances between the Darfur Mountains (15°N, 23°E) and Ethiopian Highlands (10°N, 25°E) that grow along the AEJ into mature AEWs (Hall et al. 2006; Kiladis et al. 2006; Mekonnen et al. 2006; Thorncroft et al. 2008; Leroux and Hall 2009). The Cameroon highlands (8°N, 10°E) and Fouta Djallon highlands (10°N, 10°W) may be important for spawning convection after AEWs have already developed and propagated downstream. (Thorncroft et al. 2008) contended that AEWs are initiated by a localized forcing in the form of upstream latent heating associated with topography, which is plausible given that upstream latent heating strengthens the meridional potential vorticity (PV) gradient associated with the WAM and provides a more favorable environment for AEW growth (Schubert et al. 1991). An influx of PV into this region from the midlatitudes implies that the extratropics could force AEW initiation also.

AEW characteristics evolve as these disturbances propagate to the west. For example, the phase speed of AEWs decreases from \sim 12 m s⁻¹ east of Greenwich to 8.5 m s⁻¹ over the central

Atlantic. Kiladis et al. (2006) found that the outgoing longwave radiation (OLR) signal propagates slightly slower than meridional wind and vorticity fields. In fact, convection tends to be on the west side of the wave axis while over land and on the east side of the wave axis over the East Atlantic (Kiladis et al. 2006). The wave axis appears to catch up to the convection approximately at the Greenwich Meridian. Kiladis et al. (2006) found that the meridional and zonal extents of AEWs are much greater than previously suggested. Meridionally, AEWs may extend from 20°S to 40°N, a huge expanse that opens up the possibility for interaction with the boreal midlatitudes. Analysis of the meridional wind at 10°N reveals a first baroclinic structure, with westward tilted wind maxima below 300 hPa and opposing meridional flow above 300 hPa (Reed et al. 1977; Kiladis et al. 2006). Additionally, National Centers for Environmental Prediction (NCEP) reanalysis and observations of the waves during the Global Atmospheric Research Program (GARP) Atlantic Tropical Experiment (GATE) field campaign provide evidence for a dynamical contraction of AEW zonal wavelengths as they propagate into the East Atlantic (Diediou et al. 1999; Reed et al. 1977). Due to a coupling with deep convection, AEWs feature a vertical structure that extends to the tropopause south of the AEJ. Kiladis et al. (2006) utilize reanalysis to show that the 200 hPa circulation is of the opposite sense to the low-level circulation and slightly displaced to the east. AEWs typically exhibit similar scale and structure as Pacific easterly waves (Reed and Recker 1971), although their generation mechanisms likely differ.

The growth, maintenance, and decay of AEWs are governed by energy conversions that alter the local kinetic energy of the disturbance (Norquist et al. 1977). These energy conversions are crucial to understanding the lifecycle of AEWs on different timescales. Barotropic and baroclinic energy conversions have been the focus of several studies (e.g., Norquist et al. 1977;

Thorncroft and Hoskins 1994a,b), since a reversal in the meridional gradient of PV satisfies the Charney-Stern necessary condition for instability (Charney and Stern 1962), which allows AEWs to grow via a mixed barotropic/baroclinic instability mechanism for about 50° of longitude (Dickinson and Molinari 2000). However, better observations (i.e., the African Multidisciplinary Monsoon Analyses, or AMMA, campaign in 2006) and finer-resolution modeling has increased confidence that diabatic heating within deep convection is an important driver of AEW growth. See Section 2.1 for a more detailed look into the history of research on AEW energetics.

1.3 The West African Monsoon

The West African monsoon (WAM) is a thermally-driven circulation that sets up due to the strong temperature gradient between the Sahara Desert and the Gulf of Guinea (Alaka 2010). The West African monsoon is a complex system, with several jets and circulations tightly fit into a ~ 4000 km stretch from south of the equator to Europe (Fig. 1.2). The intertropical discontinuity (ITD) is a surface front that marks the convergence of moist southwesterly monsoon flow (shaded red in Fig. 1.2) with dry northeasterly flow that resembles a weaker version of the winter Harmattan winds (shaded blue in Fig. 1.2; Sultan and Janicot 2003). This convergence, which is visible even at 850 hPa (near 20°N in Fig. 1.3a), fuels the Saharan heat low ($\sim 20^{\circ}\text{N}$) and pumps air upward in a dry adiabatic layer that extends to nearly 600 hPa (see Fig. 2.18f). This dry adiabatic layer over the Sahara Desert results in a nearly-constant potential temperature (θ) in the lower-troposphere. The reduced potential temperature gradient with respect to pressure in this region is reflected by low Ertel PV (Hoskins et al. 1985), which reverses the sign of the meridional PV gradient and satisfies the necessary condition for combined barotropic-baroclinic instability, as outlined in Charney and Stern (1962) and revisited by Eliassen (1983). It is

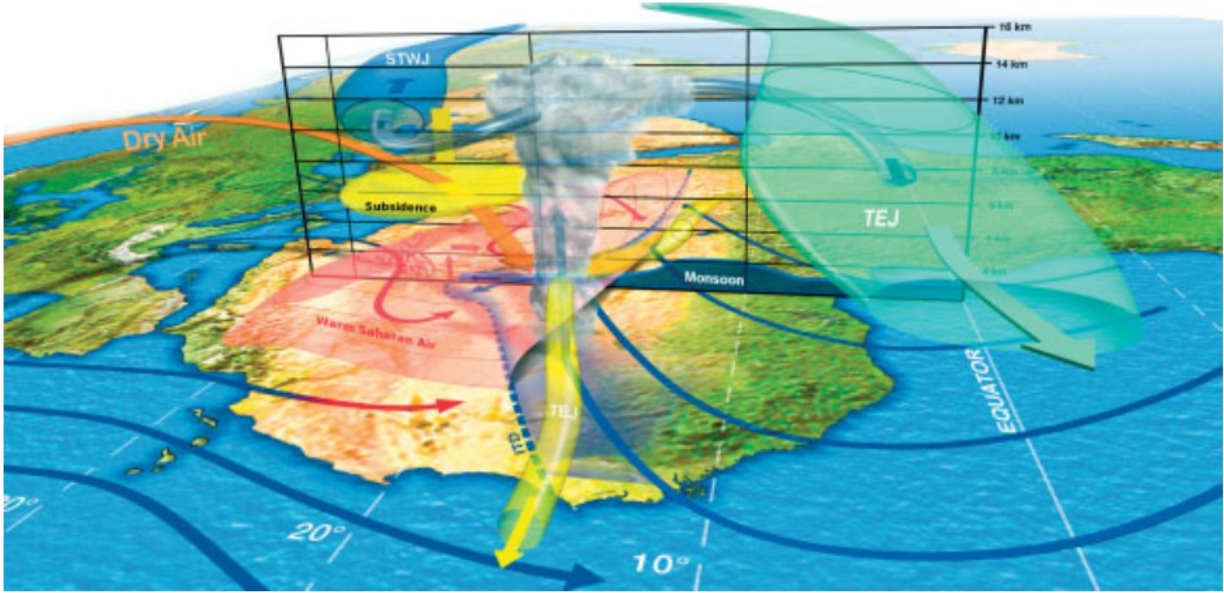


Fig. 1.2 Schematic of the West African monsoon system as viewed from the West adapted from Lafore et al. (2010). “TEJ” in the yellow tube stands for AEJ.

important to note that the Charney-Stern condition for instability is not sufficient, which implies that barotropic and baroclinic energy conversions do not automatically exist in the presence of a meridional PV gradient reversal. The nature of this barotropic-baroclinic instability and its impact of AEW activity on intraseasonal timescales is a focal point of this dissertation.

The African easterly jet (AEJ) is the WAM feature that is most relevant to African easterly waves (AEWs), given the associated barotropic and baroclinic instabilities arising from a reversal in the meridional PV gradient (Charney and Stern 1962). Positioned zonally across North Africa near 15°N, the AEJ, which resides near 650 hPa, is in thermal wind balance with the aforementioned meridional temperature gradient in the region. With maximum easterly velocities over 12 m s⁻¹ in the boreal mean, the AEJ induces significant cyclonic shear, which creates energy for AEWs through barotropic energy conversion (see Section 2.3). Although the AEJ appears as if it were a constant river of air in boreal mean plots (Fig. 1.3b), the reality is that

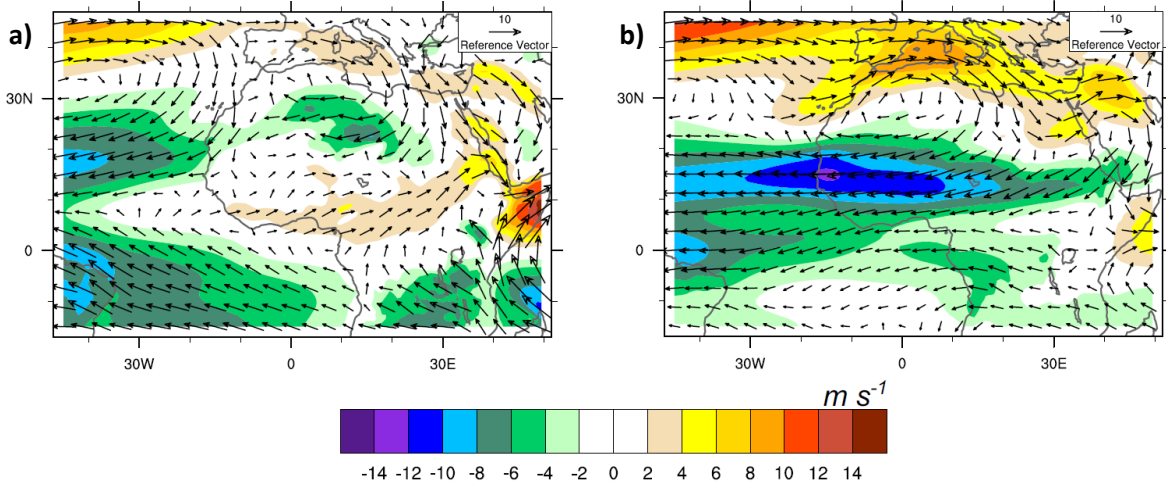


Fig. 1.3 June-September average plots for zonal wind (shading) and total wind (vectors) from 21 years (1990-2010) of ECMWF ERA-Interim data. Winds are plotted at *a)* 850 hPa and *b)* 650 hPa.

the AEJ is quite wavy, with surges of easterly flow helping to roll up 700 hPa vortices associated with AEWs and more quiescent periods with broader, weaker flow.

The tropical easterly jet (TEJ) is a feature near the tropopause over land that dips down into the upper troposphere over the equatorial Atlantic Ocean. In general, the tropical easterly jet does not significantly impact AEW activity. The subtropical jet is located at 200 hPa near 30°N. The subtropical jet might interact with AEW activity through jet breakdowns that result in injections of midlatitude PV into tropical Africa. In fact, boreal summers with stronger subtropical jet breakdowns, which might be linked to the El Nino southern oscillation, feature fewer AEWs propagating into the East Atlantic (personal correspondence with Dr. Thomas Galarneau).

Given the complexity of the WAM, it is imperative that regional climate models reproduce key features of this system in order to reliably compare model output to observations (e.g., reanalyses). Neither the tropical easterly jet nor the subtropical jet have been known to

interact much with AEW activity, so the reproduction of these features within a regional modeling framework will not be a focus.

1.4 The Madden-Julian Oscillation

The Madden-Julian oscillation (MJO) is the dominant mode of intraseasonal (i.e., 30-90-day) variability in the tropics that dominates zonal wavenumbers one to three (Zhang 2005). It was first discovered by Roland Madden and Paul Julian, for whom the phenomenon is named, when they noticed a periodic reversal in the winds every 40-50 days in rawinsonde data from several West Pacific locations (Madden and Julian 1971). When they later expanded their coverage to a more global perspective, they were able to piece together a life cycle for the MJO, with eight phases detailing the state of convection and the position of large-scale zonal circulation cells (Madden and Julian 1972). Overall, the MJO is coupled to convection from its initiation in the Indian Ocean to the International Dateline. Although the main convective envelope of the MJO erodes by the Dateline, the large scale circulation response is global. Thus, the large scale circulation associated with the MJO can produce secondary convection centers in the East Pacific, Atlantic, and Africa (e.g., Hendon and Salby 1994). While the main MJO convective signal is over the Indo-Pacific warm pool, the MJO propagates at $\sim 5 \text{ m s}^{-1}$. Once decoupled from convection east of the Dateline, the MJO signal speeds up to a velocity of 10-15 m s^{-1} (Zhang 2005), often times completing a zonal circuit and enhancing the aforementioned secondary convection centers along the way (e.g., Maloney and Esbensen 2003; Matthews 2004, 2008). In the Indian and West Pacific Oceans, the MJO envelope guides a non-uniform precipitation field that varies due to mesoscale effects.

It should be noted that the initiation and propagation mechanisms of the MJO are still up for debate. However, a recent study by Johnson and Ciesielski (2013) utilized observations from the Dynamics of the MJO (DYNAMO; Yoneyama et al. 2013; Zhang et al. 2013) field campaign to deduce that a gradual moistening of the troposphere precedes an MJO event. Moisture mode theory has emerged as a promising theory to explain the eastward propagation and destabilization of the MJO (e.g., Fuchs and Raymond 2007; Sobel and Maloney 2013). Specifically, the term “moisture mode” describes a disturbance that exists under weak temperature gradients and is regulated by the processes controlling the tropical moisture field (Sobel et al. 2001; Sugiyama 2009a,b). Hopefully, these advances will translate into improved simulations of the MJO in global models.

The MJO circulation responds to diabatic heating induced by deep convection on the equator, which produces a response that is similar to the idealized simulations in the Gill model (Heckley and Gill 1984). Consequently, the equatorial wave response includes forced equatorial Kelvin waves, which propagate ahead of the MJO heating to the east, and equatorial Rossby waves, which take the form of two low pressure systems that straddle the equator and propagate to the west (Matsuno 1966). This Kelvin-Rossby wave response is attached to the MJO heating and is dragged to the east. However, the Kelvin-Rossby response appears to grow in the zonal direction with time even with realistic damping (Heckley and Gill 1984). The MJO is also associated with transient convectively coupled Kelvin waves, which travel faster than the MJO convective envelope and tend to enhance convection in all parts of their world with their passage (Straub and Kiladis 2002, 2003; Roundy 2008; Ventrice et al. 2012; Ventrice and Thorncroft 2013).

Kelvin waves and the MJO explain about the same amount of convective variance (Wheeler and Kiladis 1999), although the former occur at a much wider range of spatial scales and are more meridionally confined to the equator. The Kelvin wave is a symmetric solution to the shallow water equations, and may be coupled or uncoupled with convection (Fig. 1.4b). Convectively coupled Kelvin waves have been shown to enhance convection along the equator with their passage, especially with existing disturbances such as a tropical cyclone (Straub and Kiladis 2002; Ventrice et al. 2012; Ventrice and Thorncroft 2013). Convectively coupled Kelvin waves propagate to the east at $10\text{-}25 \text{ m s}^{-1}$, although uncoupled Kelvin waves propagate much faster (Wheeler et al. 2000). An equatorial Rossby wave is a westward-propagating symmetric response to the shallow water equations, with two low pressure gyres situated on either side of the equator (Fig. 1.4a; Matsuno 1966). Given the cyclonic circulation associated with equatorial Rossby gyres, westerly wind bursts are commonly associated with equatorial Rossby waves. Generally, the poleward flow around each gyre is rising and convectively active, while the equatorward flow subsides and is mostly devoid of convection (Wheeler and Kiladis 1999).

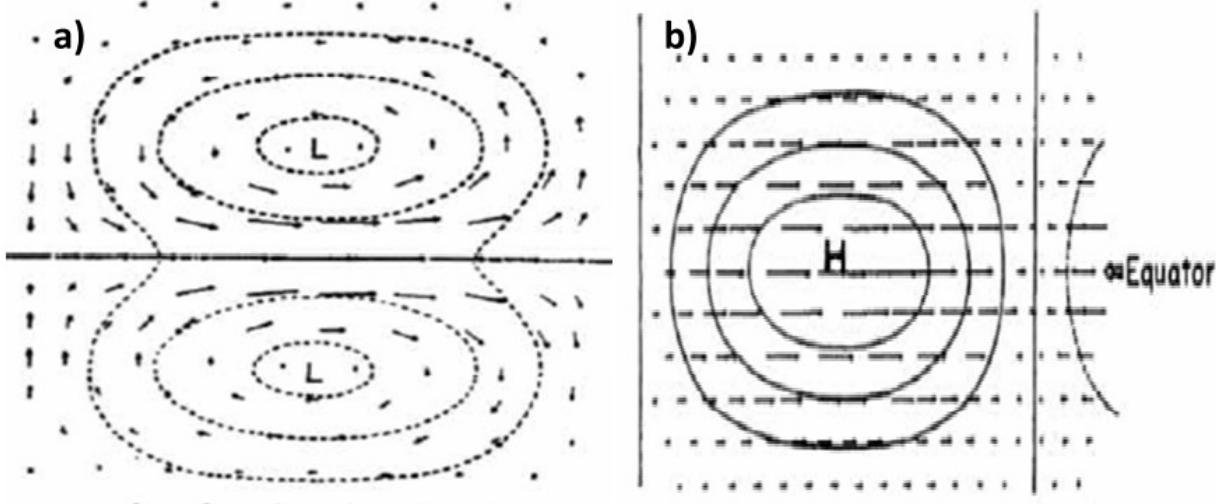


Fig. 1.4 a) Structure of an equatorial Rossby wave from Fig. 4c in Matsuno (1966). b) Structure of an equatorial Kelvin wave from Fig. 8 in Matsuno (1966).

In addition, MJO activity has been linked to worldwide tropical cyclone activity (Maloney and Hartmann 2000a,b, 2001a; Hall et al. 2001; Ventrice et al. 2011; Slade and Maloney 2013). The East Pacific exhibits significant intraseasonal variability, which may be forced partly by local dynamics and partly by the MJO signal propagating across the equatorial Pacific Ocean (Maloney and Hartmann 2000a; Maloney and Esbensen 2003; Rydbeck et al. 2013; Rydbeck and Maloney 2014). Recent studies have linked the MJO with the NAO, which has implications for the storm track and intensity of midlatitude systems on the eastern United States and Europe (Cassou 2008; Lin et al. 2009). The MJO has even been linked with severe tornado outbreaks in the United States (Thompson and Roundy 2013). Finally, as part of the foundation for this study, the MJO has been linked with the West African monsoon in previous studies (See Section 1.5).

1.5 The Influence of the Madden-Julian Oscillation on African Easterly Waves

Previous studies have documented the intraseasonal variability (ISV) of AEWs and the potential mechanisms that drive it. North African ISV may be attributed to large-scale phenomena like the MJO (Matthews 2004; Maloney and Shaman 2008; Janicot et al. 2009; Ventrice et al. 2011; Alaka Jr. and Maloney 2012) or to regional processes like land-surface interactions and local dynamics (Mounier et al. 2008; Janicot et al. 2011). Building upon the hypothesis that East Africa is a triggering region for AEWs (Thorncroft et al. 2008), Alaka and Maloney (2012) investigated how the MJO modulates AEW initiation. They observed significant 30-90-day moisture and convection anomalies in an East African “trigger region” prior to maximum, MJO-related convection and AEW activity in West Africa. Alaka and Maloney (2012) discussed that equatorial waves (i.e., Kelvin waves and equatorial Rossby waves)

spawned by the MJO are responsible for modulating convection and AEWs in tropical North Africa (Fig. 1.5). These authors found three mechanisms by which the MJO influences East African convection and, consequently, West African easterly wave activity: 1) an anomalous positive northward moisture flux, 2) eastward extension of the AEJ, and 3) decreased static stability. Positive northward moisture flux anomalies dominate the growth of moisture anomalies in the “trigger region” prior to maximum 30-90-day eddy activity in West Africa. An extension of the AEJ into the “trigger region” would increase barotropic and baroclinic energy conversions, leading to stronger AEWs (Alaka and Maloney 2012, Leroux et al. 2010). In addition, Matthews (2004) found that eastward-propagating Kelvin waves, which are initiated by the MJO in the West Pacific, increase the convection and the cyclonic shear associated with the AEJ. Upon reaching tropical Africa, the Kelvin wave appears to be associated with negative 30-90-day temperature anomalies near 400 hPa (Alaka and Maloney 2012). These Kelvin waves may impact easterly wave activity in the East Pacific (Rydbeck et al. 2013).

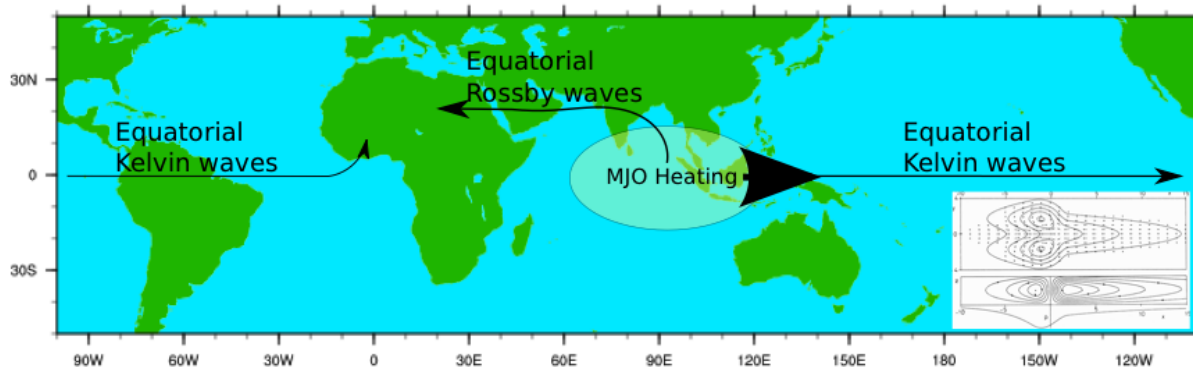


Fig. 1.5 A simple schematic of how equatorial waves propagate from MJO heating into tropical North Africa. The inset (from Heckley and Gill 1984) represents the circulation response to a heating along the equator.

The ISV of AEWs is associated with 30-90-day spectral peaks in North African rainfall, winds, and eddy activity (Sultan et al. 2003; Maloney and Shaman 2008; Pohl et al. 2009; Coëtlogon et al. 2010; Janicot et al. 2011). Using a simple modeling framework, Leroux and Hall (2009) found that ISV in the AEJ governs whether or not an upstream convective anomaly will mature into an AEW. Leroux et al. (2010) determined that convective anomalies near the Darfur Mountains preceded ISV of AEWs, which is consistent with the East African triggering hypothesis (e.g., Thorncroft et al. 2008). The ISV of AEWs may be a vital component in understanding how the MJO modulates tropical cyclone activity (Maloney and Shaman 2008; Ventrice et al. 2011; Slade and Maloney 2013). Models such as the monthly European Centre for Medium-Range Weather Forecasts (ECMWF) Ensemble Prediction System (EPS) exhibit strong sensitivity of Atlantic tropical cyclone activity to MJO phasing and amplitude (Vitart 2009; Belanger et al. 2010), which has been partly attributed to the ISV of AEWs. Predicting periods of increased or decreased eddy activity, and concurrent rainfall anomalies, in North Africa would improve precipitation forecasts across the Sahel and tropical cyclogenesis forecasts in the eastern Atlantic Ocean within a given boreal summer season.

1.6 Energy Budgets

In order to understand the growth, maintenance, and decay of AEW activity on intraseasonal time scales, we utilize the perturbation kinetic energy (PKE) and perturbation available potential energy (PAPE) budgets. Lorenz (1955) was the first to derive the zonal mean and eddy forms of the potential and kinetic energy budgets during his analysis of the general circulation of the atmosphere. In some past studies, AEWs have been analyzed as eddies relative to the zonal mean (e.g., Hsieh and Cook 2007). Here, AEWs are presented as temporal

perturbations from mean state fields that persist for several days (e.g., the AEJ). In this study, we define the terms PKE and PAPE as in previous studies on tropical energetics (Lau and Lau 1992; Maloney and Dickinson 2003):

$$PKE = \frac{\overline{u'^2 + v'^2}}{2} \quad (1.1)$$

$$PAPE = c_p \gamma \frac{\overline{T'^2}}{2\bar{T}} \quad (1.2)$$

where u is the zonal wind, v is the meridional wind, T is the temperature, c_p is the specific heat at constant pressure and γ is inversely proportional to static stability (see Appendix A). The PKE and PAPE budgets are derived by separating variables into a time mean and a perturbation from that mean. For example, \bar{T} represents the time mean temperature, while T' corresponds to the perturbation from the time mean temperature. One advantage of separating based on a temporal mean is the freedom to choose a timescale of interest.

In this study, energy conversion terms are calculated by employing an 11-day running mean and a perturbation about this mean for appropriate variables to completely capture the 2.5-6-day periods associated with AEWs (Wu et al. 2013). The PKE and PAPE budget results are robust for timescales ranging from 7 to 15 days, but the analyses to follow use the 11-day running mean. A bandpass filter is not used to formulate the PKE and PAPE budgets, consistent with previous studies (Maloney and Hartmann 2001b; Maloney and Dickinson 2003). Hence, periods less than 2.5 days will be included in the perturbation terms used to calculate budget terms, although this does not qualitatively affect our results. In subsequent chapters, intraseasonal anomalies of the various energy budgets terms are diagnosed by using a linear nonrecursive digital bandpass filter with half-power points at 30 and 90 days, which is applied after calculation of the budget terms.

Following Lau and Lau (1992) and equations A.14 and A.15 in Appendix A, the PKE and PAPE budgets are defined as:

$$\partial_t PKE = A_M + A_P + B_T + \phi_{FC} + C_{pk} + D \quad (1.3)$$

$$\partial_t PAPE = Q_T + B_C - C_{pk} + R \quad (1.4)$$

where $\partial_t PKE$ is the PKE tendency and $\partial_t PAPE$ is the PAPE tendency. The advection of PKE by the time-mean wind (A_M ; A.2) and by the perturbation wind (A_P ; A.3) both describe the movement of PKE from one location to another, but since the global integral of each term is zero, they do not provide any information about how PKE is created or destroyed. Barotropic energy conversion (B_T ; A.5) describes the transfer of mean kinetic energy to PKE in the presence of horizontal wind shear. In North Africa, the AEJ transfers momentum to AEWs via B_T , yet the AEJ is maintained due to the strong boreal summer temperature gradient between the Gulf of Guinea and the Sahara (Rennick 1976). The convergence of perturbation geopotential flux (ϕ_{FC} ; A.6) denotes the horizontal movement of perturbation geopotential height due to local convergence. “Pressure work” is defined as the addition of ϕ_{FC} and C_{pk} (A.7) and describes the work done by the pressure gradient force to accelerate/decelerate the circulation (Hsieh and Cook 2007; Diaz and Aiyyer 2013b). The conversion of PAPE to PKE (C_{pk}), which represents vertical temperature flux, creates PKE through the rising (sinking) of warm, light (cold, dense) air in a process referred to as baroclinic overturning. D represents the dissipation of PKE through friction and other sub-grid scale processes. Further, any PKE budget residual that might be due to reanalysis model deficiencies or due to errors introduced in calculating terms with post-processed data is also contained within D .

In Eq. 1.4, the PAPE tendency is balanced by four terms. The generation of PAPE by diabatic heating (Q_T ; A.8) is positive when diabatic heating and temperature anomalies covary.

Baroclinic energy conversion (B_C ; A.9) describes the conversion of mean available potential energy to PAPE and results from a perturbation temperature flux being directed down the mean temperature gradient. C_{pk} appears in the PAPE budget, in addition to the PKE budget, since this term explains the transfer between the PAPE and PKE energy reservoirs. Finally, the residual (R) represents errors in parameterizing microphysical and other subgrid-scale processes that are not captured by the reanalysis model, in addition to errors introduced from calculations.

1.7 Study Overview

African easterly waves are an important part of the climate system and have a noticeable impact on society. In particular, AEWs impact rainfall for self-sustaining Sahelian communities and seed tropical cyclones, which take lives and disrupt communities throughout North and Central America. Accordingly, improved forecasts of AEW activity have the potential to significantly improve the quality of life for a significant portion of the northern hemisphere population. The improvement of AEW predictability may depend upon linking West Africa with East Africa. Previous studies have demonstrated that East Africa is a breeding ground for AEWs (e.g., Kiladis et al. 2006; Thorncroft et al. 2008), and the ingredients for a 30-90-day uptick in AEW activity may be strongly linked to convection in this region. In light of Alaka and Maloney (2012), the MJO may have a strong link with AEW precursors in East Africa. The MJO could also have a more direct relationship with West Africa, as discussed in Ventrice et al. (2011). Overall, linking AEW activity with large-scale phenomena, such as the MJO, is paramount to lengthening reliable AEW forecasts.

The purpose of this study is to analyze the intraseasonal PKE, PAPE, and moisture budgets to provide clues as to why easterly waves vary on intraseasonal timescales, and also to

study the extent to which significant, positive 30-90-day 700 hPa PKE events are forced locally and by remote phenomena (e.g., MJO). The relationship between East African convection and West African AEW activity is a focus since East Africa has been hypothesized as an AEW initiation region in real-time (Thorncroft et al. 2008) and on intraseasonal time scales (Alaka and Maloney 2012). Overall, better insight into the influences of the MJO and East African convection on surges of 30-90-day AEW activity would help improve medium-range forecasts in this region overall, especially the prediction of local rainfall and downstream tropical cyclones.

The remainder of the study is set up as follows. In Chapter 2, the extent to which intraseasonal variability of AEW energetics is modulated by the MJO is studied using observations. Chapter 3 investigates the ability of different WRF dynamical cores and parameterizations to reproduce a realistic WAM climatology. In Chapter 4, the model found in Chapter 3 with the most accurate WAM climatology is used to analyze intraseasonal variability in West Africa and the role that eastward- and westward-propagating 30-90-day disturbances have in modulating that variability. Chapter 5 presents the main findings of this study, and explores potential avenues for future research on this topic.

CHAPTER 2 The Intraseasonal Variability of African Easterly Wave Energetics in Observations¹

2.1 Introduction

The results presented here may be found in a condensed, published form in Alaka and Maloney (2014). As discussed in Section 1.3, energy conversions dictate AEW growth as they approach the East Atlantic. The energetics of AEWs were first introduced by Burpee (1972) and first investigated by Norquist et al. (1977). Early works demonstrated that AEWs extract energy from the AEJ via barotropic and baroclinic energy conversions (Norquist et al. 1977; Thorncroft and Hoskins 1994a,b), while more recent studies have emphasized the importance of convection to AEW growth (Hsieh and Cook 2005, 2007, 2008; Berry and Thorncroft 2012). Although it was hypothesized by Norquist et al. (1977) that condensational heating is an important process for AEW growth and maintenance, adequate observations and models have only recently allowed the meaningful investigation of the relationship between AEWs and convection. Kiladis et al. (2006) found that dynamical forcing associated with the wave initiates AEW convection, with forced vertical motion at low levels that couples the wave to deeper convection as it matures. Despite the presence of an unstable jet, Hsieh and Cook (2005) suggested that associated potential vorticity gradients were insufficient to support observed AEW amplitudes. The AEJ is also too short and the residence time of AEWs in the vicinity of the AEJ is too small to produce observed AEW growth rates (Thorncroft et al. 2008). In short, normal mode growth rates are insufficient to explain observed growth rates. Hall et al. (2006) explained that realistic friction renders the AEJ stable to small anomalies. Thus, convection has been hypothesized to be

¹ Ghassan J. Alaka Jr. and Eric D. Maloney, 2014: The Intraseasonal Variability of African Easterly Wave Energetics. *J. Climate*, **27**, 6559–6580. doi: <http://dx.doi.org/10.1175/JCLI-D-14-00146.1>

important for initiating and maintaining AEWs, while barotropic and baroclinic conversions associated with the AEJ could help maintain the disturbance further downstream (Hsieh and Cook 2008). Diaz and Ayyer (2013a,b) suggest that upstream energy dispersion is a better explanation for AEW initiation than convective forcing. They diagnosed the direction of the dispersion using the ageostrophic geopotential flux, which is one component of the pressure work term. Although the energetics of AEWs have been the focal point of several recent studies, it is unclear how the intraseasonal evolution in kinetic energy-producing processes (e.g., barotropic energy conversion, baroclinic energy conversion, diabatic heating) relates to the growth of AEWs on 30-90-day timescales.

The perturbation kinetic energy (PKE) and perturbation available potential energy (PAPE) budgets have been useful for investigating tropical disturbances across the globe (Lau and Lau 1992; Maloney and Dickinson 2003). Previous studies have analyzed these budgets in other regions, such as the West Pacific and East Pacific (Maloney and Dickinson 2003; Maloney and Hartmann 2000). Leroux et al. (2010), in a West African study, found that PKE is preceded by an intraseasonal modulation of convection, which implicates the general importance of diabatic heating. This is the first study that performs a comprehensive analysis of intraseasonal PKE and PAPE budgets in tropical North Africa. We will explore how energy conversion terms in the PKE and PAPE budgets impact the ISV of AEWs. A primary focus will be on the evolution of PKE and PAPE budget terms with composites based on local (e.g., 30-90-day PKE index) and global (e.g., MJO) indices. In particular, an index of AEW activity at 700 hPa will be used to assess ISV associated with the strongest AEWs. Composites based on an MJO index will be used (e.g., Wheeler and Hendon 2004) to assess the extent to which the MJO explains local 30-90-day variability in PKE and PAPE budgets. Due to the strong ISV of moisture and the AEJ

observed in East Africa, which precedes PKE anomalies downstream in West Africa (Alaka and Maloney 2012), the role of energy budget terms in this region will be a focal point of this study.

2.2 Methodology

In this observation-based study, the intraseasonal variability of AEW energetics is diagnosed from the PKE and PAPE energy budgets (Section 1.6). The PKE and PAPE budgets analyzed in this chapter are calculated from the ECMWF Interim Re-Analysis (ERA-Interim; Dee et al. 2011) and the National Centers for Environmental Prediction (NCEP) Climate Forecast System Reanalysis (CFSR; Saha et al. 2010) datasets. ERA-Interim has a horizontal resolution of T255 (0.70°) and 60 vertical levels, while CFSR has a horizontal resolution of T382 (0.50°) and 64 vertical levels. In this study, the temporal ranges of ERA-Interim and CFSR are 21 years (1990-2010) and 11 years (2000-2010), respectively. The resolution of all input data is degraded to a 1.5° grid, and budgets are calculated using four times daily temporal resolution to capture periods of AEW growth that often occur within the scope of a single day. Boreal summer is identified as June through September, when AEWs are most active. A caveat of ERA-Interim and CFSR is a relative lack of observations in North Africa, given a decreasing number of rain gauge and sounding stations in the region (Ali et al. 2005). Additionally, it is important to remember that reanalysis models come with their own biases and data assimilation increments. For example, Mapes and Bacmeister (2012) describe shortfalls of the National Aeronautics and Space Administration (NASA) Modern-Era Retrospective analysis for Research and Applications (MERRA; Rienecker et al. 2011) tendency height fields, identifying analysis increments representative of errors in parameterized heating and drying fields. We find that a strong correlation exists between Q_T and R in North Africa for ERA-Interim, suggesting that

much of the residual in our analysis is due to misrepresenting Q_T due to errors in deep convection and boundary layer processes.

MERRA exhibits West African monsoon features and PKE variability consistent with ERA-Interim and CFSR, but is not analyzed further in this study. Since this region does not have many constraining observations, each reanalysis product may create a different representation of West African PKE budgets that is strongly influenced by model physics, a point that should be kept in mind when interpreting results below. Comparing energy budgets across a suite of reanalysis products may be a fruitful avenue for future research.

A Student's t test at the 95% confidence interval (e.g., Spiegel 1992) is performed in many of the analyses described below to determine the significance of anomalies over tropical North Africa. In MJO phase composites, we calculate the degrees of freedom by dividing the average number of days in a given MJO phase (168 days) by the characteristic number of days that the MJO resides in a given phase (~5 days). Thus, degrees of freedom (i.e., 34) represent the approximate number of individual MJO events for a single phase. In lead/lag composites generated using a West African PKE index (see Section 2.2.2), the degrees of freedom are determined as two less than the total number of individual PKE events (i.e., 34).

2.3 Remote and Local Intraseasonal Variability

The MJO is the dominant mode of ISV in the tropics, with a significant spectral peak at about 50 days (Zhang 2005). From Wheeler and Hendon (2004), a multivariate MJO index is created to investigate ISV in tropical North Africa during a composite MJO life cycle. Since the MJO is described by atmospheric circulations and moist convection that are organized on planetary scales, or eastward zonal wavenumbers 1-3 (Madden and Julian 1994), the MJO index

will be especially useful in diagnosing the 30-90-day variability in tropical North Africa that is associated with large scale, remote, MJO-influenced anomalies in the tropics. However, since the MJO might not describe all ISV in tropical North Africa (Janicot et al. 2009; Alaka and Maloney 2012), local 30-90-day 700 hPa PKE anomalies are averaged in West Africa to also create a PKE index, and composites are generated based on significant maxima in AEW activity. The evolution of PKE and PAPE budget terms is examined for both the MJO and local PKE indices. Studies have shown that the MJO emits equatorial waves that modulate the ISV in tropical North Africa (Matthews 2004; Maloney and Shaman 2008; Alaka and Maloney 2012), which suggests that the ISV diagnosed by these two indices might be related.

2.3.1 MJO Index

On the basis of methods described in Wheeler and Hendon (2004), the MJO index is created through multivariate EOF analysis performed on ERA-Interim 850- and 200-hPa zonal winds and ERA-Interim outgoing longwave radiation (OLR). Before EOF analysis, the seasonal cycle is removed, a 30-90-day bandpass filter is applied, fields are averaged from 15°S to 15°N, and each field is normalized separately. The first two EOFs explain 25.65% and 24.71% of the total combined variance, respectively, with the first EOF in quadrature with the second EOF, representative of the eastward propagation of the MJO (not shown).

MJO amplitude and phase may be calculated from the two leading principal components (Wheeler and Hendon 2004). The amplitude and phase are determined by:

$$\text{Amplitude} = \sqrt{PC1^2 + PC2^2} \quad (2.1)$$

$$\text{Phase} = \arctan\left(\frac{PC2}{PC1}\right) \quad (2.2)$$

where $PC1$ and $PC2$ are the first and second principal components, respectively. The amplitude

time series (5) describes the normalized amplitude of the MJO for any given day. The phase time series (6) describes the stage of the MJO life cycle and, consequently, the approximate longitudinal location of the MJO. For plotting purposes, the MJO life cycle is broken into eight phases of equal angular extent, with each phase representing approximately five days. In 21 years of ERA-Interim data, the average number of significant days (amplitude $>1\sigma$) per MJO phase is 168 during June-September.

2.2.2 700 hPa Perturbation Kinetic Energy Index

Since 700 hPa PKE anomalies are a proxy for AEW activity, we create an intraseasonal PKE index in West Africa by averaging 700 hPa PKE_{30-90} from $5^{\circ}\text{N} - 15^{\circ}\text{N}$, $20^{\circ}\text{W} - 0^{\circ}$. This region is near a local maximum in boreal summer PKE variance (not shown) and exhibits a significant peak at the 95% confidence level in the 30-90-day band (Fig. 2.1). The PKE index provides 36 positive, significant events ($>1\sigma$) for an average of 1.7 events per boreal summer. These events will be referred to as “positive PKE events.” In the opposite sense, negative, significant events ($<-1\sigma$) in the PKE index are referred to as “negative PKE events”. Most of the analysis to follow focuses on positive PKE events.

To compare the PKE index to the MJO index, lag correlations are calculated with respect to $PC1$ and $PC2$. The PKE index and $PC1$ have a maximum anticorrelation of -0.3 at lag 0. Similarly, the PKE index and $PC2$ have a significant correlation of 0.3 when $PC2$ leads PKE by 10 days. A Student’s t test reveals that the correlation threshold for 95% significance is -0.25. Degrees of freedom were calculated by assuming about 40 days in a typical MJO cycle, which produces 64 MJO events across the 21 boreal summers. While this correlation coefficient is statistically significant from zero at the 95% confidence level, the MJO index only explains

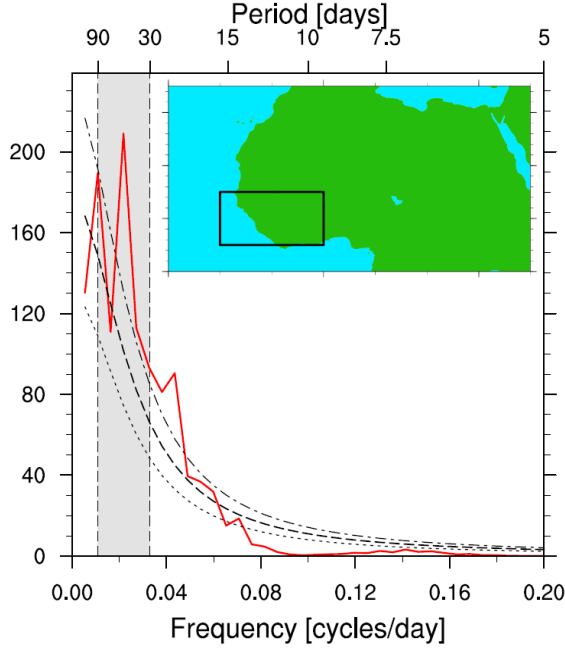


Fig. 2.1 Boreal summer power spectra for 700 hPa PKE averaged between 5°N-15°N and 20°W-0° (see map) for 1990-2010. The associated red noise spectrum with 95% confidence bounds is given by the black curves. The gray shading represents the 30-90-day band.

~10% of the variance of the PKE index, which suggests that a large amount of boreal summer ISV in this region is unrelated to the MJO. Other phenomena that could play a role in the ISV in West Africa include the North Atlantic oscillation (NAO; Walker 1924), the quasi-biweekly zonal dipole (QBZD; Mounier et al. 2008), and internal variability of the West African monsoon system.

Although the correlation between the PKE and MJO indices is significant but modest for all years, we investigate how the lag correlation changes when the analysis focuses on boreal summers with strong MJO activity. Years with strong MJO activity are identified by counting the number of significant MJO days (amplitude $>1\sigma$) between June 1 and September 30 in each year. The correlation of the PKE index with the principal components of the MJO index is compared for various thresholds of number of significant MJO days (Fig. 2.2). Thresholds of 70

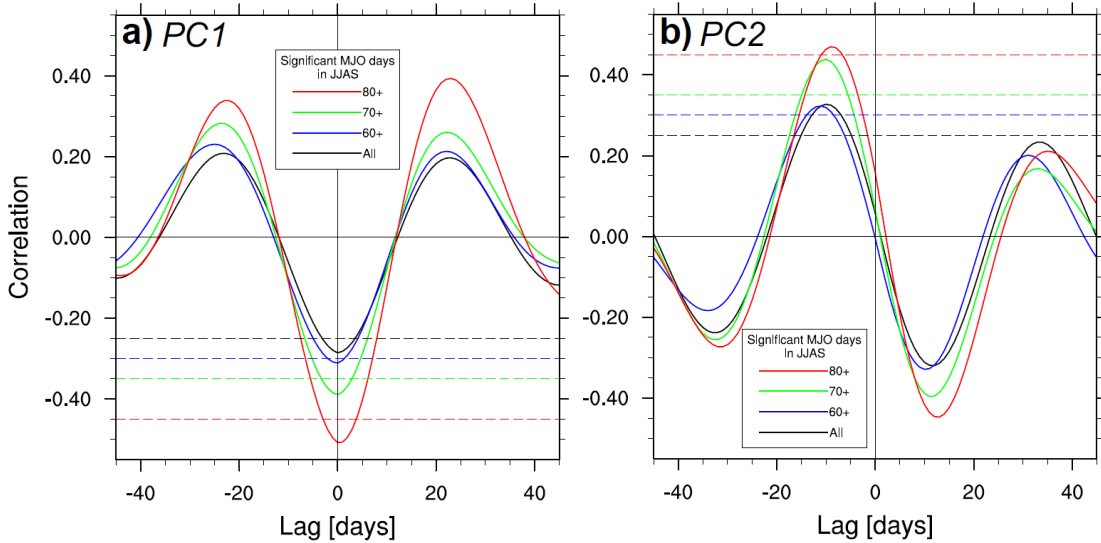


Fig. 2.2 The 30-90-day 700 hPa PKE index lag correlated with (a) PC1 of the MJO index and (b) PC2 of the MJO index. The black line includes JJAS for all 21 years. The blue line includes JJAS with at least 60 significant MJO days (14 years). The green line includes JJAS with at least 70 significant MJO days (ten years). The red line includes JJAS with at least 80 significant MJO days (six years). Dashed lines represent the 95% significant threshold for each subset.

days or higher noticeably increase the correlation (Fig. 2.2). If the threshold is set to 80 significant MJO days, six strong MJO years are retained (1996, 2000, 2001, 2002, 2004, and 2008). In these strong MJO years, the PKE index and *PC1* have a maximum anticorrelation of -0.51 at lag 0 (Fig. 2.2a), while the PKE index and *PC2* have a maximum of correlation of 0.47 when *PC2* leads PKE by 10 days (Fig. 2.2b). Positive PKE events are also sensitive to MJO phase. Most positive PKE events occur during MJO phases 2-4. The sensitivity of AEW activity to MJO amplitude and phase has been acknowledged in previous studies (e.g., Vitart 2009; Belanger et al. 2010). With these sensitivities in mind, the subsequent analysis focuses on positive PKE events within all boreal summers between 1990 and 2010.

The analyzed lag between $PC1$, $PC2$, and West African PKE can be observed by plotting time series of these indices (Fig. 2.3). In three intraseasonal PKE events captured between May and October 2002 (a strong MJO year), $PC1$ peaks first, followed by $PC2$ 1-2 weeks later, and finally by a peak in West African PKE 1-2 weeks later. This sequence does not occur consistently in boreal summers with weak MJO activity, meaning that factors other than the MJO influence positive intraseasonal PKE events in West Africa. Despite the relatively low correlation between the PKE and MJO indices, local intraseasonal PKE events exhibit a clear relationship with the MJO index during years with strong MJO activity. Future work will investigate if nonlinear correlations are more appropriate to diagnose the relationship between the PKE and MJO indices.

Further evidence for a relationship between West African PKE and the MJO can be found by analyzing the large-scale tropics and midlatitudes prior to positive PKE events. As discussed in Alaka and Maloney (2012), upper-level temperature anomalies forced by MJO convection can

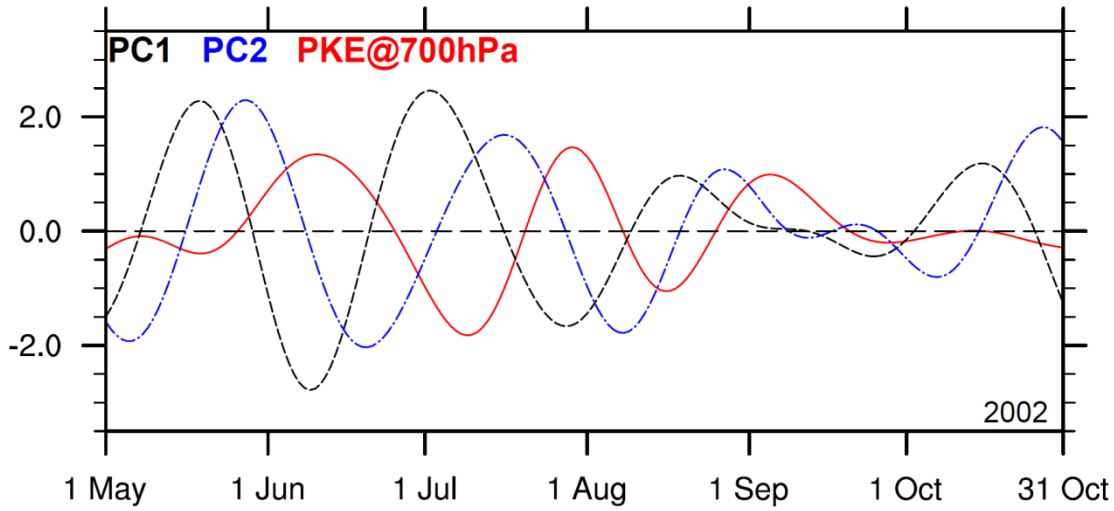


Fig. 2.3 Sample time series are shown for $PC1$ (black, dashed), $PC2$ (blue, dot-dashed), and 30-90-day 700 hPa PKE (red, solid) indices for a boreal summer with strong MJO activity (1 May 2002 and 31 October 2002). Each index is normalized by its standard deviation.

propagate into tropical North Africa and affect the stability in that region. A week prior to positive PKE events, upper-level T_{30-90} anomalies reveal a response that strongly resembles the Gill model with realistic damping (Fig. 2.4a; Heckley and Gill 1984). The northern Rossby gyre in the Gill model response is located near 30°N, 45°E at day -7, although significant 400 hPa T_{30-90} anomalies spread from India to the Greenwich Meridian. By day 0, significant T_{30-90} anomalies cover most of tropical North Africa, as the Kelvin wave and equatorial Rossby wave responses converge on the Greenwich Meridian. Although temperature anomalies in West Africa are significant on day 0, it is unclear how big of role 0.1 degrees will have on destabilizing the column. Upper-level thickness anomalies (200-400 hPa) are collocated with T_{30-90} anomalies, and actually show the Gill model response more convincingly (Fig. 2.5). A general observation

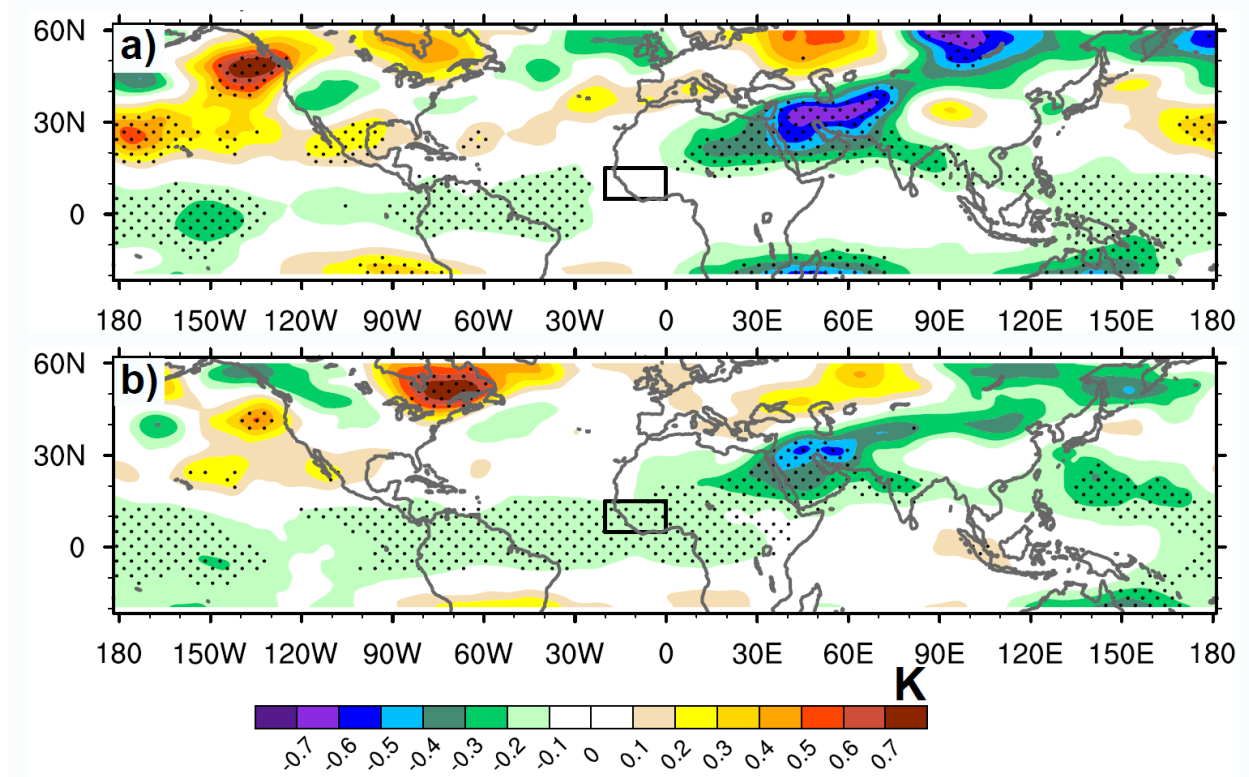


Fig. 2.4 Lead/Lag composites for a) Day -7 and b) Day 0 for ERA-Interim 400 hPa 30-90-day temperature anomalies. The shading interval is 0.1 K. Stippling represents 95% significance.

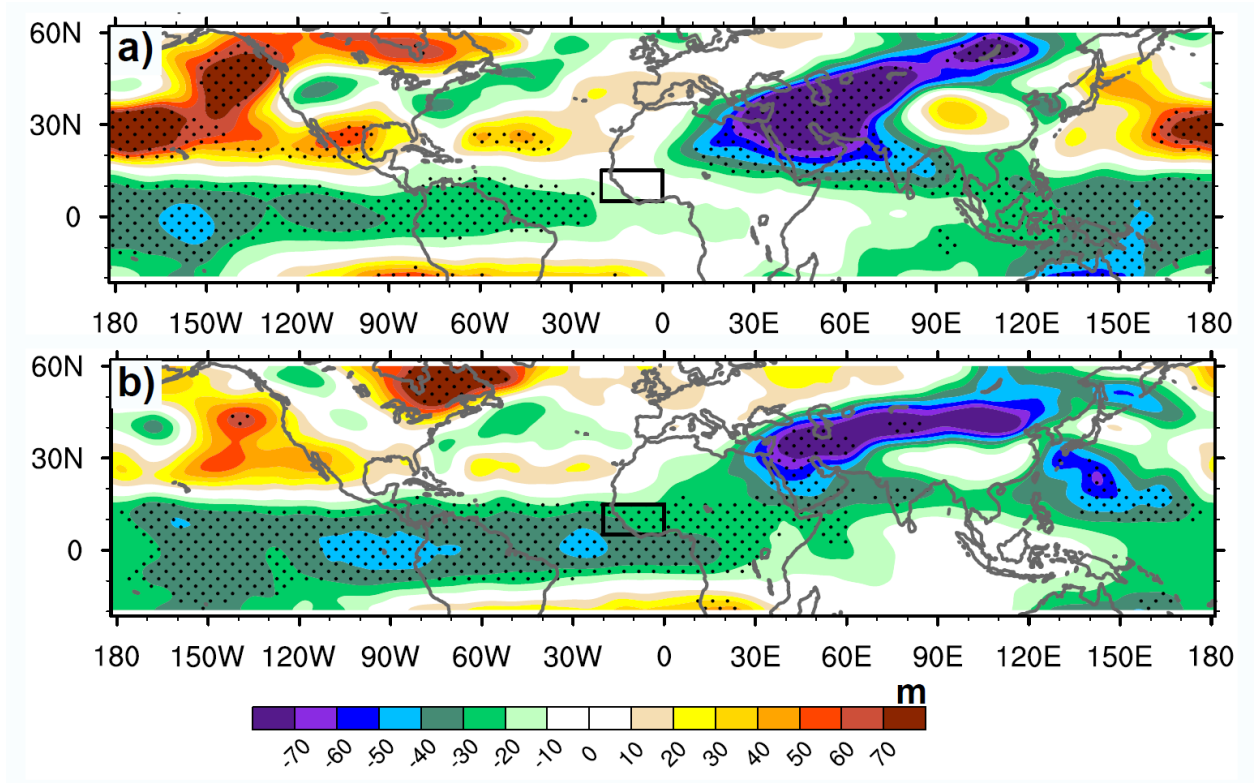


Fig. 2.5 Lead/Lag composites of a) Day -7 and b) Day 0 for ERA-Interim 30-90-day 200-400 hPa thickness anomalies. The shading interval is 10 m. Stippling represents 95% significance.

is that the equatorial Rossby wave response seems to impact East Africa a week prior to positive PKE events, while the Kelvin wave response impact West Africa near day 0.

Since the upper-tropospheric structures in Figs. 2.4 and 2.5 strongly resemble a Gill model response to equatorial heating, future research will test the robustness of the circulation response to idealized equatorial heating results attained in Heckley and Gill (1984) in a higher-order global circulation model. It is also worth noting the positive T_{30-90} anomalies centered near 55°N, 60°E are to the north of negative T_{30-90} anomalies over the Arabian peninsula, implicating midlatitude wave-breaking as a potential player. Future work will investigate the relationship between midlatitude wave-breaking the AEWs.

2.2.3 East African Indices

East Africa has been hypothesized to be a breeding ground for African easterly waves, with finite-amplitude convective events that initiate between the Darfur Mountains and Ethiopian Highlands and associated circulations gaining energy as they propagate to the west. In the analysis of Alaka and Maloney (2012), the importance of East Africa as an initiation zone for AEWs was investigated for intraseasonal timescales. As discussed in the introduction of this chapter, Alaka and Maloney (2012) concluded that the MJO does strongly modulate the East African atmosphere, with a modulation of meridional moisture fluxes and the AEJ evident near the “trigger region” (10.5°N - 24°N , 16.5°E - 37.5°E) that precedes increased downstream AEW activity. Alaka (2010) discusses the relationship between the MJO and trigger region on 30-90-day time scales in much greater depth, so those findings will not be recited here. However, the relationship between intraseasonal convective anomalies in East Africa and the MJO represents an additional pathway for the MJO to modulate AEWs. Intraseasonal convective anomalies in East Africa are investigated through the following fields: 1) CLAUS T_B , ERA-Interim OLR, and ERA-Interim total precipitable water (TPW). Since none of these variables directly quantifies convection, the use of all three variables is important to test the robustness of results in a region that is devoid of measured observations.

CLAUS T_B anomalies averaged in the trigger region exhibit significant 45-90-day spectral power when analyzed from May to October for 17 years (Fig. 2.6), suggesting that convective anomalies in East Africa could be modulated by, or at least related to, the MJO. The broad peak from 3-5 days is likely linked to AEW initiation in this region, where convective precursors grow upscale (e.g., Hall et al., 2006; Thorncroft et al. 2008; Leroux & Hall, 2009). Clearly, significant ISV in East Africa is limited to longer timescales within the intraseasonal

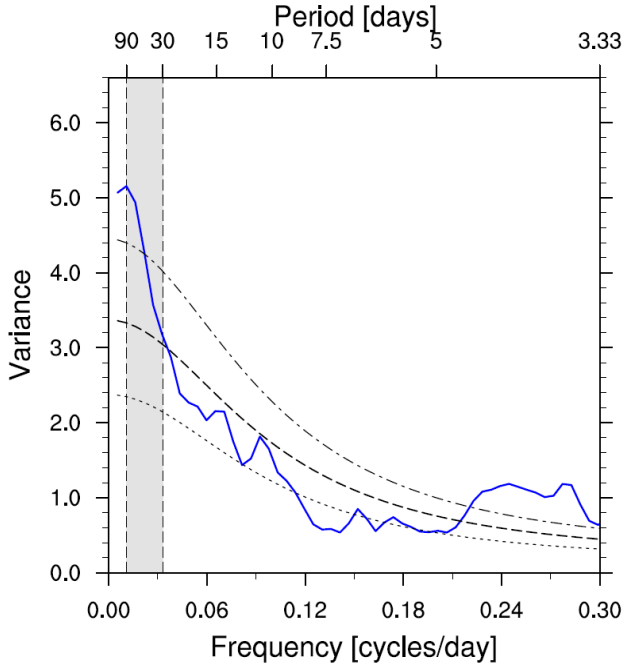


Fig. 2.6 Boreal summer power spectra for CLAUS T_B averaged between 10°N - 24°N and 16.5°E - 27.5°E for 1989-2005. The associated red noise spectrum with 95% confidence bounds is given by the black curves. The gray shading represents the 30-90-day band.

band. To investigate the relationship between the MJO and local variability further, the amplitude of 30-90-day T_B anomalies in the trigger region is compared for a local T_B index and for the MJO index. This local T_B index was created by averaging 30–90-day bandpass-filtered T_B within the trigger region. Fifty-three significant events (25 negative, 28 positive) were identified having T_B index extrema greater than one standard deviation (Fig. 2.7). This corresponds to an average of 3.1 significant T_B events in East Africa per boreal summer. For negative T_B events the composite minimum values within the trigger region for the MJO and T_B indices are -2.16 and -5.16 K, respectively. For positive T_B events, the maximum values within the trigger region for the MJO and T_B indices are 2.56 and 5.12 K, respectively. Thus, the MJO-related T_B anomalies are about 40%– 50% of the amplitude of intraseasonal T_B anomalies derived from a local T_B index.

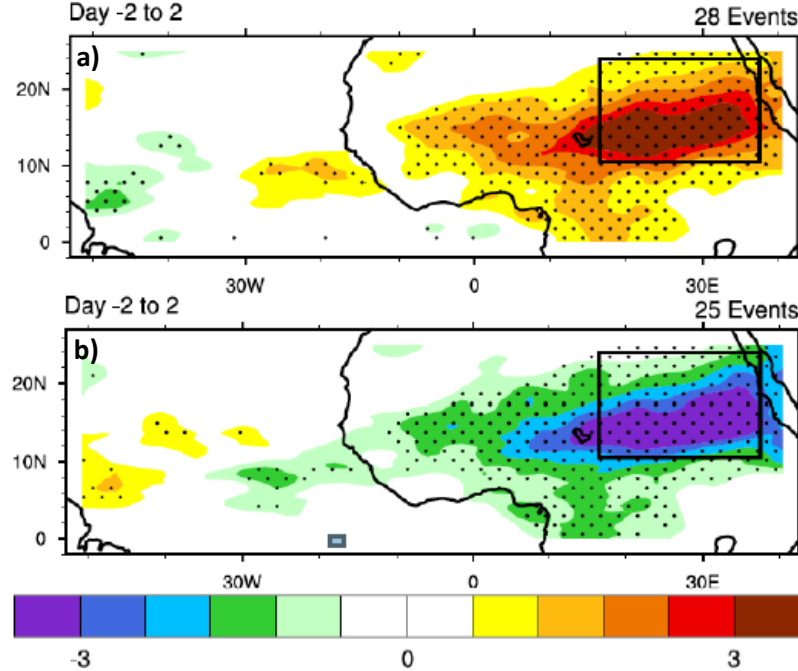


Fig. 2.7 Lead/Lag composites of 30-90-day T_B anomalies averaged for day -2 through day +2 with respect to a 30-90-day T_B index in the trigger region (marked by a black box). Composites are shown for a), significant positive 30-90-day T_B events, and b) significant negative 30-90-day T_B events. The shading interval is 0.6 K. Stippling represents 30-90-day T_B anomalies that are significant with 95% confidence.

To test the robustness of the intraseasonal convective signal in East Africa, ERA-Interim outgoing longwave radiation (OLR) data is compared to CLAUS T_B . In the trigger region, OLR exhibits significant intraseasonal variability (Fig. 2.8). Like T_B , the ISV of OLR is weighted towards longer timescales (i.e., 45-90 days). In general, changing the size and location of the OLR-averaged region in East Africa does not alter the results. Although East Africa clearly exhibits intraseasonal variability, it does not appear to be strongly linked to downstream AEW activity. This is shown in Fig. 2.9, where OLR_{30-90} averaged in the trigger region is poorly correlated with downstream PKE_{30-90} anomalies, a surprising result given the apparent relationship between these regions in MJO composites analysis of North Africa (Alaka and Maloney 2012). Fig. 2.9 shows that the highest correlation (0.07) between East African

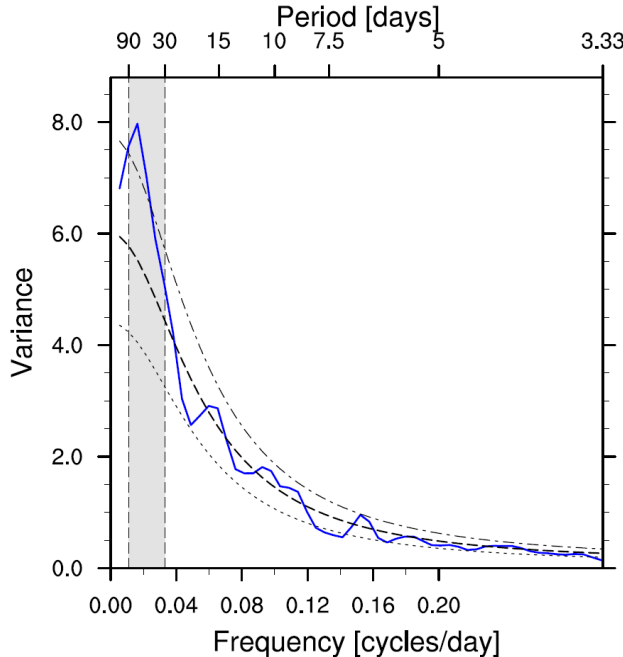


Fig. 2.8 As in 2.6, except for ERA-Interim OLR from 1990-2010.

convection and downstream AEW activity exists when the negative OLR_{30-90} anomalies lead PKE_{30-90} anomalies by 10 days.

In the East African trigger region, significant, negative OLR_{30-90} anomalies precede positive PKE events by 10 days (Fig. 2.10), which is consistent with the timescale analyzed in the power spectra. Between 5°E and 15°E , these OLR_{30-90} anomalies approach -3 W m^{-2} starting 10 days in advance of significant downstream 30-90-day PKE events. It bears noting that OLR anomalies also seem to propagate onshore from the East Atlantic, which might be indicative of an enhanced ITCZ supplying low-level moisture to the onshore monsoon flow. However, this is merely speculation and this topic will be explored in future research endeavors. When PKE_{30-90} anomalies are analyzed with respect to significant, negative OLR_{30-90} events in the trigger region, a much different verdict emerges. The aforementioned connection between East and West Africa disappears (Fig. 2.11). Although positive PKE_{30-90} anomalies follow these East African OLR_{30-90} minima, these anomalies do not appear to be linked to West African PKE maxima. These results

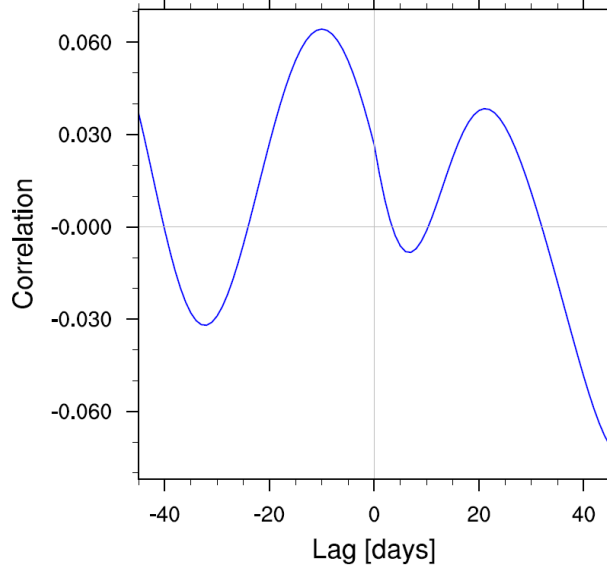


Fig. 2.9 The correlation of the PKE index with negative ERA-Interim OLR anomalies averaged in the trigger region. Negative lag days represent OLR leading PKE.

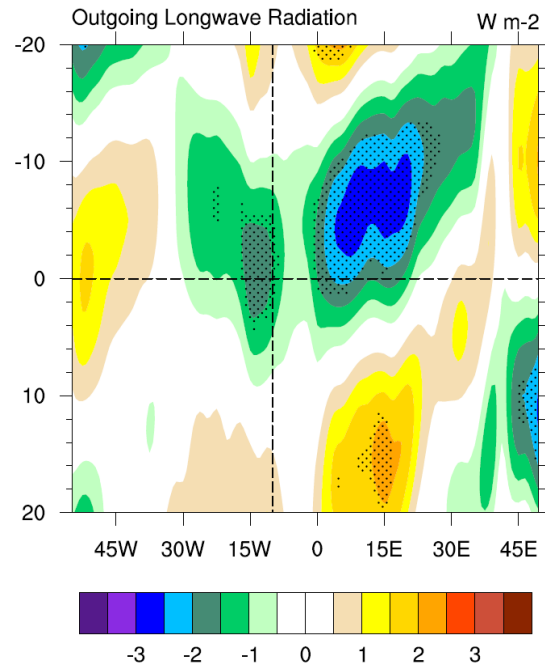


Fig. 2.10 Lead/lag composites for positive PKE events in June-September (1990-2010) are averaged between 10°N and 20°N to create a Hovmöller diagram of 30-90-day OLR anomalies. The shading interval is 0.5 W m^{-2} . Stippling represents OLR_{30-90} anomalies that are significant with 95% confidence. The thick vertical dashed line marks the longitudinal center for the PKE index region, and the thick horizontal dashed line marks Day 0..

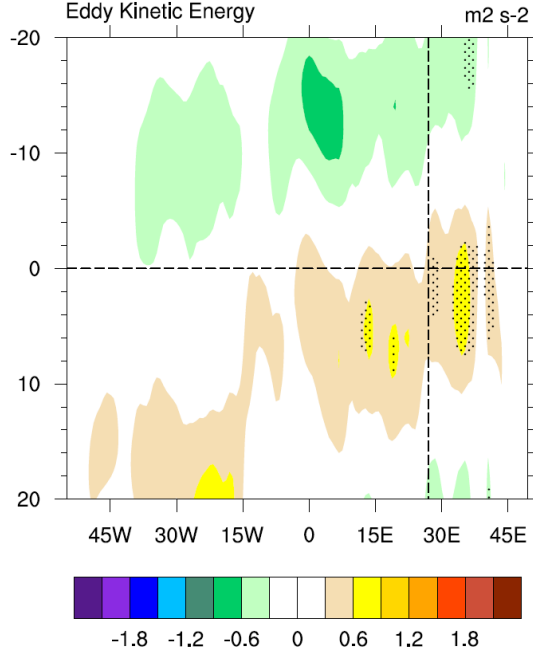


Fig. 2.11 As in 2.10, except for 700 hPa PKE₃₀₋₉₀ anomalies composited for significant OLR events in East Africa. The latitude range is changed to 10°N and 15°N.

suggest that East African OLR is not a good predictor for AEW activity in West Africa on intraseasonal timescales. The washed out signal suggests that while some upstream OLR events may influence West African PKE, no consistent relationship exists between intraseasonal convective variability in East Africa and downstream PKE in West Africa. This tempers the strength of the composite results in Alaka and Maloney (2012).

OLR and T_B are proxies for the strength of convection in tropical regions. However, column moisture anomalies can also highlight locations that are favorable for convection. ERA-Interim TPW is employed to test how the moisture-driven convective signal in East Africa relates to cloud-top measurements (i.e., OLR) and to downstream AEW activity. Unlike OLR, the 30-90-day band does not contain any significant spectral peaks (Fig. 2.12). While Alaka and Maloney (2012) demonstrated that East African convective anomalies associated with the MJO are significant, the overall 30-90-day TPW power in the trigger region lies close to the red noise

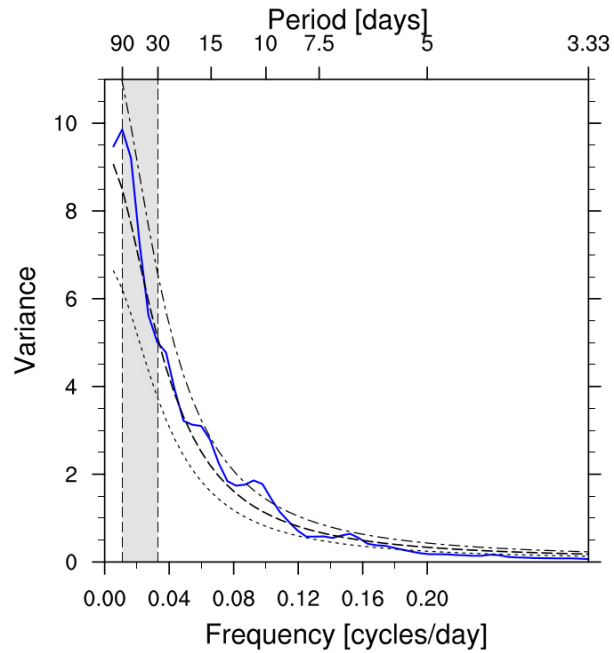


Fig. 2.12 As in 2.6, except for ERA-Interim TPW from 1990-2010.

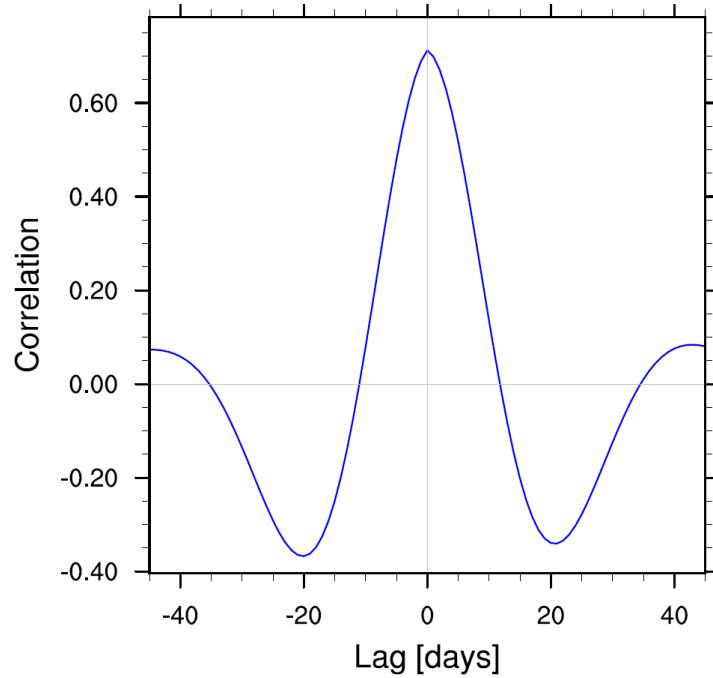


Fig. 2.13 The correlation of negative ERA-Interim OLR anomalies with ERA-Interim TPW anomalies, both averaged in the trigger region. Negative lag days represent TPW leading OLR.

spectrum. Given the strong links between deep convection and tropospheric water vapor that have been previously documented (e.g., (Sahany et al. 2012), it is not surprising that 30-90-day OLR and TPW anomalies in the trigger region are strongly correlated (0.71) and in phase with one another (Fig. 2.13). Consistent with 30-90-day OLR anomalies, intraseasonal TPW anomalies in the trigger region are weakly correlated (0.23) with PKE_{30-90} anomalies in West Africa at a lead time of 9 days (Fig. 2.14). Despite the weak correlation, the TPW_{30-90} anomalies appear to have a stronger link with West African PKE than OLR_{30-90} anomalies. It is unclear how this link to East African water vapor might work, however, if not through an influence on convection. One possibility is that water vapor anomalies are advected downstream by the AEJ, which would supply ample moisture for deep convection in maturing AEWs.

Lead/lag composites reinforce the notion of a stronger link between TPW and PKE, with TPW_{30-90} anomalies in excess of 1 mm near 13°E starting 9 days before positive PKE events

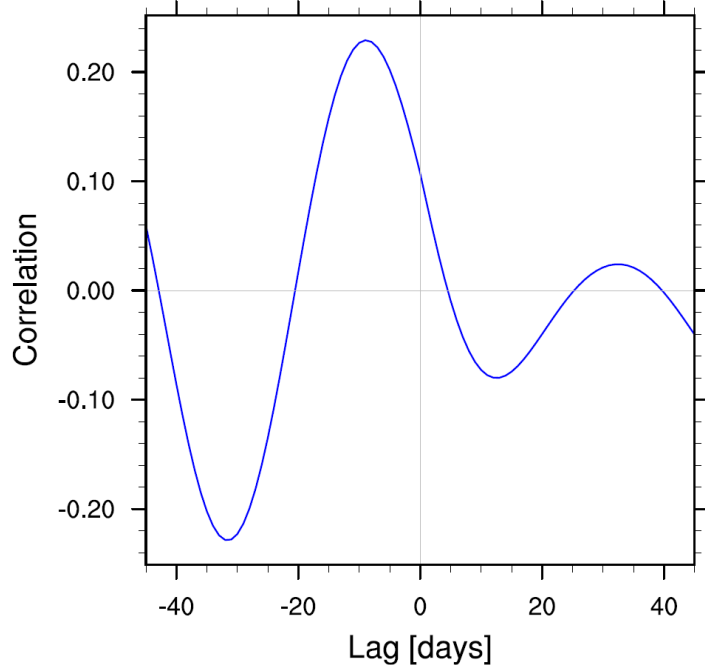


Fig. 2.14 The correlation of the PKE index with ERA-Interim TPW anomalies, averaged in the trigger region. Negative lag days represent TPW leading PKE.

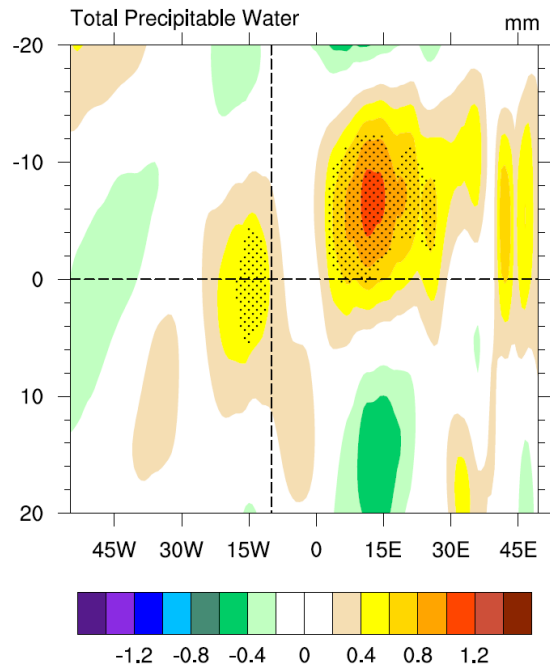


Fig. 2.15 As in 2.10, except for TPW₃₀₋₉₀ anomalies composites for significant West African 700 hPa PKE₃₀₋₉₀ events.

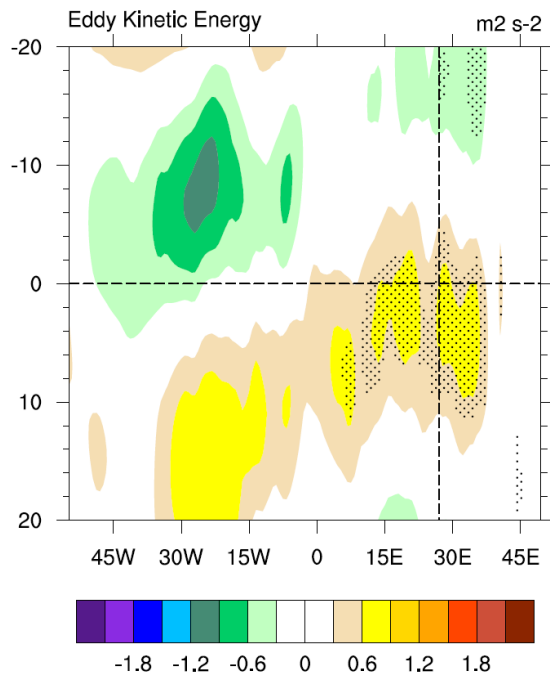


Fig. 2.16 As in 2.10, except for PKE₃₀₋₉₀ anomalies composites for significant East African TPW₃₀₋₉₀ events.

(Fig. 2.15). In relation to surges of upstream moisture anomalies, PKE_{30-90} anomalies propagate downstream from significant, positive TPW_{30-90} events in the trigger region (Fig. 2.16). However, these PKE_{30-90} anomalies are not significant in West Africa. Intraseasonal AEW activity appears to be linked to East African moisture anomalies to some degree, but this relationship is complex. In particular, surges of TPW_{30-90} anomalies in the trigger region do not always translate into positive PKE events in West Africa.

2.3 Boreal Summer Mean Energy Conversions in ERA-Interim

Boreal summer mean fields for the PKE and PAPE budget terms are analyzed first. We are not aware of a similar analysis using ERA-Interim fields. The results for the summer mean fields presented here are qualitatively similar to other studies (Lau and Lau 1992; Diedhiou et al. 2002; Hsieh and Cook 2007), even when budgets are derived with zonal filtering.

The boreal summer mean PKE budget terms are analyzed as vertically averaged, horizontal fields (Fig. 2.17a-d) and in latitudinal cross-sections averaged between 10°W and 20°E (Fig. 2.18a-d). The corresponding PAPE budgets terms are provided in Fig. 2.17e-f and Fig. 2.18e-f. Since the individual advection terms in Eq. 3 (or A.14) are relatively small in boreal summer, these terms are added together for the analysis (A_{TOT} ; see A.4). As expected, $\langle A_{TOT} \rangle$ is positive downstream of the 700 hPa PKE maximum in West Africa and negative upstream in the boreal summer mean (Fig. 2.17a). Given that the flow is easterly at most levels, especially near the AEJ where AEWs are strongest, smaller PKE values are fluxed toward the PKE maximum (14°N, 20°W).

Norquist et al. (1977) was the first study to acknowledge a relationship between barotropic energy conversions and AEWs. In tropical North Africa, B_T (see A.5) typically

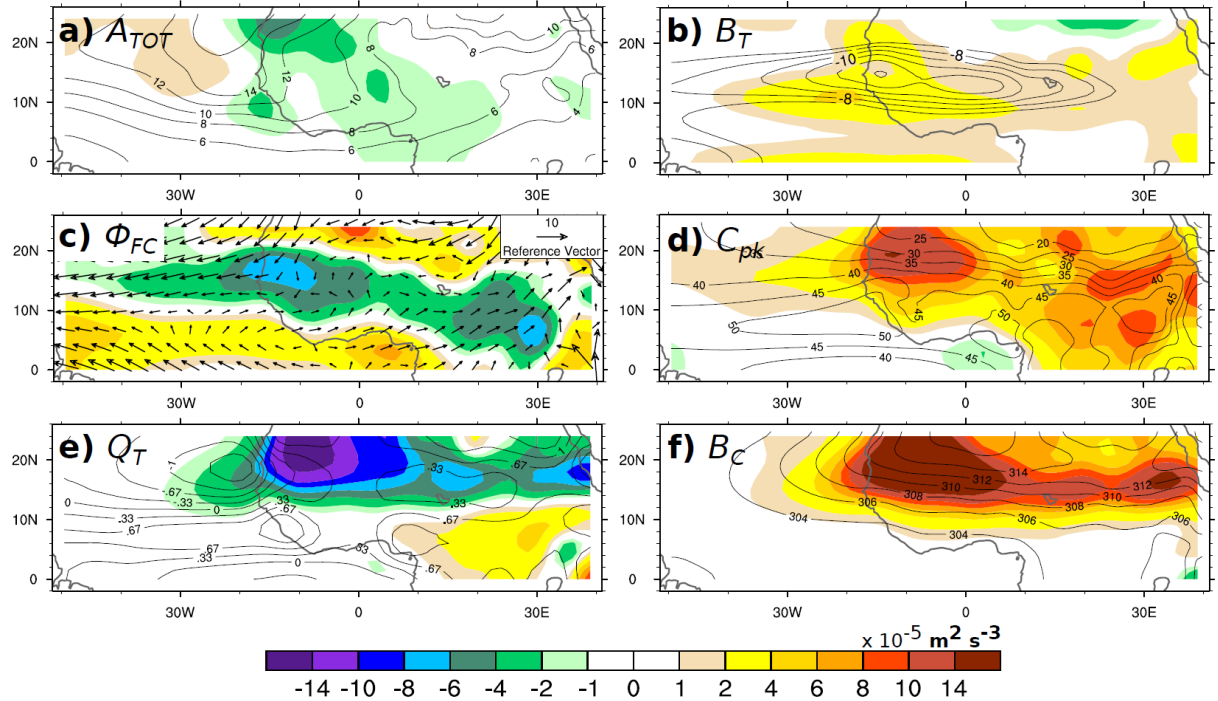


Fig. 2.17 The vertically integrated PKE and PAPE budget terms and supporting fields are averaged in boreal summer (June-September). All budget terms are shaded and use the same color bar. Shown: (a) PKE advection (A_{TOT}) and 700 hPa PKE (contours; interval of $2 \text{ m}^2 \text{ s}^{-2}$), (b) barotropic energy conversion (B_T) and 650 hPa zonal wind (contours; interval of 1 m s^{-1} less than -7 m s^{-1}), (c) geopotential flux convergence (Φ_{FC}) and 850 hPa total wind (vectors), (d) baroclinic overturning (C_{pk}) and total precipitable water (contours; interval of 5 mm), (e) diabatic generation of PAPE (Q_T) and the mean apparent heating rate (contours; interval of 0.33 K day^{-1}), and (f) baroclinic energy conversion (B_C) and 850 hPa potential temperature (contours; interval of 2 K).

describes the transfer of kinetic energy directly from the AEJ to the eddies. B_T creates PKE in a long east-west strip centered at 10°N (Fig. 2.17b) and 700 hPa (Fig. 2.18b) in the vicinity of the AEJ. The expansive longitudinal range suggests the importance of $\langle B_T \rangle$ to disturbances in West Africa and in the tropical East Atlantic Ocean. $\langle B_T \rangle$ straddles the AEJ (Fig. 2.17b, contours) between 8°W and 25°W, highlighting the importance of $\langle B_T \rangle$ to the southern and northern eddy tracks. The vertical cross-section in Fig. 2.18b reveals that a B_T maximum occurs at the southern

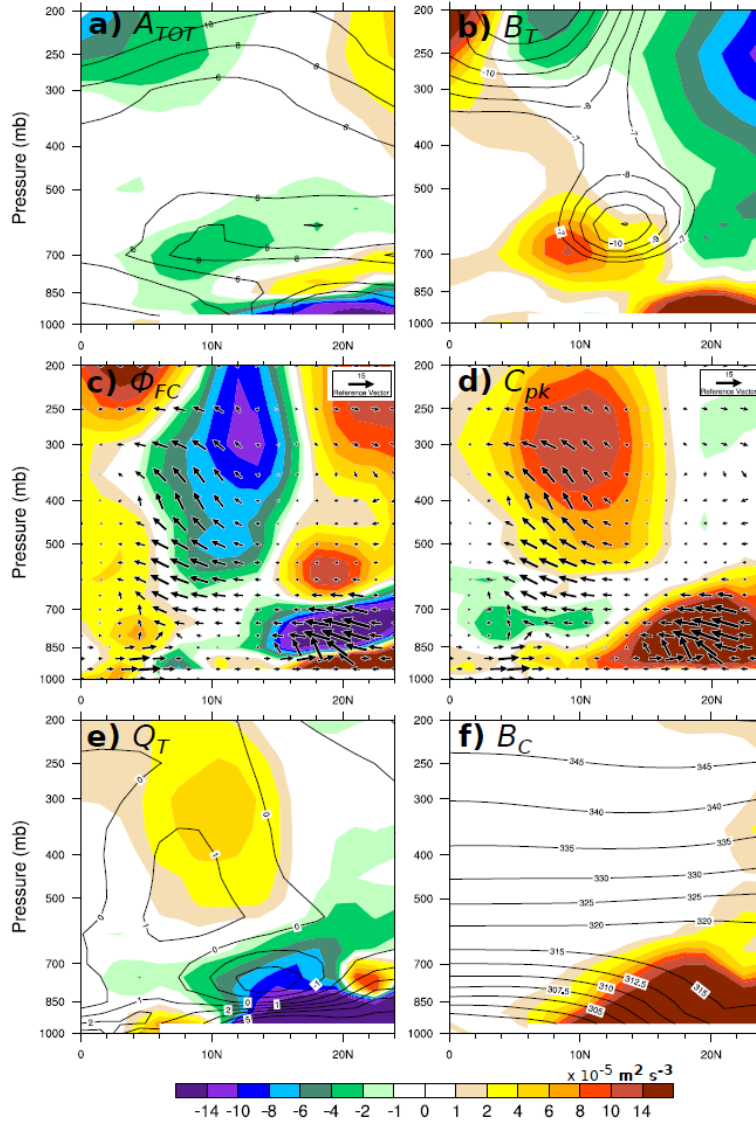


Fig. 2.18 The vertical structure of the PKE and PAPE budget terms and supporting fields are averaged between 10°W and 20°E during boreal summer (June-September). All budgets terms are shaded. Shown: (a) PKE advection (A_{TOT}) and PKE (contours; interval of $2 \text{ m}^2 \text{ s}^{-2}$), (b) barotropic energy conversion (B_T) and zonal wind (contours; interval of 1 m s^{-1} less than -7 m s^{-1}), (c) geopotential flux convergence (Φ_{FC}) and total wind (vectors), (d) baroclinic overturning (C_{pk}) and total wind (vectors), (e) diabatic generation of PAPE (Q_T) and the apparent heating rate (contours; interval of 1 K day^{-1}), and (f) baroclinic energy conversion (B_C) and potential temperature (contours; $\theta < 315$: interval of 2.5 K ; $\theta > 315$: interval of 5 K).

and lower part of the AEJ near 700 hPa for AEWs, which is supported by Hsieh and Cook (2007; their Fig. 13). Positive B_T associated with northern-track eddies occurs north of 13°N and below 850 hPa. B_T in this region is not associated with the AEJ core. Although Diedhiou et al. (2002) found that B_T north of the AEJ is linked to the subtropical jet in NCEP/NCAR reanalysis on 6-9-day time scales, Fig. 2.18b shows that B_T in this region is confined to the lower troposphere in the ERA-Interim dataset.

The convergence of perturbation geopotential flux (ϕ_{FC}), which when combined with C_{pk} is equivalent to “pressure work” (Diaz & Aiyyer, 2013a,b), generally acts as a sink of PKE that opposes C_{pk} (Figs. 2.17c, 2.18c). Since ϕ_{FC} is conserved for a global integral and is related to the movement of PKE from one location to another by pressure gradient force-driven acceleration/deceleration of the flow, a compensating ϕ_{FC} must increase PKE somewhere else on the globe. Recent work by Diaz and Aiyyer (2013b) showed the relationship between ϕ_{FC} and upstream energy dispersion in AEWs.

While $\langle C_{pk} \rangle$ is positive over most of tropical North Africa, higher amplitudes are concentrated in two regions: near 20°N, 10°W and east of 15°E (Fig. 2.17d). The northwestern maximum occurs in the lower troposphere in the vicinity of the Saharan heat low (Fig. 2.18d) and represents a conversion of PAPE created by B_C to PKE (Fig. 2.17f). Although Lau and Lau (1992) show a small portion of tropical North Africa, the tongue of positive $\langle C_{pk} \rangle$ extending out into the eastern Atlantic (their Fig. 3b) is of similar amplitude and structure in Fig. 2.17d. Hsieh and Cook (2007) also capture the conversion of PAPE to PKE at lower levels (their Fig. 12a), although they find an amplitude that is an order of magnitude less than C_{pk} in Fig. 2.18d. The eastern C_{pk} maximum (Fig. 2.17d), which is centered at 300 hPa (Fig. 2.18d), appears to be associated with diabatic heating anomalies (Fig. 2.18e). Hsieh and Cook (2007) found a similar

C_{pk} maximum in the upper troposphere.

The generation of PAPE by diabatic heating links PKE increases to moist, convective processes and associated radiative perturbations. Recent work by Berry and Thorncroft (2012) argues that convection is vital for the intensification of AEWs. Positive $\langle Q_T \rangle$ is located in East Africa south of 12°N (Fig. 2.17e), where ample column moisture (Fig. 2.17d, contours) can support deep, moist convection in boreal summer. Note that this mid- to upper-tropospheric generation of PAPE by Q_T is entirely converted to PKE by C_{pk} (Fig. 2.18d). Previous studies show similar Q_T structure in this region (Hsieh and Cook 2007; Berry and Thorncroft 2012), with positive values above and negative values below 650 hPa that reduce the vertically averaged signal (Fig. 2.17e). Analysis of the residual of the PAPE budget (Fig. 2.19b) suggests that ERA-Interim likely underestimates the amount of PAPE created from $\langle Q_T \rangle$, given that the residual is coincident with regions of positive $\langle Q_T \rangle$ in Figure 5. $\langle Q_T \rangle$ is mostly negative north of 12°N, with the minimum located near 20°N, 10°W (Fig. 2.17e). In this region, $\langle Q_T \rangle$ appears to oppose generation of PAPE by $\langle B_C \rangle$ (Fig. 2.17f), consistent with Kiladis et al. (2006). This opposition effectively reduces the importance of baroclinic energy conversions in this region, and will be discussed in more detail below (see Fig. 2.27).

Positive $\langle B_C \rangle$ occurs mostly to the north of the AEJ (Fig. 2.17f), associated with a strong meridional temperature gradient between the Sahel and the Sahara (Fig. 2.17f, contours), with a large maximum in West Africa and a smaller local maximum at 17°N, 33°E. Previous studies have found a similar $\langle B_C \rangle$ maximum in West Africa extending out into the eastern Atlantic (Lau and Lau 1992; Diedhiou et al. 2002). These B_C maxima are dominated by conversions below 650 hPa within a strong meridional potential temperature gradient (Fig. 2.18f, contours), which is supported by the results of Hsieh and Cook (2007). Positive B_C cuts off sharply near 20°N in

regional model output from Hsieh and Cook (2007) whereas Fig. 2.18f shows this term extending north of 25°N . C_{pk} converts B_C to PKE north of 10°N , with the complication mentioned above that Q_T destroys PAPE near the B_C maximum in West Africa.

The residual for the PKE budget (Fig. 2.19a) represents frictional dissipation of PKE, deficient subgrid-scale physics in the ERA-Interim model, and errors introduced by calculating budget terms on standard output variables. Although the magnitude of $\langle D \rangle$ maximizes north of 15°N , likely in association with the Saharan heat low, the local minimum at 9°N , 700 hPa suggests that AEWs are too strong in ERA-Interim. The residual for the PAPE budget (Fig. 2.19b) is small for most the domain above the boundary layer, except for near 300 hPa, where large $\langle R \rangle$ is collocated with $\langle Q_T \rangle$ and likely represents an underestimation of convective

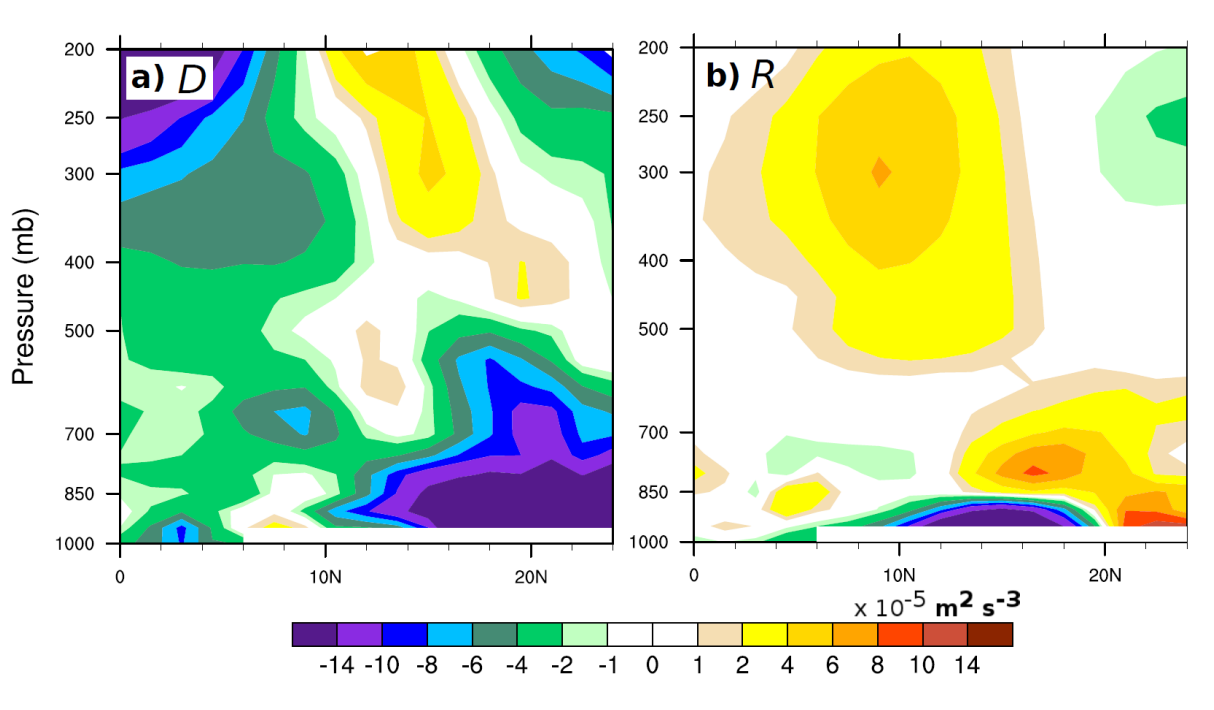


Fig. 2.19 As in Fig. 2.18, except for the vertical structure of (a) the PKE residual term (D) and (b) the PAPE residual term (R).

processes in ERA-Interim. Although not explicitly shown, $\langle R \rangle$ and $\langle Q_T \rangle$ fields are similar in the subsequent analysis.

2.4 Boreal Summer Mean Energy Conversions in CFSR

The PKE and PAPE budgets (Eqns. 1.3,1.4) are also analyzed using CFSR data (Saha et al. 2010) to test the robustness of the ERA-Interim results. Due to a lack of constraining observations in the region, each reanalysis model is free to manifest its own reality of the West African monsoon and associated AEWs. For this analysis, CFSR data is degraded to 1.5° resolution to be consistent with the ERA-Interim analysis in Section 2.3. Boreal summer mean CFSR PKE and PAPE energy budget terms are qualitatively similar to their ERA-Interim counterparts (Fig. 2.20). This agreement increases confidence that global reanalysis models are capable of balancing eddy energy budgets and that ERA-Interim produces a realistic

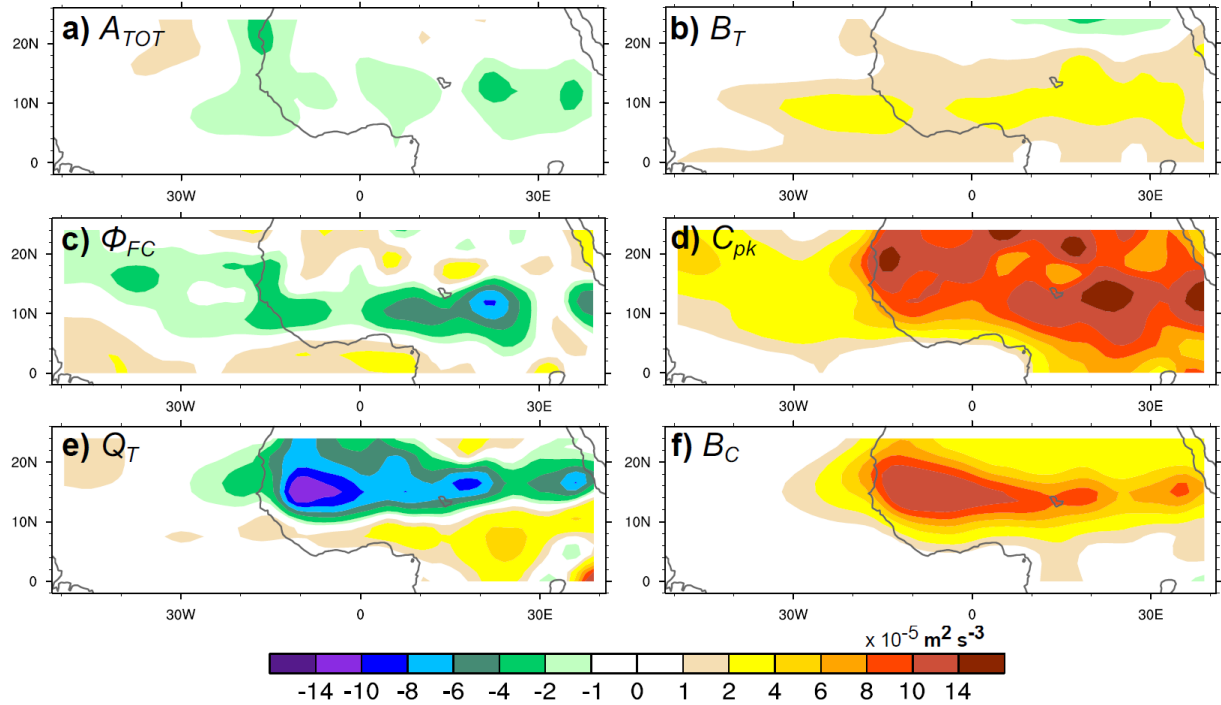


Fig. 2.20 As in Fig. 2.17, except for boreal summer mean CFSR data (2000-2010).

climatology of AEW energetics. There are a few notable differences between the CFSR and ERA-Interim derived budgets. In the CFSR budgets, C_{pk} is large over most of North Africa ($> 1 \times 10^{-4} \text{ m}^2 \text{ s}^{-3}$) and is by far the most dominant signal in the PKE budget (2.20d). The large C_{pk} amplitude suggests the importance of B_C (2.20f) and Q_T (2.20e) in creating PKE. Son the topic of PAPE terms, B_C (2.20f) and Q_T (2.20e) have slightly weaker amplitudes and are situated further south than in the ERA-Interim budgets. Unlike in the ERA-Interim budgets, positive Q_T values can be observed in a thin strip near 10N extending out into the East Atlantic. This boreal summer mean signal is like associated with deep convection within AEWs. Further to the north, negative Q_T values highlight a negative feedback with B_C that is depicted in Fig. 2.27. The remaining three PKE terms (i.e., A_{TOT} , B_T , ϕ_{FC}) are quantitatively similar to the ERA-Interim budget. CFSR and ERA-Interim strongly agree on the structure and amplitude of PKE budget terms. With such similar results in the boreal summer mean, the remainder of this chapter is dedicated to analyzing the intraseasonal variability of AEW energetics within ERA-Interim only.

2.5 Energy Budget Intraseasonal Variability in the Local PKE Index

The analysis presented in this section focuses on the ISV of 700 hPa PKE and four energy conversion terms that are crucial for PKE creation: barotropic energy conversion (B_T), baroclinic energy conversion (B_C), diabatic PAPE generation (Q_T), and how these latter two terms are converted to PKE by baroclinic overturning (C_{pk}). For each PKE or PAPE budget term analyzed, the ISV local to tropical North Africa is presented in composite lead/lag diagrams for positive PKE events in West Africa composited using the local 700 hPa PKE index. Then, MJO phase composites will be compared to those from the local PKE index to assess their similarity.

2.5.1 PKE and PKE Tendency

The creation of PKE on intraseasonal time scales is initially examined through 700 hPa PKE and the PKE tendency term (left side of Eq. A.14). Based on the local 700 hPa PKE index, positive 700 hPa PKE_{30-90} anomalies are observed to maximize at day 0 near 15°W (Fig. 2.21). Notably, these positive 700 hPa PKE_{30-90} anomalies initiate in East Africa (30°E) about 10 days before positive PKE events and propagate westward (Fig. 2.22), a progression that suggests PKE anomalies in East and West Africa might be linked on intraseasonal timescales (Leroux et al.

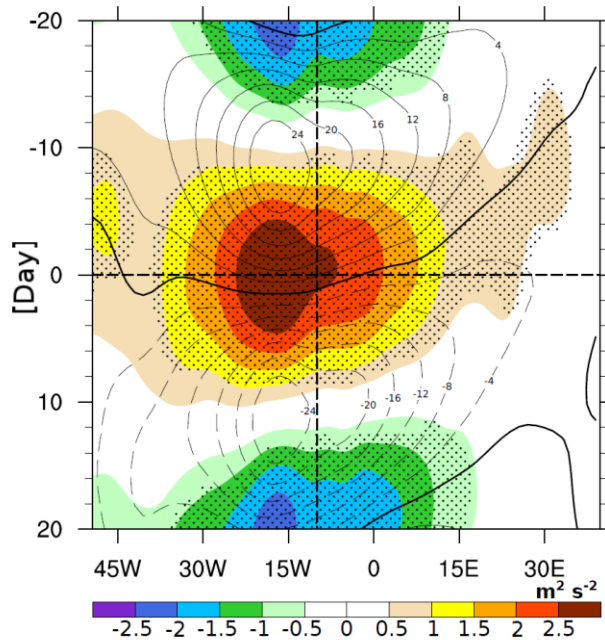


Fig. 2.21 Lead/lag composites are averaged between 10°N and 15°N to create Hovmöller diagrams. Shown: 30-90-day 700 hPa PKE anomalies (shading) and vertically averaged 30-90-day PKE tendency (contours) for June-September composited for significant events in a 30-90-day 700 hPa PKE index. The shading interval is $0.5 \text{ m}^2 \text{ s}^{-2}$. The contour interval is $4 \times 10^{-7} \text{ m}^2 \text{ s}^{-3}$. Stippling represents PKE anomalies that are significant with 95% confidence. The thick vertical dashed line marks the longitudinal center for the PKE index region. The thick horizontal dashed line marks Day 0.

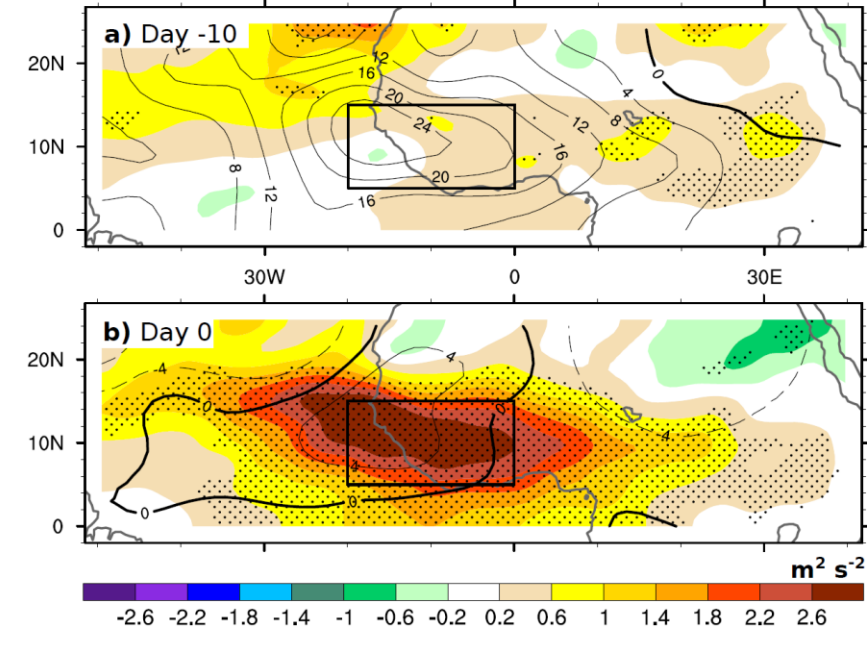


Fig. 2.22 Lead/lag maps of 30-90-day 700 hPa PKE anomalies (shading) and vertically averaged 30-90-day PKE tendency (contours) for June-September composites for significant events in a 30-90-day 700 hPa PKE index. Shown: (a) day -10 and (b) day 0. The shading interval is $0.4 \text{ m}^2 \text{ s}^{-2}$. The contour interval is $4 \times 10^{-7} \text{ m}^2 \text{ s}^{-3}$. Stippling represents PKE anomalies that are significant with 95% confidence. Coastlines are represented by a gray contour.

2010; Alaka and Maloney 2012). This envelope of increased AEW activity propagates slowly to the west between 30°E and 15°E (4.1 m s^{-1} , Fig. 2.21). This propagation is broadly consistent the westward propagation of positive 700 hPa PKE_{30-90} anomalies observed after surges of TPW_{30-90} in East Africa (Fig. 2.16), although this link is not overly robust. West of 15°E , the phase speed of the PKE envelope more than doubles (8.9 m s^{-1}) and is approximately equal to the phase speed of the individual eddies in this analysis, suggesting that a specific set of AEWs are enhanced by positive 700 hPa PKE_{30-90} anomalies. We do not know whether this is simply coincidence, or whether the phase speed of the waves somehow is setting the westward propagation speed of the intraseasonal signal. Noteworthy is the apparent eastward propagation

of PKE_{30-90} anomalies from the eastern Atlantic to West Africa between day -5 and day 0, although we have no explanation for this signal.

2.5.2 Barotropic Energy Conversion

Given that B_T is strongly influenced by horizontal wind gradients, 30-90-day variability of the AEJ is likely a strong contributor to $\langle B_T \rangle_{30-90}$ anomalies. Previous studies have found that AEW activity is associated with a northward shift in the AEJ near West Africa on intraseasonal time scales (Leroux and Hall 2009; Ventrice et al. 2011). More recently, Alaka and Maloney (2012) showed that an eastward extension of the AEJ into East Africa precedes increased intraseasonal wave activity in West Africa. South of the AEJ, positive $\langle B_T \rangle_{30-90}$ anomalies maximize near 15°W during positive PKE events (Fig. 2.23a). With values approaching $1 \times 10^{-5} \text{ m}^2 \text{ s}^{-3}$, these $\langle B_T \rangle_{30-90}$ anomalies create enough PKE to replace the vertically averaged PKE_{30-90} maximum in about 8.5 hours. $\langle PKE \rangle_{30-90}$ has a similar structure to 700 hPa PKE_{30-90} (Fig. 2.21). North of the AEJ, the $\langle B_T \rangle_{30-90}$ signal is weak and insignificant (Fig. 2.24a). Positive $\langle B_T \rangle_{30-90}$ anomalies are significant near 10°N and west of 30°E starting about 10 days prior to positive PKE events (Fig. 2.25a) and grow in place until they maximize on day 0 (Fig. 2.26a). In general, these $\langle B_T \rangle_{30-90}$ anomalies are located on the southern flank of the AEJ (Fig. 2.17b). These anomalies do not appear to initiate in East Africa, as PKE_{30-90} anomalies do (Fig. 2.21). We postulate that $\langle B_T \rangle_{30-90}$ is extremely important for maintaining PKE anomalies in existing easterly waves. However, its role in initiating periods of increased intraseasonal AEW activity appears to be limited.

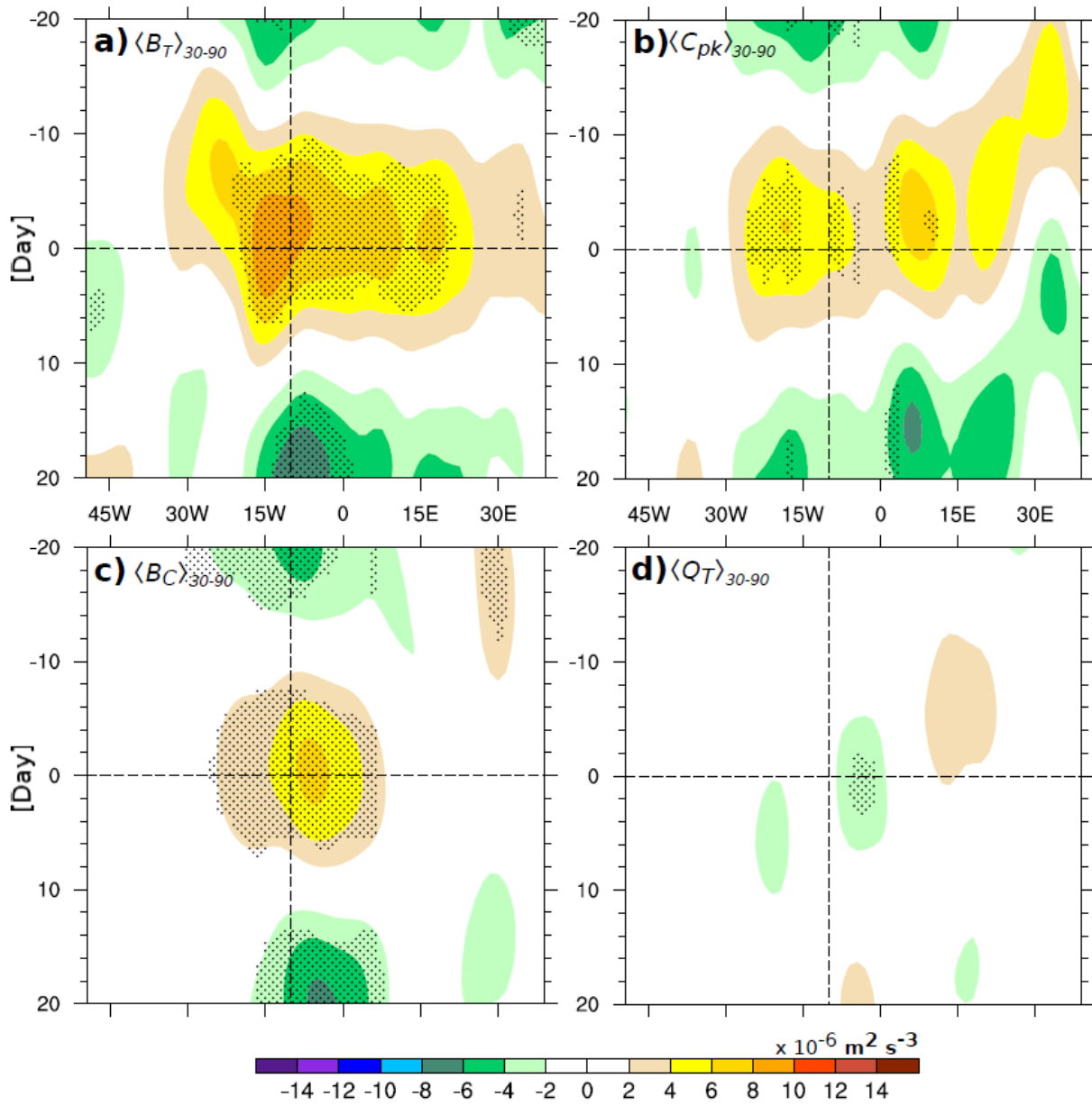


Fig. 2.23 As in Fig. 2.21, except for vertically averaged, 30-90-day PKE creation terms south of the AEJ ($7.5^\circ\text{N} - 12.5^\circ\text{N}$). Shown: (a) barotropic energy conversion, (b) baroclinic overturning, (c) baroclinic energy conversion, and (d) PAPE generation by diabatic heating. Lead/lag composites are averaged between 7.5°N and 12.5°N to create Hovmöller diagrams. The shading interval is $2 \times 10^{-6} \text{ m}^2 \text{ s}^{-3}$.

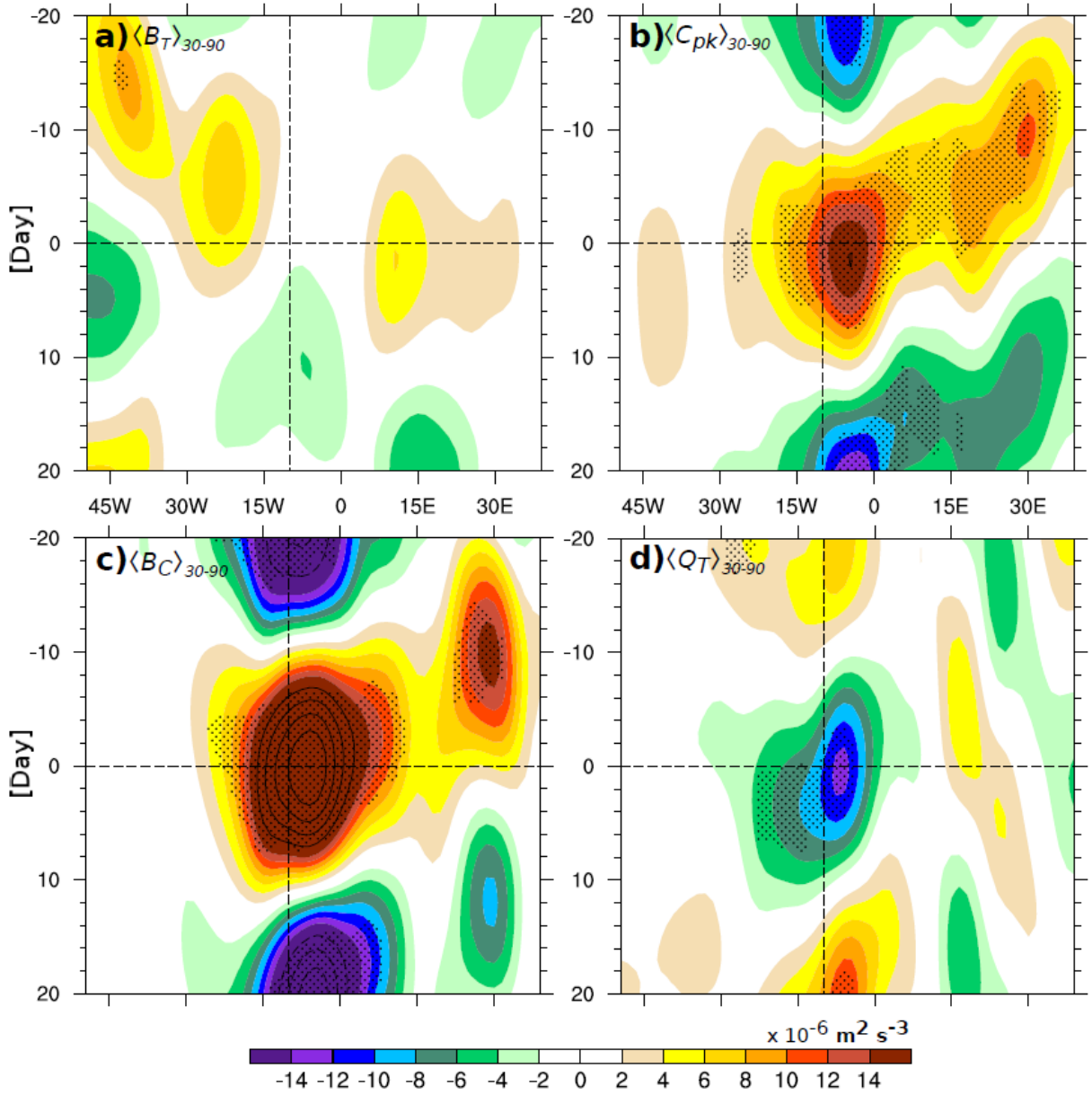


Fig. 2.24 As in Fig. 2.21, except for vertically averaged, 30-90-day PKE creation terms north of the AEJ ($12.5^\circ\text{N} - 17.5^\circ\text{N}$). Shown: (a) barotropic energy conversion, (b) baroclinic overturning, (c) baroclinic energy conversion, and (d) PAPE generation by diabatic heating. Lead/lag composites are averaged between 12.5°N and 17.5°N to create Hovmöller diagrams. The shading interval is $2 \times 10^{-6} \text{ m}^2 \text{ s}^{-3}$. If necessary, contours represent levels outside of the shading limits with an interval of $4 \times 10^{-6} \text{ m}^2 \text{ s}^{-3}$.

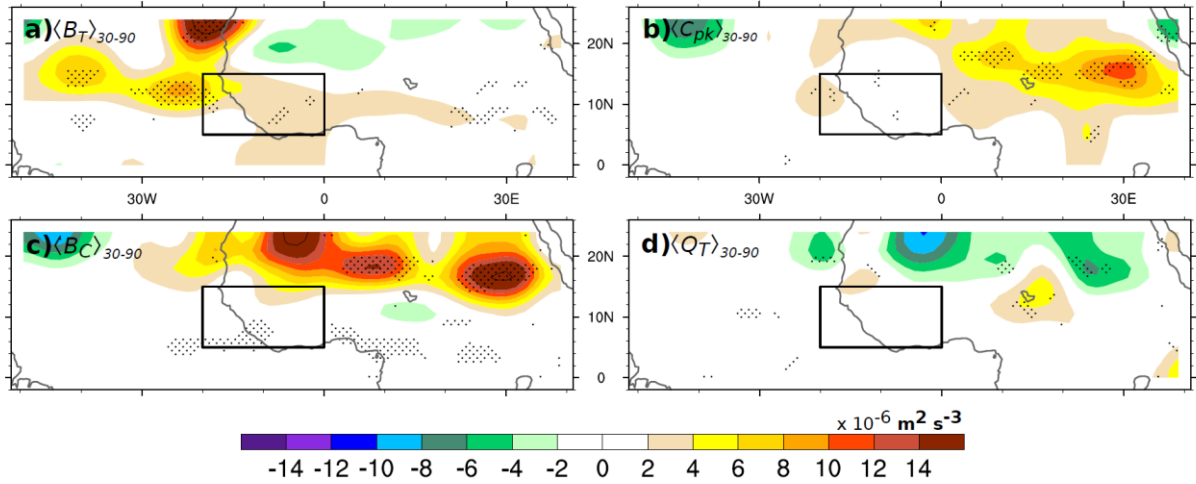


Fig. 2.25 As in Fig. 2.22, except for vertically averaged, 30-90-day PKE creation terms on day -10. Shown: (a) barotropic energy conversion, (b) baroclinic overturning, (c) baroclinic energy conversion, and (d) PAPE generation by diabatic heating. The shading interval is $2 \times 10^{-6} \text{ m}^2 \text{ s}^{-3}$. If necessary, contours represent levels outside of the shading limits with an interval of $4 \times 10^{-6} \text{ m}^2 \text{ s}^{-3}$. Coastlines are represented by a gray contour.

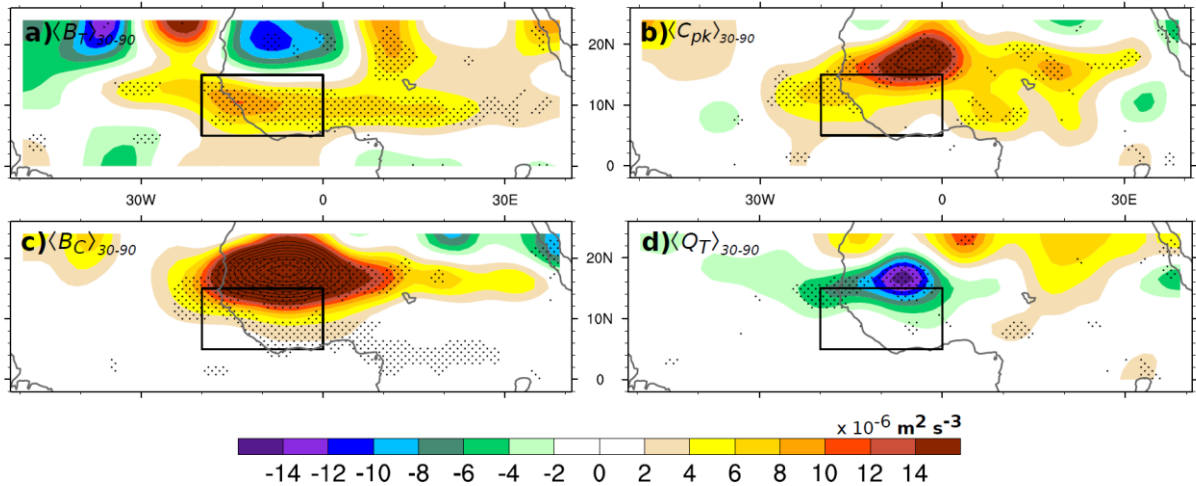


Fig. 2.26 As in Fig. 2.22, except for vertically averaged, 30-90-day PKE creation terms on day 0. Shown: (a) barotropic energy conversion, (b) baroclinic overturning, (c) baroclinic energy conversion, and (d) PAPE generation by diabatic heating. If necessary, contours represent levels outside of the shading limits with an interval of $4 \times 10^{-6} \text{ m}^2 \text{ s}^{-3}$. Coastlines are represented by a gray contour.

2.5.3 PKE/PAPE Conversion

As a means of converting $\langle B_C \rangle_{30-90}$ and $\langle Q_T \rangle_{30-90}$ anomalies to PKE, $\langle C_{pk} \rangle_{30-90}$ is now investigated. Most of the significant $\langle C_{pk} \rangle_{30-90}$ anomalies occur between 10°N and 20°N in tropical North Africa (Figs. 2.25b, 2.26b), with clear evidence of westward propagation from East to West Africa on the northern side of the AEJ (Fig. 2.24b). This signal is still clear to the south of the AEJ, but with weaker amplitude (Fig. 2.23b). North of the AEJ, positive $\langle C_{pk} \rangle_{30-90}$ anomalies initiate near 30°E between 8 and 12 days before positive PKE events and propagate into West Africa before day 0 (Fig. 2.24b). Here, the strength of $\langle C_{pk} \rangle_{30-90}$ is sufficient to replace vertically averaged PKE (not shown) in 5 hours. Overall, the similarity of the westward propagation between 700 hPa PKE_{30-90} anomalies (Fig. 2.21) and $\langle C_{pk} \rangle_{30-90}$ anomalies (Fig. 2.24b) suggests a connection between these two terms. These results suggest that $\langle C_{pk} \rangle_{30-90}$ is important for the initiation of positive PKE events in East Africa and the maintenance of this increased AEW activity downstream in West Africa.

2.5.4 Baroclinic Energy Conversion

ISV of baroclinic energy conversions are associated with several factors, such as the ISV of the Saharan heat low (Lavaysse et al. 2010; Chauvin et al. 2010). Pulsations and lateral movement of this thermally-induced circulation likely affect the temperature gradient between the Sahara and the Gulf of Guinea. Significant $\langle B_C \rangle_{30-90}$ anomalies propagate westward north of the AEJ (Fig. 2.24c). In particular, anomalies are strongest near 30°E about 10 days prior to positive PKE events (Fig. 2.25c) and maximize near 5°W at day 0 (Fig. 2.26c). The westward propagation of $\langle B_C \rangle_{30-90}$ anomalies generally agrees with the evolution of 700 hPa PKE_{30-90} anomalies (Fig. 2.21) and $\langle C_{pk} \rangle_{30-90}$ anomalies (Fig. 2.24b). $\langle B_C \rangle_{30-90}$ appears to dominate

$\langle C_{pk} \rangle_{30-90}$, with the capability to replace the maximum vertically averaged PKE in 3 hours. The propagating signal associated with $\langle B_C \rangle_{30-90}$ is not observed south of the AEJ, although a weaker maximum appears in West Africa at day 0 (Fig. 2.23c). Thus, $\langle B_C \rangle_{30-90}$ anomalies are most prominent on the north side of the AEJ in association with strong temperature and wind fluctuations along the strong climatological temperature gradient (Fig. 2.17f). Overall, positive $\langle B_C \rangle_{30-90}$ anomalies appear to be important for both upstream initiation and downstream maintenance of positive PKE events.

2.5.5 Role of Diabatic Heating

Alaka and Maloney (2012) showed that East Africa moistens before AEW activity maximizes over West Africa on intraseasonal time scales. We investigate whether a $\langle Q_T \rangle_{30-90}$ signal exists in advance of PKE_{30-90} events due to general support of convective activity by anomalously moist conditions. Although $\langle Q_T \rangle_{30-90}$ anomalies are weakly positive on both sides of the AEJ near 15°E prior to positive PKE events (Figs. 2.23d, 2.24d), they are not significant and only propagate to the west in a thin band right along the Gulf of Guinea coastline (not shown). This result is consistent with the lack of a relationship between East African convection and downstream PKE activity (see Fig. 2.9). Contrary to expectations, the largest amplitude $\langle Q_T \rangle_{30-90}$ occurs in the form of negative anomalies on the northern edge of positive PKE events (Figs. 2.25d, 2.26d). Comparing to Fig. 2.24c, these anomalies substantially cancel a large portion of the PAPE generated by $\langle B_C \rangle_{30-90}$ anomalies in West Africa. The fact that $\langle C_{pk} \rangle_{30-90}$ (Fig. b) is reduced relative to $\langle B_C \rangle_{30-90}$ is reflective of this. This tendency was also noted in the climatological mean plots (see Fig. 2.17). Q_1' anomalies appear to be damping temperature anomalies by heating (cooling) in cool (warm) regions.

To support this contention, vertically averaged, 11-day high-pass filtered diabatic heating and temperature anomalies are regressed against a West African 700 hPa eddy vorticity index (Fig. 2.27). When eddy vorticity maximizes in West Africa, Q_1' anomalies are positive on the eastern side of the waves, consistent with convection aided by moist air advected from the south. A southward flux of dry air on the west side of the disturbance suppresses convection. The phase relationship between convection and the circulation in AEWs is consistent with that found in Kiladis et al. (2006). At the same time, temperature anomalies are negative to the east of AEWs due to “cooler” air being fluxed from the Gulf of Guinea and positive to the west of AEWs in the relatively warmer Saharan air. This pattern supports a destruction of PAPE by diabatic heating as mature waves reach West Africa, reducing the impact of $\langle B_C \rangle_{30-90}$ (Fig. 2.26c). This might limit AEW amplitudes as the systems propagate offshore (e.g., Hopsch et al. 2010).

As mentioned earlier, the PAPE residual likely compensates for missing or poorly parameterized sub-grid scale processes in the ERA-Interim dataset. The strongest 30-90-day PAPE residual anomalies (not shown) are collocated with $\langle Q_T \rangle_{30-90}$ anomalies (Figs. 2.24d, 2.25d, 2.26d). In fact, PAPE destruction in this residual term actually exceeds PAPE destruction

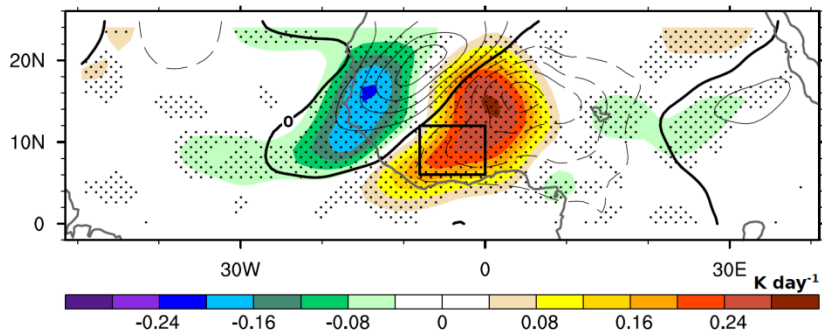


Fig. 2.27 Day 0 regression of Q_1' (shading) and T' (contours) against 700 hPa eddy vorticity averaged in the shown black box. The shading interval is 0.04 K day^{-1} . The contour interval is 0.02 K . Stippling represents shading that is 95% significant. The gray contour represents that African coastline.

by $\langle Q_T \rangle_{30-90}$ anomalies. The similarities between these two terms are strongly suggestive that errors in moist physics may be responsible for most of the residual. However, examination of the residual in this context provides no additional support for the idea that AEWs are initially invigorated by convective coupling in East Africa in advance of positive PKE events.

2.5.6 Role of Other PKE Budget Terms

While $\langle B_T \rangle_{30-90}$ and $\langle C_{pk} \rangle_{30-90}$ anomalies provide substantial intraseasonal PKE sources, other PKE budget terms in (A.14) are occasionally notable. When $\langle \phi_{FC} \rangle_{30-90}$ anomalies are composited for significant West African PKE_{30-90} and MJO events (not shown), anomalies are generally noisy in the vertical average. With growth of PKE maxima in both the MJO and PKE indices, anomalous $\langle D \rangle_{30-90}$ destroys PKE associated with increased intraseasonal AEW activity, likely with a large component due to boundary layer dissipation effects, although a budget residual also exists due to reasons discussed in Section 2.3.

Interestingly, PKE advection exhibits significant ISV relative to strong MJO and positive PKE events (not shown). $\langle A_{TOT} \rangle_{30-90}$ anomalies tend to redistribute the PKE_{30-90} field and typically oppose PKE anomalies. The variability of $\langle A_{TOT} \rangle_{30-90}$ anomalies with respect to positive PKE events (not shown) shows a westward propagation that initiates near 15°E and propagates into West Africa. Overall, $\langle A_{TOT} \rangle_{30-90}$ anomalies appear responsible for initially increasing PKE after PKE_{30-90} minimizes, especially in West Africa. Further, these anomalies ultimately partially counteract positive PKE supported by $\langle B_T \rangle_{30-90}$ and $\langle C_{pk} \rangle_{30-90}$ anomalies, which is a pattern that is robust across significant events for both MJO and local PKE indices.

2.6 ISV of Energy Budgets for the MJO Index

An interesting question is whether composites based on the MJO index indicate a similar westward progression of PKE anomalies across North Africa. Overall, a link between ISV of AEW energetics and the MJO would improve medium-range forecasts in West Africa by tying wave growth to quasi-predictable, large-scale dynamics (Matthews 2004). MJO phase composites reveal significant PKE_{30-90} variability that propagates to the west through tropical North Africa and over the eastern Atlantic Ocean (Fig. 2.28). However, MJO-related PKE_{30-90} anomalies have ~50% of the amplitude of anomalies associated with the local PKE index, which suggests that while the MJO is important in this region, it is not the only source of ISV in tropical North Africa. This result is consistent with the fact that the MJO only describes about 10% of the intraseasonal variance in easterly wave activity (see Section 2.2.2).

PKE_{30-90} anomalies maximize in West Africa in MJO phases 2-3, or 1-2 MJO phases after convection maximizes in West Africa (Alaka and Maloney 2012), and minimize in MJO phases 6-7. In most MJO phases, the highest amplitude PKE_{30-90} anomalies are concentrated to the west of 10°E. However, significant, positive PKE_{30-90} anomalies appear near 30°E in MJO phases 7, 8, and 1 (before the PKE_{30-90} maximum in MJO phases 2-3), consistent with the initial triggering in this region described by previous studies (e.g., Thorncroft et al. 2008; Leroux and Hall 2009; Alaka and Maloney 2012). Overall, the 30-90-day variability of PKE at 700 hPa is described well by the vertically averaged PKE tendency. Both $\langle \partial_t PKE \rangle_{30-90}$ and 700 hPa PKE_{30-90} anomalies maximize in the far eastern Atlantic Ocean, which suggests that AEWs experience the most growth after they have propagated offshore during significant MJO events. Since AEWs seed most Atlantic tropical cyclones (Landsea et al. 1998), an increase in AEW activity on intraseasonal time scales corresponds to more seed disturbances. Further support is

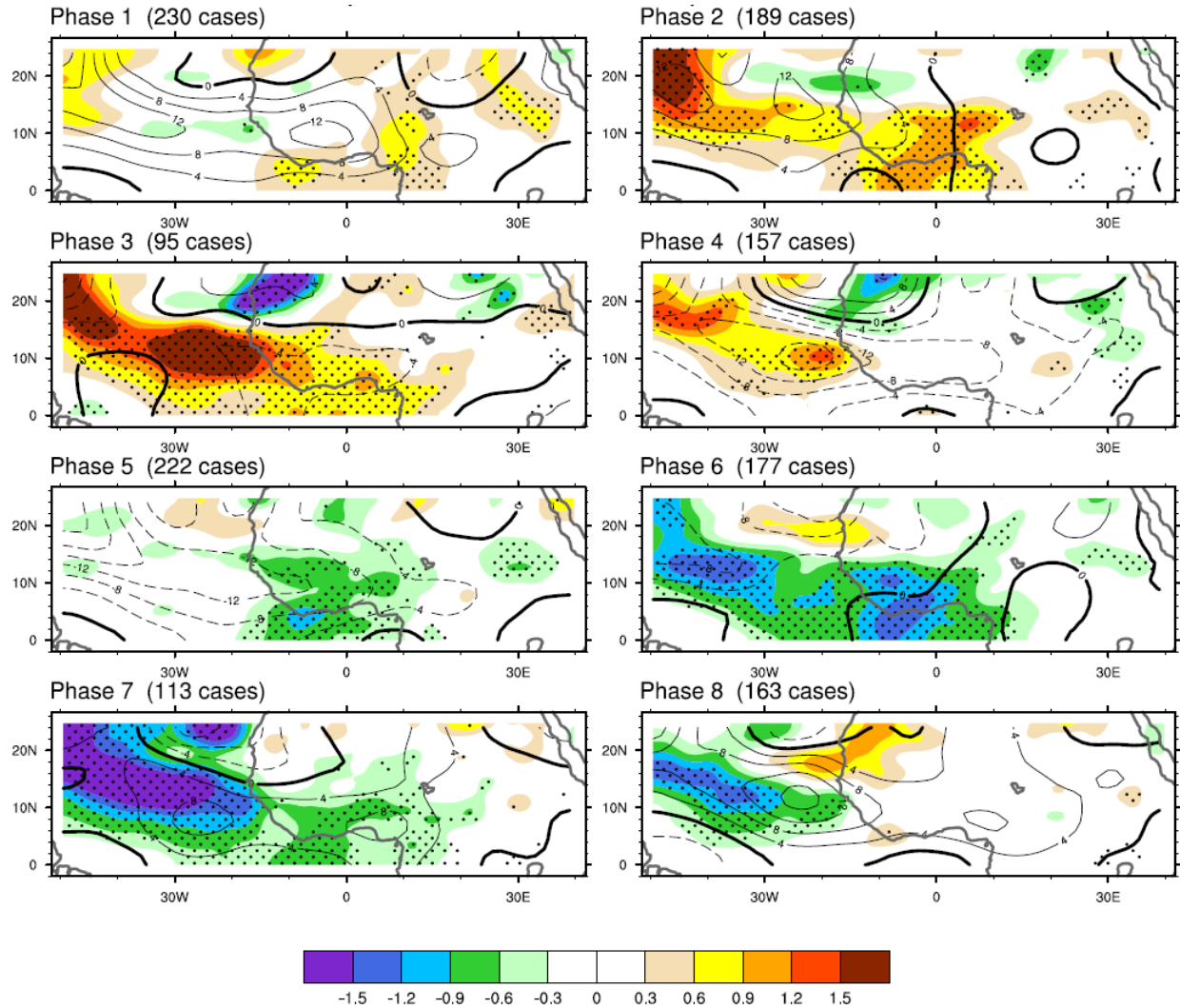


Fig. 2.28 MJO phase composites for 30-90-day 700 hPa PKE anomalies (shading) and vertically averaged 30-90-day PKE tendency (contours) for June-September. The shading interval is $0.3 \text{ m}^2 \text{ s}^{-2}$. The contour interval is $4 \times 10^{-7} \text{ m}^2 \text{ s}^{-3}$. Stippling represents PKE anomalies that are significant with 95% confidence. Coastlines are represented by a gray contour.

found in previous studies, which show that an increase in 30-90-day AEW activity coincides with a period of increased tropical cyclogenesis in the Atlantic (Maloney and Shaman 2008; Ventrice et al. 2011). To a large extent, the MJO composites in this study are a weaker version of the local PKE composites.

In general, MJO phase composites describe a similar progression of $\langle B_T \rangle_{30-90}$ anomalies, with little evidence of significant anomalies in East Africa (Fig. 2.29). Consistent with 700 hPa PKE_{30-90} anomalies, the amplitude of $\langle B_T \rangle_{30-90}$ in the MJO composites is only $\sim 50\%$ of those analyzed with the PKE index. We postulate that $\langle B_T \rangle_{30-90}$ is extremely important for creating PKE in existing easterly waves, which supports the notion that barotropic energy conversions are vital for the maintenance of AEWs in West Africa. However, its role in initiating periods of increased AEW activity appears to be limited.

During a composite MJO life cycle, $\langle B_T \rangle_{30-90}$ exhibits significant variability in a strip along 10°N (Fig. 2.29) and is collocated with 700 hPa PKE_{30-90} maxima/minima near the same latitude (Fig. 2.28). While the highest amplitude anomalies occur in the eastern Atlantic, West African $\langle B_T \rangle_{30-90}$ anomalies maximize in MJO phase 2 and minimize in MJO phase 6. In general, these $\langle B_T \rangle_{30-90}$ anomalies coincide with the southern flank of the African easterly jet (Fig. 2.17b), which suggests a potential relationship with a strengthening of the AEJ (see Section 2.7). Although $\langle B_T \rangle_{30-90}$ anomalies associated with the MJO index are only 60% of those related to the PKE index, $\langle B_T \rangle_{30-90}$ anomalies support the notion that barotropic energy conversions are vital for the maintenance of AEWs in West Africa.

Over the course of an MJO life cycle, positive, significant $\langle C_{pk} \rangle_{30-90}$ anomalies support East African PKE in MJO phase 8 and PKE downstream in West Africa in MJO phase 2 (Fig. 2.30). The amplitude of East African $\langle C_{pk} \rangle_{30-90}$ anomalies in MJO phase composites is comparable to the amplitude associated with the local PKE index (Figs. 2.25b, 2.26b). However, $\langle C_{pk} \rangle_{30-90}$ anomalies are shifted to the south in MJO phase composites, suggesting a more direct interaction with 700 hPa vorticity centers south of the AEJ during strong MJO events. Since $\langle C_{pk} \rangle_{30-90}$ is the conversion pathway for $\langle B_C \rangle_{30-90}$ and $\langle Q_T \rangle_{30-90}$ to PKE, those terms are

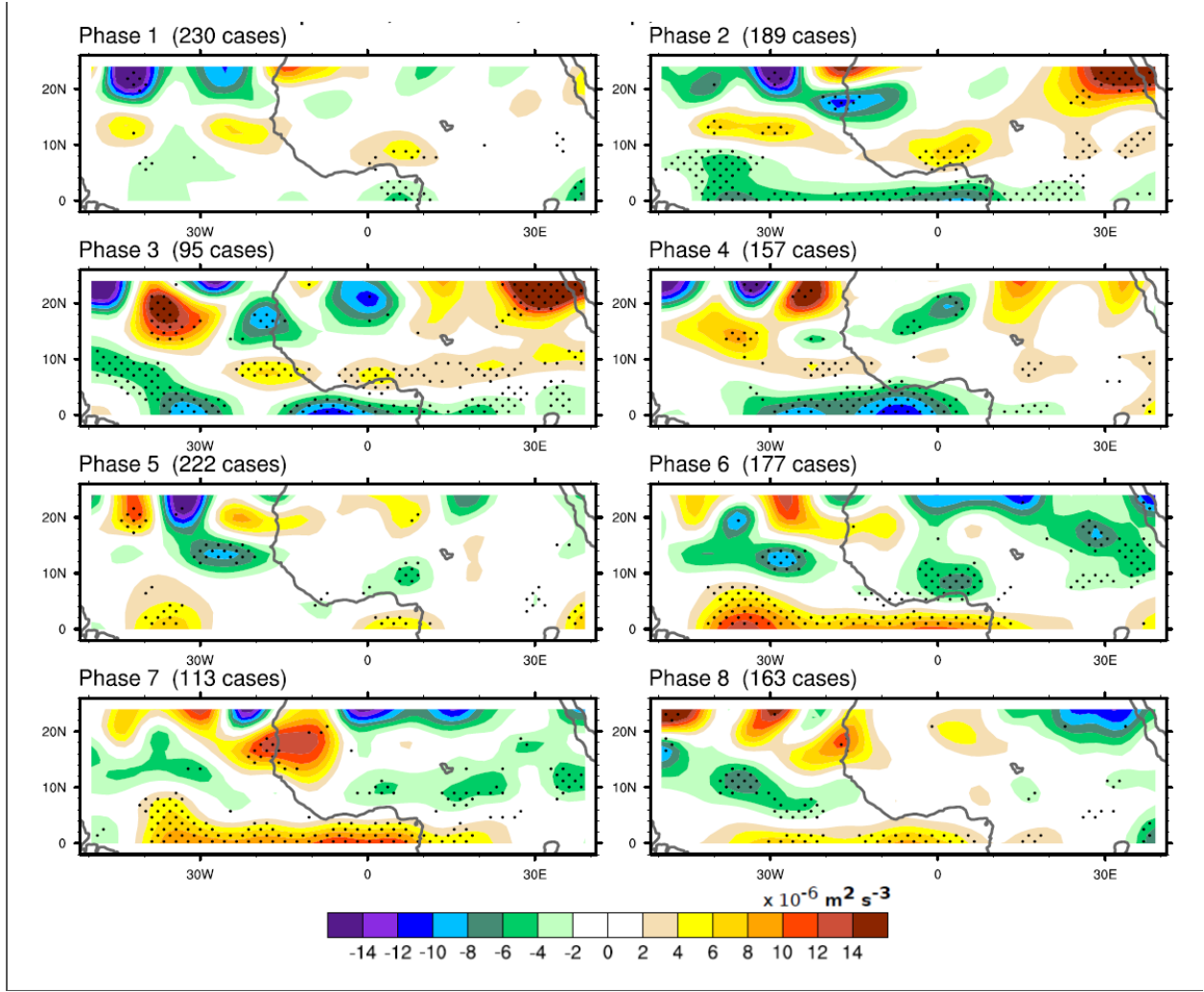


Fig. 2.29 As in Fig. 2.28, except for vertically-averaged 30-90-day B_T anomalies. The shading interval is $2 \times 10^{-6} \text{ m}^2 \text{ s}^{-3}$.

investigated the following two subsections.

MJO phase composites show significant $\langle B_C \rangle_{30-90}$ anomalies clustered between 10°N and 15°N in tropical North Africa (Fig. 2.31), near the sharp, climatological meridional potential temperature gradient (Fig. 2.17f). The importance of this temperature gradient to the amplitude of $\langle B_C \rangle_{30-90}$ is investigated further in Section 2.7. Two regions of significant, positive $\langle B_C \rangle_{30-90}$ anomalies, located near 0° and 30°E , drift slowly westward from MJO phase 1 to MJO phase 3. Significant $\langle B_C \rangle_{30-90}$ anomalies exceed $1.4 \times 10^{-5} \text{ m}^2 \text{ s}^{-3}$ in MJO phases 2, when 700 hPa

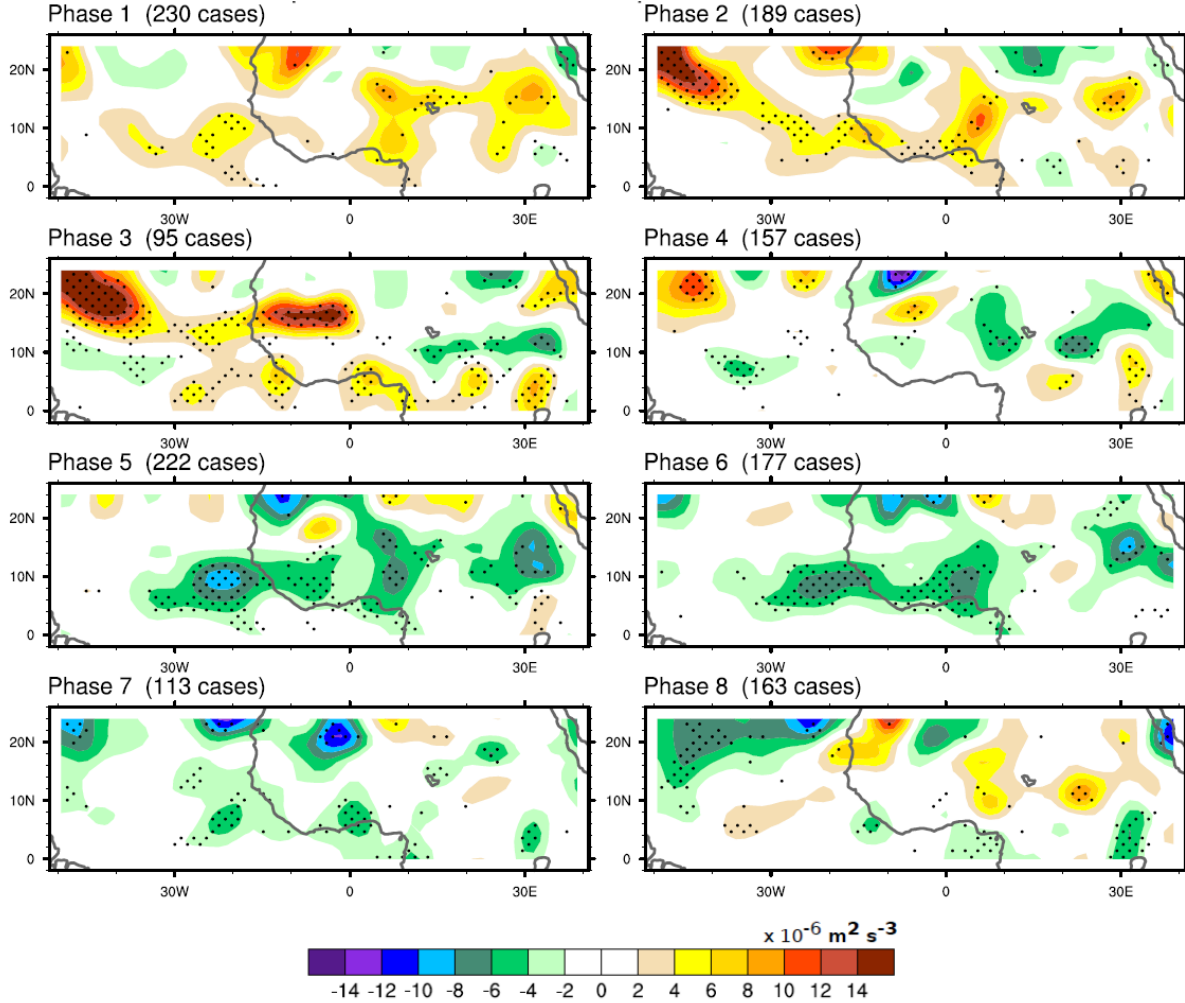


Fig. 2.30 As in Fig. 2.28, except for vertically-averaged 30-90-day C_{pk} anomalies. The shading interval is $2 \times 10^{-6} \text{ m}^2 \text{ s}^{-3}$.

PKE_{30-90} anomalies in maximize in West Africa (Fig. 2.28). By the time $\langle B_C \rangle_{30-90}$ anomalies maximize between 15°N and 20°N in MJO phase 3, 700 hPa PKE_{30-90} have already moved offshore into the East Atlantic, some 5° - 10° to the south.

This leaves little reason to believe the $\langle B_C \rangle_{30-90}$ maximum in MJO phase 3 is strongly associated with significant 30-90-day AEW activity in West Africa and the East Atlantic. While most of the $\langle B_C \rangle_{30-90}$ anomalies observed in MJO phase 3 are offset by $\langle Q_T \rangle_{30-90}$ anomalies in the same locality, the presence of $\langle B_C \rangle_{30-90}$ in the lower troposphere could signify a stronger

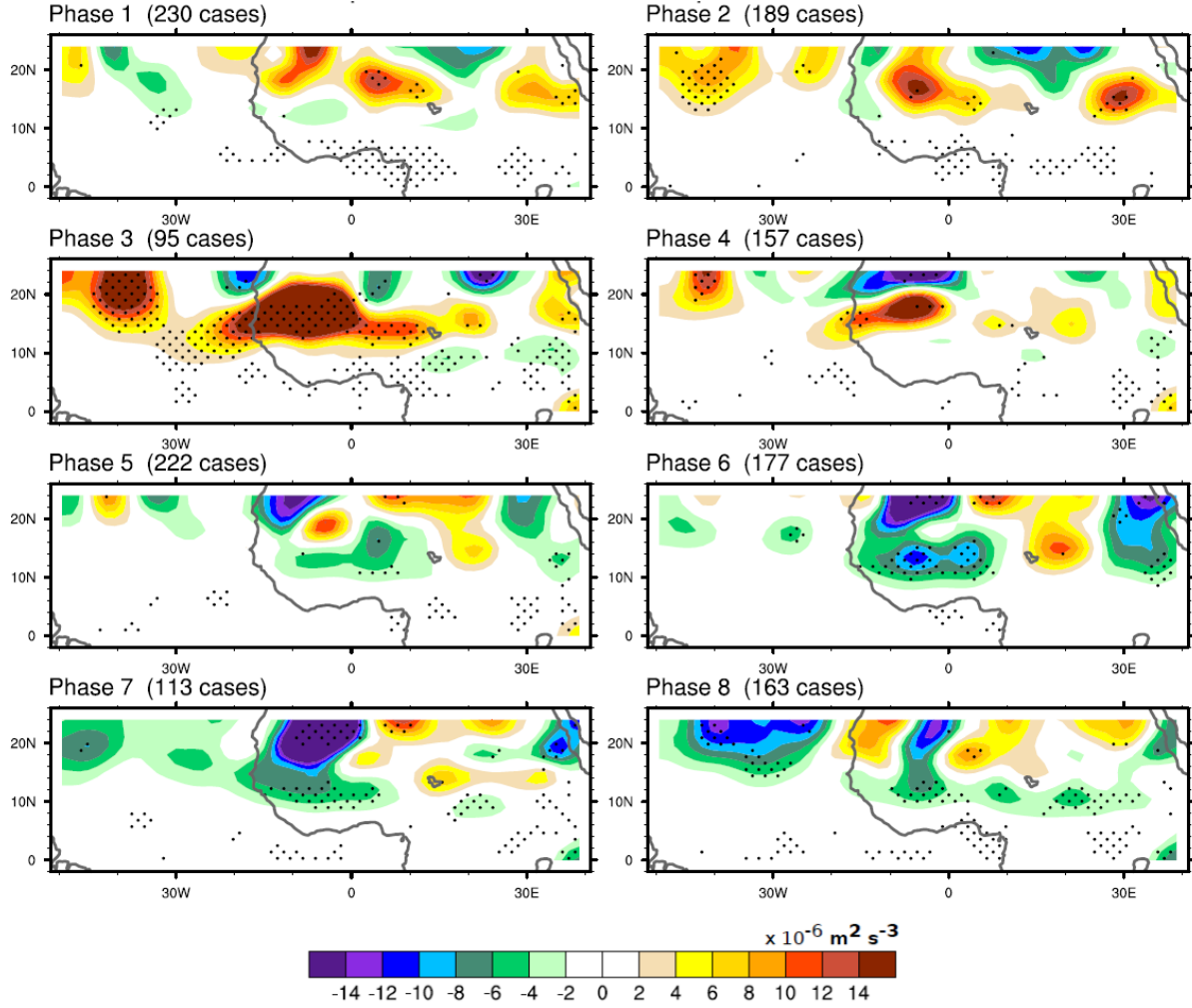


Fig. 2.31 As in Fig. 2.28, except for vertically-averaged 30-90-day B_C anomalies. The shading interval is $2 \times 10^{-6} \text{ m}^2 \text{ s}^{-3}$.

relationship with dry 900 hPa eddies on the north side of the AEJ (see Section 1.2 and Fig. 2.18f). Future analysis into how the MJO interacts with the Saharan heat low would provide insight into the relationship between the MJO and ISV of the meridional temperature gradient in North Africa. Comparisons to $\langle C_{pk} \rangle_{30-90}$ (Fig. 2.30) indicate that only some $\langle B_C \rangle_{30-90}$ anomalies are converted to PKE (e.g. – near 30°E in MJO phase 2), which suggests that the MJO index has a limited role modulating the westward propagating $\langle B_C \rangle_{30-90}$ signal observed in Fig. 2.23.

$\langle Q_T \rangle_{30-90}$ anomalies exhibit significant variability over the course of an MJO life cycle (Fig. 2.32). In particular, positive $\langle Q_T \rangle_{30-90}$ anomalies are significant in an arcing zonal strip between 10°N and 20°N (including East Africa) in MJO phase 8, which supports the notion that precursors disturbances are important in this region prior to the convective and PKE maxima in West Africa (MJO phases 1 and 2; e.g., Alaka and Maloney 2012). In fact, $\langle Q_T \rangle_{30-90}$ anomalies centered on Lake Chad increase in to near $2 \times 10^{-6} \text{ m}^2 \text{ s}^{-3}$ in MJO phase 1, which is a factor of ~5 larger than the East African amplitude associated with positive PKE events (see Figs. 2.25, 2.26). The collocation of $\langle Q_T \rangle_{30-90}$ with $\langle C_{pk} \rangle_{30-90}$ anomalies and 700 hPa PKE_{30-90} anomalies in MJO phase 1 supports a diabatically-driven increase in PKE from East African convective anomalies, as Alaka and Maloney (2012) conjectured. These results suggest that while in general strong PKE_{30-90} events do not appear to be preceded by the convective support of East African disturbances (see Figure 2.9), the PKE variability during MJO events may have a stronger connection to East African convection (e.g., Alaka and Maloney 2012).

It remains a possibility that individual positive PKE events are enhanced by anomalous reservoirs of PAPE in East Africa. As discussed in Section

2.2.3 , strong West African 700 hPa PKE_{30-90} anomalies are not strongly correlated with 30-90-day convective anomalies in East Africa (e.g., OLR, TPW). In future work, case studies of PKE events could highlight if East African convection is an important energy reservoirs for a subset of significant positive PKE events. However, the inconsistent relationship between East and West Africa on intraseasonal timescales limits the potential for reliable medium-range forecasts of downstream AEW activity based on information about East African convection (see Figs. 2.9, 2.14).

Interestingly, PKE advection exhibits significant ISV relative to significant MJO events

(not shown), as for PKE events discussed above. $\langle A_{TOT} \rangle_{30-90}$ anomalies tend to oppose

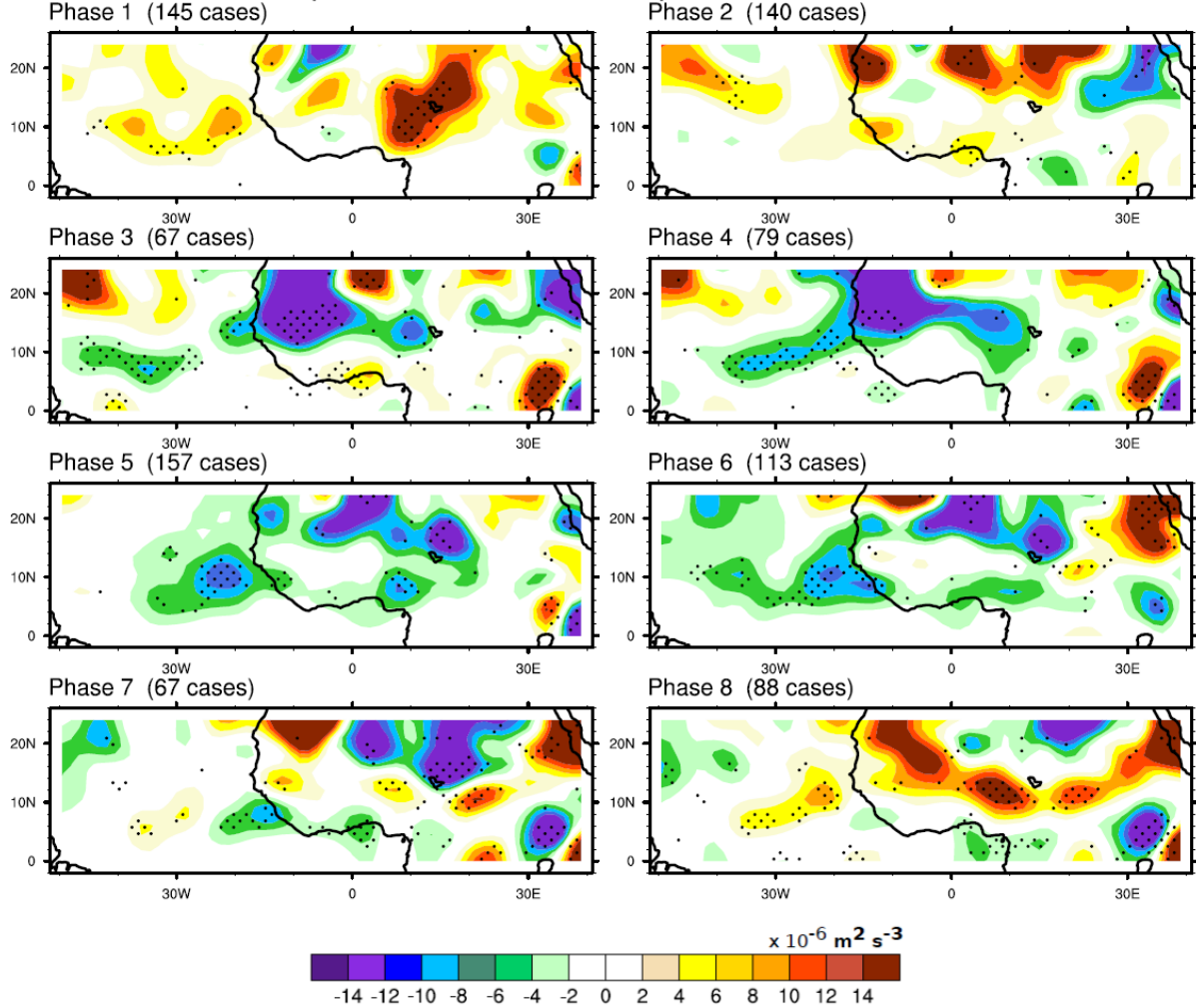


Fig. 2.32 As in Fig. 2.28, except for vertically-averaged 30-90-day Q_T anomalies. The shading interval is $2 \times 10^{-6} \text{ m}^2 \text{ s}^{-3}$.

PKE_{30-90} anomalies during MJO events. Given the occurrence of PKE creation on both sides of the AEJ, $\langle A_{TOT} \rangle_{30-90}$ may also help consolidate PKE anomalies into AEWs. The variability of $\langle A_{TOT} \rangle_{30-90}$ anomalies with respect to positive PKE events (not shown) shows a westward propagation that initiates near 15°E and propagates into West Africa. Overall, $\langle A_{TOT} \rangle_{30-90}$ anomalies appear responsible for initially increasing PKE after PKE_{30-90} minimizes, especially in West Africa. Further, these anomalies ultimately counteract positive PKE supported by

$\langle B_T \rangle_{30-90}$ and $\langle C_{pk} \rangle_{30-90}$ anomalies, which is a pattern that is robust across significant events for both MJO and local PKE indices.

2.7 Role of Meridional Gradients in PKE Sources

The ISV of barotropic and baroclinic energy conversions is investigated further by specifically decomposing each term during composite PKE events. An inspection of the formulations for B_T and B_C (A.5 and A.9) reveals that both terms are the product of a mean gradient component and a covariance component. Since strong mean meridional gradients are observed in tropical North Africa during boreal summer, the meridional components of A.5 and A.9 are dominant and, therefore, are the focus of the analysis to follow. The AEJ produces a strong meridional gradient in the zonal wind in North Africa (Fig. 2.17b). Strengthening or weakening of this meridional momentum gradient on intraseasonal time scales may be reflected in $\langle B_T \rangle_{30-90}$ (Section 2.5.2). With respect to the local PKE index, ISV of the meridional 700 hPa zonal wind gradient ($\partial \bar{u} / \partial y_{30-90}$) reveals an eastward shift of the AEJ centered near 14°N on day -10 (Fig. 2.33a), with easterly amplitudes of at least 7 m s⁻¹ extending ~10° further into East Africa than the climatological jet (Fig. 2.17b). By day 0, the eastward shift of the AEJ has been reinforced, with 700 hPa $\partial \bar{u} / \partial y_{30-90}$ anomalies reflect a strengthening of the AEJ in between 10°E and 40°E (e.g., Alaka and Maloney 2012). The AEJ also shifts north with positive PKE events, consistent with Leroux et al. (2010). Intraseasonal fluctuations in the sharpness of the basic state meridional temperature gradient, which may be modulated by large-scale phenomena such as the MJO, would impact the amplitude of $\langle B_C \rangle_{30-90}$ (Section 2.5.4). On 30-90-day timescales, 850 hPa $d\bar{T} / dy_{30-90}$ is strengthened in East Africa 10 days prior to positive PKE

events (Fig. 2.33b), which is in thermal wind balance with the AEJ extension into this region.

The shift of 850 hPa $d\bar{T}/dy_{30-90}$ anomalies from West Africa to East Africa might reflect ISV

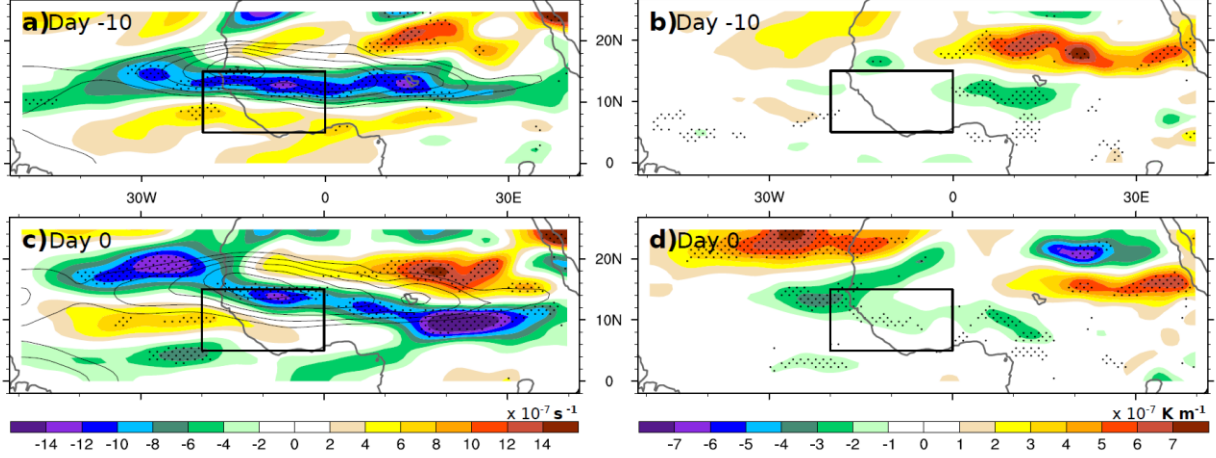


Fig. 2.33 As in Fig. 2.22, except for: (a) 30-90-day 700 hPa meridional zonal wind gradient anomalies (shading) and 30-90-day 700 hPa zonal wind $\leq -7 \text{ m s}^{-1}$ (contours) on day -10, (b) (a) on day 0, (c) 30-90-day 850 hPa meridional temperature gradient anomalies on day -10, and (d) (c) on day 0. Please note that the shading interval is $2 \times 10^{-7} \text{ s}^{-1}$ in (a), (c) and $1 \times 10^{-7} \text{ K m}^{-1}$ in (b), (d). The contour interval is 1 m s^{-1} in (a), (c). Coastlines are represented by a gray contour.

of the Saharan heat low (Lavaysse et al. 2010, Chauvin et al. 2010). Like the AEJ extension, this anomalously strong low-level temperature gradient persists through day 0 (Fig. 2.33d).

For each energy conversion term, the covariance component ($\overline{v'u'}$ or $\overline{v'T'}$) represents the contribution of strong perturbations (i.e., AEWs) to the amplitude of $B_{T_{30-90}}$ or $B_{C_{30-90}}$. Thus, we will investigate the role of large-scale fluctuations in meridional gradients (see Fig. 2.33) versus the role of strong eddy covariances (i.e., strong AEWs) in the variability of $B_{T_{30-90}}$ and $B_{C_{30-90}}$ anomalies. This is accomplished by selectively setting the eddy covariance or meridional gradient component equal to the boreal summer mean to assess the contribution of ISV in the other component to total $\langle B_T \rangle_{30-90}$ or $\langle B_C \rangle_{30-90}$ (see Appendix). For reference, the

meridional components of 700 hPa B_{T30-90} (Fig. 2.34a) and 850-hPa B_{C30-90} (Fig. 2.34b) exhibit the behavior of their vertically averaged counterparts on intraseasonal timescales.

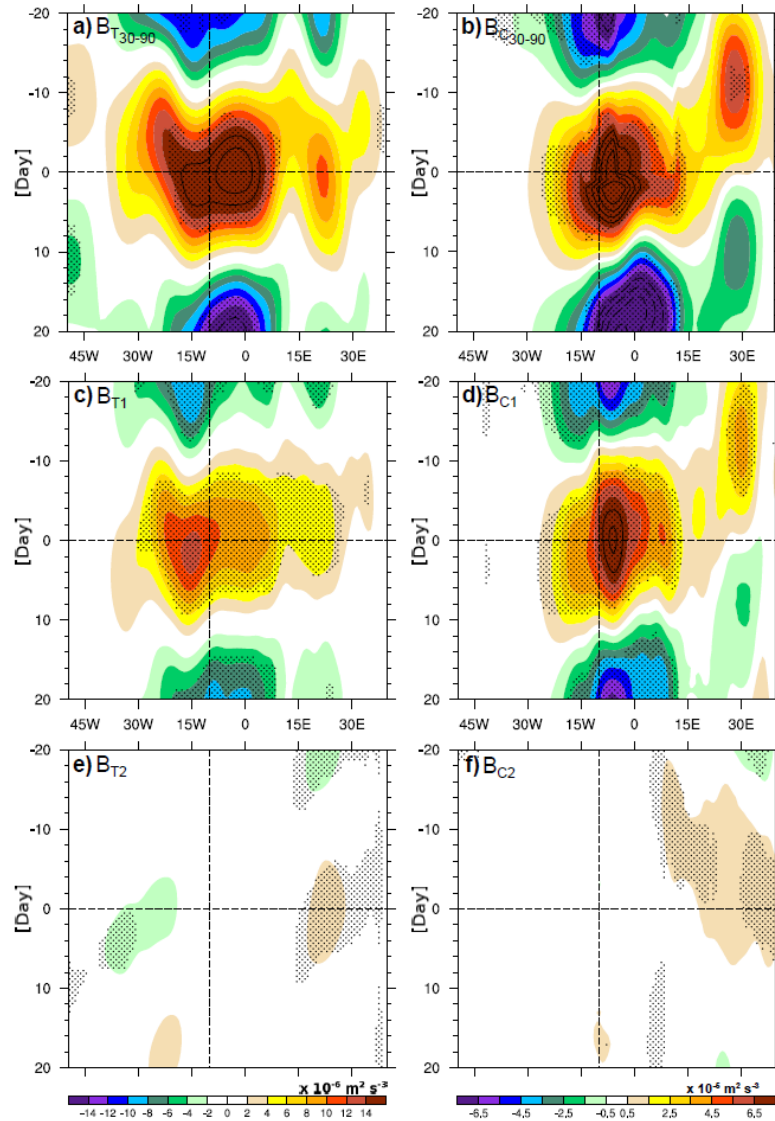


Fig. 2.34 As in Fig. 2.21, except for: (a) 30-90-day 700 hPa barotropic energy conversion anomalies, (b) 30-90-day 850 hPa baroclinic energy conversion anomalies north of the AEJ, (c) B_{T1} anomalies, (d) B_{C1} anomalies, (e) B_{T2} anomalies, and (f) B_{C2} anomalies. (a), (c), and (e) have a shading interval of $2 \times 10^{-6} \text{ m}^2 \text{ s}^{-3}$ and are analyzed south of the AEJ. (b), (d), and (f) have a shading interval of $1 \times 10^{-5} \text{ m}^2 \text{ s}^{-3}$ and are analyzed north of the AEJ. If necessary, contours extend above/below the shading limits with an interval of $2 \times 10^{-6} \text{ m}^2 \text{ s}^{-3}$.

Throughout tropical North Africa, positive 700 hPa $B_{T_{30-90}}$ anomalies are predominantly driven by strong eddies ($\overline{v'u'}$) on intraseasonal time scales (B_{T1} ; A.10). Strong eddies increase 700 hPa B_{T1} amplitudes west of 10°E, supporting the amplitude of AEWs across most of tropical North Africa (Fig. 2.34c). Maximum 700 hPa B_{T1} amplitudes have comparable magnitudes to the meridional component of B_T at the same level (Fig. 2.34a), which suggests that strong eddies increase $B_{T_{30-90}}$ across tropical North Africa prior to and during positive PKE events. The 700 hPa mean meridional zonal wind gradient ($\partial\bar{u}/\partial y$) was bandpass filtered to 30-90 days and multiplied by boreal summer mean $\overline{v'u'}$ (B_{T2} ; A.11). Significant, positive 700 hPa B_{T2} anomalies in East Africa indicate increased shear on the south side of the AEJ during positive PKE events (Fig. 2.34e). However, B_{T2} are insignificant in East Africa in advance of PKE events, which points to the notion that the AEJ extension observed prior to positive PKE events plays little role in initiating ISV through barotropic energy conversions in this region.

The ISV of the eddy covariance term ($\overline{v'T'}$) is investigated through 850 hPa B_{C1} anomalies (Fig. 2.34d). With a maximum greater than $1.2 \times 10^{-4} \text{ m}^2 \text{ s}^{-3}$ in West Africa at day 0, B_{C1} anomalies closely mimic the meridional component of 850 hPa $B_{C_{30-90}}$ anomalies in location and amplitude (Fig. 2.34b). Westward propagation of 850 hPa B_{C1} anomalies is evident, although these anomalies have a gap near 15°E. Next, the 850 hPa meridional temperature gradient is filtered to 30-90-days ($d\bar{T}/dy_{30-90}$) and multiplied by boreal summer mean $\overline{v'T'}$ (B_{C2} ; A.13). Positive B_{C2} anomalies reflect positive 850 hPa $d\bar{T}/dy_{30-90}$ anomalies that extend east prior to positive PKE events (Fig. 2.34f). Since 850 hPa B_{C2} anomalies are positive and significant prior to positive PKE events, a sharpened temperature gradient in East Africa may help initiate periods of increased AEW activity (Fig. 2.33). Of note is the fact that significant B_{C2} anomalies in East Africa account for ~20% of the 850 hPa $B_{C_{30-90}}$ maxima near 30°E.

Elsewhere, 850 hPa $B_{C_{30-90}}$ anomalies appear to be dominated by strong eddies throughout tropical North Africa. In East Africa, a strengthened meridional temperature gradient may help initiate intraseasonal AEW activity before positive PKE events.

2.8 Intraseasonal Variability of Tropical Cyclogenesis in the East Atlantic

An important topic is the relationship between positive PKE events in West Africa and tropical cyclogenesis in the East Atlantic. If increased tropical cyclone formation follows from positive 30-90-day PKE anomalies in West Africa, the predictability of cyclogenesis in this region would greatly improve. Although AEWs seed most Atlantic tropical cyclones (Avila and Pasch 1992; Landsea et al. 1998), the favorability of further development is based primarily on a set of environmental conditions introduced in Gray 1998. Thus, increased West African PKE may only impact tropical cyclogenesis when other environmental factors are favorable for development.

The link between West African PKE and Atlantic tropical cyclogenesis is investigated for both the local PKE and MJO indices. East of 45°W, positive and negative 30-90-day PKE events are associated with similar numbers of cyclogenesis between 10°N and 15°N (Fig. 2.35). However, if only cyclogenesis events collocated with significant 700 hPa anomalies are considered, twice as many cyclogenesis events are directly associated with positive PKE events (0.57/yr) than with negative PKE events (0.29/yr). In addition, tropical cyclogenesis events appear to be closer to the West African coastline around positive PKE events. The lack of a coherent signal is direct evidence of the role that other environmental factors can play in directing cyclogenesis from an AEW.

When the MJO index is considered, tropical cyclogenesis events populate the East Atlantic during MJO phases 8, 1 and 2 (Fig. 2.36). However, significant West African PKE

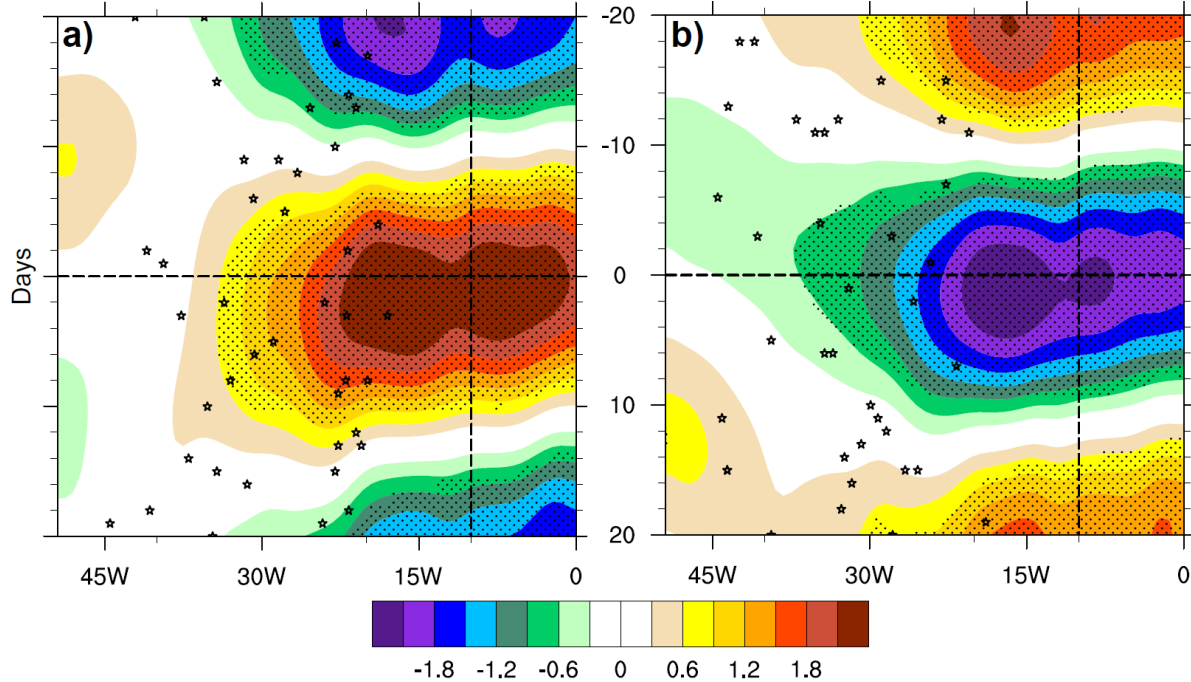


Fig. 2.35 As in Fig. 2.21, except for: (a) 30-90-day 700 hPa PKE anomalies associated with positive PKE events over the East Atlantic and (b) 30-90-day 700 hPa PKE anomalies associated with negative PKE events over the East Atlantic. Hovmöller are averaged between 10°N and 15°N . Tropical cyclogenesis events (stars) are from the Revised Hurricane Database (HURDAT2). The shading interval is $0.3 \text{ m}^2 \text{ s}^{-2}$.

anomalies lag East Atlantic cyclogenesis events, suggesting that the MJO does not robustly modulate tropical cyclogenesis through AEW variability. On the other hand, 30-90-day OLR anomalies reveal that Atlantic tropical cyclogenesis is strongly linked to a more convectively active ITCZ on intraseasonal timescales (Fig. 2.37). As a result, MJO phases 8, 1, and 2 feature 25 cyclogenesis events between 1990 and 2010 versus 14 cyclogenesis events in the other five MJO phases combined.

2.9 Discussion

In this study, the PKE and PAPE budgets are investigated using ERA-Interim fields to determine the sources of PKE variability associated with the West African monsoon on

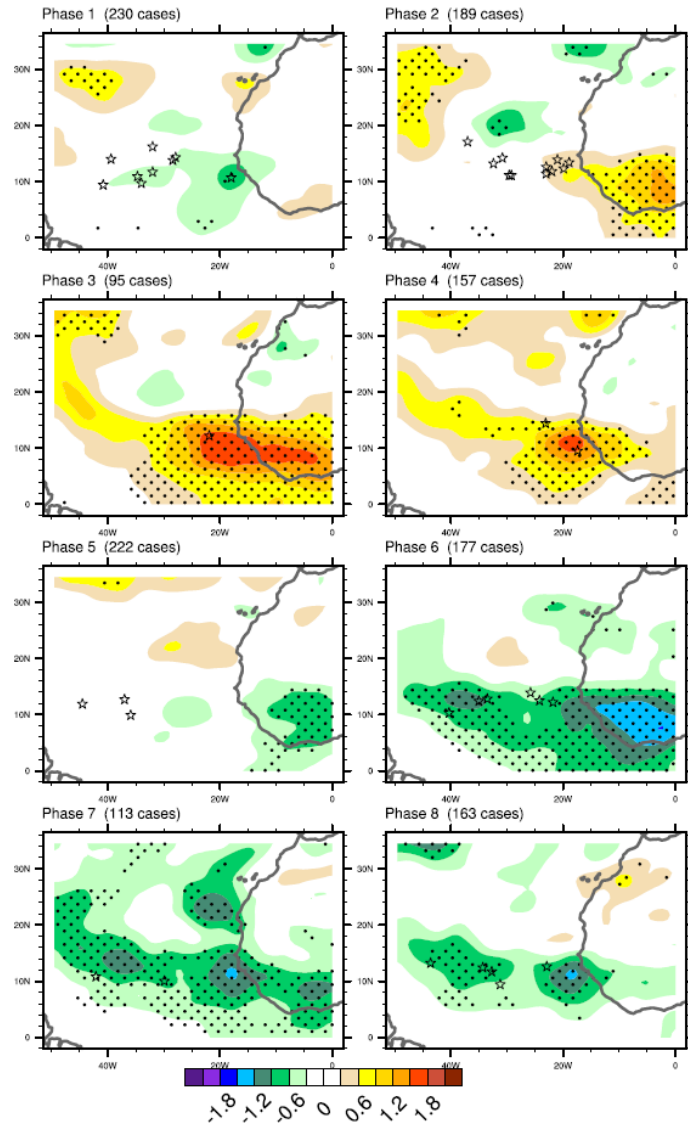


Fig. 2.36 MJO phase composites for ERA-Interim 30-90-day 700 hPa PKE anomalies Tropical cyclogenesis events (stars) are from the Revised Hurricane Database (HURDAT2). The shading interval is $0.3 \text{ m}^2 \text{ s}^{-2}$.

intraseasonal time scales. Four budget terms are critical to the creation of PKE_{30-90} : barotropic energy conversion (B_T), baroclinic overturning (C_{pk}), baroclinic energy conversion (B_C), and the diabatic generation of PAPE (Q_T). We examine how 30-90-day anomalies of these four budget terms combine to produce periods of increased intraseasonal AEW activity in West Africa,

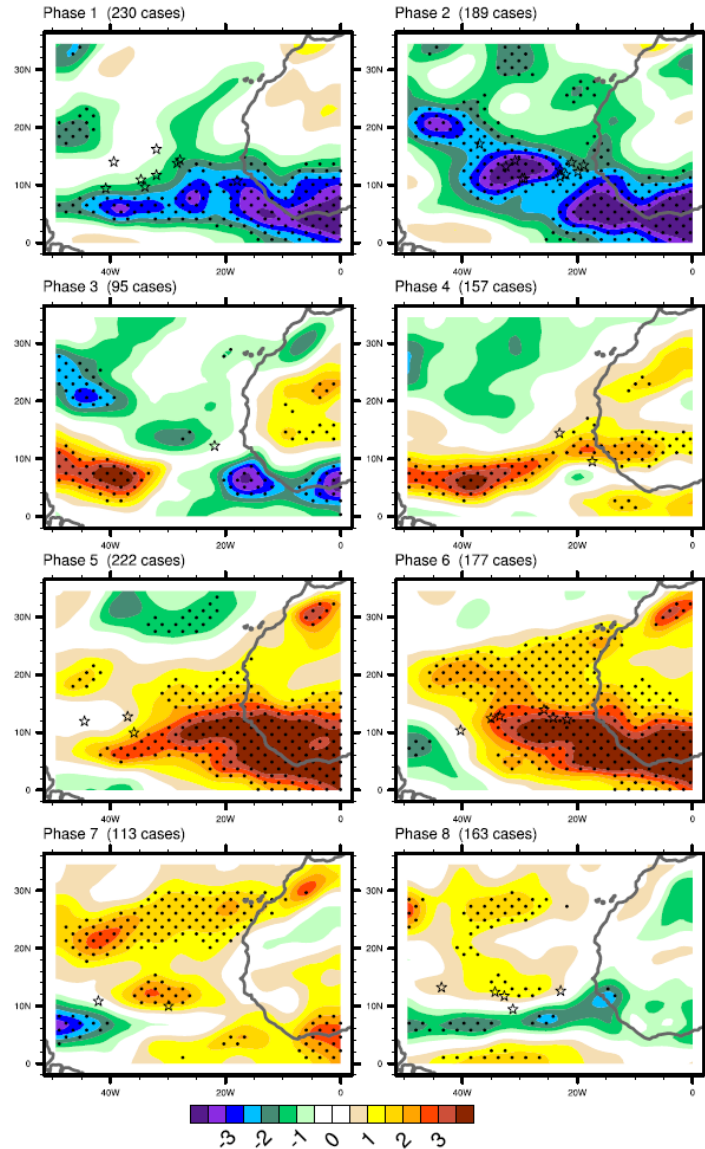


Fig. 2.37 MJO phase composites for ERA-Interim 30-90-day OLR anomalies. Tropical cyclogenesis events (stars) are from the Revised Hurricane Database (HURDAT2). The shading interval is 0.5 W m^{-2} .

which has been shown to be significant on these time scales in previous studies (Leroux and Hall

2009; Ventrice et al. 2011; Alaka and Maloney 2012).

To provide context for the analysis of ISV, boreal mean PKE and PAPE budgets were first analyzed. The horizontal and vertical distributions of boreal summer mean ERA-Interim PKE and PAPE budget terms (Figs. 4 and 5) generally agree with past studies (Lau and Lau 1992; Thorncroft and Hoskins 1994a,b; Diedhiou et al. 2002; Hsieh and Cook 2007), including important roles for B_T , C_{pk} , B_C , and Q_T in AEW generation. We draw the following conclusions about the ISV of PKE and PAPE energy budgets and their role in producing intraseasonal PKE anomalies:

- The MJO explains a significant, but small, fraction ($\sim 10\%$) of 30-90 day intraseasonal PKE variability in West Africa. During strong MJO years, the intraseasonal West African PKE variance explained by the MJO increases to about 25%. In general, MJO PAPE and PKE budget composites are consistent with those described by a local PKE index, although with $\sim 50\%$ the amplitude. However, MJO events may exhibit a stronger link between East African heating and West African PKE than for locally-determined PKE events.
- A stronger meridional temperature gradient ($d\bar{T}/dy_{30-90}$) appears important for initiating periods of increased intraseasonal PKE in East Africa through enhanced B_C . This signal is consistent with the ISV of the Saharan heat low (Lavaysse et al. 2010; Chauvin et al. 2010).
- Although the AEJ is extended into East Africa prior to positive PKE events (e.g., Leroux and Hall 2009; Alaka and Maloney 2012), $\partial\bar{u}/\partial y_{30-90}$ does not support PKE in this region until day 0. Thus, the AEJ extension does not appear to initiate ISV through B_T .
- The anomalous Q_T signal is weak and insignificant in East Africa in advance of periods

of enhanced PKE, a surprising result in the context of earlier studies citing the importance of strong diabatic heating in this region for seeding enhanced AEW activity (Leroux et al. 2010; Alaka and Maloney 2012). However, the link might be stronger for MJO events.

- $\langle B_C \rangle_{30-90}$ and its conversion to PKE maintains PKE_{30-90} activity downstream in West Africa, primarily through $\bar{v}'T'$ acting on the climatological temperature gradient.
- $\langle Q_T \rangle_{30-90}$ destroys PAPE in West Africa where $\langle B_C \rangle_{30-90}$ is strong, providing a negative feedback onto generation of PAPE by $\langle B_C \rangle_{30-90}$. This signal results from convection being suppressed (enhanced) in warm (cold) northerly (southerly) flow associated with stronger AEWs, consistent with previous results by Kiladis et al. (2006).
- $\langle B_T \rangle_{30-90}$ maintains PKE_{30-90} activity in West Africa through strengthened $\bar{u}'v'$ acting on the climatological zonal wind gradient (i.e., AEJ).
- Tropical cyclogenesis in the East Atlantic is more common after positive PKE events in West Africa than after negative PKE events in West Africa. Positive 30-90-day PKE anomalies lag tropical cyclogenesis events in the Atlantic, suggesting that the MJO does not dominantly modulate Atlantic tropical cyclones through AEW variability. Instead, 30-90-day OLR anomalies associated with the Atlantic ITCZ are associated with East Atlantic cyclogenesis.

One possible reason for the diminished role of Q_T in supporting the initiation of increased intraseasonal PKE is that the ERA-Interim model likely underestimates the heating associated with convective and microphysical processes, as evidenced by the structure and amplitude of the PAPE residual. However, even adding the residual to Q_T does not significantly alter our conclusions. The role of Q_T may be more accurately assessed in future studies with more precise

heating rate measurements.

As is to be expected in an observation-based study, this analysis stimulates several questions pertaining to the relationship of the PKE and PAPE energy budgets with each other and with the large scale environment. The ISV in West Africa is significantly correlated with an MJO index, especially during years with strong MJO activity. However, it remains unclear how the MJO actually forces ISV in this region, including an extension of the AEJ or increases the temperature gradient in tropical North Africa. Modeling studies could clarify the importance of equatorial waves (i.e., equatorial Kelvin and Rossby waves) to AEW activity, as suggested in Alaka and Maloney (2012). In particular, selectively filtering 30-90-day activity from the boundaries of a regional model would be useful in examining how the nature of ISV in North Africa changes in the absence of MJO influence. This is the topic of subsequent chapters in this dissertation. Even if the MJO teleconnection to West Africa is completely understood, about 90% of the intraseasonal variance in this region is related to other processes (even during strong MJO years), which include internal variability, the NAO, and the QBZD. Further observation-based and modeling studies are necessary to investigate the extent to which ISV in the West African monsoon region is locally versus remotely regulated, and the processes responsible for producing variability local to the West African monsoon system.

CHAPTER 3 Simulation of the West African Monsoon in the WRF-ARW and WRF-NMM Dynamical Cores

3.1 Introduction

Regional climate models (RCMs) are computational tools that are capable of running high resolution simulations in a particular region of interest. In a regional climate model, lateral boundary conditions, which represent input from the rest of the globe, are supplied at the lateral edges so that the simulation may react consistently with large-scale features. Regional climate models are initialized with input data that is interpolated to the grid of interest. In global models, only the initialization is necessary due to the periodicity of the planet, but resolutions are typically coarser and computational costs higher than regional climate models. Like their global counterparts, a myriad of parameterization options typically exist in regional climate models in order to account for sub-grid scale processes. In particular, the most common parameterizations include: radiation, convection, microphysics, land surface, and boundary layer. Even with the finer meshes afforded in most regional climate models, a “high-resolution” grid spacing might be 1 km x 1 km. In high-resolution cases that are becoming more common, cumulus parameterization is turned off when grid spacing is less than ~4 km (e.g., Marsham et al. 2011). Other parameterizations, such as the microphysics parameterization, are not typically turned off in non-idealized simulations. The microphysics simulates the distribution of water species in vapor, liquid, and solid states on scales too fine to be resolved by present-day high-resolution grids.

Several flavors of regional climate models exist, some of which are discussed here. The description of all RCMs is avoided since so many variations exist and most are not well-

documented. One of the first regional climate models was the Regional Atmosphere Modeling System (RAMS; Pielke et al. 1992), which uses a fixed Arakawa C grid in the parent and nested domains. A successor to RAMS, the Ocean-Atmosphere-Land Model (OLAM; Walko and Avissar 2008a,b) is a global version of RAMS that allows fluid downscaling to finer resolutions in a particular region. A newer model (and similar concept to OLAM) is the Model for Prediction Across Scales (MPAS; Skamarock et al. 2012), which uses a quasi-uniform Voronoi mesh that can seamlessly nest down to fine scales in a region of interest. These Voronoi meshes are similar in nature to icosahedral, or hexagonal, grids. The Regional Climate Model version 3 (RegCM3; Pal et al. 2007) is a three-dimensional, regional, primitive equation climate model that was originally developed by Dickinson et al. (1989). RegCM3 is maintained by the Abdus Salam International Centre for Theoretical Physics (ICTP).

Despite the value in a diverse set of RCMs, this study focuses on the Weather Research and Forecasting (WRF) model, first introduced with the Advanced Research WRF (WRF-ARW) dynamical core (e.g., Skamarock and Klemp 2008). The WRF-ARW core has become a staple for regional climate modeling studies. A vital part of this project is to model AEWs and the associated energetics. Before the WRF-ARW was even released to the research community, the need for a different dynamical core for real-time forecasting applications was obvious. However, this undermined the goal of WRF being a singular model framework for users to interchange parameterizations based on their research needs. Nevertheless, the Nonhydrostatic Mesoscale Model WRF (WRF-NMM; Janjic et al. 2001) is now the dynamical core that drives the North American Mesoscale (NAM) model. As shown in Table 3.1, the WRF-ARW and WRF-NMM dynamical cores have significant differences from one another. The most important of these differences are the conservation principles adhered to by each core. The WRF-ARW conserves

Table 3.1 Comparison of attributes within the WRF-ARW and WRF-NMM dynamical cores.

	WRF Dynamical Core	
	WRF-ARW	WRF-NMM
Equation Form	Flux	Advection
Vertical Coordinate	Terrain-following σ	Terrain-following σ that relaxes to pressure
Grid Type	C grid	E grid
Explicit Integration	Only acoustic/gravity waves	Fully explicit
Conserved Quantities	Momentum, dry entropy, mass, moisture	Enstrophy, energy

momentum, dry entropy, mass, and moisture. On the other hand, the WRF-NMM conserves enstrophy and energy. These differences in conserved quantities may impact a simulation in a variety of ways. For example, near topography, the WRF-ARW will be concerned with balancing the mass that is flowing up or down the slope of the terrain. In the vicinity of the same topography, however, the WRF-NMM will invoke vorticity balance through enstrophy conservation. Thus, the diurnal cycle of winds and precipitation near topography is likely to be quite different in the two dynamical cores. Having two dynamical cores within WRF has made the model more versatile, with an ability to serve an operational agenda with the WRF-NMM core and to further research efforts with the WRF-ARW core

For over a decade, regional climate modeling has played an integral role in simulating the West African monsoon at resolutions finer than most global climate models (Druyan et al. 2009; Sylla et al. 2013). Dynamical downscaling in RCMs has allowed for the in-depth interpretation of the West African monsoon and its complicated features (see Section 1.3). Since observations in West Africa are likely decreasing (e.g., Ali et al. 2005) and computational power has been increasing, the necessity for reliable simulations in the West African monsoon region is on the rise. Vizy and Cook (2002) were the first to study the West African monsoon with an RCM (or a

“mesoscale climate model”, as they called it) adapted from the Penn State University/National Center for Atmospheric Research mesoscale model 5 (PSU/NCAR MM5; Grell et al. 1994). The PSU/NCAR MM5 was modified in three ways to reproduce the WAM in Vizy and Cook (2002) study: 1) the cumulus scheme was invisible to solar radiation in fractional cloud grid boxes, 2) excessive upper-level moisture was eliminated, and 3) the seasonal cycle for surface variables was added. A finer resolution version of this MM5-adapted RCM is utilized in series of studies focused on AEW dynamics (Hsieh and Cook 2005, 2007, 2008). An RCM from the Max-Planck Institute for Meteorology called REMO adequately simulated precipitation variability in West Africa over the course of a 25-year run (Paeth et al. 2005). Several studies have utilized RegCM3 to study the West African monsoon with modest reproduction of key WAM features (Afiesimama et al. 2006; Abiodun et al. 2007; Sylla et al. 2009).

WRF-ARW has been widely used as a research tool for investigating the large-scale features of the WAM region (Flaounas et al. 2010; Nicholson 2013; Noble et al. 2014). These studies have horizontal grid spacing on the order of tens of kilometers. AEW case studies have also a focus of recent research efforts with the WRF-ARW (Torn 2010; Wolters et al. 2010; Berry and Thorncroft 2012; Ross et al. 2012). Recently, Cook and Vizy (2013) utilized WRF-ARW to analyze the rainy season in East Africa. Although WRF-NMM has not been used extensively in the research of the WAM region, (Xue et al. 2014) show that the WRF-NMM might simulate WAM precipitation better than the WRF-ARW. With so many different regional climate models to choose from, it is to be expected that some RCMs will provide more realistic simulations than others. However, past studies have yielded encouraging results on the ability of various RCMs to reproduce primary WAM features (see Section 1.3). Upon comparing WAM climatology in eight RCMs, Sylla et al. (2013) determined that, while no RCM is perfect, all

members realistically captured the mean rainfall, the annual cycle, and variability between wet and dry years.

Although not the focus of this study, the WRF-ARW has been used in regional research efforts from different parts of the globe. In particular, the sensitivity of North American precipitation and temperature to land surface models and cumulus parameterizations in the WRF-ARW show that model solutions in this region are quite sensitive to the model setup (Bukovsky and Karoly 2009, 2011; Bukovsky 2012). In addition, the WRF-ARW has been used to successfully model the Indian monsoon region (Routray et al. 2009), Southeast Asia and Japan (Hayashi et al. 2008), and Southwest Asia (Xu et al. 2009). The WRF-ARW is a versatile tool for the assessment of regional climate in different parts of the globe.

Recall that the intraseasonal band represents the time scales of interest to this dissertation. However, if we are to study the variability about a baseline state, then the accurate simulation of the baseline state is vital to the interpretation of results. Thus, this chapter is dedicated to determining the configuration of the dynamical core and parameterizations we will use throughout the rest of the study to reproduce key components of the WAM.

3.2 Models and Input Data

The WRF-ARW version 3.5.1 uses a single mesh (no nesting) with a grid spacing of 30km, 38 vertical levels (up to 50 hPa), and a time step of 90 seconds. The model domain stretches from 10°S to 40°N, and from 53°W to 42°E, and was chosen specifically to include tropical North Africa and the East Atlantic. This domain is wide enough to capture the full life cycle of AEWs, including the potential development into tropical cyclones after propagating into the Atlantic Ocean. However, this domain was carefully chosen to not include: 1) the western

Indian Ocean, where the MJO initiates, 2) the East Pacific, where a strong amplification of the intraseasonal signal occurs, and 3) the northern midlatitudes, where baroclinic eddies periodically propagate through Europe. Fixed parameterizations in this study include the new NASA Goddard longwave and shortwave radiation schemes (Chou and Suarez 1999), the Grell 3D cumulus scheme (Grell and Devenyi 2002), the Mellor-Yamada-Janjić (MYJ) planetary boundary layer scheme (Janjić 1994), and the Eta similarity surface scheme (Janjić 1994), which is based on Monin and Obukhov (1954). Sensitivity tests will be performed for microphysics parameterization and land surface model for the WRF-ARW, so these options are discussed in more detail below.

The WRF-NMM version 3.1 coupled to the Simplified Simple Biosphere (SSiB) land surface model was provided by Drs. Yongkang Xue and Fernando de Sales at the University of California-Los Angeles (UCLA). The WRF-NMM is a single mesh (no nesting) setup with a grid spacing of 0.25° , 51 vertical levels (up to 50 hPa), and a time step of 60 seconds. The model domain covers 10°S to 35°N and 38°W to 48°E . Other parameterizations included in the WRF-NMM are the GFDL longwave/shortwave radiation schemes, the Betts-Miller-Janjić cumulus scheme (Janjić 1994), Ferrier microphysics from the Eta model (Rogers et al. 2001), the MYJ planetary boundary layers scheme, and the Eta similarity surface scheme. These features were fixed since the version of WRF-NMM provided had been optimized for producing a realistic West African climatology (personal correspondence with Dr. Fernando De Sales).

ERA-Interim data (0.75° grid spacing) will be used as the initial and lateral boundary conditions for boreal summer runs of both of the WRF-ARW and WRF-NMM. Sylla et al. (2013) found that the simulation accuracy of RCMs is strongly linked to the boundary conditions. Thus, the flow impacting the model boundaries will be the same in both cases,

allowing each WRF version to create its own realization of the WAM. In the search for a suitable model version to explore WAM variability, these first sensitivity experiments are initialized on May 15, 2001 and run through August 31, 2001 (unless the model crashes). The first 16 days are considered spin-up and are not included in the plots shown below. Therefore, June, July, and August are analyzed in each experiment. The model data is output every six hours in order to partially resolve the strong diurnal variability associated with the WAM. These simulations were run on NCAR's Yellowstone supercomputer.

3.3 Running the WRF-NMM Dynamical Core with ERA-Interim Boundary Conditions

As described earlier, WRF-NMM version 3.1 is coupled to the Simplified Simple Biosphere (SSiB) land surface model for the following simulations. Initially, this version of WRF-NMM would only run with NCEP reanalysis data as the initial and lateral boundary conditions. In order to be consistent with other aspects of this study, including sensitivity tests for the WRF-ARW model, we reconfigured WRF-NMM to accept ERA-Interim reanalysis data as the initial and lateral boundary conditions. Specifically, the SSiB land surface model did not previously have the infrastructure to interpret the different soil layers offered in ERA-Interim (Fig 3.1). ERA-Interim offers a four-layer system that extends down to 255cm beneath the surface, while NCEP data has three layers that extend down to 200cm. Additionally, the maximum depth of vegetation root systems is reconciled with the different ERA-Interim soil levels. The specific layer from which each type of vegetation draws moisture is set in a lookup table, which is updated so that the maximum root depth for each vegetation type extended into the proper soil layer. While this sounds trivial, the moisture available to the boundary layer is strongly influenced by how much moisture the vegetation can access. Anomalies in the surface

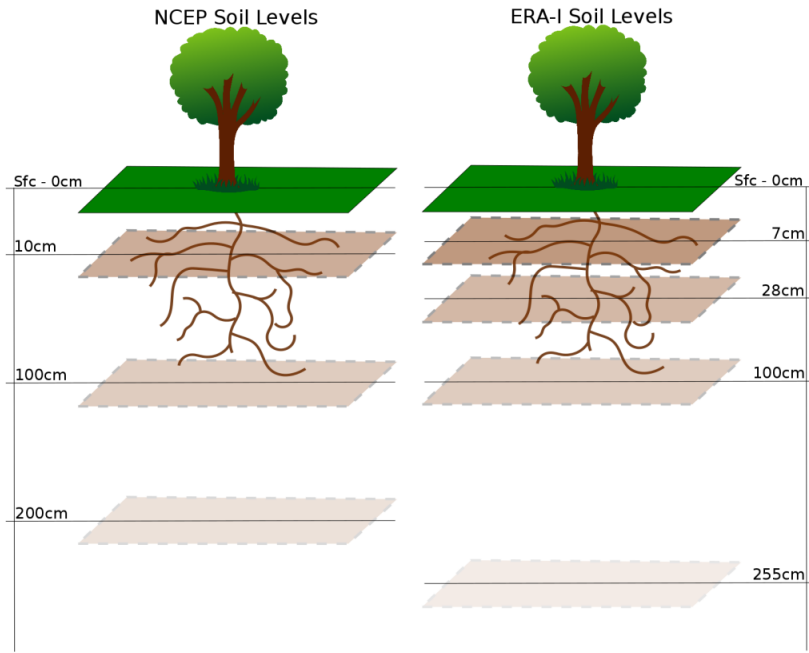


Fig. 3.1 A schematic showing how the root system of modeled vegetation penetrates into different layers for NCEP soil data (left) and ERA-Interim soil data (right).

moisture can have significant impacts on the structure and propagation of convection in North Africa, and, hence, the resulting AEWs (e.g., Wolters et al. 2010). With the WRF-ARW and the WRF-NMM input now reconciled, the comparison between these two dynamical cores can be diagnosed for identical large-scale input.

3.4 Sensitivity of Parameterization Options Using WRF-ARW

Testing a mix of different parameterizations is an important first step in any modeling study. Before comparing the WRF-ARW to the WRF-NMM, sensitivity studies were conducted with the WRF-ARW to find the best mix of parameterization options to represent the long-term mean of key WAM features. Specifically, two microphysics parameterizations and two land surface models are scrutinized here. Although available computing resources prevented the inclusion of cumulus parameterizations in these sensitivity experiments, this is an obvious choice

for future work given the documented sensitivity of tropical North Africa to the convection scheme (Berry and Thorncroft 2012). The two microphysics parameterizations are the Thompson scheme (Thompson et al. 2008), which calculates the mass of five water species and the number concentrations for ice and rain, and the WRF Single-Moment 6-class scheme (WSM6; Hong and Lim 2006), which calculates mass for the same five species as the Thompson scheme, but does not calculate any number concentrations. Overall, the Thompson scheme is more sophisticated than the WSM6, but this author is not sure which scheme performs better when the grid scale is larger than the cloud scale. The two land surface models for WRF-ARW are the Noah scheme and the old Rapid Update Cycle (RUC) scheme (Smirnova et al. 2000), which had been shown to perform quite well in the WAM region (Flaounas et al. 2010). Therefore, four sensitivity tests are created from the following parameterization combinations: 1) WSM6/RUC, 2) WSM6/Noah, 3) Thompson/RUC, 4) Thompson/Noah.

With rainfall data from the Tropical Rainfall Measurement Mission (TRMM) 3B42 product as a baseline (Fig. 3.2a), the June-August (JJA) average precipitation is compared for the four sensitivity tests (Figs. 3.2b-e). Overall, the most obvious conclusion is that all instances of WRF-ARW precipitate too much over tropical North Africa. In East Africa, all sensitivity tests feature JJA averages in excess of 15 mm day^{-1} between the Darfur Mountains and the Ethiopian Highlands. The two sensitivity tests with the RUC land surface model (Figs. 3.2b,d) produce too much rainfall over most of tropical North Africa, with most of the region averaging over 15 mm day^{-1} over the three-month period. Sensitivity tests with the Noah land surface model feature lower rainfall averages between 10°W and 18°E (Figs. 3.2c,e). TRMM 3B42 over North Africa is not a perfect baseline, considering that this product is corrected by rain gauges and this region has actually seen a decline in such observations (Ali et al. 2005; Tian et al. 2007). In general,

TRMM has been known to underestimate rainfall rates over land due to issues predicting emissivity (Tian et al. 2007). Nonetheless, TRMM 3B42 is one of the best rainfall products available and all sensitivity tests produce too much rainfall by this standard.

Realistic simulation of the African easterly jet (AEJ) is vital to properly analyze the energetics associated with AEWs, especially barotropic energy conversion, which transfers momentum from the AEJ to AEWs. It is common to show the AEJ in the 650 hPa zonal wind (Fig. 3.3). Here, WRF-ARW sensitivity tests are compared to 21 JJAs from ERA-Interim. Although the maximum amplitudes of the simulated AEJs are all smaller than the ERA-Interim data, it is encouraging that the AEJ is simulated with some degree of accuracy in all of the sensitivity tests. Like the precipitation data (Fig. 3.2), the AEJ is much more sensitive to the land surface model than it is to the microphysics. Perhaps, at these coarser resolutions, the mass of various water species do not vary much between different microphysics schemes. On this topic, the Thompson microphysics scheme does produce an AEJ that is slightly weaker than in the WSM6 scheme. Clearly, the sensitivity tests with the RUC land surface model capture the broad zonal expanse of westward flow greater than 10 m s^{-1} (Fig. 3.3b,d). Despite the more accurate velocity maximum, the AEJ also tends to be shifted northward when the RUC land surface model is used. The sensitivity tests that employ the Noah land surface model produce a tongue of easterly flow greater than 8 m s^{-1} extending out into the East Atlantic that is similar to the reanalysis products (Fig. 3.3b,d). However, these simulations underestimate the AEJ maximum by $\sim 2 \text{ m s}^{-1}$.

Vertical cross-sections to the west ($20^{\circ}\text{W}-0^{\circ}\text{E}$; Fig. 3.4) and east ($0^{\circ}\text{E}-20^{\circ}\text{E}$; Fig. 3.5) of Greenwich reveal that all sensitivity tests struggle to reproduce the weak mid-level easterly flow that extends from south of the AEJ to south of the equator. In ERA-Interim, this mid-level

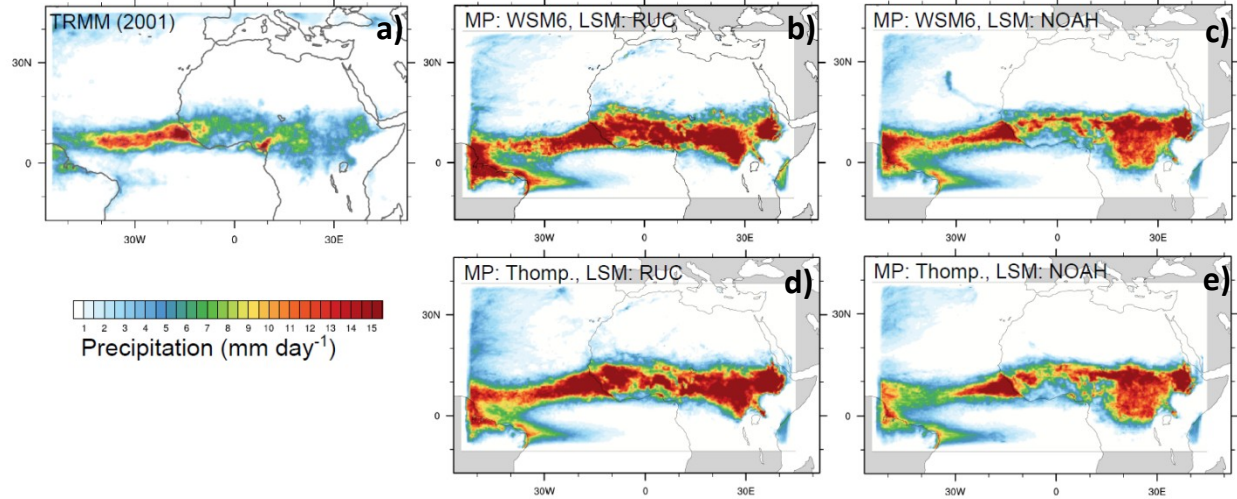


Fig. 3.2 Boreal summer mean (June-August) precipitation maps for a) TRMM 3B42, b) WSM6 microphysics and RUC land surface model, c) WSM6 microphysics and Noah land surface model, d) Thompson microphysics and RUC land surface model, and e) Thompson microphysics and NOAH land surface model. The shading interval is 0.5 mm day^{-1} . All plots are on the same scale.

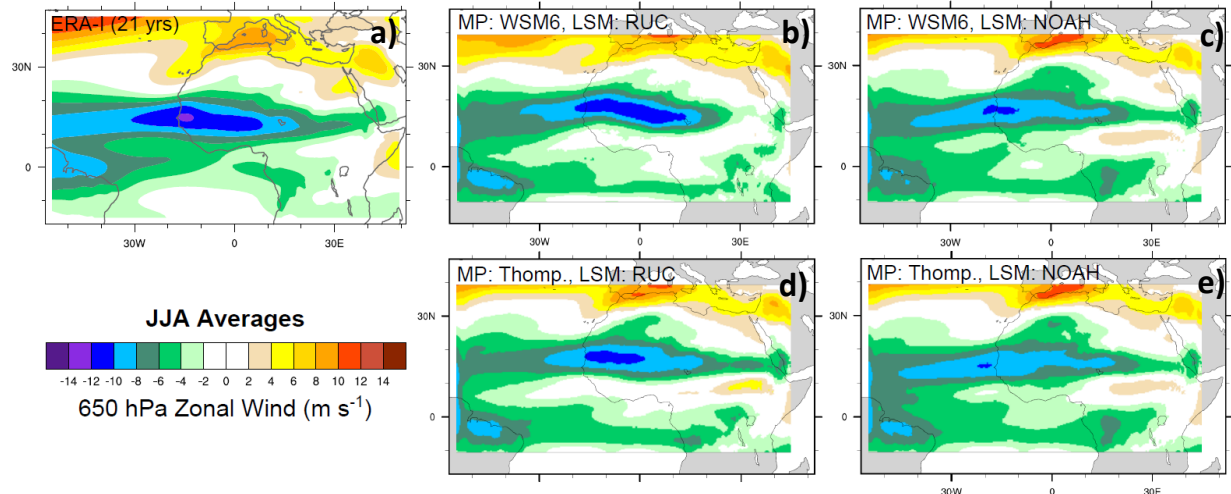


Fig. 3.3 Boreal summer mean (June-August) 650 hPa zonal wind maps for a) ERA-Interim, b) WSM6 microphysics and RUC land surface model, c) WSM6 microphysics and Noah land surface model, d) Thompson microphysics and RUC land surface model, and e) Thompson microphysics and NOAH land surface model.. The shading interval is 2 m s^{-1} . All plots are on the same scale.

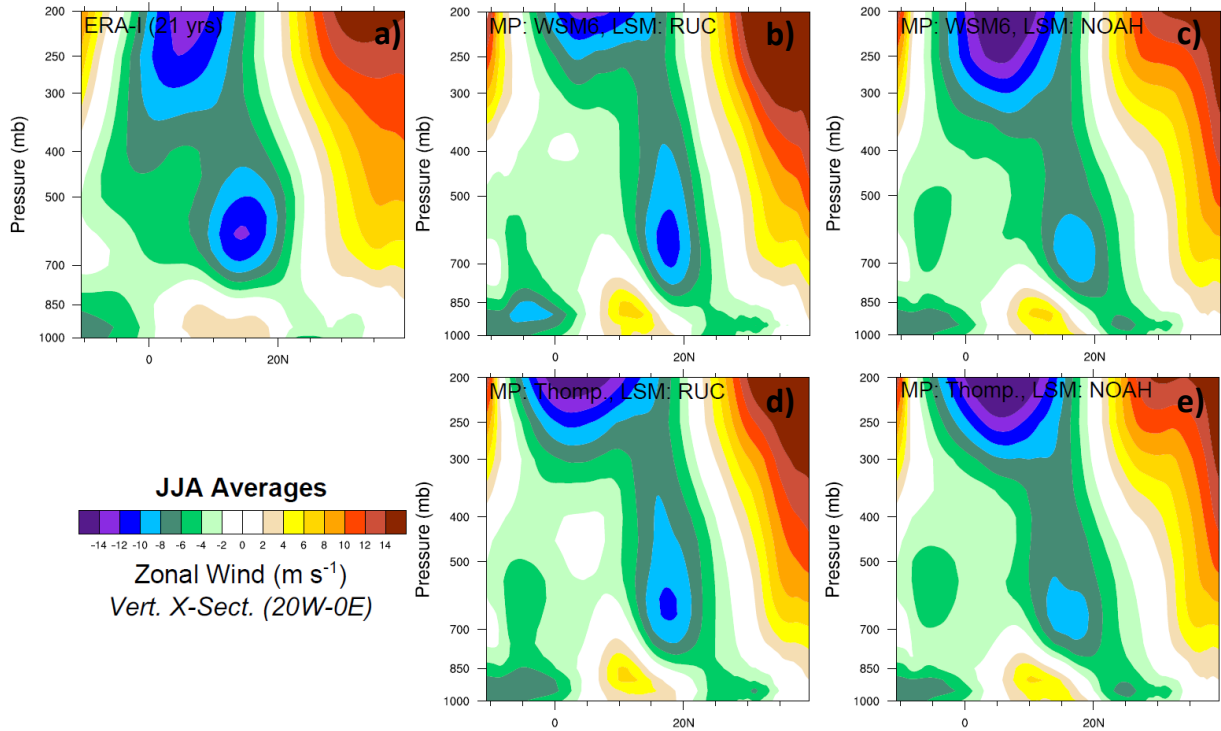


Fig. 3.4 As in Fig. 3.3, except for zonal wind cross-sections averaged between 20°W and 0°E . The shading interval is 2 m s^{-1} . All plots are on the same scale.

easterly flow is in the range of $2\text{-}4 \text{ m s}^{-1}$ (Figs. 3.4a, 3.5a) from 10°S to 10°N . Shifting the discussion to the sensitivity tests, a similar story emerges from these vertical cross-sections. The RUC land surface model produces a much more realistic AEJ core than the Noah land surface model. The AEJ appears to be meridionally squeezed in the RUC simulations (Figs. 3.4b,d, 3.5b,d), which might be related to surface westerlies that extend up to 700 hPa. In ERA-Interim, these surface westerlies are confined below 850 hPa. Although the flow is still easterly above 700 hPa in the RUC simulations, it is much weaker than in reanalysis data and results in a much sharper gradient on the south side of the AEJ, which is where AEWs grow. Sensitivity tests with the Noah land surface model restrict westerly flow to below 800 hPa, but also feature a weaker AEJ core (Figs. 3.4c,e, 3.5c,e). East of Greenwich, all four sensitivity tests produce a closed jet feature near 5°S . Although Diedhiou et al. (2002) found a similar feature in the NCEP/NCAR

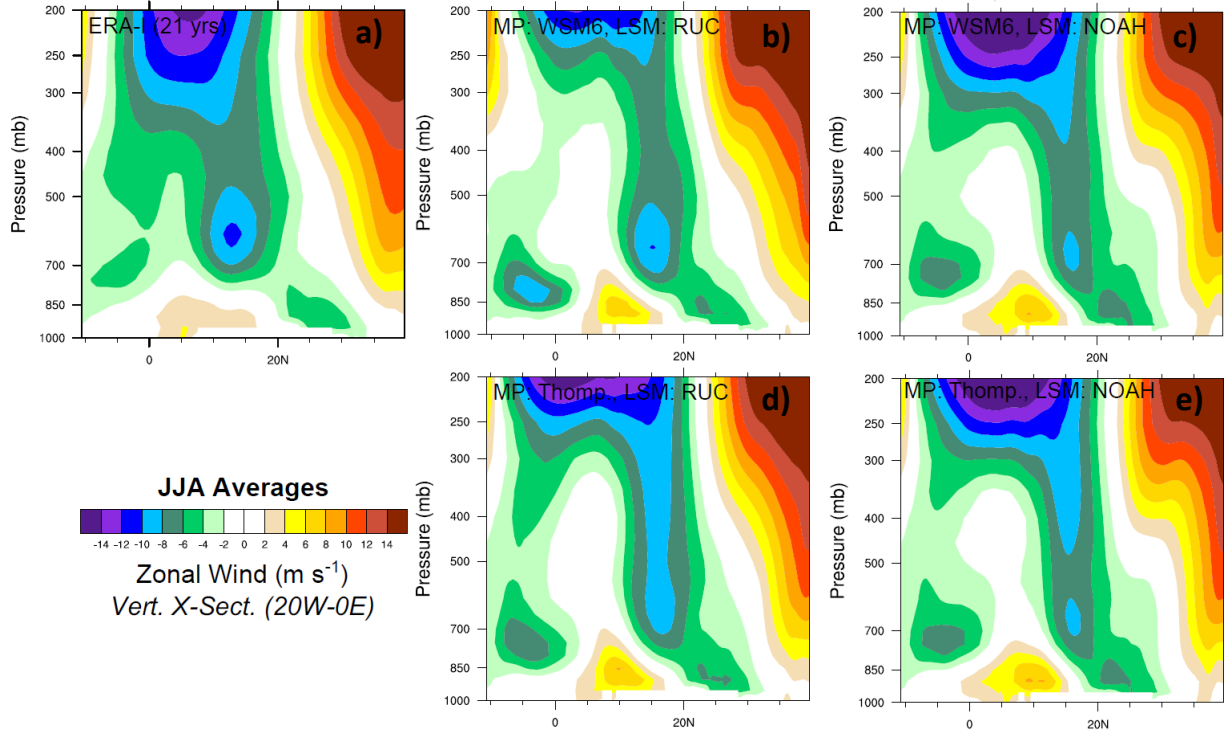


Fig. 3.5 As in Fig. 3.3, except for zonal wind cross-sections averaged between 0°E and 20°E . The shading interval is 2 m s^{-1} . All plots are on the same scale.

reanalysis, it is not as isolated as in Figs. 3.5b-e. This “southern AEJ” would impose anticyclonic shear between the equator and 5°N , which would force AEWs to track further to the north. It is unclear how the “southern AEJ” impacts AEW amplitude.

AЕW activity is robustly simulated in all of the sensitivity tests, with 700 hPa relative vorticity used as a proxy (Fig. 3.6). In fact, modeled AEW amplitudes far exceed values observed in ERA-Interim, which might be due to the stronger zonal wind gradient on the south side of the AEJ. The WSM6/RUC sensitivity test crashed on July 14, 2001, which is why the Hovmöller diagram does not show the entire JJA period (Fig. 3.6b). Although the individual disturbances differ in timing and amplitude, it is safe to say that AEW activity is robustly reproduced in the WRF-ARW, regardless of the choice of microphysics and/or land surface model. In addition to strong amplitudes, all of the sensitivity tests produce slower-propagating

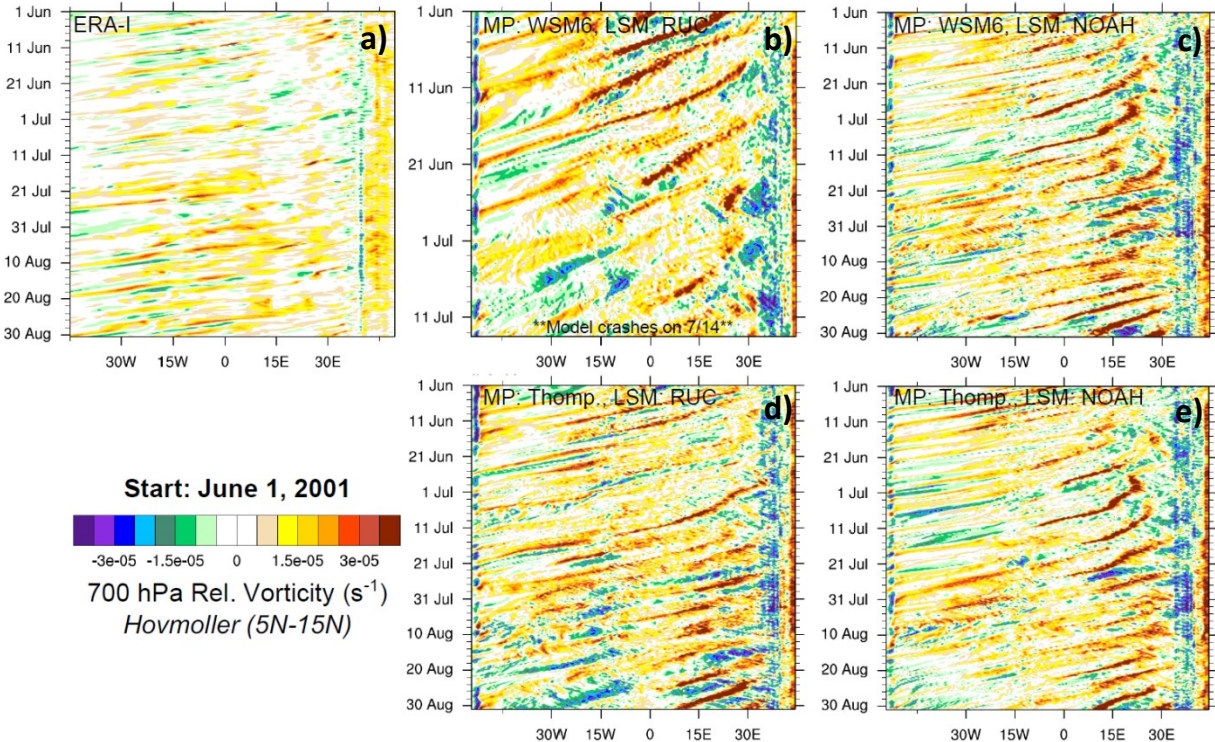


Fig. 3.6 Hovmöller diagrams of 700 hPa relative vorticity for a) ERA-Interim, b) WSM6 microphysics and RUC land surface model, c) WSM6 microphysics and NOAH land surface model, d) Thompson microphysics and RUC land surface model, and e) Thompson microphysics and NOAH land surface model.. The shading interval is $0.5 \times 10^{-5} \text{ m s}^{-1}$. All plots are on the same scale.

700 hPa vorticity features in East Africa than in ERA-Interim, and the strongest 700 hPa relative vorticity values are shifted to the east relative to ERA-Interim in the sensitivity tests. In ERA-Interim, the vorticity associated with AEWs maximizes west of Greenwich. This discrepancy between the model and reanalysis products might arise from a stronger horizontal shear gradient in East Africa or from increased East African convection.

These sensitivity tests provide strong evidence that the WRF-ARW performs well in the simulation of the West African monsoon. Ultimately, the WSM6/Noah configuration was chosen based on the results presented here. The WSM6/Noah sensitivity test has the most consistent behavior relative to ERA-Interim. The average precipitation rate is higher than ERA-Interim, but

not as grossly exaggerated as in the RUC simulations. Although the AEJ is weaker than in ERA-Interim, the large scale flow is generally realistic. Furthermore, the AEJ maximum (Fig. 3.3c) is positioned along the West African coast, as shown in reanalysis products. Although the Thompson microphysics scheme is considered more sophisticated, the computationally more cost-effective WSM6 scheme outperforms the Thompson scheme in the WAM region. With tested parameterizations in the WRF-ARW that reproduce a realistic WAM climatology, the same exercise of comparing WAM realizations is repeated for comparisons of the WRF-ARW and WRF-NMM models.

3.5 Simulation of the West African Monsoon in the WRF-ARW and WRF-NMM Dynamical Cores

RCMs are valuable analysis tools, especially in regions with scant observations. Tropical North Africa is no exception, with RCMs filling the niche of “observations” by downscaling large scale environmental conditions to the order of tens of kilometers. Reanalysis products (e.g., ERA-Interim, CFSR) are useful tools for regional analysis, but most RCMs can run finer-resolution simulations for a smaller computational cost. In this study, the grid spacing of 30 km or less is finer than ERA-Interim ($\sim 0.7^\circ$) and CFSR data (0.5°). Therefore, RCMs that capture the long-term climatology of data-sparse regions, such as North Africa, provide a platform for the meaningful investigation of mesoscale (or smaller) processes. WAM climatology has never been compared for the WRF-ARW and WRF-NMM dynamical cores. However, considering the wide use of the WRF-ARW and WRF-NMM models in the atmospheric science community, this comparison should help guide future modeling studies in the WAM region. In relation to this

study, the “better” package of tested dynamical core and parameterizations will be used to study the intraseasonal variability of AEW energetics in Chapter 4.

The suite of parameterizations used in each model is outlined in Table 3.2. The only two parameterizations consistent between the WRF-ARW and WRF-NMM configurations are the MYJ planetary boundary scheme and the Eta similarity surface layer scheme. As a consequence, each model will use different parameterizations for microphysics, cumulus, land surface model, and radiation. Based on the sensitivity tests conducted with the WRF-ARW model (see Section 3.4), differences between the WRF-ARW and the WRF-NMM are likely to have a strong influence from the land surface models (Noah vs. SSiB).

Boreal summer mean precipitation maps are shown in Fig. 3.7. Although the WRF-NMM produces too much rainfall in the WAM region, it still performs better than the WRF-ARW. The local precipitation maxima in WRF-NMM (Fig. 3.7c) appear to be located just downstream of sizeable topographical features across tropical North Africa, specifically the Darfur Mountains and Ethiopian Highlands (i.e., the two easternmost precipitation maxima). In the WRF-NMM, precipitation in the East Atlantic is more representative of an ITCZ than in the WRF-ARW,

Table 3.2 Comparison of the parameterizations used in the WRF-ARW and WRF-NMM dynamical cores.

	WRF Dynamical Core	
	WRF-ARW	WRF-NMM
Microphysics	WSM6	Ferrier
Cumulus	Grell 3D	Betts-Miller-Janjic
Land Surface Model	Noah	SSiB
Boundary Layer	MYJ	MYJ
Radiation	New Goddard	GFDL
Surface Layer	Eta similarity	Eta similarity

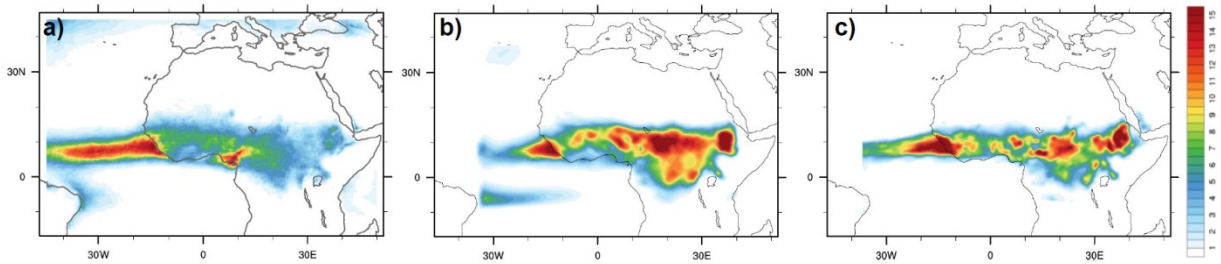


Fig. 3.7 Boreal summer mean (June-August) precipitation maps for a) TRMM 3B42, b) WRF-ARW, and c) WRF-NMM. The shading interval is 0.5 mm day^{-1} .

although it still much shorter than the observed ITCZ in TRMM data. Additionally, the WRF-ARW produces too much rainfall near the equator over central Africa. The WRF-NMM has lower rainfall totals in this region that are closer to observations. Finally, the WRF-NMM has no evidence of a double ITCZ in the Atlantic, as is observed in the WRF-ARW precipitation map. The excess precipitation in WRF-ARW suggests more convectively active AEWs, which may affect associated energetics (especially Q_T). Overall, the WRF-NMM produces more realistic rainfall climatology in the WAM region than the WRF-ARW.

As expressed earlier, reproduction of the AEJ is paramount to the study of AEW energetics. In particular, barotropic and baroclinic energy conversions are closely related to the position and strength of the AEJ. The WRF-NMM fails to effectively reproduce a realistic AEJ. Although the WRF-NMM captures the AEJ maximum, it is displaced into the East Atlantic. In fact, the AEJ itself is shifted to the west and curiously jogs to the north near the West African coast (Fig. 3.8). Additionally, the “southern AEJ” feature is more prominent across the equatorial Atlantic Ocean than in reanalysis data or the WRF-ARW. Complicating this issue, the primary AEW track is located between the two jets shown in the WRF-NMM (Fig. 3.8c). Vertical cross-sections reinforce the conclusions drawn from the plan view plots (Figs. 3.9, 3.10), with the double jet feature clearly visible across Africa. In fact, the “southern AEJ” is actually stronger

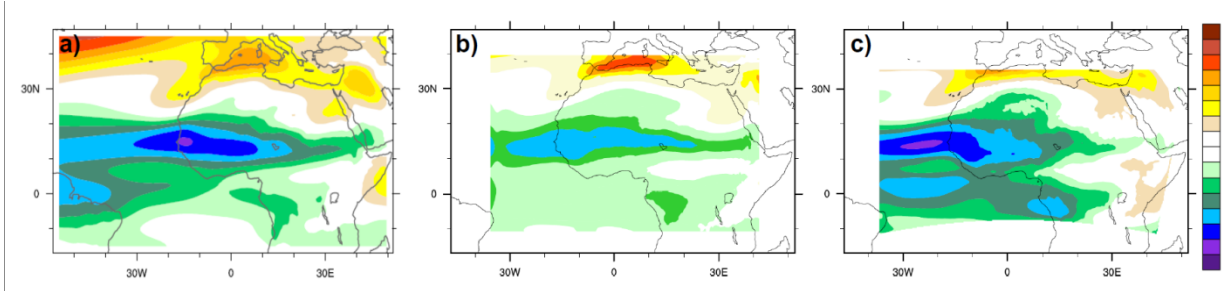


Fig. 3.8 Boreal summer mean (June-August) 650 hPa zonal wind maps for a) ERA-Interim, b) WRF-ARW, and c) WRF-NMM. The shading interval is 2 m s^{-1} .

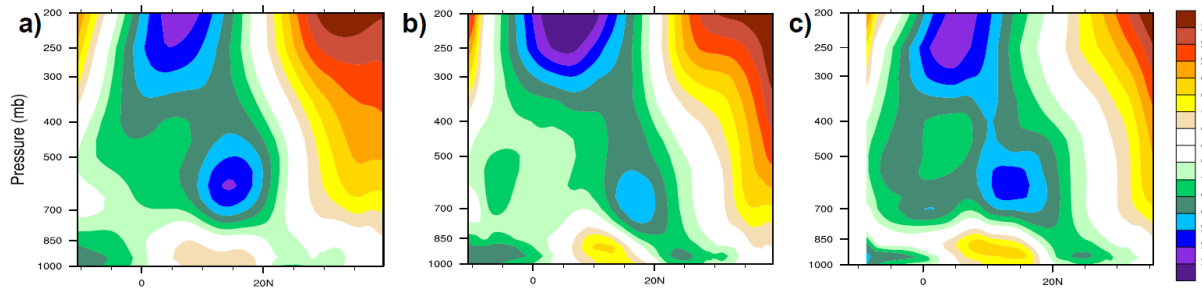


Fig. 3.9 Boreal summer mean (June-August) zonal wind cross-sections for a) ERA-Interim, b) WRF-ARW, and c) WRF-NMM. Plots are averaged between 20°W and 0°E . The shading interval is 2 m s^{-1} .

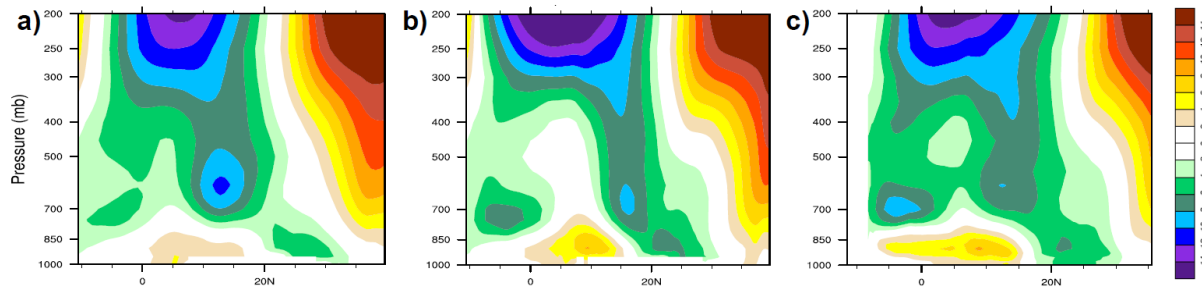


Fig. 3.10 Boreal summer mean (June-August) zonal wind cross-sections for a) ERA-Interim, b) WRF-ARW, and c) WRF-NMM. Plots are averaged between 0°E and 20°E . The shading interval is 2 m s^{-1} .

than the actual AEJ east of Greenwich (Fig. 3.10c). In an attempt to remedy the WRM-NMM jet problem, different resolutions and domains were briefly tested (not shown). However, the double jet was a robust feature as long as the WRF-NMM used ERA-Interim boundary conditions. It should be noted that the use of NCEP reanalysis as the initial and lateral boundary conditions for WRF-NMM may produce a more realistic AEJ (personal correspondence with Drs. Yongkang Xue and Fernando De Sales). However, the reason for this sensitivity to the boundary conditions is unknown, although it might be related to how the SSiB land surface model handles surface/soil variables from the input data. The emergence of the “southern AEJ” in the WRF-NMM simulation decreases the cyclonic shear on the south side of the actual AEJ, which correspondingly decreases the barotropic energy conversion in this region (see A.5).

The WRF-ARW produces robust AEW activity, with strong westward-propagating circulations evidence in the 700 hPa relative vorticity (Fig. 3.11b, 3.12b). AEW amplitudes in the WRF-ARW are stronger than both ERA-Interim and WRF-NMM. When relative vorticity is regressed against West African eddy vorticity, both models produce realistic AEW structures, with a southwest-to-northeast tilt south of the AEJ. Throughout North Africa, AEW activity exhibits intraseasonal variability in the WRF-ARW (Fig. 3.13b). Despite the weaker cyclonic forcing in West Africa, the WRF-NMM produces realistic AEW activity. WRF-NMM 700 hPa relative vorticity in the period from June 1-July 20, 2001 shows easterly wave amplitudes similar to ERA-Interim (Fig. 3.11a,c). In the second half of the summer of the WRF-NMM simulation, PKE amplitudes recover, but they are weighted toward East Africa when compared with ERA-Interim (Fig. 3.13a,c). Once again, the WRF-ARW outperforms the WRF-NMM.

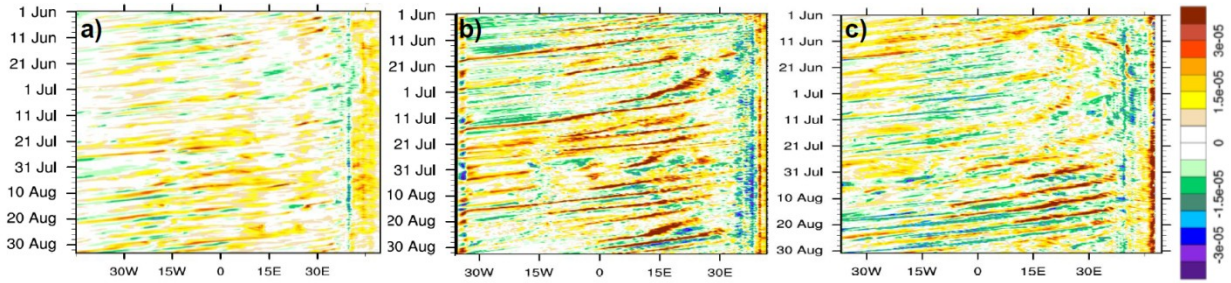


Fig. 3.11 Hovmöller diagrams of 700 hPa relative vorticity for a) ERA-Interim, b) WRF-ARW, and c) WRF-NMM. Plots are averaged between 5°N and 15°N. The shading interval is $0.5 \times 10^{-5} \text{ m s}^{-1}$. The time axis is positive going down.

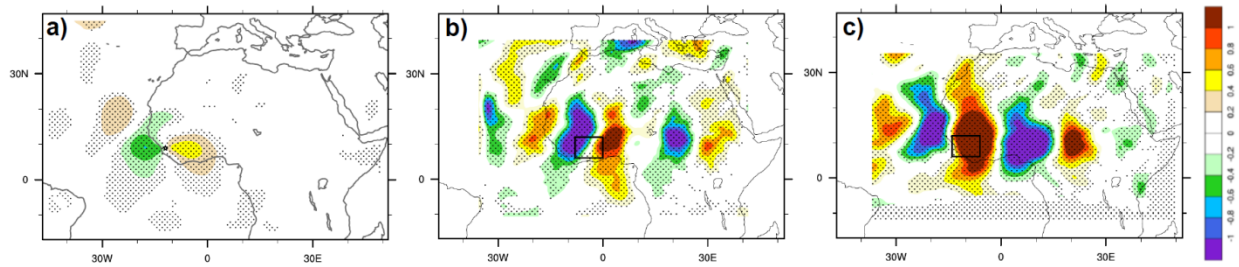


Fig. 3.12 Boreal summer (June-August) meridional wind regressed against eddy 700 hPa vorticity for a) ERA-Interim, b) WRF-ARW, and c) WRF-NMM. In a), eddy vorticity is measured at the star. In b) and c), eddy vorticity is averaged in the black box. The shading interval is 0.2 m s^{-1} .

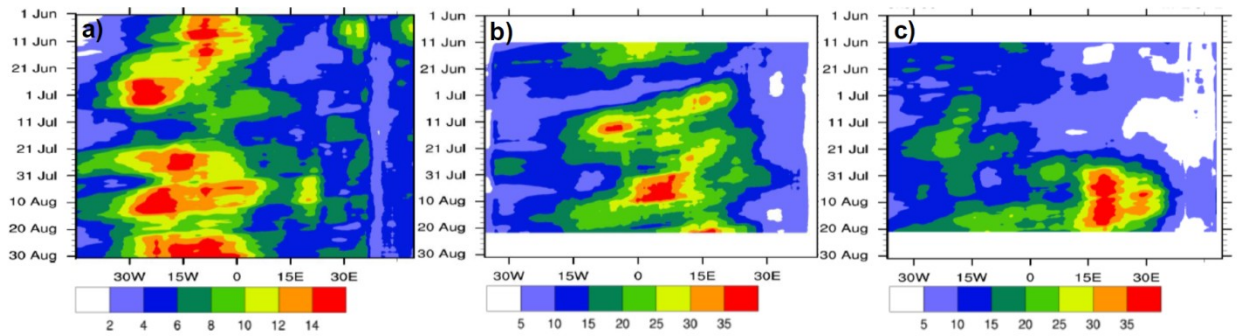


Fig. 3.13 As in Fig. 3.11, except for 700 hPa PKE. The scales vary for each plot.

3.6 Discussion

The WRF-ARW and WRF-NMM dynamical cores are compared to determine the RCM most suitable to analyze the intraseasonal variability of AEW energetics (Chapter 4). The models are evaluated based on their ability to simulate crucial WAM characteristics in one boreal summer season. Although the difference in parameterizations (see Table 3.2) adds another degree of freedom between the WRF-ARW and WRF-NMM simulations, the consistency of the ERA-Interim boundary conditions ensures that the large-scale impact on the WAM domain is the same in the two simulations. Thus, the differences observed in this chapter are entirely based on the internal manifestation of the WAM in each model. As with any modeling study, the conclusions garnered here rely on how the primitive equations of the atmosphere are solved (e.g., ARW vs. NMM), but are also dependent on the boundary conditions, parameterizations, and temporal/spatial resolution used in each simulation. It is plausible that different combinations of the aforementioned can change the conclusions. The WRF-ARW and WRF-NMM were configured with horizontal resolutions of 30 km and ~25 km, respectively, to which the results presented here are sensitive.

The WRF-NMM has an advantage over the WRF-ARW in the reproduction of rainfall across tropical North Africa. Although both models produce too much rainfall when compared to TRMM 3B42, the WRF-NMM precipitates less over land in a narrower band than in the WRF-ARW. However, the story flips when the AEJ is analyzed. Although the AEJ is weaker by 2-3 m s⁻¹ in the WRF-ARW, the general structure of the WAM flow across North Africa is more realistic than in the WRF-NMM. Most glaringly, the WRF-NMM produces a significant “southern AEJ”, which reduces shear on the southern side of the actual AEJ. Given the vitality of the AEJ to the AEW lifecycle, the WRF-ARW is chosen over the WRF-NMM to analyze the

energetic of AEWs. However, if the double jet problem in the WRF-NMM can be remedied, the WRF-NMM could be a valuable tool for studying AEWs. If a more realistic baseline can be achieved, future research will utilize the WRF-NMM to study AEW energetics to test the robustness of the WRF-ARW results presented in Chapter 4.

CHAPTER 4 The Intraseasonal Variability of African Easterly Wave Energetics in the WRF-ARW Model

4.1 Introduction

The MJO is often considered the “Holy Grail” of tropical meteorology (Raymond 2001; Zhang 2005). As the dominant mode of intraseasonal variability in the tropics, the MJO is teleconnected with atmospheric and oceanic phenomena worldwide (see Section 1.4). With a 40–50-day spectral peak, the oscillatory nature of the MJO could improve forecasts across the globe on subseasonal timescales. In particular, the relationship between the MJO and the WAM has been a focal point of recent literature (Matthews 2004; Ventrice et al. 2011, Alaka and Maloney 2012). As presented in Chapter 2, AEW activity in West Africa exhibits significant intraseasonal variability, about 10% of which is explained by the MJO. A better understanding of the relationship between the MJO and the WAM would improve precipitation and AEW forecasts in West Africa, and is the main motivation for results presented in this chapter.

The large-scale circulation response to MJO heating follows from idealized experiments in Heckley and Gill (1984), with a combined Kelvin-Rossby-wave response that is dragged eastward with the main envelope of MJO convection (see Section 1.4). Even with realistic damping, these equatorial waves expand in the zonal direction over time after being initiated by the MJO heat source, increasing the influence of the MJO to other parts of the tropics and subtropics. Both Kelvin and equatorial Rossby waves are observed propagating from MJO heating in the Indian Ocean into West Africa in reanalysis products (Matthews 2004; Alaka and Maloney 2012). However, collocation does not imply causality and the role that equatorial waves play in forcing West African precipitation and AEW activity is unclear. Of particular uncertainty

is whether signals propagating into tropical North Africa have an essential role in producing intraseasonal variability in this region.

Regional climate models (RCMs) are tools that allow for high-resolution simulation without the computational cost of a global model. Details about RCMs and how they relate to global climate models are discussed in Section 3.1. Since tropical North Africa has a sparse observing network (Ali et al. 2005), RCMs have been employed to attain resolutions that allow for meaningful investigation of the WAM and associated AEWs. In particular, RCM simulations have focused on the role of convection in AEWs (Berry and Thorncroft 2012; Ross et al. 2012), the impacts of parameterizations on AEW/WAM simulations (Flouanas et al. 2010; Noble et al. 2014), the impacts of soil moisture gradients on squall lines (Wolters et al. 2010) and the energetics of AEWs (Hsieh and Cook 2007). Two of the most popular RCMs used to study tropical North Africa are the RegCM and the WRF-ARW. Both are these models are discussed in greater detail in Section 3.1.

RCM applications to study intraseasonal variability have become more common in recent years (e.g., Xue et al. 2012; Rydbeck et al. 2013), but RCMs are typically used for short-term (e.g., one week) forecasts. This is the first study to investigate the intraseasonal variability of the WAM and AEWs in the WRF-ARW model. By running multi-year RCM simulations over a North African domain, the modulation of convection and AEW activity in West Africa by MJO-spawned equatorial Kelvin and equatorial Rossby waves is diagnosed. Are these equatorial waves vital for the observed intraseasonal variability in West Africa?

4.2 Methodology

4.2.1 Experimental Design

Based on the results presented in Chapter 3, the WRF-ARW model version 3.5.1 is chosen to study the intraseasonal variability of the WAM and associated AEW energetics. The details of the WRF-ARW dynamical core are presented in the left column in Table 3.1. Additionally, a list of parameterization options utilized in the WRF-ARW simulations described in this chapter can be found in the left column of Table 3.2. The parameterizations used in this particular version of WRF-ARW produce the most accurate simulation of the WAM, which provides a solid background upon which to analyze the intraseasonal variability in this section. The WRF-ARW model is setup with a grid spacing of 30 km, 37 vertical levels, and a time step of 90 s. ERA-Interim data (0.7°) is used as the initial and lateral boundary conditions, which is consistent with sensitivity tests presented in Chapter 3.

The WRF-ARW experiments described in this chapter are designed to determine the extent to which the modulation of West African AEW activity is explained by external intraseasonal variability, which includes the MJO and associated equatorial waves. Three WRF-ARW experiments are designed to investigate the role of this external modulation by filtering the lateral boundary conditions (Fig. 4.1). Each simulation spans from January 1, 2001 at 0Z to December 31, 2010 at 18Z, which provide a large sample of intraseasonal variability over 10 boreal summer seasons (i.e., June-September). The first experiment (C1) is a control simulation and uses unfiltered ERA-Interim data (Fig. 4.1a). This control simulation is representative of 30-90-day AEW variability with the full influence of external forcings. The second and third experiments are sensitivity simulations that filter the ERA-Interim boundary conditions to different extents. In the second experiment (S1), 30-90-day variability is removed for all zonal

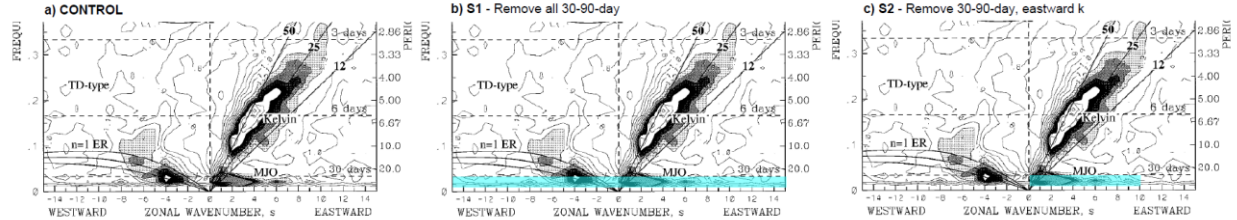


Fig. 4.1 Wavenumber-frequency filtering of the boundary conditions for the three proposed WRF experiments. In a), no filtering is applied. In b), all 30-90-day variability is removed. In c), only eastward-propagating wavenumbers 0 to 10 are removed from the 30-90-day band. Filtered parts of the wavenumber-frequency domain are represented by blue shading. Figure is adapted from Wheeler and Kiladis (1999).

wavenumbers, which completely eliminates the influence of external 30-90-day variability on the WAM (Fig. 4.1b). As a result, both Kelvin and equatorial Rossby waves that project onto MJO timescales are filtered from the boundary conditions. In the third experiment (S2), 30-90-day variability is only removed for zonal wavenumbers 0-10, which eliminates Kelvin waves (but permits equatorial Rossby waves) in the boundary conditions. The power of most large-scale equatorial Rossby waves falls within the 30-90-day band. However, the power of Kelvin waves extends to much shorter timescales and smaller zonal wavelengths, suggesting that these equatorial waves are incompletely filtered. While this is true, a distinction is drawn here between convectively-coupled Kelvin waves and a dry Kelvin wave mode. Here, the fast-propagating, dry Kelvin wave mode characteristic of the Gill model and forced by MJO convection is removed by the filtering.

The wavenumber-frequency filter utilized in the aforementioned experiments is applied through two-dimensional fast Fourier transform (FFT) analysis. A boxcar-type filter is applied to the ERA-Interim boundary data once it has been converted to wavenumber-frequency space. In essence, the periods and wavelengths to be removed from the boundary conditions are set to zero before the data is converted back to real space. The filtering process is extensive, including

three-dimensional data from all 37 levels and most surface variables. Soil moisture and soil temperature fields are not filtered to save on computational costs. Since the main convective region in association with AEWs and the WAM is confined to the interior of the model domain, intraseasonal variability contained within ERA-Interim soil variables should have little impact on the WRF-ARW experiments described here. In order to ensure a representative power spectrum for each variable on each level, the full ten years of ERA-Interim data is input into the filter.

4.2.2 Conversion to Unformatted Binary

One major hurdle of the WRF model is that only Grib data may be used as input into the WRF pre-processing system (WPS). In the typical WPS, Grib data is converted to unformatted binary by the WPS executable *ungrib.exe*. Next, another WPS executable, called *metgrid.exe*, interpolates the input data to the model grid and, in the process, reformats the unformatted binary data to NetCDF. However, the two-dimensional FFT program described in Section 4.2.1 outputs NetCDF, making it necessary to build an alternative package that inputs NetCDF data into the WPS. This new executable, called *unpack_netcdf.exe*, converts NetCDF input data into unformatted binary, which can then be read by *metgrid.exe*. In essence, *unpack_netcdf.exe* replaces the responsibilities of *ungrib.exe*. The code for the *unpack_netcdf.exe* package can be found in Appendix B. Although this executable only inputs ERA-Interim data at the moment, future work will expand capabilities to include other reanalysis products (e.g., NCEP/NCAR, CFSR, MERRA).

4.3 Simulated West African Monsoon in Boreal Summer

The boreal summer mean WAM is analyzed for each of the WRF-ARW experiments. The precipitation field is qualitatively similar across the three experiments (Fig. 4.2), with local maxima at the West African coast and in the Ethiopian Highlands (40°E). In the sensitivity tests, one notable difference from the control simulation is the reduction of rainfall near equatorial Africa, which is actually more consistent with observations (Fig. 3.7a). Additionally, the S1 and S2 simulations produce oceanic precipitation that exceeds 10 mm day^{-1} across the Atlantic Ocean, especially approaching the western boundary of the model domain. While WRF-ARW precipitation far exceeds TRMM 3B42 values over land, the observed and modeled rainfall rates are quite similar near the West African coastline. It is worth noting that the precipitation maps for S1 and S2 are nearly identical, which potentially downplays the importance of westward-propagating 30-90-day disturbances (e.g., equatorial Rossby waves) in the simulation of WAM climatology.

Upon inspection of the 650 hPa zonal wind, the AEJ in the control experiment (Fig. 4.3a) is qualitatively similar to ERA-Interim (Fig. 3.8a). However, the maximum amplitude of the AEJ in C1 is $\sim 3 \text{ m s}^{-1}$ slower than in the reanalysis data. The sensitivity tests produce a much different manifestation of the 650 hPa flow. The glaring feature in S1 and S2 is the extension of the

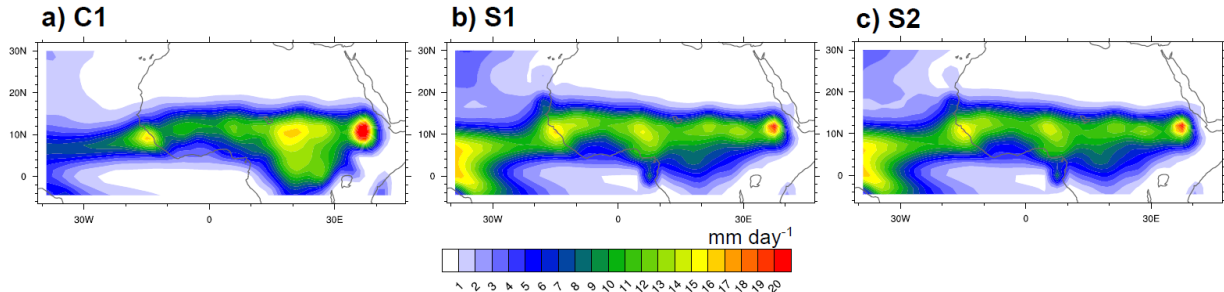


Fig 4.2 Boreal summer mean precipitation for three WRF-ARW experiments: a) C1, b) S1, and c) S2. The shading interval is 1 mm day^{-1} .

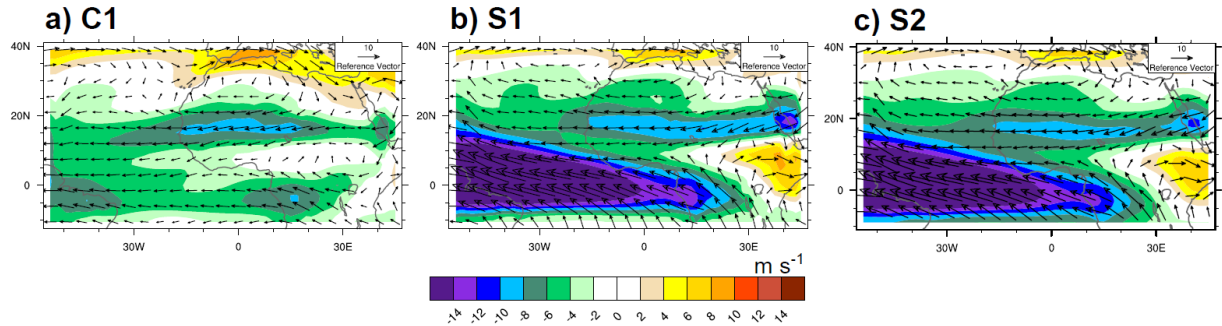


Fig. 4.3 Boreal summer mean 650 hPa zonal wind for three WRF-ARW experiments: a) C1, b) S1, and c) S2. The shading interval is 2 m s^{-1} . 650 hPa total wind vectors are overlaid.

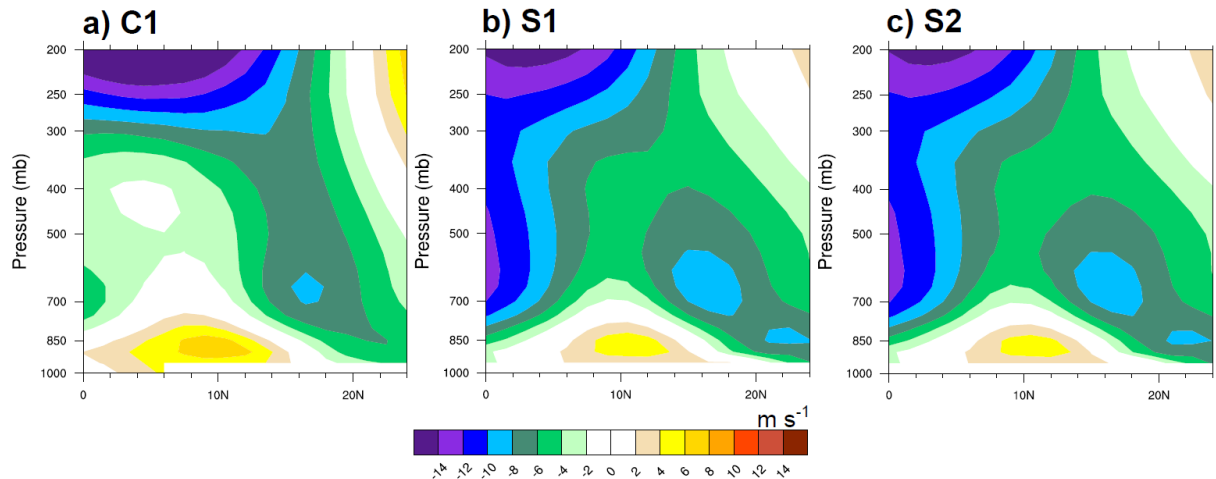


Fig 4.4 Boreal summer mean zonal wind averaged between 10°W and 20°E for three WRF-ARW experiments: a) C1, b) S1, and c) S2. The shading interval is 2 m s^{-1} .

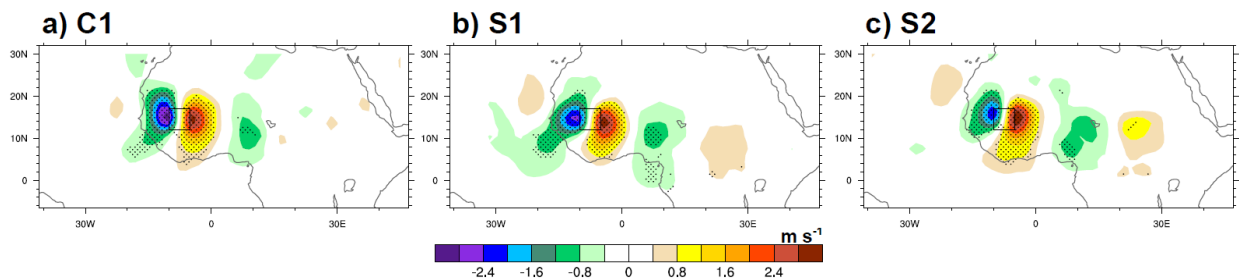


Fig 4.5 Eddy 700 hPa meridional wind regressed against eddy 700 hPa vorticity averaged in the black box for three WRF-ARW experiments: a) C1, b) S1, and c) S2. The shading interval is 0.4 m s^{-1} . Stippling represents values that exceed the 95% confidence threshold.

tropical easterly jet down into the middle and lower troposphere. Without eastward-propagating 30-90-day variability in the boundary conditions, forcing of the momentum field may be deficient in the southwest part of the domain (near the equator). It is possible that the maintenance of this momentum balance is governed by equatorial Kelvin waves propagating through the domain. Chen and van Loon (1987) discuss the maintenance of the tropical easterly jet, but do not mention any specific interaction with eastward flow along the equator. Despite this glaring error in the simulation of the tropical easterly jet, the S1 and S2 simulations produce a realistic AEJ core that is located near 20°N (Fig. 4.4b,c). The 650 hPa flow in the three WRF-ARW simulations exhibits a tongue of westerly flow on the southern flank of the AEJ in East Africa. This increased momentum gradient has strong implications for barotropic energy conversions in East Africa, and is which is discussed in the next section.

When measured by meridional wind anomalies, AEW activity is robustly reproduced in all three WRF-ARW experiments (Fig. 4.5). Although the mid-level flow in the sensitivity experiments shows significant biases relative to the control experiment and the reanalysis data, AEW activity is largely unaffected, with similar meridional wind maxima ($>2.5 \text{ m s}^{-1}$) despite different background flows. In all simulations, the classic southwest-northeast tilt is clearly observed (e.g., Kiladis et al. 2006), which supports the notion that the biases in the tropical easterly jet in S1 and S2 do not significantly alter AEW structure.

4.4 Boreal Summer Mean African Easterly Wave Energetics

With confidence that AEW activity is well-simulated in C1, S1, and S2, the boreal mean of AEW energetics is investigated and compared to observation-based analysis in Chapter 2. For reference, the PKE and PAPE budgets are provided in equations 1.3 and 1.4, respectively.

Following the methodology presented in Chapter 2, PKE and PAPE budget terms are analyzed as vertically-averaged, horizontal fields (Figs. 4.6, 4.8, 4.10) and in latitude-pressure cross sections averaged between 10°W and 20°E (Figs. 4.7, 4.9, 4.11). Simulated PKE and PAPE budget terms are qualitatively similar to ERA-Interim budget terms in Section 2.3 (Figs. 2.17, 2.18), and previous studies (e.g., Lau and Lau 1992; Diedhiou et al. 2002; Hsieh and Cook 2007). However, noticeable differences are observed and highlighted below.

In the control simulation (C1), 700 hPa PKE amplitudes across tropical North Africa are larger than ERA-Interim PKE at the same level by a factor of 3-4 (Figs. 4.6a, 4.7a). C1 produces a 700 hPa PKE maximum that is located near 13°E, which highlights a shift of the strongest AEW activity from near the West Africa coast in observations to East Africa in the model simulations. The total PKE advection term (A_{TOT} ; see A.4) is a factor of two larger than in ERA-

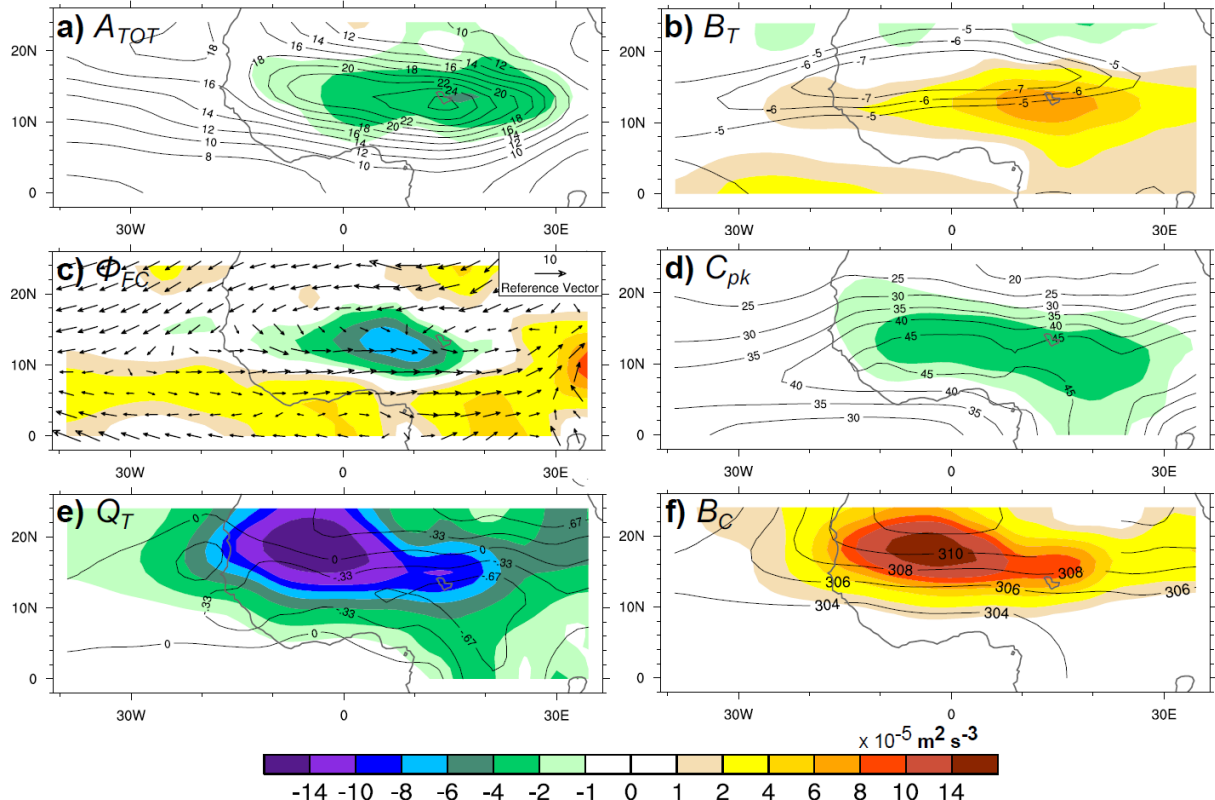


Fig 4.6 As in Fig. 2.17, except for C1.

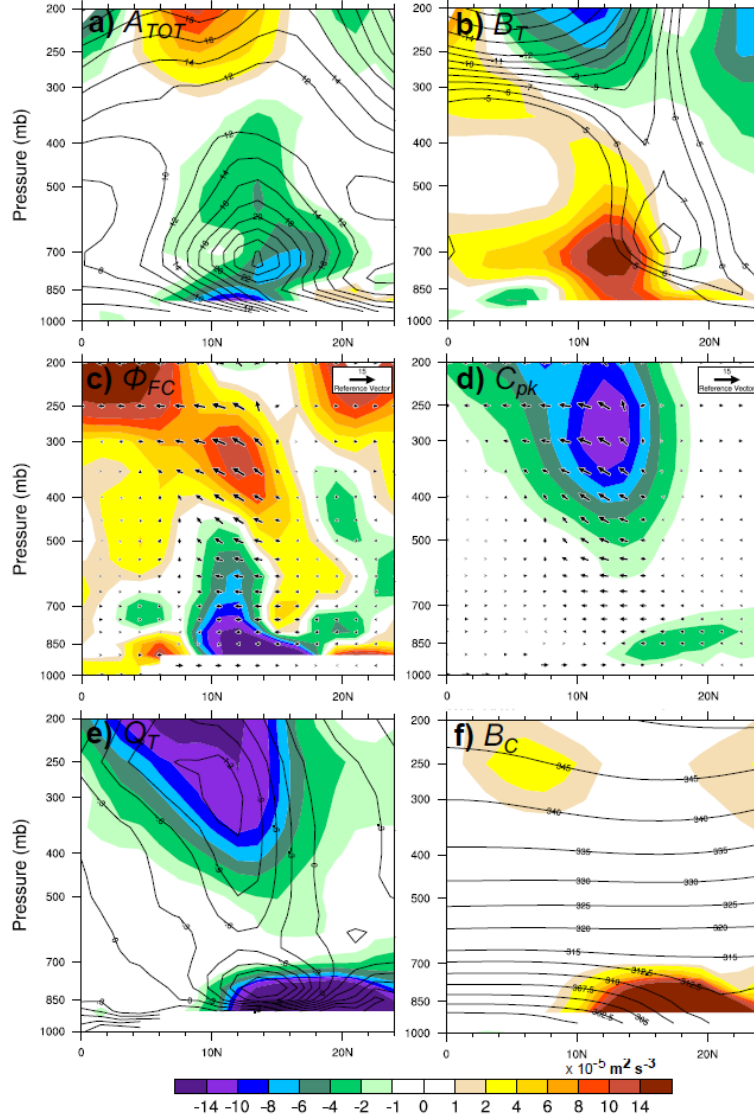


Fig 4.7 As in Fig. 2.18, except for C1.

Interim, but this is to be expected given the stronger 700 hPa PKE values in the region. Surprisingly, $\langle A_{TOT} \rangle$ is negative downstream from the PKE maximum, suggesting an increased role for meridional PKE advection in simulated AEW energetics. In addition, it is interesting that A_{TOT} is strongest on the northern flank of the strongest AEW activity (Fig. 4.7a).

On the southern flank of the AEJ, barotropic energy conversions (B_T ; see A.5) convert mean kinetic energy (i.e., AEJ flow) into PKE in regions of strong horizontal wind shear (Figs.

4.6b, 4.7b). Unlike in ERA-Interim (Fig. 2.17b), $\langle B_T \rangle$ is strongest in East Africa in the C1 simulation, with a local maxima centered on Lake Chad (12°E) that is a factor of two larger than the East Atlantic maximum observed in ERA-Interim. Despite the smaller AEJ amplitudes, which are weaker by 3-4 m s⁻¹, the tongue of westerlies on the southern flank of the AEJ in East Africa creates a sharp momentum gradient near Lake Chad and leads to higher $\langle B_T \rangle$ amplitudes (see Fig. 4.3). Two final differences to note in C1 are: 1) B_T does not appear to assist wave disturbances on the northern side of the AEJ and 2) the role of B_T diminishes in the East Atlantic.

Although the simulated geopotential flux convergence (ϕ_{FC} ; see A.6) appears reasonable in Fig. 4.6c, the vertical structure of ϕ_{FC} in C1 (Fig. 4.7c) is much different than in ERA-Interim (Fig. 2.18c). For example, the upper-level ϕ_{FC} minimum in ERA-Interim is replaced by a 350 hPa maxima in C1. The sign of ϕ_{FC} in the upper troposphere is also negative in Hsieh and Cook (2007), which is inconsistent with the C1 results discussed here. In essence, the sign reversal of ϕ_{FC} indicates an acceleration of the pressure-gradient-driven flow. Consistent with ERA-Interim, baroclinic overturning (C_{pk} ; see A.7) is strongly anticorrelated with ϕ_{FC} above 600 hPa in the troposphere (Fig. 4.7d), a relationship in the tropics noted by Lau and Lau (1992). Although the signs of both ϕ_{FC} and C_{pk} in the C1 simulation results oppose reanalysis data and previous studies, the sum of these terms (i.e., pressure work) is near zero in the boreal summer mean, which is consistent with ERA-Interim data. In reanalysis data, the flow is accelerated by buoyancy ($C_{pk} > 0$), which is counteracted by pressure-gradients that decelerate the flow ($\phi_{FC} < 0$). In C1, the perturbation flow is decelerated by buoyancy, but the balance between them is maintained through a pressure-gradient-driven acceleration.

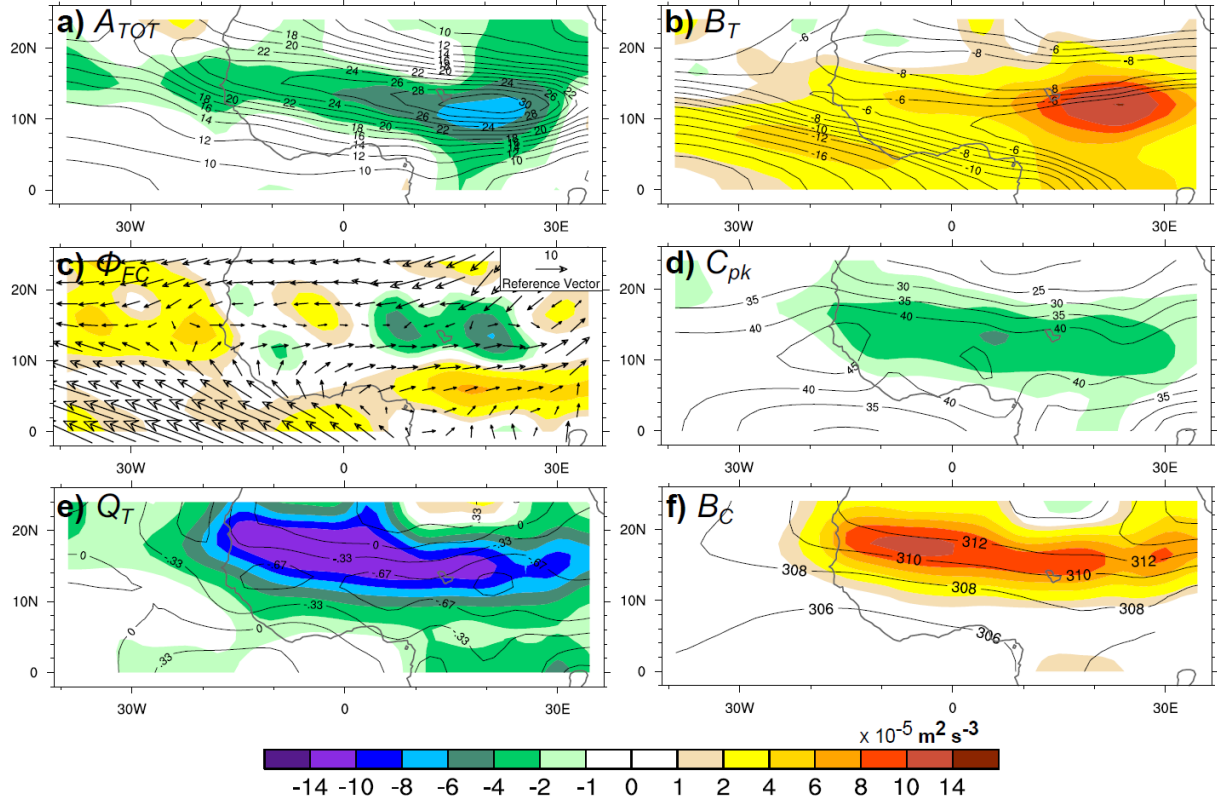


Fig 4.8 As in Fig. 2.17, except for S1.

In general, the sign reversal of C_{pk} in the C1 results can be attributed to poorly simulated 10-day high-pass temperature anomalies in the mid- to upper-troposphere. The sign reversal of temperature anomalies above 600 hPa results in cold (warm) air rising (sinking), which decelerates the perturbation flow and destroys PKE. These temperature anomalies also induce a destruction of PAPE due to diabatic heating (Q_T ; see A.8) that is collocated with mid- to upper-tropospheric C_{pk} . By comparison, ERA-Interim suggests a creation of PAPE due to diabatic heating in the mid- to upper-troposphere (Fig. 2.18e). It is unclear if these incorrect temperature anomalies are related to the cumulus parameterization (Grell 3D).

On the other hand, the PAPE budget is much more agreeable with ERA-Interim in the lower troposphere. In particular, baroclinic energy conversions (B_C ; see A.9) straddle the

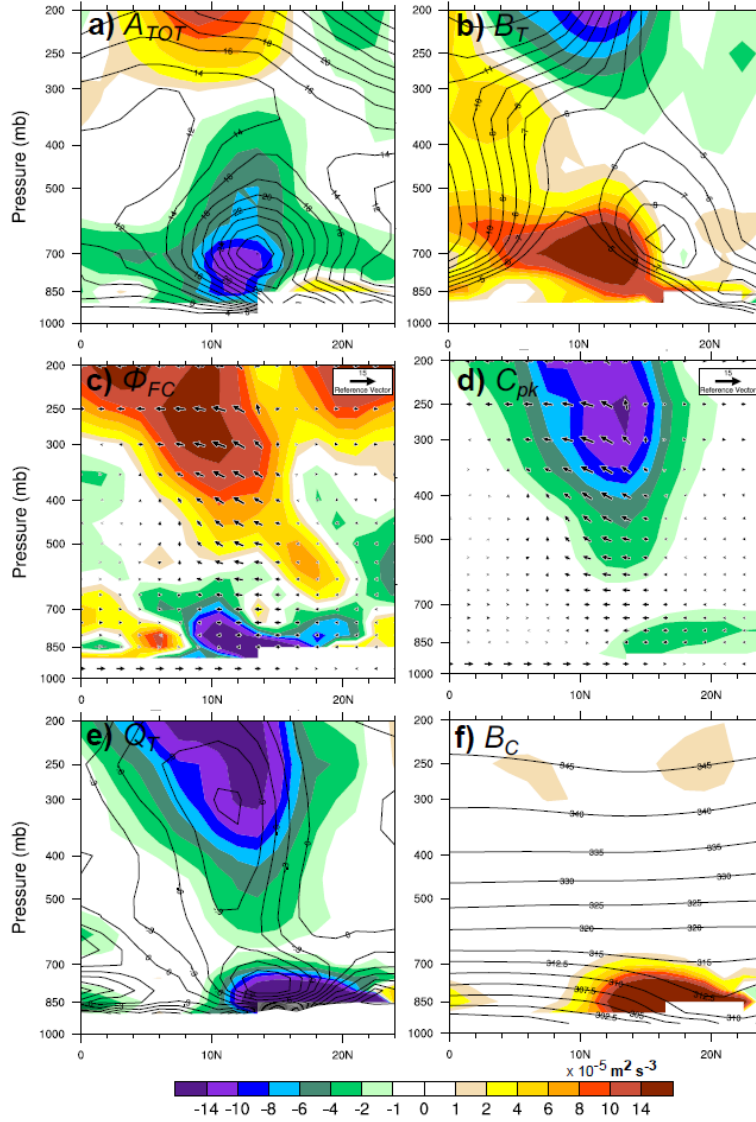


Fig 4.9 As in Fig. 2.18, except for S1.

strongest low-level potential temperature gradient, with a local maximum in sub-Saharan West Africa (Figs. 4.6f, 4.7f). It is worth noting that the meridional temperature gradient is $\sim 50\%$ weaker in C1 (0.06 K km^{-1}) than in ERA-Interim (0.1 K km^{-1} ; see Fig. 2.18f), which produces simulated $\langle B_C \rangle$ amplitudes that are about a factor of two smaller than observations. Despite the reduction of $\langle B_C \rangle$ in the C1 results, the destruction of PAPE at low levels by Q_T is quite comparable to the reanalyses and actually outweighs the PAPE created through baroclinicity.

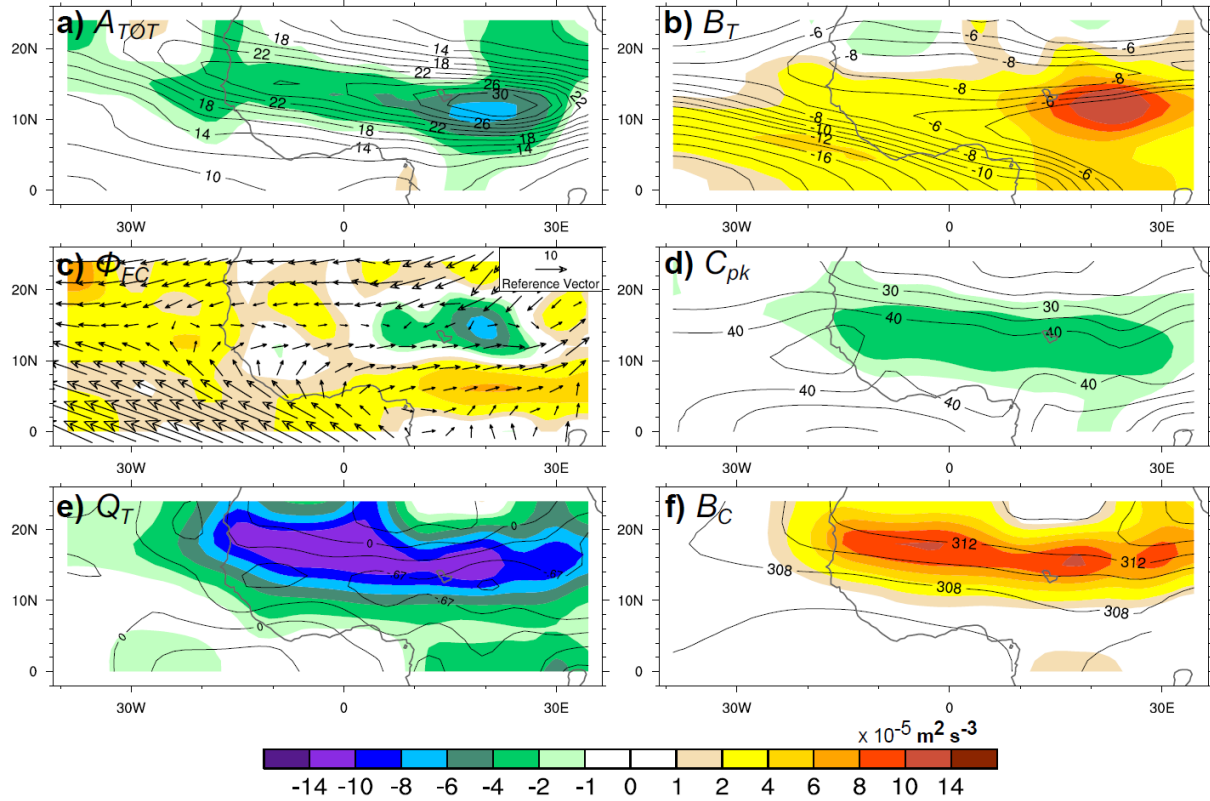


Fig 4.10 As in Fig. 2.17, except for S2.

Of course, this imbalance is reflected in lower-tropospheric C_{pk} , the opposite sign of which is discussed earlier in this section. This problem within the PAPE budget is related to improperly simulated temperature, this time within the meridional temperature gradient that exists in the boreal summer mean between the Sahara and the Gulf of Guinea. The weaker mean temperature gradient in the C1 simulation reduces B_C , but has minimal impact on the amplitude of Q_T (see Fig. 2.27). Thus, heating cold air that is moist (cooling warm air that is dry) prevails as the dominant energy conversion near the surface and acts to decelerate the flow through C_{pk} .

The PKE and PAPE budgets computed from the sensitivity test (S1 and S2) output are very consistent with the C1 results analyzed earlier in this section (Figs. 4.8, 4.9, 4.10, 4.11). Both S1 and S2 have a similar bias of AEW activity toward East Africa, which is a robust result

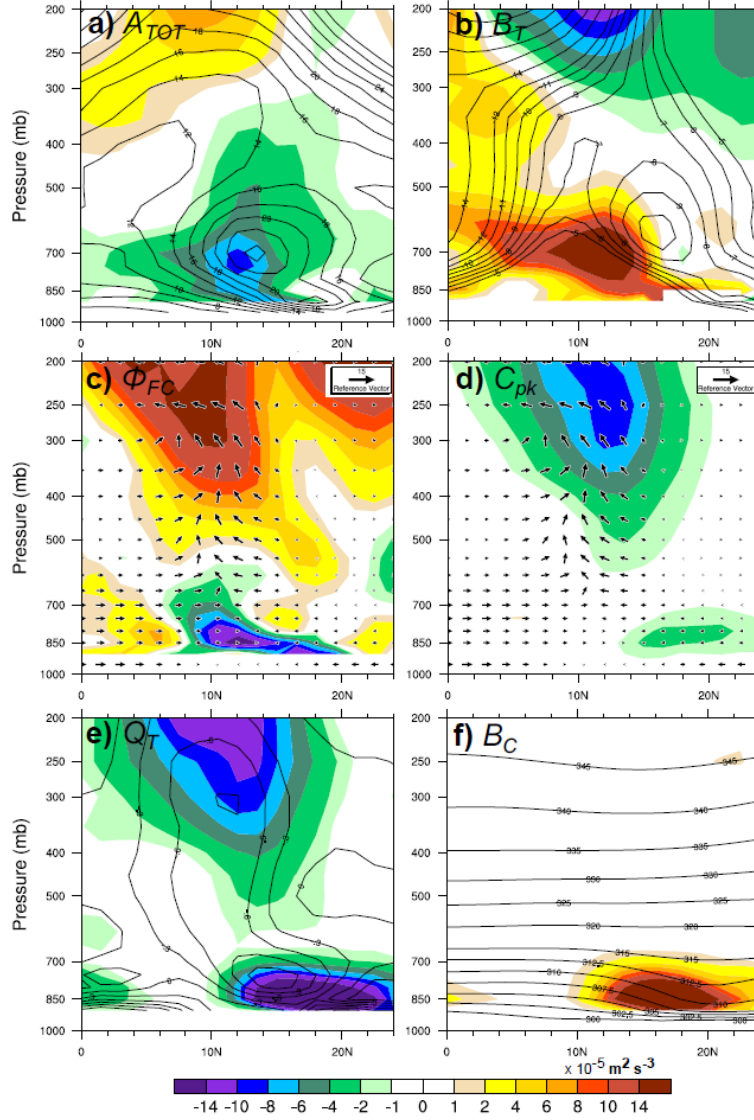


Fig 4.11 As in Fig. 2.18, except for S2.

in these ARW-ARW simulations. S1 and S2 also feature similar problems with modeled temperature within the PAPE budget as in C1, with Q_T outweighing B_C and acting to reduce the PAPE available to AEWs. The boreal summer mean meridional temperature gradient is weaker in both sensitivity tests than in C1 (Figs. 4.8f, 4.10f).

The similarity of boreal summer mean energetics within all three ARW-ARW experiments highlights the relatively modest role that external forcing has on the mean PKE and

PAPE budgets. However, S1 and S2 both produce Q_T and B_C with weaker amplitudes in West Africa and stronger amplitudes in East Africa. It is unclear what governs this amplitude shift toward East Africa, but it is a robust result in the absence of large-scale eastward-propagating 30-90-day flow (removed from boundary conditions in both S1 and S2). In fact, the boreal summer mean energetic fields are almost identical for S1 and S2, which deemphasizes the role of westward-propagating 30-90-day disturbances (e.g., equatorial Rossby waves) in the modulation of mean West African AEW activity and associated energetics. The similarity of S1 and S2 fields extends into the analyzed intraseasonal variability in tropical North Africa, which will be discussed below (see Section 4.5). Additionally, these results stress a limited role of eastward-propagating 30-90-day disturbances (e.g., Kelvin waves) to mean budgets given the strong similarities between C1 and S1 boreal summer mean energetics.

4.5 Intraseasonal Variability of West African Perturbation Kinetic Energy

Following the methodology described in Chapter 2, a 30-90-day 700 hPa PKE index is created in West Africa for each WRF experiment (C1, S1, and S2). Despite deficiencies in the simulated boreal summer mean AEW energetics (see Section 4.4), the WRF-ARW experiments all produce realistic AEW structure, with an accurate southwest to northeast tilt south of the AEJ (Fig. 4.5). A robust result across the three WRF-ARW simulations is the presence of strong AEW activity on intraseasonal time scales, as reflected by the 30-90-day variance of 700 hPa PKE (Fig. 4.12). In fact, the 30-90-day variance of 700 hPa PKE is higher in the sensitivity experiments than in C1, suggesting that 30-90-day forcing from the model boundary conditions is not necessary to produce intraseasonal variability of AEW activity. Consistent with the analysis of the boreal summer mean energetics, S1 and S2 are almost identical (Fig. 4.12b,c). In

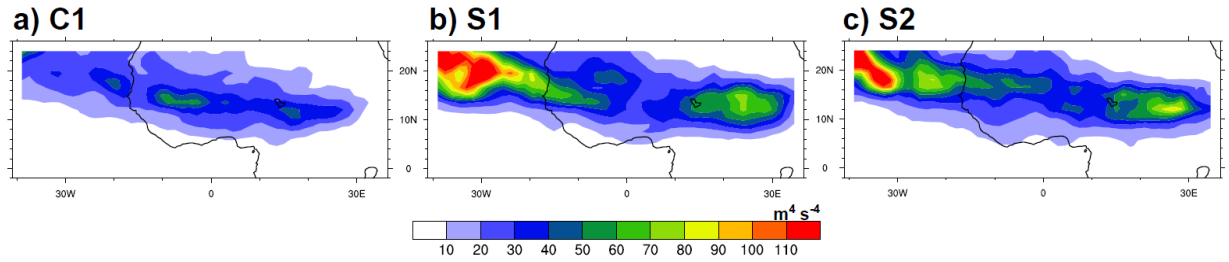


Fig 4.12 Boreal summer 30-90-day variance maps of 700 hPa PKE for three WRF-ARW experiments (C1, S1, S2).

these sensitivity tests, strong intraseasonal 700 hPa PKE variance east of Lake Chad is collocated with boreal summer mean $\langle B_T \rangle$ and $\langle B_C \rangle$, which suggests the role of these energy conversions in initiating and growing AEWs in East Africa (e.g., Thorncroft et al. 2008; Alaka and Maloney 2012). The high PKE variance in the eastern and central Atlantic Ocean is related to differences in the amplitude and track of developing AEWs. For example, some tropical systems curve into the midlatitude flow sooner than others.

The PKE index for each WRF-ARW experiment is produced based on the latitudinal location of the strongest West African 30-90-day 700 hPa PKE variance. In order to be consistent with the ERA-Interim PKE index (see Chapter 2), all three PKE indices span 20°W to 0°E with a variable 10° latitudinal range. In ERA-Interim, the intraseasonal 700 hPa PKE variance maximizes between 5°N and 15°N, which is south of the variance maximum observed in all three WRF-ARW experiments (Fig. 4.12). For C1, the box is moved north to cover 10°N – 20°N (Fig. 4.13a). In S1, the PKE index box is spans 11°N – 21°N (Fig. 4.13b). In S2, the PKE index is computed between 13°N and 23°N (Fig. 4.13c).

In C1, the 700 hPa PKE index has a spectral peak with significant (95%) power within the 30-90-day band (Fig. 4.13a), which indicates that with unfiltered boundary conditions, WRF-ARW is able to reproduce the intraseasonal peak in West African AEW activity with reasonable

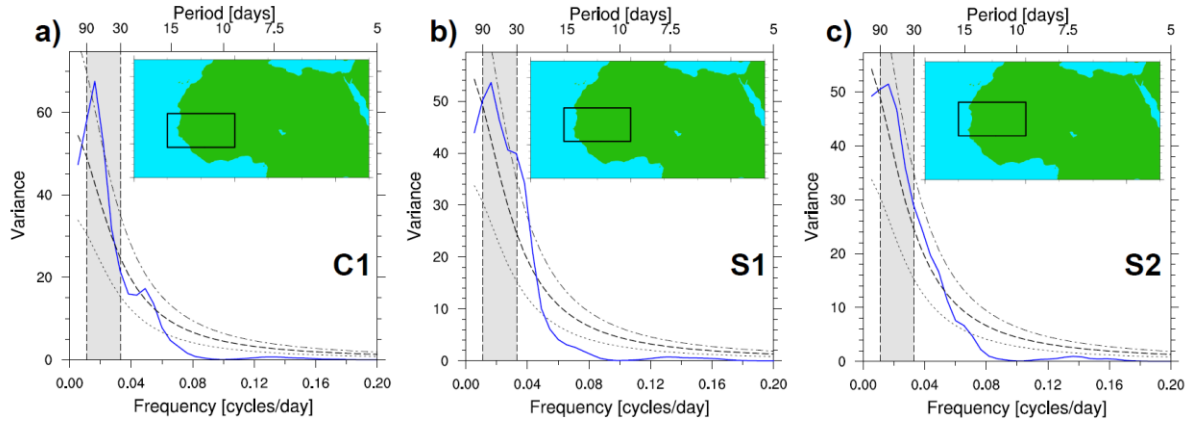


Fig 4.13 Boreal summer power spectra for 700 hPa PKE for different WRF simulations from 2001 to 2010 for: a) C1), b) S1, and c) S2. Maps show the area where spectra are computed. The associated red noise spectrum with 95% confidence bounds is given by the black curves. The gray shading represents the 30-90-day band.

accuracy, although the dominant timescale in C1 is longer than that in ERA-Interim (Fig. 2.1). The S1 and S2 experiments have a 30-90-day spectral peak that is comparable to the C1 experiment, although the power spectra for the sensitivity experiments are not significant at the 95% confidence interval. The intraseasonal variance in S1 and S2 is ~80% of that observed in C1. Therefore, even in the absence of 30-90-day input from the boundary conditions, WRF-ARW still produces strong power at intraseasonal frequencies. In other words, most of the intraseasonal variability of West African AEW activity is produced internally, which is consistent with the Chapter 2 result that the MJO index explains ~10% of the intraseasonal variance of the local PKE index. In S1 and S2, there is some evidence for a shift of power from the intraseasonal band to higher frequencies, which implicates a faster oscillation in the WAM without the large-scale intraseasonal pacing provided by the MJO. This fact will be discussed in more detail below.

A key question is whether or not the number and timing of PKE events is consistent between reanalysis products and WRF-ARW output. ERA-Interim (36 total events in 21 boreal summers) features the fewest number of PKE events in June, builds up to a maximum in August, and drops off quickly again in September (Fig. 4.14). Encouragingly, CFSR (16 events in 11 boreal summers) exhibit a progression that is similar to ERA-Interim results, with a minimum in June and a maximum in August. While the three WRF-ARW experiments produce PKE events in numbers consistent with ERA-Interim and CFSR (17, 17, and 15, respectively, in 10 years), none of these simulations follow the observed seasonal evolution of West African PKE events, including, surprisingly, the control simulation. Despite the retention of MJO influence in the C1 boundary conditions, the C1 PKE index exhibits a correlation with the ERA-Interim PKE index of only 0.22, an insignificant value that corresponds to less than 5% of the variance explained (see Table 4.1). One explanation for the small correlation coefficient is that the intraseasonal

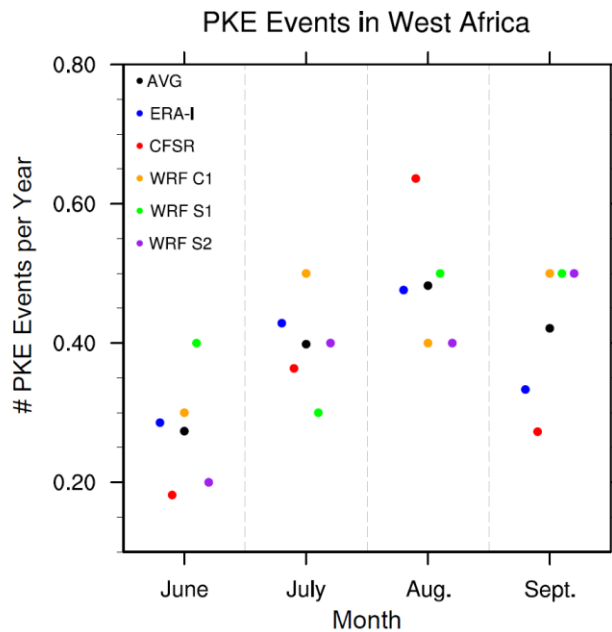


Fig 4.14 Correlation coefficients for West African 700 hPa PKE indices for observations (ERA-I) and three WRF-ARW experiments (C1, S1, S2). Correlations are performed for June-Sept from 2001-2010.

Table 4.1 Correlation coefficients for West African 700 hPa PKE indices for observations (ERA-I) and three WRF-ARW experiments (C1, S1, S2). Correlations are performed for June-Sept from 2001-2010.

	PKE Index Correlations		
	C1	S1	S2
ERA-I	0.22	0.11	0.06
C1		0.32	0.37
S1			0.52

variability of AEW activity is dominated by internal forcing, in support of the conclusions drawn from Figure 4.13. Not to be overlooked, another explanation might be related to the longer timescale of intraseasonal power in the C1 simulation (Fig. 4.13a). The ERA-Interim PKE index is mostly uncorrelated with the S1 and S2 PKE indices. The highest correlation can be found between the S1 and S2 PKE indices (0.52), which implies some consistency in the evolution of intraseasonal 700 hPa PKE variability in the absence of 30-90-day eastward-propagating disturbances. However, the similarity of the S1 and S2 PKE indices alludes to a phase-locking to the seasonal cycle, which is a puzzling result that deserves more attention in future research. The high correlation between S1 and S2 also supports the notion that the role of 30-90-day westward-propagating disturbances is limited. Even so, the number of significant ($> 1\sigma$) PKE events per month in S1 and S2 are mostly inconsistent with one another, which suggests that other timescales may play an important role in determining whether or not a particular PKE event becomes significant. The conclusion to be gleaned here is that the WRF-ARW produces its own realization of the 30-90-day AEW activity whether or not the influence of the MJO is included in the boundary conditions.

4.6 Intraseasonal Variability of African Easterly Wave Energetics in the Local PKE Index

The intraseasonal variability of the PKE and PAPE budgets presented in this section follows from Sections 2.5 and 2.6. In particular, the analysis focuses on the ISV of 700 hPa PKE and four energy conversion terms that are crucial for PKE creation: barotropic energy conversion (B_T), baroclinic energy conversion (B_C), diabatic PAPE generation (Q_T), and how these latter two terms are converted to PKE by baroclinic overturning (C_{pk}). First, local 700 hPa PKE indices for each WRF-ARW experiment are used to determine the local ISV in tropical North Africa. This local 30-90-day variability is then compared to the evolution and creation of PKE in MJO phase composites. In the following analysis, 30-90-day AEW energetics in the WRF-ARW experiments are broadly consistent with the ERA-Interim results (see Chapter 2), except for simulated $\langle C_{pk} \rangle_{30-90}$, which is negative due to the dominance of negative $\langle Q_T \rangle_{30-90}$ anomalies in the PAPE budget. The other three PKE creation terms (B_T , B_C , and Q_T) are quantitatively similar to the ISV of AEW energetics analyzed in reanalysis products.

4.6.1 PKE

As in Section 2.5, the local intraseasonal variability of AEW activity in each WRF-ARW simulation is assessed by a local 700 hPa PKE index (see Section 4.5). The three WRF-ARW simulations produce qualitatively similar composites of 700 hPa PKE_{30-90} anomalies, with West African maxima exceeding $7 \text{ m}^2 \text{ s}^{-2}$ (Figs. 4.15, 4.16). These simulated AEWs have a more dominant column-integrated presence than in ERA-Interim, as supported by vertically-averaged PKE in excess of $3 \text{ m}^2 \text{ s}^{-2}$ in the WRF-ARW experiments (not shown). Additionally, simulated 700 hPa PKE_{30-90} anomalies initiate in East Africa at least 10 days prior to positive PKE events

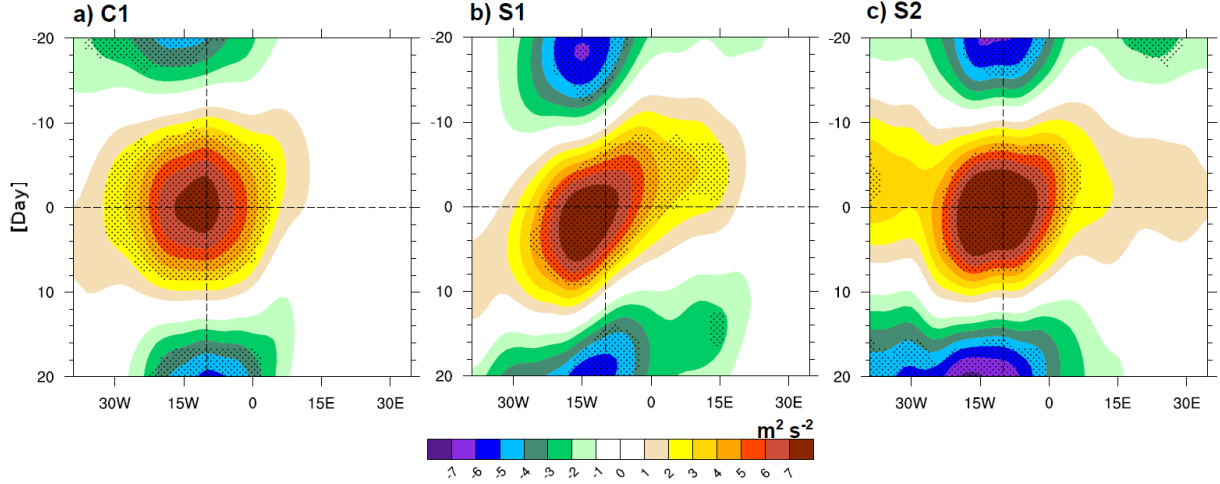


Fig 4.15 As in Fig. 2.21, except for the three WRF-ARW experiments averaged over different latitudes: a) C1 (10°N - 20°N), b) S1 (11°N - 21°N), and c) S2 (13°N - 23°N). The shading interval is $1 \text{ m}^2 \text{ s}^{-2}$. Stippling represents significance at the 95% confidence level.

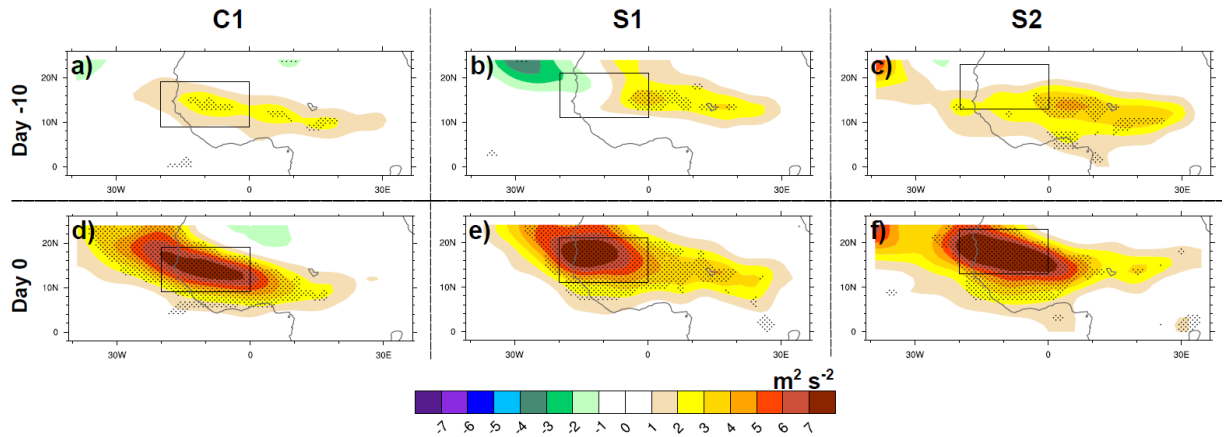


Fig 4.16 As in Fig. 2.22, except for the three WRF-ARW experiments: a) C1 day -10, b) S1 day -10, c) S2 day -10, d), C1 day 0, e) S1 day 0, and f) S2 day 0. The shading interval is $1 \text{ m}^2 \text{ s}^{-2}$. Stippling represents significance at the 95% confidence level.

(Fig. 4.16), consistent with previous studies (Alaka and Maloney 2012). This tendency for East Africa to lead is also apparent, most notable for S1 and S2 (Fig. 4.15). Westward propagation is also observed in Fig. 4.15a,c, although its representation is weakened due to the west-northwest propagation of AEWs in the C1 and S2 simulations, as these systems propagate through the

latitude ranges in each Hovmöller diagram. The more meridional component to propagation is captured in plan-view maps (Fig. 4.16). On the other hand, the S1 simulation features more zonal AEW propagation in tropical North Africa. Given the strong similarity observed between the S1 and S2 simulations, the remainder of the analysis will focus on comparisons between ISV in C1, S1 and the ERA-Interim (see Chapter 2). Therefore, westward-propagating 30-90-day disturbances (e.g., equatorial Rossby waves) appear to have a lesser role on the ISV of AEW activity in the WRF-ARW. The modeling results presented here are in contention with previous studies that have emphasized the importance of both Kelvin and equatorial Rossby waves (e.g., Matthews 2004; Janicot et al. 2011).

4.6.2 Barotropic Energy Conversion

In the C1 simulation, the largest $\langle B_T \rangle_{30-90}$ anomalies populate the south side of the AEJ and appear to be more important for the maintenance of AEW activity than its initiation (Figs. 4.17a, 4.18a, 4.19a, 4.20a), as observed in ERA-Interim. In West Africa, $\langle B_T \rangle_{30-90}$ anomalies are 50% larger than in ERA-Interim, which could be related to a sharper meridional momentum gradient. As will be discussed in Section 4.8, $\langle B_T \rangle_{30-90}$ anomalies appear to be directly related to an eastward extension and strengthening of the AEJ. However, the increased 700 hPa PKE_{30-90} anomalies in the WRF-ARW experiments also imply stronger AEWs and associated circulations, which would translate into increased eddy momentum flux as described by $\overline{u'v'}$ (see A.5). These $\langle B_T \rangle_{30-90}$ anomalies replace the vertically averaged PKE_{30-90} maximum ($\sim 3 \text{ m}^2 \text{ s}^{-2}$) in about 2.9 days. Since modeled $\langle PKE \rangle_{30-90}$ anomalies are larger than in ERA-Interim by an order of magnitude (not shown), $\langle B_T \rangle_{30-90}$ anomalies take on the order of days (rather than hours) to create the equivalent of $3 \text{ m}^2 \text{ s}^{-2}$. In C1, $\langle B_T \rangle_{30-90}$ anomalies appear to be even

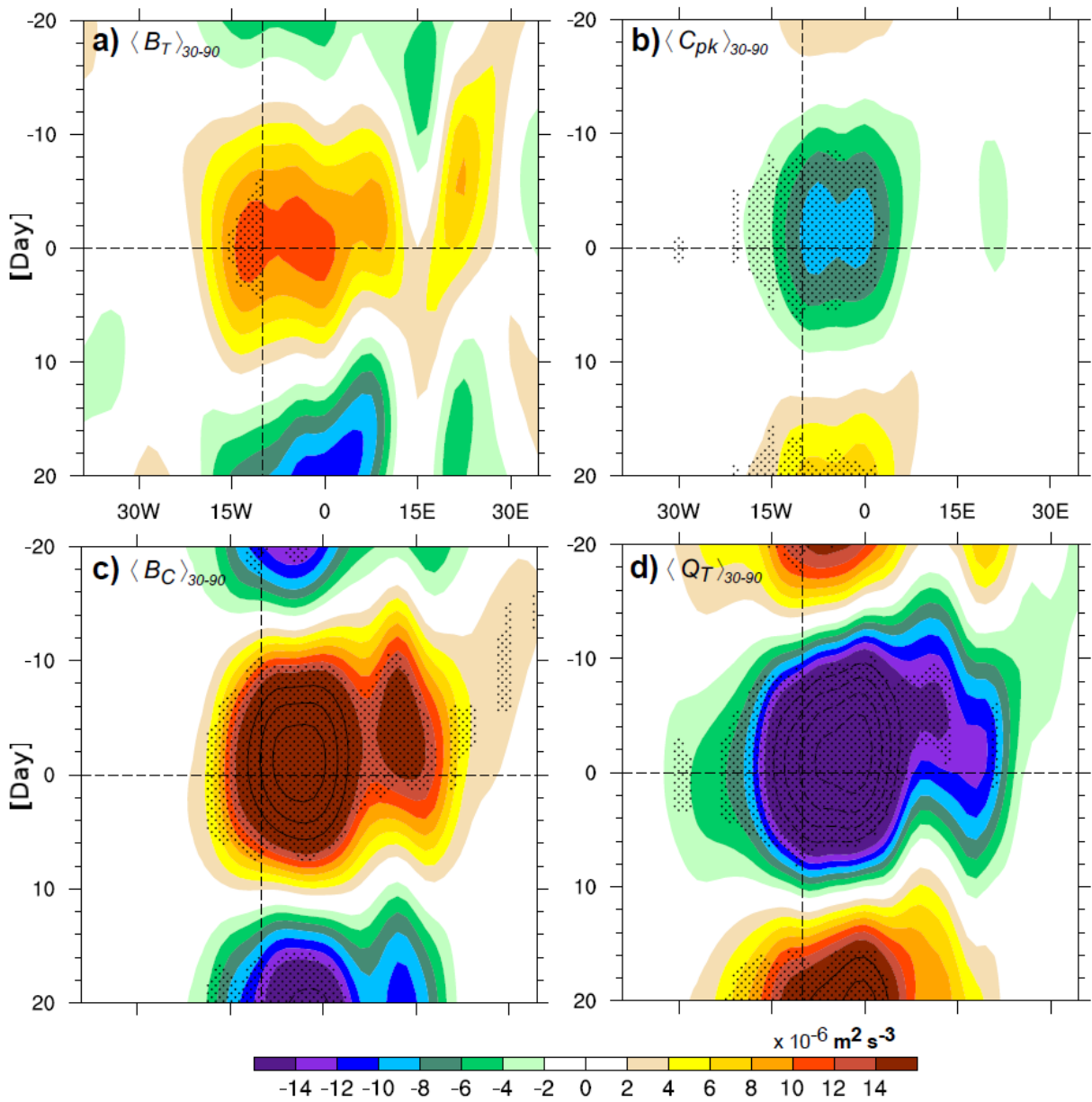


Fig 4.17 As in Fig. 2.21, except for vertically averaged, 30-90-day PKE creation terms south of the AEJ ($10^\circ\text{N} - 15^\circ\text{N}$) in the C1 simulation. Shown: (a) barotropic energy conversion, (b) baroclinic overturning, (c) baroclinic energy conversion, and (d) PAPE generation by diabatic heating. Lead/lag composites are averaged between 10°N and 15°N to create Hovmöller diagrams. The shading interval is $2 \times 10^{-6} \text{ m}^2 \text{ s}^{-3}$. Contours represent levels outside of the shading limits with an interval of $4 \times 10^{-6} \text{ m}^2 \text{ s}^{-3}$.

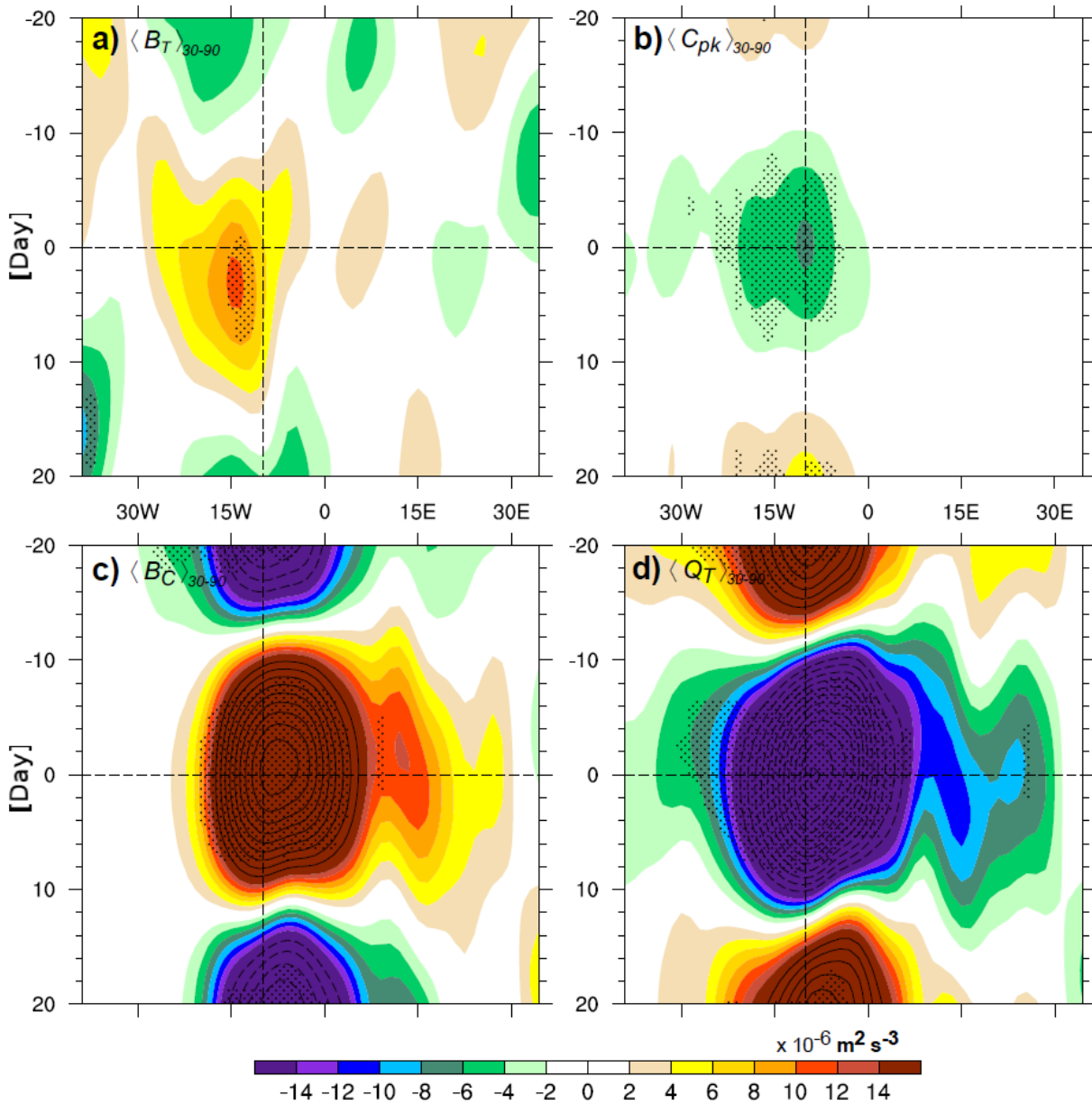


Fig 4.18 As in Fig. 2.21, except for vertically averaged, 30-90-day PKE creation terms north of the AEJ (15°N – 20°N) in the C1 simulation. Shown: (a) barotropic energy conversion, (b) baroclinic overturning, (c) baroclinic energy conversion, and (d) PAPE generation by diabatic heating. Lead/lag composites are averaged between 15°N and 20°N to create Hovmöller diagrams. The shading interval is $2 \times 10^{-6} \text{ m}^2 \text{ s}^{-3}$. Contours represent levels outside of the shading limits with an interval of $4 \times 10^{-6} \text{ m}^2 \text{ s}^{-3}$.

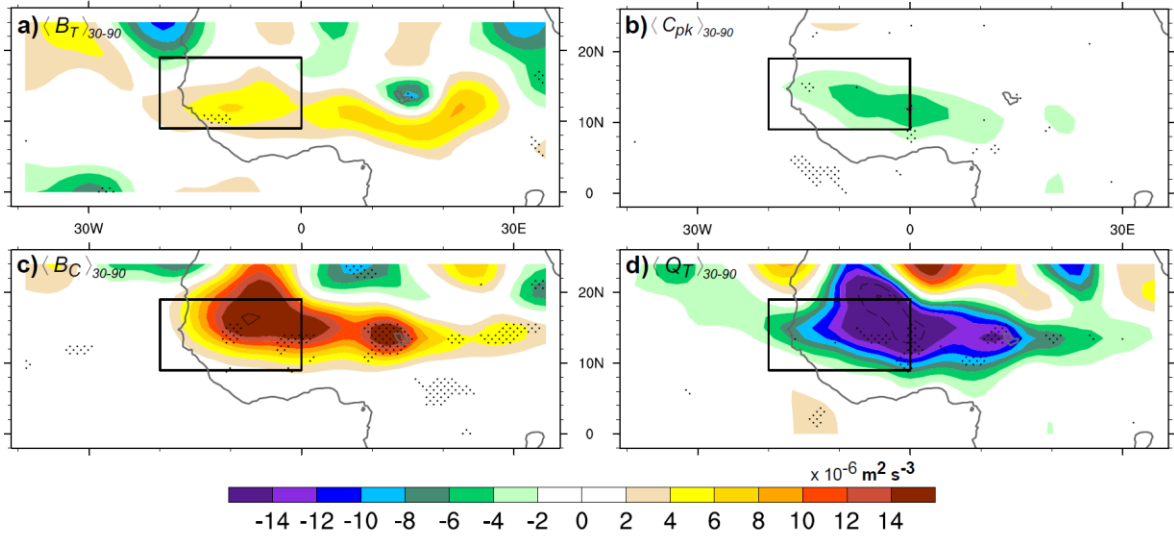


Fig 4.19 As in Fig. 2.22, except for vertically averaged, 30-90-day PKE creation terms on day -10 in the C1 simulation. Shown: (a) barotropic energy conversion, (b) baroclinic overturning, (c) baroclinic energy conversion, and (d) PAPE generation by diabatic heating. The shading interval is $2 \times 10^{-6} \text{ m}^2 \text{ s}^{-3}$. Contours represent levels outside of the shading limits with an interval of $4 \times 10^{-6} \text{ m}^2 \text{ s}^{-3}$.

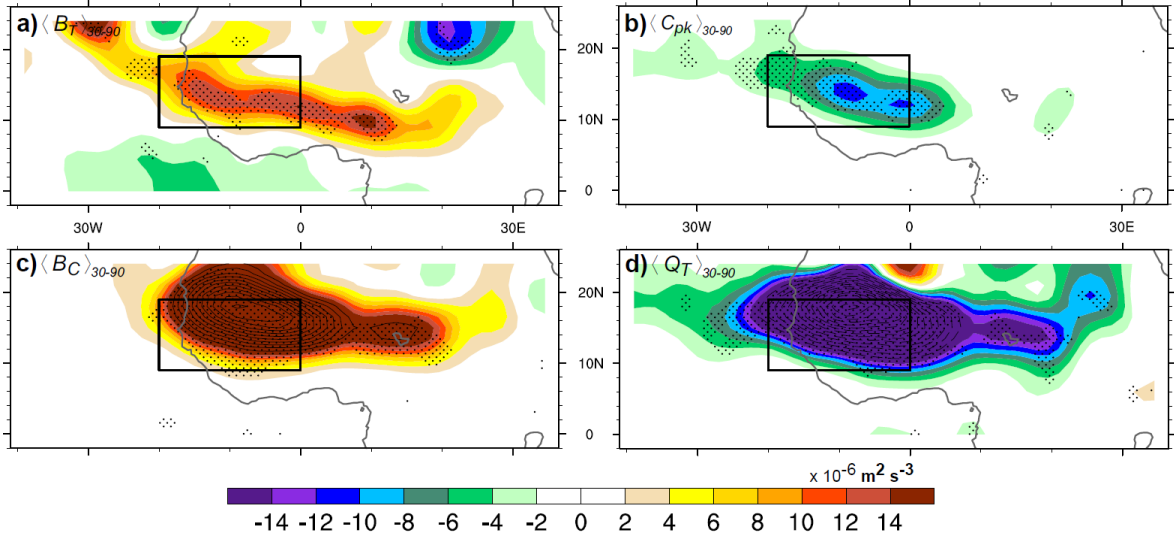


Fig 4.20 As in Fig. 2.22, except for vertically averaged, 30-90-day PKE creation terms on day 0 in the C1 simulation. Shown: (a) barotropic energy conversion, (b) baroclinic overturning, (c) baroclinic energy conversion, and (d) PAPE generation by diabatic heating. The shading interval is $2 \times 10^{-6} \text{ m}^2 \text{ s}^{-3}$. Contours represent levels outside of the shading limits with an interval of $4 \times 10^{-6} \text{ m}^2 \text{ s}^{-3}$.

less important to the initiation of positive PKE events in East Africa, with no significant anomalies east of the Greenwich Meridian to the north or the south of the AEJ (Figs. 4.17a, 4.18a).

In West Africa, $\langle B_T \rangle_{30-90}$ anomalies from S1 output are three times larger than in ERA-Interim and are observed on both sides of the AEJ (Figs. 4.21a, 4.22a). This increased amplitude is reflective of a more prominent role of $\langle B_T \rangle_{30-90}$ anomalies in creating West African PKE. However, these West African $\langle B_T \rangle_{30-90}$ anomalies appear to propagate eastward from the East Atlantic and are not directly related to intraseasonal variability in East Africa. On the other hand, significant $\langle B_T \rangle_{30-90}$ anomalies are located in East Africa in association with a secondary maximum (Figs. 4.23a, 4.24a). The East Africa $\langle B_T \rangle_{30-90}$ maxima in S1 represents the initiation and growth of AEWs due to an increased meridional momentum gradient (see Section 4.8 below). Thus, the role of $\langle B_T \rangle_{30-90}$ in the initiation of positive PKE events increases in the absence of MJO forcing. Despite the increased role of $\langle B_T \rangle_{30-90}$ anomalies in East Africa, West African $\langle B_T \rangle_{30-90}$ anomalies are vital for the maintenance of positive PKE events in both C1 and S1.

4.6.3 PKE/PAPE Conversion

Baroclinic overturning in the WRF-ARW experiments is generally unimportant for PKE creation, a surprising result given the vital role observed in reanalysis products. Since PAPE tendency values are so small in tropical North Africa on intraseasonal timescales, $\langle C_{pk} \rangle_{30-90}$ anomalies reflect the addition of $\langle B_C \rangle_{30-90}$ and $\langle Q_T \rangle_{30-90}$ anomalies. In West African reanalysis data, $\langle B_C \rangle_{30-90}$ anomalies are positive as AEWs grow on the strong meridional temperature gradient between the Sahara and the Gulf of Guinea, while $\langle Q_T \rangle_{30-90}$ anomalies depict a

negative feedback (see Fig. 2.27). While these PAPE terms maintain the same sign, the roles are reversed, with negative $\langle Q_T \rangle_{30-90}$ anomalies outweighing $\langle B_C \rangle_{30-90}$ anomalies and causing a net destruction of PKE by $\langle C_{pk} \rangle_{30-90}$ anomalies (Figs. 4.17b, 4.18b, 4.19b, 4.20b). As discussed for the boreal mean analysis of AEW energetics, the sign change of $\langle C_{pk} \rangle_{30-90}$ anomalies can be attributed to poorly-simulated temperature anomalies in the upper-troposphere. One culprit within WRF-ARW that might produce temperature anomalies in this region of the wrong sign is the cumulus parameterization. However, it is unclear if this is the case. Analysis of the S1 simulation yields conclusions that are consistent with the C1 results.

4.6.4 Baroclinic Energy Conversion

Simulated baroclinic energy conversions are quite important across tropical North Africa on intraseasonal timescales, which is consistent with the prominent role of observed $\langle B_C \rangle_{30-90}$ anomalies in ERA-Interim. The main driver of $\langle B_C \rangle_{30-90}$ anomalies is the meridional temperature gradient between the Sahara and the Gulf of Guinea. Specifically, $\langle B_C \rangle_{30-90}$ anomalies are influenced by the sharpness of this temperature gradient and stronger meridional fluxes across this gradient. As discovered in Chapter 2, a sharper temperature gradient helps initiate positive PKE events in East Africa, but most of the observed $\langle B_C \rangle_{30-90}$ amplitude can be attributed to strong meridional temperature fluxes. On the north side of the AEJ, $\langle B_C \rangle_{30-90}$ anomalies analyzed in the C1 simulation are two times larger than in ERA-Interim (Fig. 4.18c). Since a weaker meridional temperature gradient (Fig. 4.6f) reduces $\langle B_C \rangle_{30-90}$ anomalies, the increased magnitude of $\langle B_C \rangle_{30-90}$ anomalies must be associated with stronger AEW circulations that flux more heat in the meridional direction. Positive $\langle B_C \rangle_{30-90}$ anomalies are vital for PKE creation, with the ability to replace the vertically averaged PKE_{30-90} maximum ($\sim 3 \text{ m}^2 \text{ s}^{-2}$) in

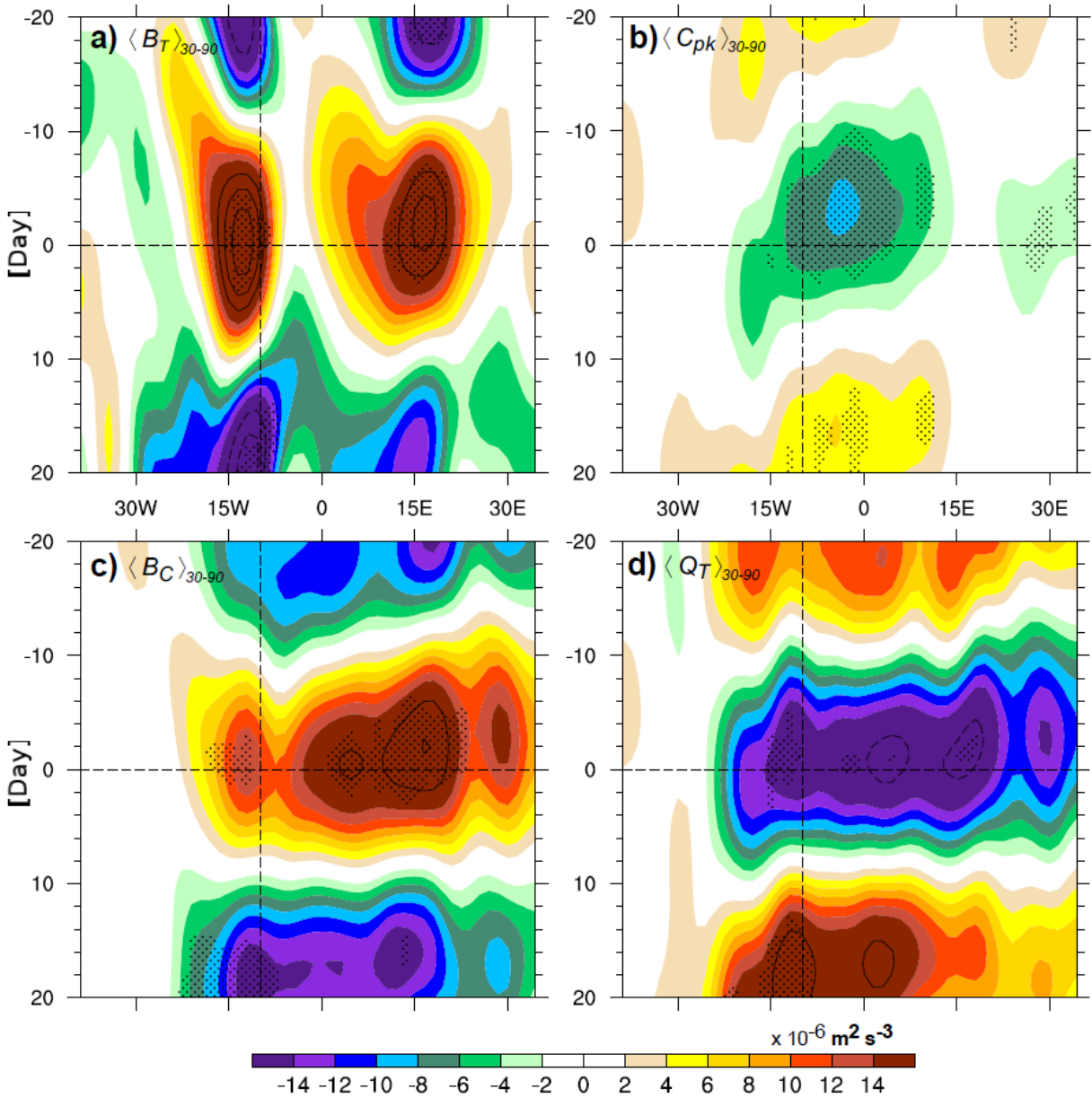


Fig 4.21 As in Fig. 2.21, except for vertically averaged, 30-90-day PKE creation terms south of the AEJ ($13^{\circ}\text{N} - 18^{\circ}\text{N}$) in the S1 simulation. Shown: (a) barotropic energy conversion, (b) baroclinic overturning, (c) baroclinic energy conversion, and (d) PAPE generation by diabatic heating. Lead/lag composites are averaged between 13°N and 18°N to create Hovmöller diagrams. The shading interval is $2 \times 10^{-6} \text{ m}^2 \text{ s}^{-3}$. Contours represent levels outside of the shading limits with an interval of $4 \times 10^{-6} \text{ m}^2 \text{ s}^{-3}$.

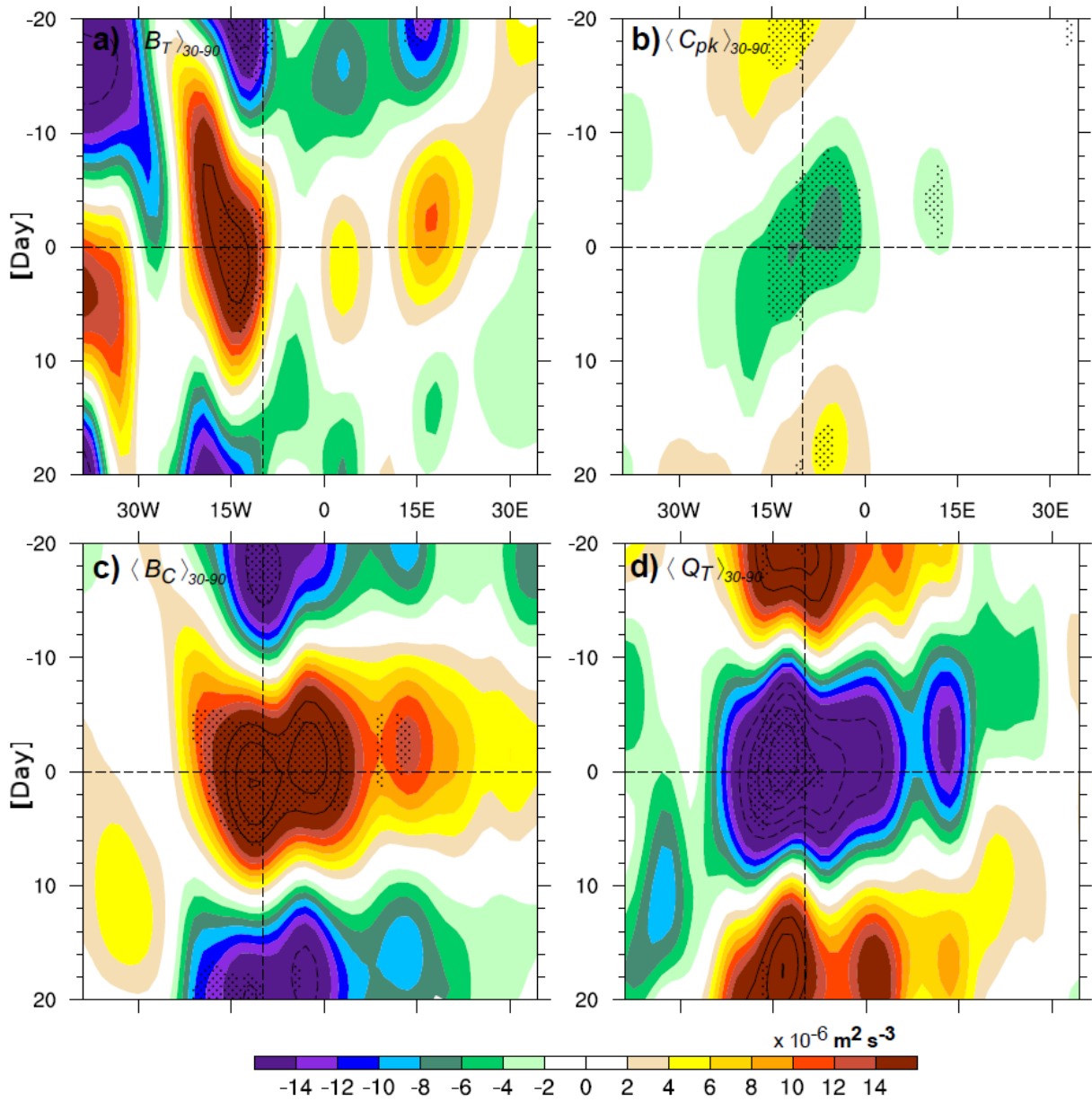


Fig 4.22 As in Fig. 2.21, except for vertically averaged, 30-90-day PKE creation terms north of the AEJ ($18^\circ\text{N} - 23^\circ\text{N}$) in the S1 simulation. Shown: (a) barotropic energy conversion, (b) baroclinic overturning, (c) baroclinic energy conversion, and (d) PAPE generation by diabatic heating. Lead/lag composites are averaged between 18°N and 23°N to create Hovmöller diagrams. The shading interval is $2 \times 10^{-6} \text{ m}^2 \text{ s}^{-3}$. Contours represent levels outside of the shading limits with an interval of $4 \times 10^{-6} \text{ m}^2 \text{ s}^{-3}$.

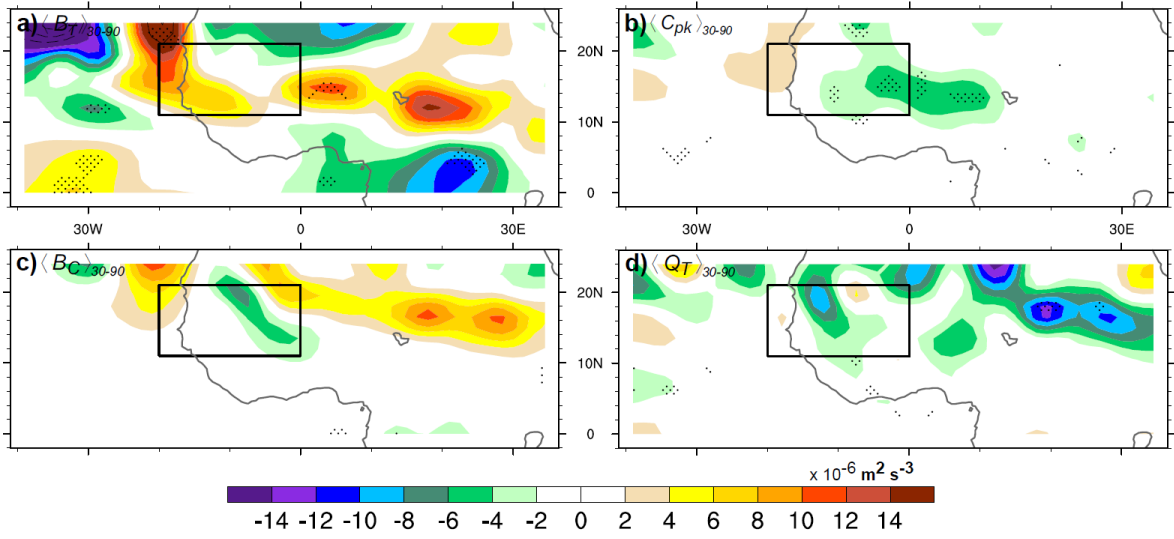


Fig 4.23 As in Fig. 2.22, except for vertically averaged, 30-90-day PKE creation terms on day -10 in the S1 simulation. Shown: (a) barotropic energy conversion, (b) baroclinic overturning, (c) baroclinic energy conversion, and (d) PAPE generation by diabatic heating. The shading interval is $2 \times 10^{-6} \text{ m}^2 \text{ s}^{-3}$.

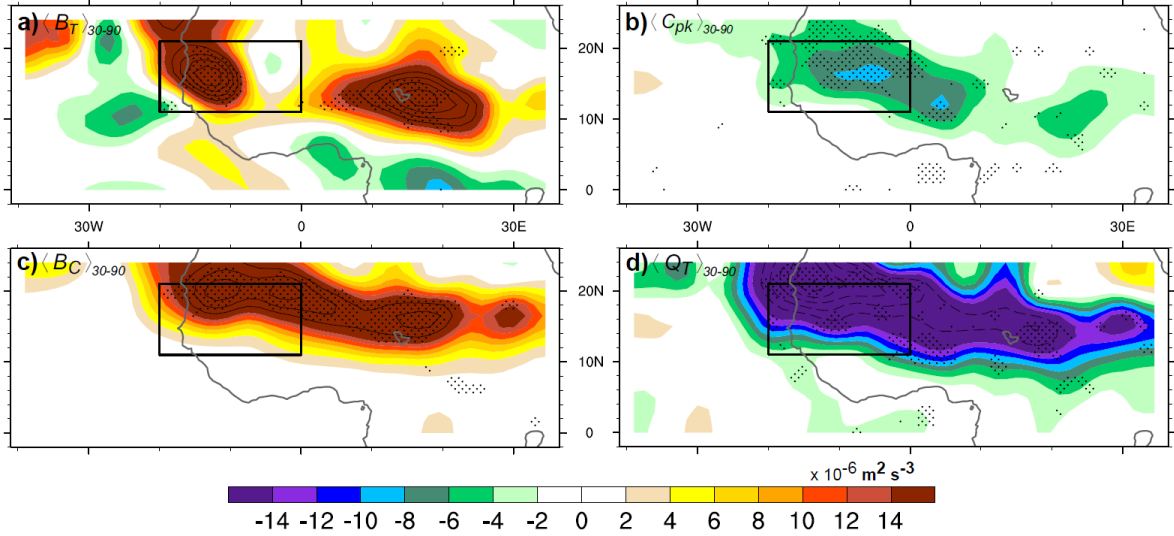


Fig 4.24 As in Fig. 2.22, except for vertically averaged, 30-90-day PKE creation terms on day 0 in the S1 simulation. Shown: (a) barotropic energy conversion, (b) baroclinic overturning, (c) baroclinic energy conversion, and (d) PAPE generation by diabatic heating. The shading interval is $2 \times 10^{-6} \text{ m}^2 \text{ s}^{-3}$. Contours represent levels outside of the shading limits with an interval of $4 \times 10^{-6} \text{ m}^2 \text{ s}^{-3}$.

about 16.5 hours. Unlike in the reanalysis data, simulated $\langle B_C \rangle_{30-90}$ anomalies dominate over $\langle B_T \rangle_{30-90}$ anomalies on the south side of the AEJ, which highlights the wide influence $\langle B_C \rangle_{30-90}$ anomalies have in the WRF-ARW simulations.

In the S1 simulation, $\langle B_C \rangle_{30-90}$ anomalies are weaker than in C1, but the westward propagation of these anomalies from East Africa to West Africa are still evident. With a propagation speed of $\sim 7 \text{ m s}^{-1}$, $\langle B_C \rangle_{30-90}$ anomalies in S1 propagate to the west at approximately the same speed as 30-90-day AEW activity. One interesting feature in the S1 simulation is the shorter timescale over which positive $\langle B_C \rangle_{30-90}$ anomalies act. In S1, $\langle B_C \rangle_{30-90}$ anomalies in excess of $1.4 \times 10^{-5} \text{ m}^2 \text{ s}^{-3}$ span from day -5 to day 7, or 13 days. In C1, the timescale is noticeably longer, with $\langle B_C \rangle_{30-90}$ anomalies greater than $1.4 \times 10^{-5} \text{ m}^2 \text{ s}^{-3}$ observed from day -8 to day 8, or 17 days. The shorter timescale in the absence of 30-90-day boundary conditions suggests that ISV in West Africa may be paced by the large-scale variability associated with the MJO. A tendency toward a shorter timescale in the S1 simulation is also noted in Fig. 4.13b. For example, the quasi-regular passage of dry MJO-emitted Kelvin wave events along the equator is one way the MJO might modulate preferred timescales of ISV in remote regions. Without this guiding MJO timescale, the ISV produced in the WAM region may prefer faster intraseasonal variability.

4.6.5 Role of Diabatic Heating

Part of the motivation to model AEW energetics on intraseasonal timescales is test the robustness of the diabatic heating term (Q_T) in ERA-Interim. Most of the errors observed in Q_T are a consequence of the cumulus parameterization used to simulate this heating. Since the WRF-ARW and ERA-Interim output employ different parameterizations, the Q_T results

presented here will offer a different perspective on the same bulk heating rate. Previous studies argue that diabatic heating in East Africa is vital for the initiation of AEWs (Thorncroft et al. 2008; Alaka and Maloney 2012; Berry and Thorncroft 2012). This author argued that an underrepresentation of diabatic heating (and related processes) in the ERA-Interim dataset limited the role of this term in East Africa. It was hypothesized that modeling would uncover a stronger relationship between East African diabatic heating and PKE creation. However, the WRF-ARW experiments analyzed here do not support a role for diabatic heating in the initiation of positive PKE events in East Africa (Figs. 4.17d, 4.18d, 4.19d, 4.20d). Consistent with Chapter 2, diabatic heating is calculated as the material derivative of dry static energy in this analysis. Therefore, Q_1 includes the impacts of radiation, which might not be ideal for isolating the signal due to convective heating. The dominant role of $\langle Q_T \rangle_{30-90}$ anomalies is to act as a negative feedback to $\langle B_C \rangle_{30-90}$ anomalies across tropical North Africa. Again, the hypothesized mechanism destroys PAPE on both sides of an AEW circulation is West Africa ($\overline{Q_1' T'} < 0$). Ahead (west) of an AEW, the associated circulation advects warm, dry air from the Sahara, with the dry air suppressing convection. Behind (east) an AEW, the associated circulation advects cool, moist air from the Gulf of Guinea, with the moist air enhancing convection. On both sides of the AEW, $\langle Q_T \rangle_{30-90}$ anomalies act to lower the center of mass of the column. As a result, the PAPE available for PKE creation is reduced. In both the C1 and S1 simulations, $\langle Q_T \rangle_{30-90}$ anomalies propagate westward and are strongly collocated with $\langle B_C \rangle_{30-90}$ anomalies, which is consistent with ERA-Interim results. Like baroclinic energy conversions, the timescale of $\langle Q_T \rangle_{30-90}$ shortens in the absence of MJO forcing and could also be related to a shorter preferred timescale for ISV in West Africa. An important question that will be addressed in future work is how AEW energetics are affected by model errors in the representation of convection.

4.7 Intraseasonal Variability of African Easterly Wave Energetics in the MJO Index

A focal point of this analysis is to determine the role (and the extent of the role) of the MJO forcing in West Africa. Previous sections in this chapter have highlighted strong evidence that the MJO is weakly related to the ISV of AEWs, which is consistent with the Chapter 2 finding that the MJO explains ~10% of the intraseasonal variance of West African AEW activity. While the MJO does not strongly govern the amplitude of 700 hPa PKE and associated AEW energetics, it may still play a role in pacing the timescale of WAM variability. In the C1 simulation, the evolution of 700 hPa PKE_{30-90} anomalies over a composite MJO life cycle is in agreement with ERA-Interim, especially the timing (Fig. 4.25). In addition, the amplitude of PKE_{30-90} anomalies is about 50% of the amplitude of anomalies associated with the local PKE index. A key difference is that the largest 700 hPa PKE_{30-90} anomalies are located over land in the C1 simulation, while these anomalies are observed in the East Atlantic in ERA-Interim. The reason for this discrepancy is unclear and future work will incorporate more WRF-ARW experiments to test the robustness of the land signal observed in the C1 simulation (Fig. 4.25). Nonetheless, the 700 hPa PKE_{30-90} signal is associated with barotropic and baroclinic energy conversions (Figs. 4.26, 4.27). These $\langle B_T \rangle_{30-90}$ and $\langle B_C \rangle_{30-90}$ anomalies are qualitatively similar to identical terms in the ERA-Interim analysis. The magnitudes of $\langle B_T \rangle_{30-90}$ and $\langle B_C \rangle_{30-90}$ anomalies are higher in the C1 simulation than in ERA-Interim, which is consistent with a stronger 700 hPa PKE_{30-90} signal in C1. Otherwise, the MJO composites in C1 tell a similar story to the ERA-Interim data.

Even in the absence of MJO forcing in the boundary conditions, 700 hPa PKE_{30-90} anomalies from the S1 simulation still exhibit significant intraseasonal variability over the course of an MJO life cycle (Fig. 4.28). While this result is perplexing originally, it is well within the

realm of possibilities that 30-90-day filtered 700 hPa PKE (or any 30-90-day filtered variable) would project onto a 30-90-day MJO index. A clue that this signal might be due to random chance is reflected by a phase shift of 1-2 phases in the S1 simulation. This phase shift, in the absence of MJO forcing, might be another manifestation of how the MJO paces ISV in West Africa. Further investigation into the MJO index reveals the potential for phase-locking to the

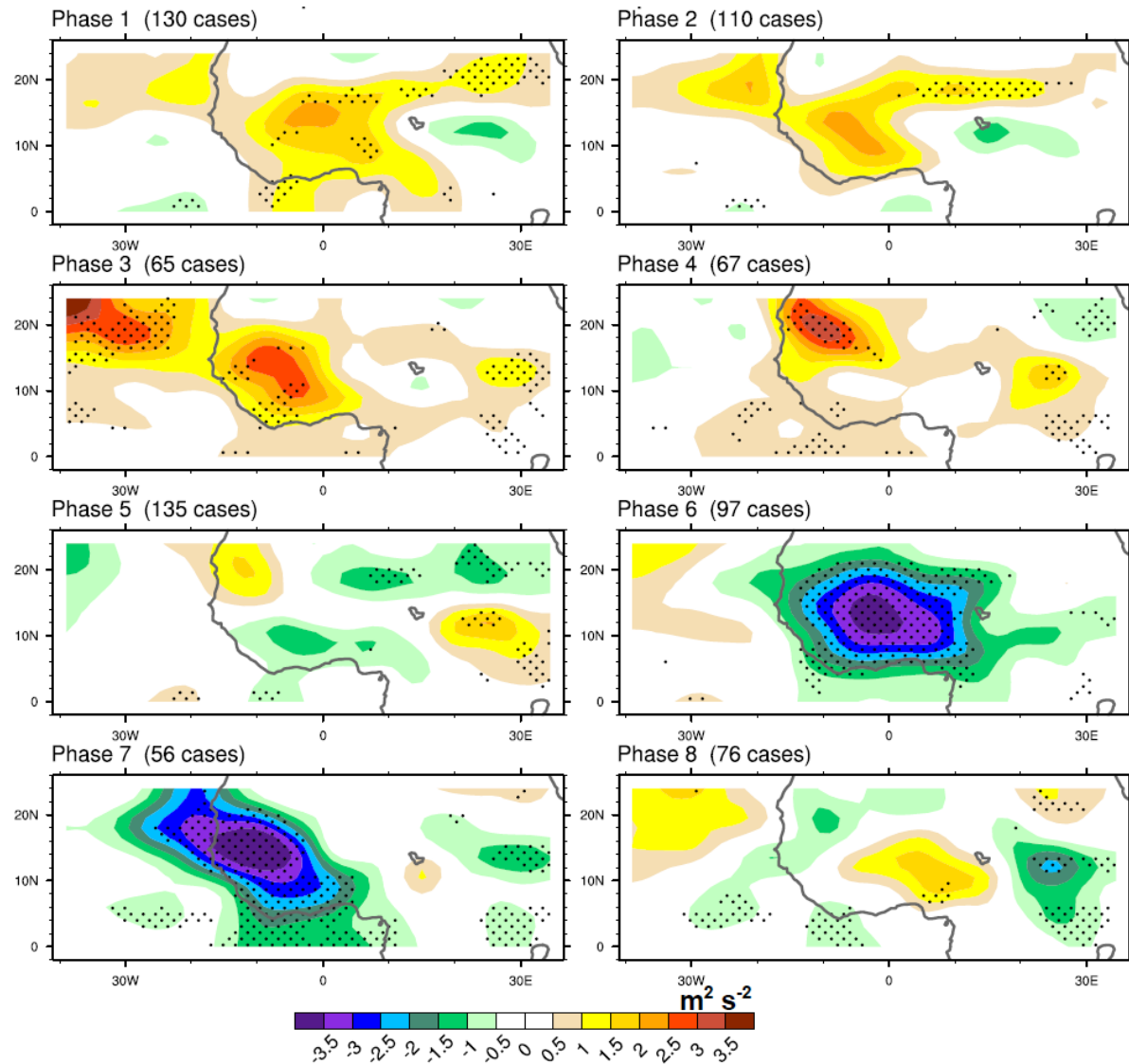


Fig 4.25 As in Fig. 2.28, except for 700 hPa 30-90-day PKE anomalies in the C1 simulation. The shading interval is $0.5 \text{ m}^2 \text{ s}^{-2}$.

seasonal cycle. Analysis of the MJO index reveals preferential significant MJO phases in different boreal summer months. For example, significant MJO amplitudes tend to reside in phases 7,8 and 1 in July, while, in September, phases 3-5 tend to be more significant. A less likely, but still plausible, scenario is that the MJO indirectly influences ISV in West Africa by projecting onto timescales not removed by the 30-90-day bandpass filter applied to model boundary conditions. Overall, the amplitude of simulated AEW energetics in West Africa in

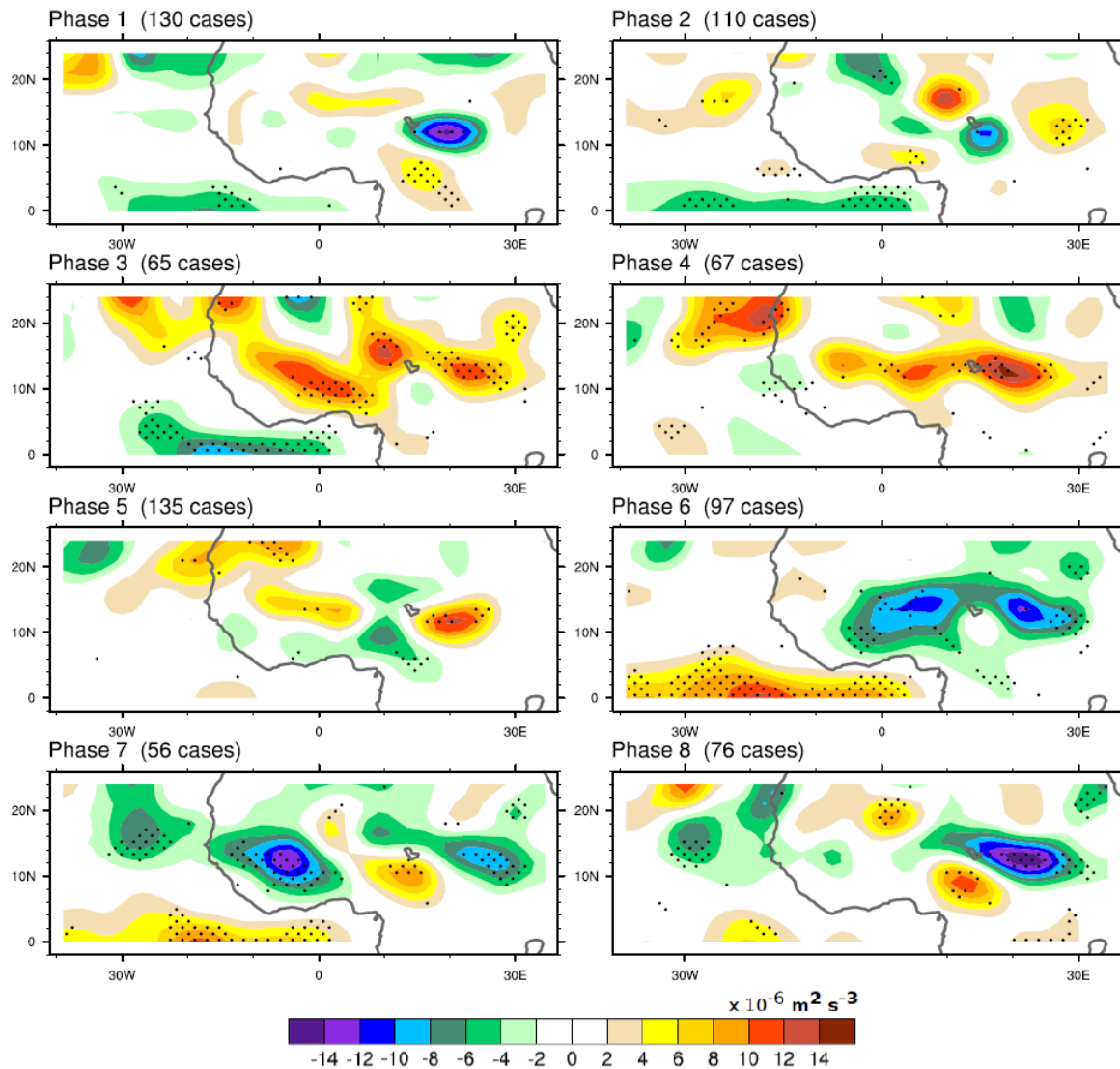


Fig 4.26 As in Fig. 2.28, except for vertically-averaged 30-90-day B_T anomalies in the C1 simulation. The shading interval is $2 \times 10^{-6} \text{ m}^2 \text{ s}^{-3}$.

MJO phase composites is about 50% of the amplitude analyzed from the local PKE index composites. This supports the growing notion that the MJO does not dominantly modulate ISV in the WAM region, but, rather, is limited to a role of officiating the timing of positive PKE events in West Africa.

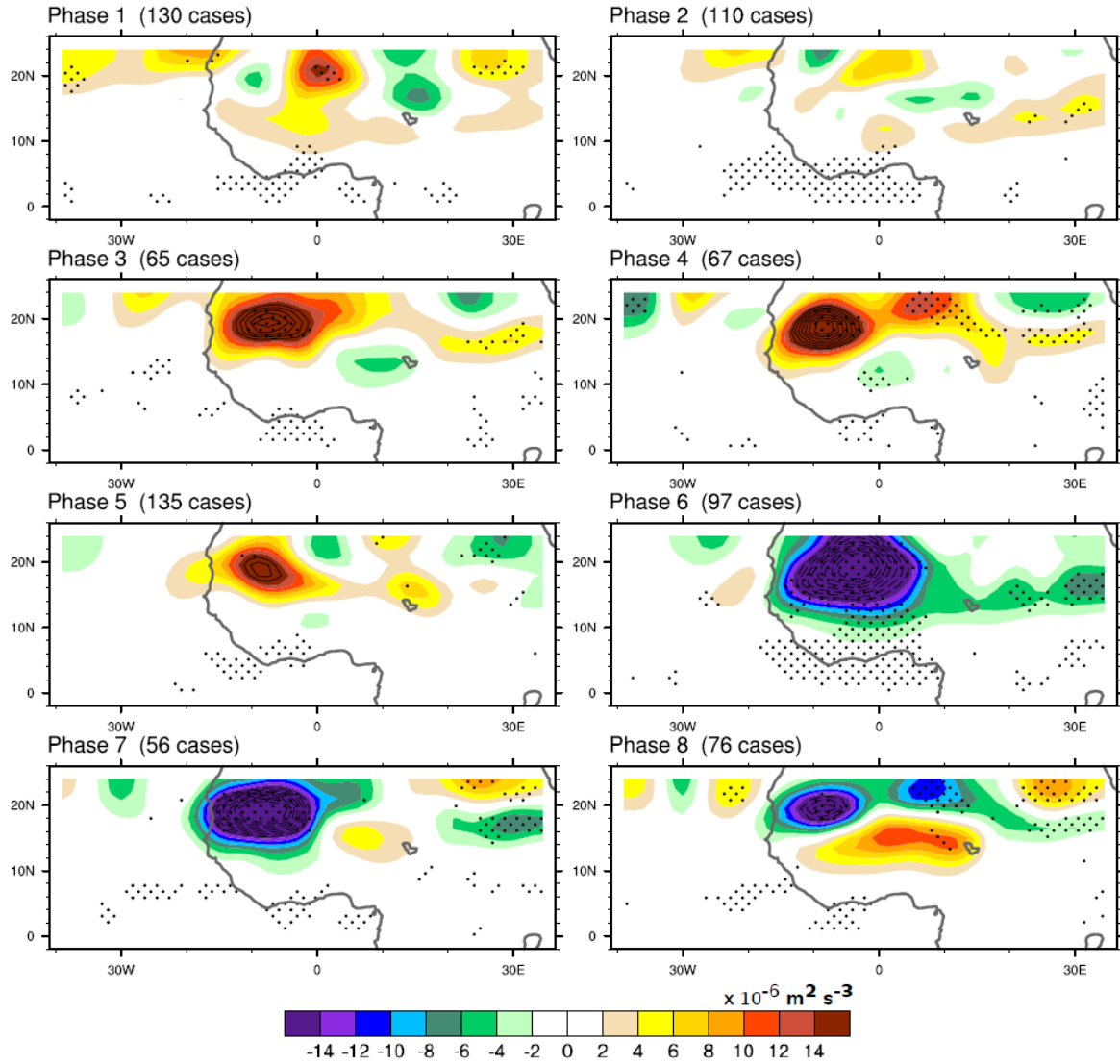


Fig 4.27 As in Fig. 2.28, except for vertically-averaged 30-90-day B_C anomalies in the C1 simulation. The shading interval is $2 \times 10^{-6} \text{ m}^2 \text{ s}^{-3}$.

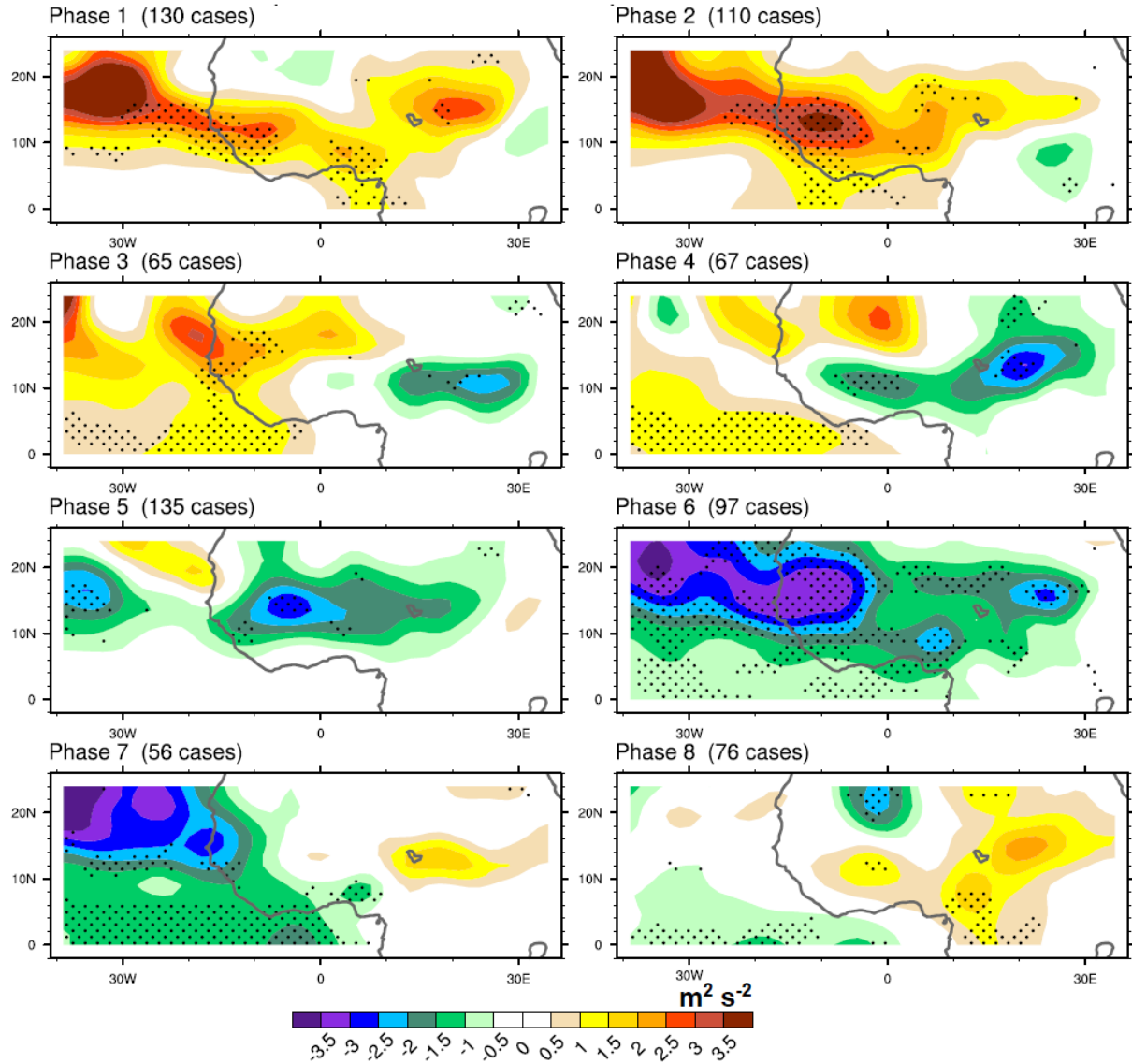


Fig 4.28 As in Fig. 2.28, except for 700 hPa 30-90-day PKE anomalies in the S1 simulation. The shading interval is $0.5 \text{ m}^2 \text{ s}^{-2}$.

4.8 Intraseasonal Variability of AEW Trigger Mechanisms in East Africa

Following the conclusions of Alaka and Maloney (2012), three mechanisms for triggering 30-90-day AEW activity in East Africa are investigated further within the WRF-ARW experiments (see Section 1.5). These three AEW initiation mechanisms are: 1) an eastward

extension of the AEJ, 2) decreased static stability, and 3) meridional moisture advection. In particular, the reproduction of these three trigger mechanisms in the C1 simulation is scrutinized and then compared to results from S1 and S2 to explore how MJO forcing modulates these AEW triggers. Previous results in this chapter reveal that simulated PKE events are, in fact, initiated in East Africa, which indicates that the role of trigger mechanisms in this region could be quite significant.

4.8.1 Eastward AEJ Extension

The first trigger mechanism is the extension of the AEJ into East Africa, as noted in previous studies (Leroux et al. 2010; Alaka and Maloney 2012). A stronger AEJ in East Africa is indicative is a larger reversal of the meridional PV gradient and increased barotropic-baroclinic energy conversions (e.g., Charney and Stern 1962). Specifically, the phrase “AEJ extension into East Africa” refers to an increase in easterly flow in this region. An AEJ extension is clearly observed in all three WRF-ARW experiments in advance of the downstream PKE maximum (Fig. 4.29). Furthermore, the AEJ extension is a robust feature in East Africa prior to increased AEW activity in West Africa in both reanalysis and model data. The similarity of the AEJ extension among the WRF-ARW experiments highlights that MJO forcing is not necessary to produce this feature. The AEJ appears to pulse with increased easterly flow in East Africa, a consequence of thermal wind balance associated with warm lower-tropospheric temperature anomalies in the Sahara (not shown). In addition, a strengthened reversal of the meridional PV gradient would aid in the growth of small, isolated convective events into more robust AEWs from combined barotropic-baroclinic instability. Adding further evidence to the importance of the AEJ extension, $\langle B_T \rangle_{30-90}$ and $\langle B_C \rangle_{30-90}$ anomalies from the C1 and S1 simulations appear to

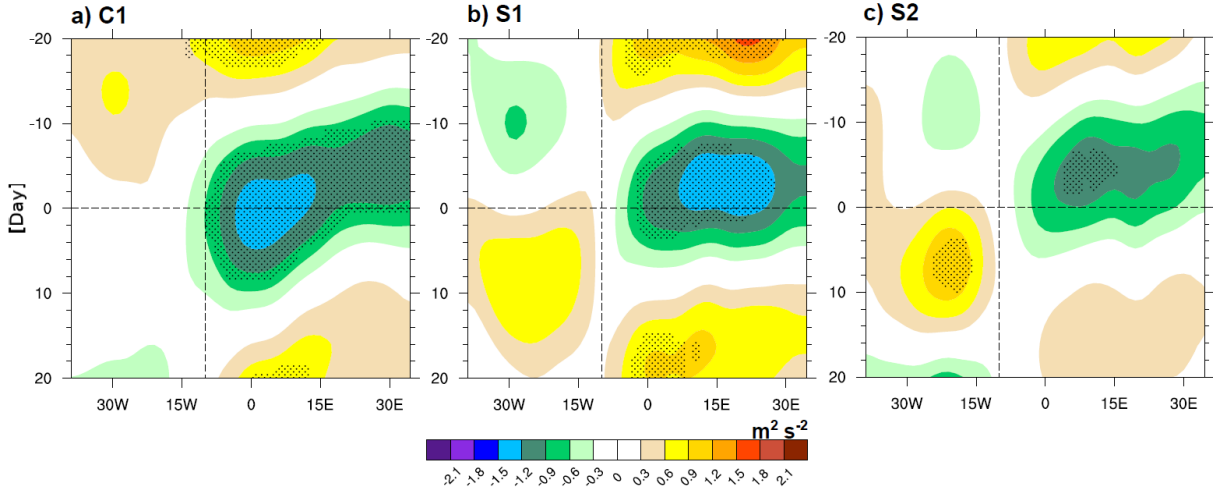


Fig 4.29 As in Fig. 2.21, except for 30-90-day 650 hPa zonal wind anomalies from three WRF-ARW experiments averaged over different latitudes: a) C1 (12.5°N - 17.5°N), b) S1 (15.5°N - 20.5°N), and c) S2 (18°N - 23°N). The shading interval is 0.3 m s^{-1} . Stippling represents significance at the 95% confidence level.

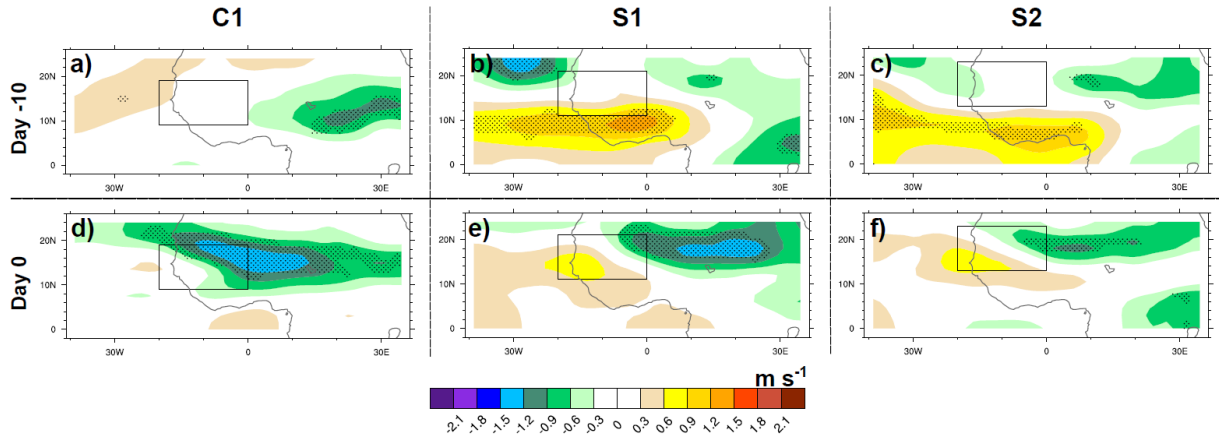


Fig 4.30 As in Fig. 2.22, except for 30-90-day 650 hPa zonal wind anomalies from three WRF-ARW experiments: a) C1 day -10, b) S1 day -10, c) S2 day -10, d) C1 day 0, e) S1 day 0, and f) S2 day 0. The shading interval is 0.3 m s^{-1} . Stippling represents significance at the 95% confidence level.

follow the growth of 650 hPa easterly flow (Figs. 4.18, 4.21). These positive 800 hPa T_{30-90} anomalies responsible for the AEJ extension appear to be related fluctuations in the Saharan heat low, which has been shown in other studies to exhibit significant intraseasonal variability (e.g.,

Lavaysse et al. 2009). Previous studies have attributed the intraseasonal variability of the Saharan heat low to a complex interaction with midlatitude flow (Chauvin et al. 2010; Poan et al. 2013). These 650 hPa easterly anomalies associated with an AEJ extension into East Africa spread westward with time in all three WRF-ARW simulations, which aids cyclonic vorticity in West Africa (Fig. 4.30d-f).

4.8.2 Static Stability Reduction

As described in Alaka and Maloney (2012), mid- to upper-tropospheric temperature anomalies in East Africa steepen the lapse rate and prime the column for increased convection. In the C1 simulation, 400 hPa T_{30-90} anomalies are found in the northeast part of the model domain, which leads to the static stability reduction for much of East Africa prior to the peak of positive PKE events (Figs. 4.31a, 4.32a,d). In ERA-Interim, 400 hPa T_{30-90} anomalies exhibited a similar westward propagation across tropical North Africa, as found in the control simulation C1. A large-scale view of the tropics revealed a structure that resembles the Gill model response to heating anomalies in the Indian Ocean. However, the WRF-ARW experiments do not support the association of these 400 hPa T_{30-90} anomalies with westward-propagating 30-90-day disturbances (e.g., equatorial Rossby waves). In S1, the 400 hPa T_{30-90} signal disappears with the removal of all 30-90-day variability from the boundary conditions. However, even when westward-propagating 30-90-day disturbances are restored (S2), the 400 hPa T_{30-90} signal still does not exist. In addition, the 400 hPa T_{30-90} signal is too far removed from the equator to be directly related to Kelvin wave. A closer inspection of Fig. 4.32a reveals a strong connection of these 400 hPa T_{30-90} anomalies to the midlatitudes, suggesting a role for periodic wave-breaking that coincidentally precedes positive PKE events in West Africa. However, given the robust

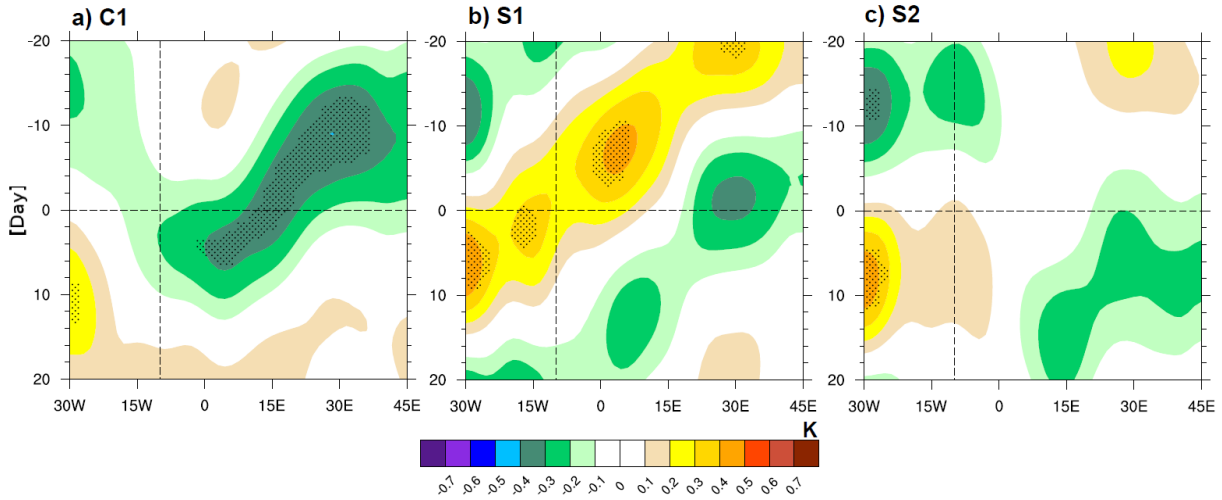


Fig 4.31 As in Fig. 2.21, except for 30-90-day 400 hPa temperature anomalies from three WRF-ARW experiments averaged between 22.5°N-27.5°N: a) C1, b) S1, and c) S2. The shading interval is 0.1 K. Stippling represents significance at the 95% confidence level.

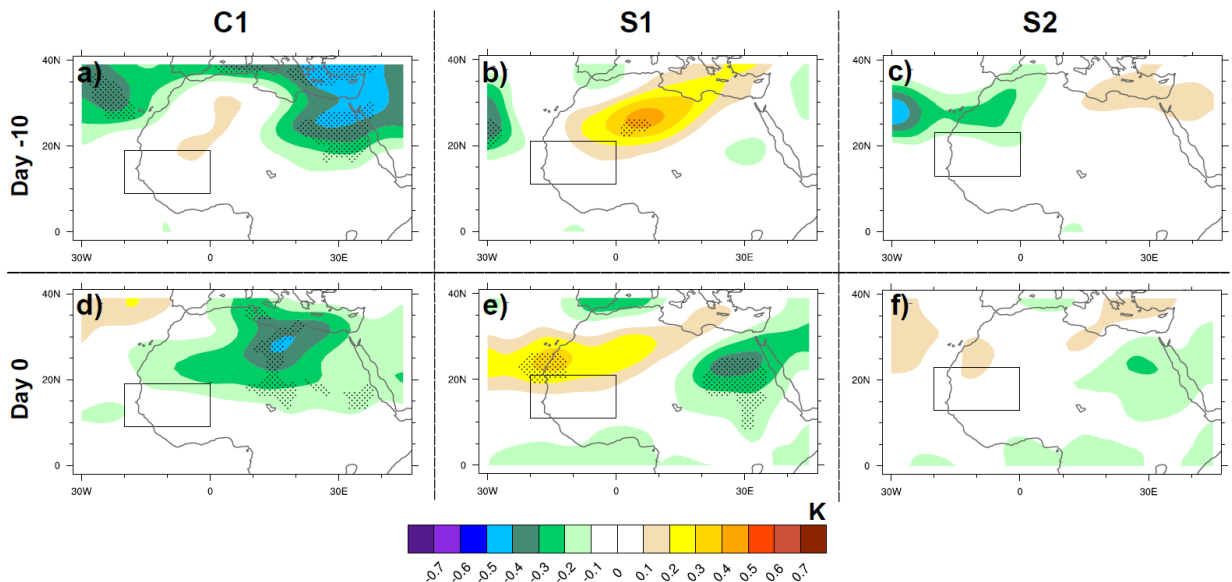


Fig 4.32 As in Fig. 2.22, except for 30-90-day 400 hPa temperature anomalies from three WRF-ARW experiments: a) C1 day -10, b) S1 day -10, c) S2 day -10, d) C1 day 0, e) S1 day 0, and f) S2 day 0. The shading interval is 0.3 m s^{-1} . Stippling represents significance at the 95% confidence level.

AEW activity and similarity of positive PKE events in all three WRF-ARW experiments, the reduction of static stability by 400 hPa T_{30-90} anomalies does not appear to be crucial for the production of ISV in the North African model domain.

4.8.3 Moisture Budget

In ERA-Interim, the intraseasonal variability of the moisture budget was governed by meridional moisture fluxes in East Africa (Alaka and Maloney 2012). Since tropical North Africa features a sharp meridional moisture gradient between the Sahara and the Gulf of Guinea, meridional fluxes regulate the available moisture on intraseasonal timescales. The vertically-integrated moisture budget was derived by Maloney et al. (2010) and is given by:

$$\langle \partial_t q \rangle = -\langle u \partial_x q \rangle - \langle v \partial_y q \rangle - \langle q \nabla \cdot \vec{v}_H \rangle + E - P - R \quad 4.1$$

where q is the specific humidity, E is the evaporation rate, P is the precipitation rate, and R is the residual. The brackets represent a vertical integral from the surface to 200 hPa.

The moisture budget does not appear to be regulated in a consistent and coherent manner by intraseasonal variability in the WRF-ARW model, unlike ERA-Interim results presented in Alaka and Maloney (2012). The vertically-integrated 30-90-day moisture tendency ($\langle \partial_t q \rangle_{30-90}$) reveals no direct relationship with East African moistening. In fact, positive $\langle \partial_t q \rangle_{30-90}$ anomalies are observed to propagate southeastward from the Northeast Atlantic, which might be related to a reduction in the Saharan air layer (Figs. 4.33a, 4.34a,d). Typically, the Northeast Atlantic is very dry in part due to intrusions of the Saharan air layer. However, a reduction in the strength of the Saharan air layer would allow moisture anomalies to build and would likely coincide with an enhanced phase of AEW activity, which is precisely what is observed. Future work will analyze the relationship between the Saharan air layer and AEW activity on

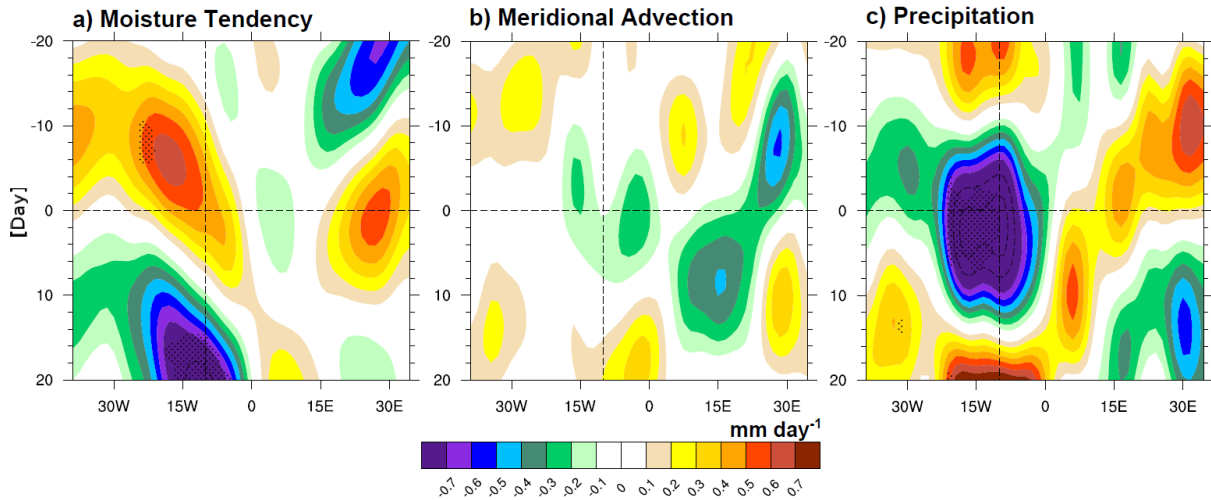


Fig 4.33 As in Fig. 2.21, vertically-integrated 30-90-day anomalies of the following moisture budget terms from the C1 simulation averaged over different latitudes: a) C1 (12.5°N-17.5°N), b) S1 (15.5°N-20.5°N), and c) S2 (18°N-23°N). The shading interval is 0.1 mm day^{-1} . Stippling represents significance at the 95% confidence level.

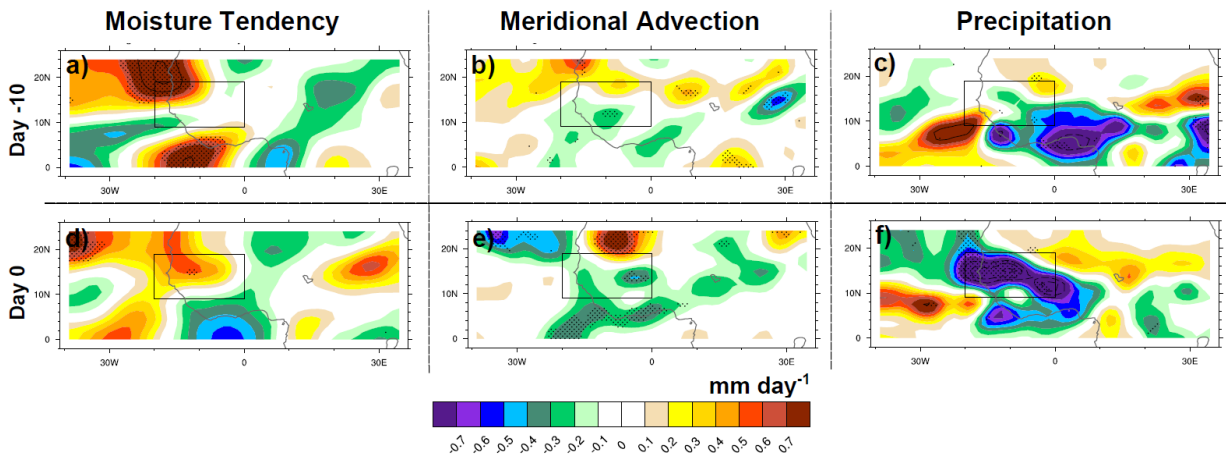


Fig 4.34 As in Fig. 2.22, except for vertically-integrated 30-90-day anomalies of the following moisture budget terms from the C1 simulation: a) moisture tendency day -10, b) meridional moisture advection day -10, c) precipitation day -10, d), moisture tendency day 0, e) meridional moisture advection day 0, and f) precipitation day 0. The shading interval is 0.1 mm day^{-1} . Stippling represents significance at the 95% confidence level.

intraseasonal timescales. Although meridional moisture advection is a vital trigger mechanism in ERA-Interim, it has no role in moistening East Africa prior to positive PKE events (Figs. 4.33b, 4.34b,e). Although 30-90-day precipitation anomalies propagate to the west-northwest (Figs. 4.34c,f), they appear to be acting without the aid of other moisture budget terms, which calls into question, once again, the accuracy of the Grell 3D cumulus parameterization output. While moisture budget terms are not shown for S1 and S2, they equally lack coherence. Although enhanced intraseasonal moisture advection and subsequent forcing of enhanced convection appears important for the generation of AEW precursors in ERA-Interim, the WRF-ARW experiments propose that it is not a necessary trigger of positive PKE events. These results are supported by the notion that East African heating does not help initiate periods of enhanced AEW activity in the WRF-ARW (Fig. 4.17d). However, if finite amplitude convective disturbances are of normal strength in East Africa, they could still play a vital role in seeding positive 30-90-day PKE events significant moisture budget and convective heating anomalies on these timescales.

For completeness, $\langle \partial_t q \rangle_{30-90}$ anomalies are analyzed over the course of an MJO life cycle (Fig. 4.35). While Alaka and Maloney 2012 found a bulls-eye of moistening in East Africa (see MJO phases 6-7 in their Fig. 12), no such signal exists in the C1 simulation. The weak moistening signal ($< 0.3 \text{ mm day}^{-1}$) does coincide with observed moistening in MJO phases 6-7. However, this simulated moistening is located between the Greenwich Meridian and Lake Chad, or $\sim 20^\circ$ further west than in ERA-Interim. The intraseasonal moistening signal is not well-simulated by the WRF-ARW model.

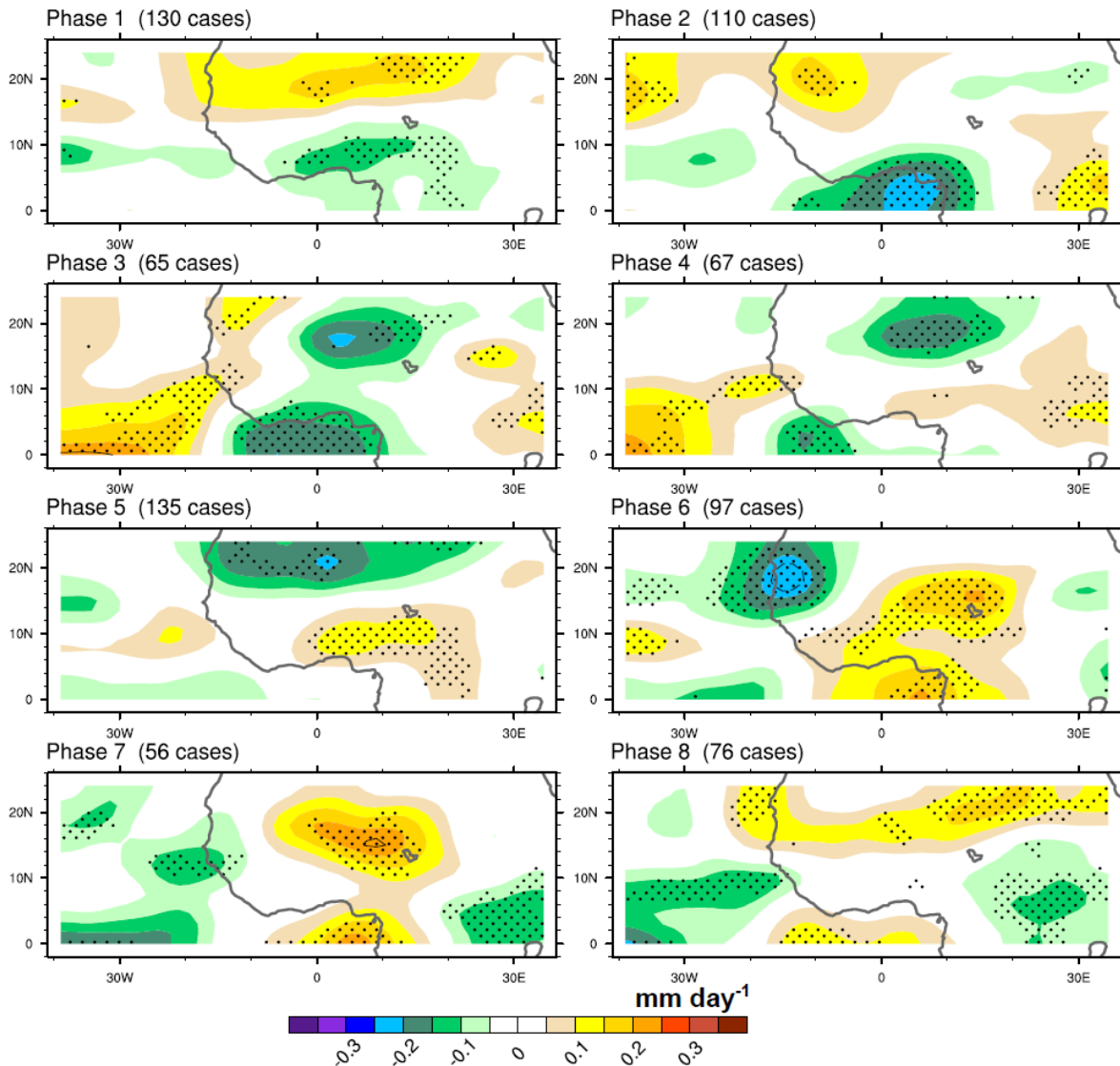


Fig 4.35 As in Fig. 2.28, except for vertically-integrated 30-90-day moisture tendency anomalies in the C1 simulation. The shading interval is 0.5 mm day^{-1} .

4.9 Discussion

In this chapter, the intraseasonal variability of AEW energetics is investigated with three 10-year WRF-ARW simulations. These three experiments (C1, S1, and S2) are identical except for the boundary conditions, in which 30-90-day variability is removed to varying extents to test the

importance of MJO forcing on ISV of AEWs in West Africa. In particular, the importance of MJO forcing is investigated for four critical PKE_{30-90} creation terms: barotropic energy conversion (B_T), baroclinic overturning (C_{pk}), baroclinic energy conversion (B_C), and the diabatic generation of PAPE (Q_T). The role of these AEW energetic terms in producing positive West African PKE events is a focal point of this study. In addition, the relationship between East and West Africa is examined through the simulation of AEW trigger mechanisms (e.g., Alaka and Maloney 2012).

The following conclusions may be gleaned from the regional climate modeling study described in this chapter:

- The WAM produces internal intraseasonal variability. In the absence of all 30-90-day variability in the boundary conditions, the S1 simulations exhibits AEW activity and variability that is consistent with C1 and reanalysis products.
- Reanalysis products (i.e., ERA-Interim, CFSR) exhibit a clear seasonal evolution of PKE events, with a minimum in June and a maximum in August. However, all three WRF-ARW simulations fail to reproduce this seasonal cycle of PKE events.
- Westward-propagating 30-90-day disturbances (e.g., equatorial Rossby waves) have little role in the amplitude and evolution of positive PKE events in the model. This is reflected by the similarity of the S1 and S2 simulations.
- Qualitatively, simulated B_T , B_C , and Q_T exhibit a similar evolution prior to positive PKE events as in ERA-Interim. However, baroclinic overturning destroys PKE on 30-90-day timescales due to $Q_T > B_C$. Q_T still acts as a negative feedback to B_C , which is weaker due to a reduced meridional temperature gradient in tropical North Africa.

- Consistent with ERA-Interim, the C1 simulation exhibits 30-90-day anomalies associated with the MJO index that are ~50% of the amplitude of 30-90-day anomalies associated with the local PKE index. However, collocation does not infer causality and the actual MJO influence in this region appears to be very weak.
- The MJO appears to be important for setting the timescale of ISV in West Africa. In the absence of MJO forcing, the timescale of intraseasonal oscillations appears to decrease, highlighting a preference for shorter periods without the guidance of large-scale phenomena.
- An extension of the AEJ prior to positive PKE events is a robust feature in reanalyses and model output. The AEJ extension can be an internally-forced mechanism that occurs in isolation from MJO forcing. The AEJ extension is associated with a sharpened surface temperature gradient, which indicates a stronger barotropic-baroclinic instability, and a potential role of the Saharan heat low.
- Static stability anomalies related to 400 hPa temperature anomalies are not associated with equatorial Rossby waves despite westward propagation through the domain. These static stability anomalies may instead be related to midlatitude wave-breaking and do not appear to be necessary for producing enhanced PKE in West Africa.
- The modeled vertically-integrated moisture budget shows no coherent variations on intraseasonal timescales in East Africa. Unlike in ERA-Interim, meridional moisture advection does not moisten or produce enhanced convection in East Africa prior to positive PKE events. Hence, enhanced convection in East Africa associated with a moisture mid-troposphere does not appear to be a necessary condition for positive PKE

events in the WRF-ARW. This may signal the growth of 30-90-day PKE anomalies from average convective precursors in East Africa instead of strong ones.

These modeling experiments reveal the complexity of the WAM region. The MJO is the dominant mode of intraseasonal variability in the tropics and previous studies have found evidence of MJO-induced equatorial waves propagating into tropical North Africa during boreal summer. However, the role of this MJO influence appears to be limited to pacing the ISV in West Africa. The common trigger found in all three WRF-ARW experiments is the extension of the AEJ into East Africa. This AEJ extension first appears ~10 days prior to positive PKE events in West Africa. It follows that the increased barotropic and baroclinic energy conversions help isolated, normal-amplitude convective disturbances grow upscale into synoptic-scale AEWs.

A major caveat of these WRF-ARW results is the inability to simulate an accurate PAPE response to diabatic heating anomalies in the upper-troposphere. Persistent diabatic heating within deep convection should increase PAPE when correlated with positive temperature anomalies. However, all three WRF-ARW experiments destroyed PAPE in the upper-troposphere due to poorly-simulated temperature anomalies. Future work will explore simulations with finer resolutions in which the convection parameterization is turned off, with the goal of using a grid spacing that will more realistically simulate deep convection and its interaction with the large-scale circulation.

CHAPTER 5 Conclusions

5.1 Main Findings

African easterly wave (AEW) activity exhibits significant intraseasonal variability in West Africa during boreal summer. In this study, AEW energetics are analyzed to understand the energy conversions that are vital to the initiation and maintenance of positive intraseasonal PKE events in West Africa. This documentation of the 30-90-day variability of AEW energetics is utilized to assess the extent to which the intraseasonal variability of AEW activity is modulated by the Madden-Julian oscillation (MJO). The relationship between the MJO and the West African monsoon has been examined in past studies (Matthews 2004; Maloney and Shaman 2008; Ventrice et al. 2011; Alaka and Maloney 2012). However, this study directly compares the local variability of AEW activity with large-scale 30-90-day variability associated with the MJO by examining the growth, maintenance, and decay of 700 hPa PKE_{30-90} anomalies across tropical North Africa. In particular, local intraseasonal variability is measured by a West African 700 hPa PKE_{30-90} index and the MJO is represented by an EOF-based circulation and convection index (e.g., Wheeler and Hendon 2004). Since the MJO phase and amplitude are quasi-predictable out to three weeks or more, high correlations between the MJO index and local AEW variability would add medium-range forecast skill to the prediction of Sahelian precipitation and potentially Atlantic tropical cyclogenesis. This study has three main parts: 1) examination of the intraseasonal variability of AEW energetics in observations, 2) investigation of WAM climatology using different dynamical cores and parameterizations in the WRF model, and 3) evaluation of intraseasonal variability of AEW energetics in the WRF-ARW model. The sensitivity tests described in Chapter 3 are used to define the combination of dynamical core and

parameterizations that reproduces realistic WAM climatology for use in Chapter 4. Therefore, the majority of the conclusions related to the intraseasonal variability of AEWs are gleaned from Chapters 2 and 4.

The primary conclusions from this dissertation may be summarized as follows:

- Barotropic and baroclinic energy conversions are crucial for the initiation, growth, and maintenance of 30-90-day PKE anomalies prior to positive PKE events in West Africa. These energy conversions are directly associated with an eastward shift of the Saharan heat low and a corresponding extension of the AEJ in East Africa ~10 days prior to positive PKE events.
- East African diabatic heating anomalies, which represent upstream AEW precursor disturbances, are “red” in nature in the 30-90-day band. Unlike the a priori hypothesis of this author, positive 30-90-day heating anomalies in East Africa are not a prerequisite of positive PKE events in West Africa.
- The MJO and AEW activity are related to one another, especially during boreal summers with strong MJO activity. However, the MJO only explains ~10% of the intraseasonal variance in West African AEW activity. The MJO is especially important for pacing the intraseasonal oscillation of AEWs through regular dry Kelvin wave activity near the equator.
- In the WRF-ARW model, AEW energetics are largely unaffected when all 30-90-day variability is removed from the boundary conditions (e.g., MJO), which indicates that the intraseasonal variability of AEWs is produced internally and/or the consequence of nonlinear interactions with external atmospheric phenomena.

In both model and reanalysis data, positive PKE events are initiated and maintained by barotropic and baroclinic energy conversions. In particular, East African B_C is enhanced in advance of West African PKE events by a sharpened meridional temperature gradient, which creates PKE in this region. In East Africa, a sharpened momentum gradient exists in the mid-troposphere due to the AEJ extension into this region, and, although ERA-Interim is inconclusive, B_T appears to be important for initiating positive PKE events in the WRF-ARW model. The meridional flux of momentum (temperature) by the perturbation (i.e., AEW) flow dominates the amplitude of B_T (B_C) in West Africa. In general, barotropic energy conversions reside near 700 hPa on the south side of the AEJ, while baroclinic energy conversions are observed near 900 hPa on the north side of the AEJ, which is consistent with previous studies (Lau and Lau 1992; Diedhiou et al. 2002; Hsieh and Cook 2007). Although this author expected a significant role for creation of PKE by the diabatic heating term (Q_T) due to strong latent heating within persistent deep convection, neither reanalysis data nor model output exhibited a significant, positive contribution from Q_T prior to positive PKE events. Instead, positive PKE events are likely initiated by East African convection that is red in nature and exhibits small 30-90-day anomalies. The primary function of Q_T is to act as a negative feedback to B_C in West Africa by destroying PAPE via the heating (cooling) or cool (warm) regions.

Although the MJO appears to be important for guiding the timescale of intraseasonal variability in West Africa, MJO forcing is not necessary to reproduce this local 30-90-day variability. Previous studies have shown strong evidence that the MJO significantly modulates winds, precipitation, and PKE in West Africa through MJO-induced equatorial Kelvin and equatorial Rossby waves propagating into this region. However, in the absence of MJO forcing in the WRF-ARW model, the WAM produces robust intraseasonal variability, which

diminishes the vitality of the MJO to the variability of AEWs. In reanalysis products, the MJO only explains ~10% of the intraseasonal variance of West African AEW activity (see Chapter 2). Although AEW energetics in the MJO index exhibit amplitudes that are up to 50% of those examined in the local PKE index, the low boreal summer correlation between the two indices highlights a weak relationship between the MJO and 30-90-day WAM variability. Modeling studies support this weak relationship, with PKE spectral power in the 30-90-day band of the same order in all three WRF-ARW experiments (C1, S1, S2). The S1 test, in which all 30-90-day variability is removed from the initial and lateral boundary conditions, still produces reobust 30-90-day variability in West Africa that is consistent with the C1 test despite no external forcing from the MJO (see Chapter 4). Independent of MJO, the AEJ extends into East Africa ~10 days prior to positive PKE events in West Africa. This AEJ extension is in thermal wind balance with a sharpened near-surface temperature gradient in East Africa, and may be related to intraseasonal oscillations of the Saharan heat low (e.g., Chauvin et al. 2010). The intraseasonal variability in West Africa exhibits a shorter timescale in the absence of MJO forcing. MJO forcing is important for pacing the timescale of 30-90-day AEW activity in West Africa, likely through recurrent dry Kelvin waves passing along the equator. On the other hand, the similarity of the S1 and S2 simulations emphasizes that, in at least the model, equatorial Rossby waves are not necessary to produce intraseasonal variability of AEW activity in tropical North Africa.

Finally, the success in using the 10-year WRF-ARW simulations to analyze intraseasonal variability is noted here. Overall, the WRF-ARW produces robust AEW activity and WAM climatology. Most importantly, the WRF-ARW generates significant intraseasonal variability in West Africa. Of course, with increasing computational power available and improving parameterizations, these simulations will only improve in their accuracy. In observation-starved

regions such as tropical North Africa, the WRF-ARW is a viable tool that can accurately simulate key atmospheric phenomena.

5.2 Outstanding Questions

One of the most pressing problems in this study is the inconsistent role of diabatic heating in AEW energetics between ERA-Interim and the model. Furthermore, diabatic heating in ERA-Interim should be interpreted with caution given that convection is mostly model-derived in data sparse regions. In general, the model-dependence of convection parameterizations are the largest uncertainty in the estimation of diabatic heating. Smaller errors may exist from the calculation of diabatic heating from the material derivative of dry static energy (e.g., Yanai et al. 1973), but this large-scale heating estimate has been successfully used in previous studies. One possibility is that East African diabatic heating does not exhibit significant 30-90-day fluctuations. Instead, East Africa might feature consistent daily convection that seeds stronger AEWs in the presence of enhanced 30-90-day barotropic and baroclinic energy conversions. Perhaps improved physics and finer grid spacing in future versions of the WRF-ARW will allow for the fruitful examination of diabatic heating within AEWs on intraseasonal timescales. For example, a grid spacing on the order of 1 km would allow the study of diabatic heating within explicit convection since convection parameterizations could be turned off.

There are two issues with the WRF-ARW simulations that are worth mentioning. First, future iterations of the filtering method will include a correction to improve the balance of geopotential field in the lateral boundary conditions. The strong barotropic easterly jet along the equator in the S1 and S2 simulations may be one consequence of an imbalanced mass field.

Second, upper-level 10-day high-pass temperature anomalies are inaccurate in the WRF-ARW simulations, which leads to opposite-sign values for Q_T and C_{pk} in the upper-troposphere. This could be an error with the heating tendencies that are generated by the cumulus parameterization. On the topic of parameterizations, different combinations will certainly produce different realizations of the WAM. Other parameterization combinations not tested in Chapter 3 might actually outperform the specific WRF-ARW setup used in this study, although time and computational power restricted the number of options that could be tested here.

Of course, there are other measures of MJO activity other than the Wheeler and Hendon (2004) index. These alternative indices might alter the conclusions drawn here. Considering that the MJO index utilized in this study might depend too strongly on the upper- and lower-tropospheric zonal winds, incorporating more information about the convective activity is a good first step. Straub (2013) provided a list of MJO indices found in the literature and analyzed the strengths and weaknesses of several. With a focus on convection in the Indo-Pacific region, the OLR-based MJO index (Kiladis et al. 2014) is a promising candidate.

5.3 Future Work

The analysis performed in this study has revealed several avenues for future research projects related to the intraseasonal variability of AEWs. The most obvious supplement to this analysis is a third sensitivity test that removes only large-scale westward-propagating 30-90-day activity. While the similarity of the S1 and S2 simulations implies a limited role for equatorial Rossby waves, this third sensitivity test would strengthen those conclusions. In addition, the robustness of the results presented in this study should be tested by swapping parameterizations and increasing the resolution to improve the simulation of Q_T and C_{pk} in the upper-troposphere.

If issues simulating the AEJ can be fixed in the WRF-NMM model, the analysis in Chapter 4 could be repeated with the different WRF dynamical core. Perhaps the improved representation of precipitation in WRF-NMM would help simulate a more realistic response to diabatic heating. Finally, calculating AEW energetics from other datasets and reanalyses (e.g., MERRA) would certainly increase the robustness of the observation-based results presented in Chapter 2.

Other topics that would be fruitful for future research are represented with the following questions:

- What is the relationship between midlatitude wave-breaking and AEW activity?
- The ITCZ represents an important moisture supply for AEWs emerging from West Africa. Does the ITCZ exhibit an intraseasonal signal that modulates the favorability for cyclogenesis in the East Atlantic?
- The Saharan heat low exhibits significant intraseasonal variability and is important for strengthening temperature and momentum gradients across tropical North Africa on 30-90-day timescales. Is this variability linked to the midlatitudes or the tropics?
- The Saharan air layer modulates the available moisture and instability in the East Atlantic and is often cited as an inhibitor of tropical cyclogenesis. Does the Saharan air layer exhibit significant intraseasonal variability that alters the favorability for cyclogenesis in the East Atlantic? Could this intraseasonal variability (if it exists) be related to oscillations of the Saharan heat low?
- In Chapter 4, this study explored how AEW activity in West Africa was altered in the absence of MJO forcing. The same question can be asked of tropical cyclogenesis in the East Atlantic. How does modeled tropical cyclogenesis relate to positive PKE events?

- How does modeled tropical cyclogenesis in the East Atlantic depend on the presence of MJO forcing in the boundary conditions?

5.4 Final Remarks

While this study primarily focuses on the intraseasonal variability of AEWs in West Africa, the downstream implications for tropical cyclogenesis in the East Atlantic are extremely valuable. The relationship between AEWs and tropical cyclogenesis is a complex one that is difficult to capture with large-scale dynamics alone. Based on the reliable HURDAT database, surges of West African AEW activity on intraseasonal timescales, like the one in August 2012 (see Chapter 1), are not always affiliated with a noticeable increase in East Atlantic cyclogenesis. Overall, countless observations of AEWs traversing the West African coastline have helped this author arrive at the following conclusion about the link between AEWs and tropical cyclones: stronger AEW activity in West Africa does not translate into a significant increase of tropical cyclogenesis in the East Atlantic, although it is certainly part of the recipe. Clearly, AEWs are necessary seed disturbances for most Atlantic tropical cyclones, especially in the East Atlantic. However, the strength of this seed is lost in the dominance of other environmental factors important for tropical cyclogenesis. These environmental conditions include, but are not limited to, sea surface temperatures, vertical wind shear, and mid-level moisture. As AEWs emerge from Africa, the low-level conditions change drastically. In particular, the sharp meridional temperature gradient is a strong contributor to the barotropic-baroclinic instability that drives AEWs. However, the amplitude of these energy conversions decreases quickly as AEWs propagate into the East Atlantic, which allows environmental conditions in the East Atlantic to determine the favorability for tropical cyclogenesis. The same ideology is true on intraseasonal

timescales. In addition to the environmental factors mentioned above, East Atlantic tropical cyclogenesis exhibits strong seasonality based on the latitude at which an AEW emerges from the African coast. In June, when the sun is directly over the Tropic of Cancer, AEWs are concentrated too far north in an environment of cooler sea-surface temperatures and a drier mid-troposphere. However, in August and September, the sun has progressed southward and AEWs are observed closer to the Gulf of Guinea coast, where the ocean heat content is abundant and ITCZ moisture is more accessible.

REFERENCES

- Abiodun, B. J., J. S. Pal, E. a. Afiesimama, W. J. Gutowski, and a. Adedoyin, 2007: Simulation of West African monsoon using RegCM3 Part II: impacts of deforestation and desertification. *Theor. Appl. Climatol.*, **93**, 245–261.
- Afiesimama, E. A., J. S. Pal, B. J. Abiodun, W. J. Gutowski, and A. Adedoyin, 2006: Simulation of West African monsoon using the RegCM3. Part I: Model validation and interannual variability. *Theor. Appl. Climatol.*, **86**, 23–37.
- Alaka Jr., G. J., 2010: Intraseasonal Variability of the West African Monsoon and African Easterly Waves During Boreal Summer. Colorado State University, 1-122.
- Alaka Jr., G. J., and E. D. Maloney, 2012: The Influence of the MJO on Upstream Precursors to African Easterly Waves. *J. Clim.*, **25**, 3219–3236.
- Alaka Jr., G. J., and E. D. Maloney, 2014: The Intraseasonal Variability of African Easterly Wave Energetics. *J. Clim.*, **27**, 6559–6580.
- Ali, A., A. Amani, A. Diedhiou, and T. Lebel, 2005: Rainfall estimation in the Sahel. Part II: Evaluation of rain gauge networks in the CILSS countries and objective intercomparison of rainfall products. *J. Appl. Meteorol.*, **44**, 1707–1722.
- Avila, L. A., 1991: Eastern North Pacific Hurricane Season of 1990. *Mon. Weather Rev.*, **119**, 2034–2046.
- Avila, L. A., and R. J. Pasch, 1992: Atlantic Tropical Systems of 1991. *Mon. Weather Rev.*, **120**, 2688–2696.
- Belanger, J. I., J. A. Curry, and P. J. Webster, 2010: Predictability of North Atlantic Tropical Cyclone Activity on Intraseasonal Time Scales. *Mon. Weather Rev.*, **138**, 4362–4374.

- Berry, G. J., and C. D. Thorncroft, 2012: African Easterly Wave Dynamics in a Mesoscale Numerical Model: The Upscale Role of Convection. *J. Atmos. Sci.*, **69**, 1267–1283.
- Bukovsky, M. S., 2012: Temperature Trends in the NARCCAP Regional Climate Models. *J. Clim.*, **25**, 3985–3991.
- Bukovsky, M. S., and D. J. Karoly, 2009: Precipitation Simulations Using WRF as a Nested Regional Climate Model. *J. Appl. Meteorol. Climatol.*, **48**, 2152–2159.
- Bukovsky, M. S., and D. J. Karoly, 2011: A Regional Modeling Study of Climate Change Impacts on Warm-Season Precipitation in the Central United States *. *J. Clim.*, **24**, 1985–2002.
- Burpee, R. W., 1972: The Origin and Structure of Easterly Waves in the Lower Troposphere of North Africa. *J. Atmos. Sci.*, **29**, 77–90.
- Burpee, R. W., 1974: Characteristics Of North African Easterly Waves During The Summers Of 1968 And 1969. *J. Atmos. Sci.*, **31**, 1556–1570.
- Carlson, T. N., 1969a: Some remarks on African disturbances and their progress over the tropical Atlantic. *Mon. Weather Rev.*, **97**, 716–726.
- Carlson, T. N., 1969b: Synoptic histories of three African disturbances that developed into Atlantic hurricanes. *Mon. Weather Rev.*, **97**, 256–276.
- Cassou, C., 2008: Intraseasonal interaction between the Madden-Julian Oscillation and the North Atlantic Oscillation. *Nature*, **455**, 523–527.
- Charney, J. G., and M. E. Stern, 1962: On the Stability of Internal Baroclinic Jets in a Rotating Atmosphere. *J. Atmos. Sci.*, **19**, 159–172.
- Chauvin, F., R. Roehrig, and J.-P. Lafore, 2010: Intraseasonal Variability of the Saharan Heat Low and Its Link with Midlatitudes. *J. Clim.*, **23**, 2544–2561.

- Chen, T.-C., and H. van Loon, 1987: Interannual variation of the tropical easterly jet. *Mon. Weather Rev.*, **115**, 1739–1759.
- Coëtlogon, G. De, S. Janicot, and A. Lazar, 2010: Intraseasonal variability of the ocean - atmosphere coupling in the Gulf of Guinea during boreal spring and summer. *Q. J. R. Meteorol. Soc.*, **136**, 426–441.
- Cook, K. H., and E. K. Vizy, 2013: Projected Changes in East African Rainy Seasons. *J. Clim.*, **26**, 5931–5948.
- Dee, D. P. and Coauthors, 2011: The ERA-Interim reanalysis: configuration and performance of the data assimilation system. *Q. J. R. Meteorol. Soc.*, **137**, 553–597.
- Diaz, M., and A. R. Aiyyer, 2013a: Energy Dispersion in African Easterly Waves. *J. Atmos. Sci.*, **70**, 130–145.
- Diaz, M., and A. R. Aiyyer, 2013b: The Genesis of African Easterly Waves by Upstream Development. *J. Atmos. Sci.*, **70**, 3492–3512.
- Dickinson, M., and J. Molinari, 2000: Climatology of Sign Reversals of the Meridional Potential Vorticity Gradient over Africa and Australia. *Mon. Weather Rev.*, **128**, 3890–3900.
- Dickinson, R. E., R. M. Errico, F. Giorgi, and G. T. Bates, 1989: A regional climate model for the western United States. *Clim. Change*, **15**, 383–422.
- Diedhiou, A., S. Janicot, A. Viltard, and P. De Felice, 1998: Evidence of two regimes of easterly waves over West Africa and the tropical Atlantic. *Geophys. Res. Lett.*, **25**, 2805–2808.
- Diedhiou, A., S. Janicot, A. Viltard, P. de Felice, and H. Laurent, 1999: Easterly wave regimes and associated convection over West Africa and tropical Atlantic: results from the NCEP/NCAR and ECMWF reanalyses. *Clim. Dyn.*, **15**, 795–822.

- Diedhiou, A., S. Janicot, A. Viltard, and P. de Félice, 2002: Energetics of easterly wave disturbances over West Africa and the tropical Atlantic: A climatology from the 1979–95 NCEP/NCAR reanalyses. *Clim. Dyn.*, **18**, 487–500.
- Druyan, L. M. and Coauthors, 2009: The WAMME regional model intercomparison study. *Clim. Dyn.*, **35**, 175–192.
- Eliassen, A., 1983: The Charney-Stern theorem on barotropic-baroclinic instability. *Pure Appl. Geophys.*, **121**, 563–572.
- Flaounas, E., S. Bastin, and S. Janicot, 2010: Regional climate modelling of the 2006 West African monsoon: sensitivity to convection and planetary boundary layer parameterisation using WRF. *Clim. Dyn.*, **36**, 1083–1105.
- Fuchs, Ž., and D. J. Raymond, 2007: A simple, vertically resolved model of tropical disturbances with a humidity closure. *Tellus A*, **59**, 344–354.
- Gray, W. M., 1998: The formation of tropical cyclones. *Meteorol. Atmos. Phys.*, **69**, 37–69.
- Grell, G. A., and D. Devenyi, 2002: A generalized approach to parameterizing convection combining ensemble and data assimilation techniques. *Geophys. Res. Lett.*, **29**, 10–13.
- Grell, G. A., J. Dudhia, and D. R. Stauffer, 1994: A description of the fifth-generation Penn State/NCAR mesoscale model (MM5). 1–128.
- Hall, J. D., A. J. Matthews, and D. J. Karoly, 2001: The modulation of tropical cyclone activity in the Australian region by the Madden-Julian Oscillation. *Mon. Weather Rev.*, **129**, 2970–2982.
- Hall, N. M. J., G. N. Kiladis, and C. D. Thorncroft, 2006: Three-dimensional structure and dynamics of African easterly waves. Part II: Dynamical modes. *J. Atmos. Sci.*, **63**, 2231–2245.

- Hayashi, S., K. Aranami, and K. Saito, 2008: Statistical Verification of Short Term NWP by NHM and WRF-ARW with 20 km Horizontal Resolution around Japan and Southeast Asia. *Sci. Online Lett. Atmos.*, **4**, 133–136.
- Heckley, W. A., and A. E. Gill, 1984: Some simple analytical solutions to the problem of forced equatorial long waves. *Q. J. R. Meteorol. Soc.*, **110**, 203–217.
- Hendon, H. H., and M. L. Salby, 1994: The Life Cycle of the Madden-Julian Oscillation. *J. Atmos. Sci.*, **51**, 2225–2237.
- Hong, S.-Y., and J.-O. J. Lim, 2006: The WRF single-moment 6-class microphysics scheme (WSM6). *J. Korean Meteor. Soc.*, **42**, 129–151.
- Hopsch, S. B., C. D. Thorncroft, K. Hodges, and A. R. Aiyyer, 2007: West African Storm Tracks and Their Relationship to Atlantic Tropical Cyclones. *J. Clim.*, **20**, 2468–2483.
- Hopsch, S. B., C. D. Thorncroft, and K. R. Tyle, 2010: Analysis of African Easterly Wave Structures and Their Role in Influencing Tropical Cyclogenesis. *Mon. Weather Rev.*, **138**, 1399–1419.
- Hoskins, B. J., M. E. McIntyre, and A. W. Robertson, 1985: On the use and significance of isentropic potential vorticity maps. *Q. J. R. Meteorol. Soc.*, **111**, 877–946.
- Hsieh, J.-S., and K. H. Cook, 2005: Generation of African Easterly Wave Disturbances: Relationship to the African Easterly Jet. *Mon. Weather Rev.*, **133**, 1311–1327.
- Hsieh, J.-S., and K. H. Cook, 2007: A Study of the Energetics of African Easterly Waves Using a Regional Climate Model. *J. Atmos. Sci.*, **64**, 421–440.
- Hsieh, J.-S., and K. H. Cook, 2008: On the Instability of the African Easterly Jet and the Generation of African Waves: Reversals of the Potential Vorticity Gradient. *J. Atmos. Sci.*, **65**, 2130–2151.

- Janicot, S., F. Mounier, N. M. J. Hall, S. Leroux, B. Sultan, and G. N. Kiladis, 2009: Dynamics of the West African Monsoon. Part IV: Analysis of 25–90-Day Variability of Convection and the Role of the Indian Monsoon. *J. Clim.*, **22**, 1541–1565.
- Janicot, S. and Coauthors, 2011: Intraseasonal variability of the West African monsoon. *Atmos. Sci. Lett.*, **12**, 58–66.
- Janjic, Z. I., 1994: The step-mountain eta coordinate model: Further developments of the convection, viscous sublayer, and turbulence closure schemes. *Mon. Weather Rev.*, **122**, 927–945.
- Janjic, Z. I., J. P. Gerrity Jr., and S. Nickovic, 2001: An alternative approach to nonhydrostatic modeling. *Mon. Weather Rev.*, **129**, 1164–1178.
- Johnson, R. H., and P. E. Ciesielski, 2013: Structure and Properties of Madden–Julian Oscillations Deduced from DYNAMO Sounding Arrays. *J. Atmos. Sci.*, **70**, 3157–3179.
- Kiladis, G. N., C. D. Thorncroft, and N. M. J. Hall, 2006: Three-Dimensional Structure and Dynamics of African Easterly Waves. Part I: Observations. *J. Atmos. Sci.*, **63**, 2212–2230.
- Kiladis, G. N., J. Dias, K. H. Straub, M. C. Wheeler, S. N. Tulich, K. Kikuchi, K. M. Weickmann, and M. J. Ventrice, 2014: A Comparison of OLR and Circulation-Based Indices for Tracking the MJO. *Mon. Weather Rev.*, **142**, 1697–1715.
- Lafore, J.-P., C. Flamant, V. Giraud, F. Guichard, P. Knippertz, J.-F. Mahfouf, P. Mascart, and E. R. Williams, 2010: Introduction to the AMMA Special Issue on “Advances in understanding atmospheric processes over West Africa through the AMMA field campaign.” *Q. J. R. Meteorol. Soc.*, **136**, 2–7.

- Landsea, C. W., G. D. Bell, W. M. Gray, and S. B. Goldenberg, 1998: The extremely active 1995 Atlantic hurricane season: Environmental conditions and verification of seasonal forecasts. *Mon. Weather Rev.*, **126**, 1174–1193.
- Landsea, C. W., R. A. Pielke Jr., A. M. Mestas-Nunez, and J. A. Knaff, 1999: Atlantic Basin Hurricanes: Indices of Climatic Changes. *Clim. Change*, **42**, 89–129.
- Lau, K.-H., and N.-C. Lau, 1992: The Energetics and Propagation Dynamics of Tropical Summertime Synoptic-Scale Disturbances. *Mon. Weather Rev.*, **120**, 2523–2539.
- Lavaysse, C., C. Flamant, S. Janicot, D. J. Parker, J.-P. Lafore, B. Sultan, and J. Pelon, 2009: Seasonal evolution of the West African heat low: a climatological perspective. *Clim. Dyn.*, **33**, 313–330.
- Lavaysse, C., C. Flamant, S. Janicot, and P. Knippertz, 2010: Links between African easterly waves, midlatitude circulation and intraseasonal pulsations of the West African heat low. *Q. J. R. Meteorol. Soc.*, **136**, 141–158.
- Leroux, S., and N. M. J. Hall, 2009: On the Relationship between African Easterly Waves and the African Easterly Jet. *J. Atmos. Sci.*, **66**, 2303–2316.
- Leroux, S., N. M. J. Hall, and G. N. Kiladis, 2010: A climatological study of transient-mean-flow interactions over West Africa. *Q. J. R. Meteorol. Soc.*, **136**, 397–410.
- Lin, H., G. Brunet, and J. Derome, 2009: An Observed Connection between the North Atlantic Oscillation and the Madden–Julian Oscillation. *J. Clim.*, **22**, 364–380.
- Lorenz, E. N., 1955: Available potential energy and the maintenance of the general circulation. *Tellus*, **7**, 157–167.
- Madden, R. A., and P. R. Julian, 1971: Detection of a 40-50 day oscillation in the zonal wind in the tropical Pacific. *J. Atmos. Sci.*, **28**, 702–708.

- Madden, R. A., and P. R. Julian, 1972: Description of global-scale circulation cells in the tropics with a 40-50 day period. *J. Atmos. Sci.*, **29**, 1109–1123.
- Madden, R. A., and P. R. Julian, 1994: Observations of the 40–50-Day Tropical Oscillation—A Review. *Mon. Weather Rev.*, **122**, 814–837.
- Maloney, E. D., and D. L. Hartmann, 2000a: Modulation of eastern North Pacific hurricanes by the Madden-Julian oscillation. *J. Clim.*, **13**, 1451–1460.
- Maloney, E. D., and D. L. Hartmann, 2000b: Modulation of Hurricane Activity in the Gulf of Mexico by the Madden-Julian Oscillation. *Science (80-.)*, **287**, 2002–2004.
- Maloney, E. D., and D. L. Hartmann, 2001a: The Madden-Julian oscillation, barotropic dynamics, and North Pacific tropical cyclone formation. Part I: Observations. *J. Atmos. Sci.*, **58**, 2545–2558.
- Maloney, E. D., and D. L. Hartmann, 2001b: The sensitivity of intraseasonal variability in the NCAR CCM3 to changes in convective parameterization. *J. Clim.*, **14**, 2015–2034.
- Maloney, E. D., and M. J. Dickinson, 2003: The intraseasonal oscillation and the energetics of summertime tropical western North Pacific synoptic-scale disturbances. *J. Atmos. Sci.*, **60**, 2153–2168.
- Maloney, E. D., and S. K. Esbensen, 2003: The amplification of east Pacific Madden-Julian oscillation convection and wind anomalies during June–November. *J. Clim.*, **16**, 3482–3497.
- Maloney, E. D., and J. Shaman, 2008: Intraseasonal Variability of the West African Monsoon and Atlantic ITCZ. *J. Clim.*, **21**, 2898–2918.
- Maloney, E. D., A. H. Sobel, and W. M. Hannah, 2010: Intraseasonal variability in an aquaplanet general circulation model. *J. Adv. Model. Earth Syst.*, **2**, 1–22.

- Mapes, B. E., and J. T. Bacmeister, 2012: Diagnosis of Tropical Biases and the MJO from Patterns in the MERRA Analysis Tendency Fields. *J. Clim.*, **25**, 6202–6214.
- Marsham, J. H., P. Knippertz, N. S. Dixon, D. J. Parker, and G. M. S. Lister, 2011: The importance of the representation of deep convection for modeled dust-generating winds over West Africa during summer. *Geophys. Res. Lett.*, **38**, 1–6.
- Matsuno, T., 1966: Quasi-Geostrophic Motions in the Equatorial Area. *J. Meteorol. Soc. Japan*, **44**, 25–43.
- Matthews, A. J., 2004: Intraseasonal Variability over Tropical Africa during Northern Summer. *J. Clim.*, **17**, 2427–2440.
- Matthews, A. J., 2008: Primary and successive events in the Madden–Julian oscillation. *Q. J. R. Meteorol. Soc.*, **453**, 439–453.
- Mekonnen, A., C. D. Thorncroft, and A. R. Aiyyer, 2006: Analysis of convection and its association with African easterly waves. *J. Clim.*, **19**, 5405–5421.
- Monin, A. S., and A. M. Obukhov, 1954: Basic laws of turbulent mixing in the surface layer of the atmosphere. *Contrib. Geophys. Inst. Acad. Sci. USSR*, **151**, 163–187.
- Mounier, F., S. Janicot, and G. N. Kiladis, 2008: The West African Monsoon Dynamics. Part III: The Quasi-Biweekly Zonal Dipole. *J. Clim.*, **21**, 1911–1928.
- Nicholson, S. E., 2013: The West African Sahel : A Review of Recent Studies on the Rainfall Regime and Its Interannual Variability. *ISRN Meteorol.*, 1–32.
- Noble, E., L. M. Druyan, and M. Fulakeza, 2014: The Sensitivity of WRF Daily Summertime Simulations over West Africa to Alternative Parameterizations. Part I: African Wave Circulation. *Mon. Weather Rev.*, **142**, 1588–1608.

- Norquist, D. C., E. E. Recker, and R. J. Reed, 1977: The energetics of African wave disturbances as observed during phase III of GATE. *Mon. Weather Rev.*, **105**, 334–342.
- Paeth, H., K. Born, R. Podzun, and D. Jacob, 2005: Regional dynamical downscaling over West Africa: model evaluation and comparison of wet and dry years. *Meteorol. Zeitschrift*, **14**, 349–367.
- Pal, J. S. and Coauthors, 2007: Regional Climate Modeling for the Developing World: The ICTP RegCM3 and RegCNET. *Bull. Am. Meteorol. Soc.*, **88**, 1395–1409.
- Pielke Jr, R. A., J. Gratz, C. W. Landsea, D. Collins, M. A. Saunders, and R. Musulin, 2008: Normalized Hurricane Damage in the United States: 1900 – 2005. *Nat. Hazards Rev.*, **9**, 29–42.
- Pielke, R. A. and Coauthors, 1992: A Comprehensive Meteorological Modeling System- RAMS. *Meteorol. Atmos. Phys.*, **91**, 69–91.
- Poan, D. E., R. Roehrig, F. Couvreux, and J.-P. Lafore, 2013: West African Monsoon Intraseasonal Variability: A Precipitable Water Perspective. *J. Atmos. Sci.*, **70**, 1035–1052.
- Pohl, B., S. Janicot, B. Fontaine, and R. Marteau, 2009: Implication of the Madden–Julian Oscillation in the 40-Day Variability of the West African Monsoon. *J. Clim.*, **22**, 3769–3785.
- Pytharoulis, I., and C. Thorncroft, 1999: The low-level structure of African easterly waves in 1995. *Mon. Weather Rev.*, **127**, 2266–2280.
- Reed, R. J., and E. E. Recker, 1971: Structure and properties of synoptic-scale wave disturbances in the equatorial western Pacific. *J. Atmos. Sci.*, **28**, 1117–1133.

- Reed, R. J., D. C. Norquist, and E. E. Recker, 1977: The structure and properties of African wave disturbances as observed during Phase III of GATE. *Mon. Weather Rev.*, **105**, 317–333.
- Reed, R. J., E. Klinker, and A. Hollingsworth, 1988: Meteorology and Atmospheric Physics The Structure and Characteristics of African Easterly Wave Disturbances as Determined from the ECMWF Operational Analysis / Forecast System. *Meteorol. Atmos. Phys.*, **38**, 22–33.
- Rennick, M. A., 1976: Generation of African Waves. *J. Atmos. Sci.*, **33**, 1955–1969.
- Rienecker, M. M. and Coauthors, 2011: MERRA: NASA’s Modern-Era Retrospective Analysis for Research and Applications. *J. Clim.*, **24**, 3624–3648.
- Rogers, E., T. Black, B. Ferrier, Y. Lin, D. Parrish, and G. DiMego, 2001: NCEP Meso Eta Analysis and Forecast System: Increase in resolution, new cloud microphysics, modified precipitation assimilation, modified 3DVAR analysis. *NWS Tech. Proced. Bull.*, **488**, 1–15.
- Ross, R. S., T. N. Krishnamurti, and S. Pattnaik, 2012: Interactions of Diabatic Heating in Convective Superbursts with Energy Conversion Processes in the Genesis of Cape Verde Hurricanes from African Easterly Waves. *Mon. Weather Rev.*, **140**, 748–773.
- Roundy, P. E., 2008: Analysis of Convectively Coupled Kelvin Waves in the Indian Ocean MJO. *J. Atmos. Sci.*, **65**, 1342–1359.
- Routray, A., U. C. Mohanty, D. Niyogi, S. R. H. Rizvi, and K. K. Osuri, 2009: Simulation of heavy rainfall events over Indian monsoon region using WRF-3DVAR data assimilation system. *Meteorol. Atmos. Phys.*, **106**, 107–125.
- Rydbeck, A. V., and E. D. Maloney, 2014: Energetics of East Pacific Easterly Waves during Intraseasonal Events. *J. Clim.*, in press.

- Rydbeck, A. V., E. D. Maloney, S.-P. Xie, J. Hafner, and J. Shaman, 2013: Remote Forcing versus Local Feedback of East Pacific Intraseasonal Variability during Boreal Summer. *J. Clim.*, **26**, 3575–3596.
- Saha, S. and Coauthors, 2010: The NCEP Climate Forecast System Reanalysis. *Bull. Am. Meteorol. Soc.*, **91**, 1015–1057.
- Sahany, S., J. D. Neelin, K. Hales, and R. B. Neale, 2012: Temperature–Moisture Dependence of the Deep Convective Transition as a Constraint on Entrainment in Climate Models. *J. Atmos. Sci.*, **69**, 1340–1358.
- Schubert, W. H., P. E. Ciesielski, D. E. Stevens, and H.-C. Kuo, 1991: Potential vorticity modeling of the ITCZ and the Hadley circulation. *J. ...*, **48**, 1493–1509.
- Skamarock, W. C., and J. B. Klemp, 2008: A time-split nonhydrostatic atmospheric model for weather research and forecasting applications. *J. Comput. Phys.*, **227**, 3465–3485.
- Skamarock, W. C., J. B. Klemp, M. G. Duda, L. D. Fowler, S.-H. Park, and T. D. Ringler, 2012: A Multiscale Nonhydrostatic Atmospheric Model Using Centroidal Voronoi Tesselations and C-Grid Staggering. *Mon. Weather Rev.*, **140**, 3090–3105.
- Slade, S. A., and E. D. Maloney, 2013: An Intraseasonal Prediction Model of Atlantic and East Pacific Tropical Cyclone Genesis. *Mon. Weather Rev.*, **141**, 1925–1942.
- Smirnova, T. G., J. M. Brown, S. G. Benjamin, and D. Kim, 2000: Parameterization of cold-season processes in the MAPS land-surface scheme. *J. Geophys. ...*, **105**, 4077–4086.
- Sobel, A., and E. Maloney, 2013: Moisture Modes and the Eastward Propagation of the MJO. *J. Atmos. Sci.*, **70**, 187–192.
- Sobel, A. H., J. Nilsson, and L. M. Polvani, 2001: The Weak Temperature Gradient Approximation and Balanced Tropical Moisture Waves. *J. Atmos. Sci.*, **58**, 3650–3665.

- Straub, K. H., 2013: MJO Initiation in the Real-Time Multivariate MJO Index. *J. Clim.*, **26**, 1130–1151.
- Straub, K. H., and G. N. Kiladis, 2002: Observations of a convectively coupled Kelvin wave in the eastern Pacific ITCZ. *J. Atmos. Sci.*, **59**, 30–53.
- Straub, K. H., and G. N. Kiladis, 2003: The observed structure of convectively coupled Kelvin waves: Comparison with simple models of coupled wave instability. *J. Atmos. Sci.*, **60**, 1655–1668.
- Sugiyama, M., 2009a: The Moisture Mode in the Quasi-Equilibrium Tropical Circulation Model. Part I: Analysis Based on the Weak Temperature Gradient Approximation. *J. Atmos. Sci.*, **66**, 1507–1523.
- Sugiyama, M., 2009b: The Moisture Mode in the Quasi-Equilibrium Tropical Circulation Model. Part II: Nonlinear Behavior on an Equatorial β Plane. *J. Atmos. Sci.*, **66**, 1525–1542.
- Sultan, B., and S. Janicot, 2003: The West African monsoon dynamics. Part II: The “preonset” and “onset” of the summer monsoon. *J. Clim.*, **16**, 3407–3427.
- Sultan, B., S. Janicot, and A. Diedhiou, 2003: The West African monsoon dynamics. Part I: Documentation of intraseasonal variability. *J. Clim.*, **16**, 3389–3406.
- Sultan, B., C. Baron, M. Dingkuhn, B. Sarr, and S. Janicot, 2005: Agricultural impacts of large-scale variability of the West African monsoon. *Agric. For. Meteorol.*, **128**, 93–110.
- Sylla, M. B., E. Coppola, L. Mariotti, F. Giorgi, P. M. Ruti, a. Dell’Aquila, and X. Bi, 2009: Multiyear simulation of the African climate using a regional climate model (RegCM3) with the high resolution ERA-interim reanalysis. *Clim. Dyn.*, **35**, 231–247.
- Sylla, M. B., I. Diallo, and J. S. Pal, 2013: West African Monsoon in State-of-the-Science Regional Climate Models. *Climate Variability - Regional and Thematic Patterns*, 3–36.

- Thompson, D. B., and P. E. Roundy, 2013: The Relationship between the Madden–Julian Oscillation and U.S. Violent Tornado Outbreaks in the Spring. *Mon. Weather Rev.*, **141**, 2087–2095.
- Thompson, G., P. R. Field, R. M. Rasmussen, and W. D. Hall, 2008: Explicit Forecasts of Winter Precipitation Using an Improved Bulk Microphysics Scheme. Part II: Implementation of a New Snow Parameterization. *Mon. Weather Rev.*, **136**, 5095–5115.
- Thorncroft, C. D., and B. J. Hoskins, 1994a: An idealized study of African easterly waves. I: A linear view. *Q. J. R. Meteorol. Soc.*, **120**, 953–982.
- Thorncroft, C. D., and B. J. Hoskins, 1994b: An idealized study of African easterly waves. II: A nonlinear view. *Q. J. R. Meteorol. Soc.*, **120**, 983–1015.
- Thorncroft, C. D., and K. Hodges, 2001: African easterly wave variability and its relationship to Atlantic tropical cyclone activity. *J. Clim.*, **14**, 1166–1179.
- Thorncroft, C. D., N. M. J. Hall, and G. N. Kiladis, 2008: Three-Dimensional Structure and Dynamics of African Easterly Waves. Part III: Genesis. *J. Atmos. Sci.*, **65**, 3596–3607.
- Tian, Y., C. D. Peters-Lidard, B. J. Choudhury, and M. Garcia, 2007: Multitemporal Analysis of TRMM-Based Satellite Precipitation Products for Land Data Assimilation Applications. *J. Hydrometeorol.*, **8**, 1165–1183.
- Torn, R. D., 2010: Ensemble-Based Sensitivity Analysis Applied to African Easterly Waves. *Weather Forecast.*, **25**, 61–78.
- Ventrice, M. J., and C. D. Thorncroft, 2013: The Role of Convectively Coupled Atmospheric Kelvin Waves on African Easterly Wave Activity. *Mon. Weather Rev.*, **141**, 1910–1924.

- Ventrice, M. J., C. D. Thorncroft, and P. E. Roundy, 2011: The Madden–Julian Oscillation’s Influence on African Easterly Waves and Downstream Tropical Cyclogenesis. *Mon. Weather Rev.*, **139**, 2704–2722.
- Ventrice, M. J., C. D. Thorncroft, and C. J. Schreck III, 2012: Impacts of Convectively Coupled Kelvin Waves on Environmental Conditions for Atlantic Tropical Cyclogenesis. *Mon. Weather Rev.*, **140**, 2198–2214.
- Vitart, F., 2009: Impact of the Madden Julian Oscillation on tropical storms and risk of landfall in the ECMWF forecast system. *Geophys. Res. Lett.*, **36**, 1–6.
- Vitart, F., and F. Molteni, 2010: Simulation of the Madden– Julian Oscillation and its teleconnections in the ECMWF forecast system. *Q. J. R. Meteorol. Soc.*, **136**, 842–855.
- Vizy, E. K., and K. H. Cook, 2002: Development and application of a mesoscale climate model for the tropics: Influence of sea surface temperature anomalies on the West African monsoon. *J. Geophys. Res.*, **107**, 1–22.
- Waliser, D. and Coauthors, 2006: The Experimental MJO Prediction Project. *Bull. Am. Meteorol. Soc.*, **87**, 425–431.
- Walker, G. T., 1924: Correlation In Seasonal Variations Of Weather IX - A Further Study of World Weather. *Mem. India Meteorol. Dep.*, **24**, 275–333.
- Walko, R. L., and R. Avissar, 2008a: The Ocean–Land–Atmosphere Model (OLAM). Part I: Shallow-Water Tests. *Mon. Weather Rev.*, **136**, 4033–4044.
- Walko, R. L., and R. Avissar, 2008b: The Ocean–Land–Atmosphere Model (OLAM). Part II: Formulation and Tests of the Nonhydrostatic Dynamic Core. *Mon. Weather Rev.*, **136**, 4045–4062.

- Wang, Z., T. J. Dunkerton, and M. T. Montgomery, 2012: Application of the Marsupial Paradigm to Tropical Cyclone Formation from Northwestward-Propagating Disturbances. *Mon. Weather Rev.*, **140**, 66–76.
- Wheeler, M., and G. N. Kiladis, 1999: Convectively Coupled Equatorial Waves: Analysis of Clouds and Temperature in the Wavenumber–Frequency Domain. *J. Atmos. Sci.*, **56**, 374–399.
- Wheeler, M., G. N. Kiladis, and P. J. Webster, 2000: Large-scale dynamical fields associated with convectively coupled equatorial waves. *J. Atmos. Sci.*, **57**, 613–640.
- Wheeler, M. C., and H. H. Hendon, 2004: An All-Season Real-Time Multivariate MJO Index: Development of an Index for Monitoring and Prediction. *Mon. Weather Rev.*, **132**, 1917–1932.
- Wolters, D., C. C. van Heerwaarden, J. V.-G. de Arellano, B. Cappelaere, and D. Ramier, 2010: Effects of soil moisture gradients on the path and the intensity of a West African squall line. *Q. J. R. Meteorol. Soc.*, **136**, 2162–2175.
- Wu, M.-L. C., O. Reale, and S. D. Schubert, 2013: A characterization of African Easterly Waves on 2.5–6 day and 6–9 day time scales. *J. Clim.*, 6750–6774.
- Xu, J., S. Rugg, L. Byerle, and Z. Liu, 2009: Weather Forecasts by the WRF-ARW Model with the GSI Data Assimilation System in the Complex Terrain Areas of Southwest Asia. *Weather Forecast.*, **24**, 987–1008.
- Xue, Y., Z. Janjic, J. Dudhia, R. Vasic, and F. De Sales, 2014: A review on regional dynamical downscaling in intraseasonal to seasonal simulation/prediction and major factors that affect downscaling ability. *Atmos. Res.*, **147–148**, 68–85.

- Yanai, M., S. Esbensen, and J.-H. Chu, 1973: Determination of Bulk Properties of Tropical Cloud Clusters from Large-Scale Heat and Moisture Budgets. *J. Atmos. Sci.*, **30**, 611–627.
- Yoneyama, K., C. Zhang, and C. N. Long, 2013: Tracking Pulses of the Madden–Julian Oscillation. *Bull. Am. Meteorol. Soc.*, **94**, 1871–1891.
- Zawislak, J., and E. J. Zipser, 2010: Observations of Seven African Easterly Waves in the East Atlantic during 2006. *J. Atmos. Sci.*, **67**, 26–43.
- Zhang, C., 2005: Madden-Julian Oscillation. *Rev. Geophys.*, **43**, 1–36.
- Zhang, C., J. Gottschalck, E. D. Maloney, M. W. Moncrieff, F. Vitart, D. E. Waliser, B. Wang, and M. C. Wheeler, 2013: Cracking the MJO nut. *Geophys. Res. Lett.*, **40**, 1223–1230.

APPENDIX A Definitions for Perturbation Kinetic Energy and Perturbation Available Potential Energy Budget Terms

All budget terms are represented so that positive values increase the perturbation kinetic energy (PKE) or the perturbation available potential energy (PAPE). The definitions of PKE and PAPE conversion terms are as follows:

$$PKE_p = \frac{\overline{u'^2 + v'^2}}{2} \quad (\text{A.1})$$

$$A_M = -\bar{\vec{v}} \cdot \nabla \overline{PKE} \quad (\text{A.2})$$

$$A_P = -\bar{\vec{v}'} \cdot \nabla \overline{PKE_p} \quad (\text{A.3})$$

$$A_{TOT} = A_M + A_P \quad (\text{A.4})$$

$$B_T = -[\bar{\vec{v}'_H} \cdot (\bar{\vec{v}'} \cdot \nabla) \bar{\vec{v}_H}] \quad (\text{A.5})$$

$$\phi_{FC} = -\nabla \cdot (\bar{\vec{v}'} \phi') \quad (\text{A.6})$$

$$C_{pk} = -\frac{R}{p} \overline{\omega' T'} \quad (\text{A.7})$$

$$Q_T = \frac{\gamma}{T} \overline{T' Q'_1} \quad (\text{A.8})$$

$$B_C = -\frac{\gamma c_p}{T} \bar{\vec{v}'} \bar{T'} \cdot \nabla \bar{T} \quad (\text{A.9})$$

$$B_{T1} = -\overline{\bar{u}' \bar{v}'}_{30-90} \frac{\partial \bar{u}}{\partial y} \quad (\text{A.10})$$

$$B_{T2} = -\overline{\bar{u}' \bar{v}'}_{30-90} \frac{\partial \bar{u}}{\partial y} \quad (\text{A.11})$$

$$B_{C1} = -\frac{\gamma c_p}{T} \bar{v}' \bar{T'}_{30-90} \frac{\partial \bar{T}}{\partial y} \quad (\text{A.12})$$

$$B_{C2} = -\frac{\gamma c_p}{T} \bar{v}' \bar{T'}_{30-90} \frac{\partial \bar{T}}{\partial y} \quad (\text{A.13})$$

- v : 3-dimensional wind [m s^{-1} or Pa s^{-1}]
 v_H : horizontal wind [m s^{-1}]
 ω : pressure velocity [Pa s^{-1}]
 T : Air temperature [K]
 ϕ : geopotential height [$\text{m}^2 \text{s}^{-2}$]
 p : air pressure [Pa]
 Q_1 : apparent heat source [$\text{m}^2 \text{s}^{-3}$]
 R : specific gas constant for dry air = 287.058 [$\text{J kg}^{-1} \text{K}^{-1}$]
 c_p : specific heat at constant pressure = 1004 [$\text{J kg}^{-1} \text{K}^{-1}$]
 g : gravitational acceleration = 9.81 [m s^{-2}]
 ∇ : 3-dimensional gradient operator [m^{-1} or Pa^{-1}]
 γ : inverted static stability = $\frac{\Gamma_d}{\Gamma_a - \Gamma}$
 Γ_d : dry adiabatic lapse rate = $\frac{g}{c_p}$ [K m^{-1}]
 Γ : environmental lapse rate = $\partial_z \bar{T}$ [K m^{-1}]
 D : PKE dissipation [$\text{m}^2 \text{s}^{-3}$]
 R : PAPE residual [$\text{m}^2 \text{s}^{-3}$]

Taking into account the definitions from A.1-A.9, the PKE (1) and PAPE (2) budgets are given in their entirety below:

$$\begin{aligned} \partial_t PKE &= -\bar{\vec{v}} \cdot \nabla PKE - \overline{\vec{v}' \cdot \nabla PKE_p} - \overline{[\vec{v}'_H \cdot (\vec{v}' \cdot \nabla) \bar{\vec{v}}_H]} \\ &\quad - \nabla \cdot (\bar{\vec{v}' \phi'}) - \frac{R}{p} \overline{\omega' T'} - D \end{aligned} \quad (\text{A.14})$$

$$\partial_t PAPE = \frac{\gamma}{T} \overline{T' Q_1'} - \frac{\gamma c_p}{T} \overline{\vec{v}' T'} \cdot \nabla \bar{T} + \frac{R}{p} \overline{\omega' T'} + R \quad (\text{A.15})$$

In the definitions described above, \bar{X} and X' represent the 11-day running mean and deviations from the 11-day running mean, respectively. To represent boreal summer averages, $\bar{\bar{X}}$

is used. Throughout the text, vertical averages will be denoted by X and subscripts will share information about temporal filtering in the form of X_{30-90} . Vertical averages are calculated by averaging values in the vertical dimension and normalizing by the difference between the upper troposphere (defined as 200 hPa) and the surface.

APPENDIX B The code for *unpack_netcdf.f90*

```
!-----  
!  
! Program:          unpack_netcdf.f90  
!  
! Written By:       Ghassan Alaka Jr.  
!  
! Date Created:    February 12, 2014  
! Last Modified:   June 30, 2014  
!  
! This is a simple program to write data in the WPS intermediate  
! format from NetCDF input. This will allow the WRF model to ingest  
! NetCDF data in addition to GRIB.  
!  
! Update 06-30-2014 -- Fixed an error where the "slab" was being unnecessarily  
!                      transposed. The error actually stemmed to an incorrect  
!                      matrix ("slab_tmp") that did not read in the NetCDF  
!                      data in the right order.  
!  
!-----  
program unpack_netcdf  
    ! Fortran 90 version.  
    !-----  
    ! Start script and define variables  
    !-----  
    use netcdf  
    implicit none  
  
    ! User-Defined Variables  
    character(len = 100) :: idir = "/maloney-scratch/galaka/datasets/ERAi/0.75/WRF_S2/"  
    character(len = 150) :: odir = "/maloney-  
scratch/galaka/datasets/ERAi/0.75/WRF_S2/intermediate_files/"  
    ! Output directory  
    character(len = 8) :: startloc = "SWCORN" ! Start location of data. Could be  
"CENTER" or "SWCORN". "SWCORN" is typical.  
    character(len = 15) :: currentYr = "2004"  
    integer :: version = 5  
    integer :: nvars_pres = 5  
    integer :: nvars_sfc = 18  
    integer :: iproj = 0 ! Map Projection: 0 = cylindrical  
equidistant, 1 = mercator  
    integer, parameter :: ounit = 10 ! Outfile unit
```

integer processed real*4 in the slab real*4 real*4 real*4 real*4, parameter logical winds are	:: maxrecs = 10000 :: xfest = 0 :: truelat1 = 0 :: truelat2 = 0 :: xlonc = 0 :: earth_radius = 6367470.*.001 ! Earth radius, km :: is_wind_grid_rel = .FALSE. ! Flag indicating whether	! Maximum Number of files ! Forecast time (in hours) of the data ! Standard longitude of projection ! relative to source grid (TRUE) or ! relative to earth (FALSE)
--	---	---

! Empty Variables		
integer integer integer character(len = 8) character(len = 19) character(len = 21) character(len = 32) character(len=10) character(len=24) character(len=200) character(len=50) , dimension(1:nvars_pres) :: field_pres_i, units_pres_i, VAR_pres_i, desc_pres_i character(len=50) , dimension(1:nvars_sfc) :: field_sfc_i, units_sfc_i, VAR_sfc_i, desc_sfc_i character(len=10) character(len=25) character(len=46) character(len=1) real*4	:: tsz, latsz, ny, lonsz, nx, levsz, nlats, nfiles :: ios ! Read file integers :: tt, kk, ns, np, ff, gg, nsfc ! Counters :: lev_name, lat_name, lon_name :: time_name :: timestamp_name :: map_source :: tmp_str :: hdate, xlvl_str :: ifile, ofile, filelist, system_call, var_line :: field_pres_i, units_pres_i, VAR_pres_i, desc_pres_i character(len=50) , dimension(1:nvars_sfc) :: field_sfc_i, units_sfc_i, VAR_sfc_i, desc_sfc_i :: field :: units, VAR :: desc :: junk :: startlat, startlon, &	! Lat/lon of point in array indicated by deltalat, deltalon, & ! Grid spacing, degrees dx, dy, & ! Grid spacing, km xlvl ! Pressure Level logical :: lat_flip_flag, lon_flip_flag, sfc_flag, pres_flag, var_exists

! Allocatable Variables		
double precision, dimension (:), allocatable !real*4, dimension (:,:,:,::), allocatable !real*4, dimension (:,:,:,::), allocatable real*4, dimension (:), allocatable	:: timestamp_dbl :: VARS_pres :: VARS_sfc :: lat, lon, pres	

```

real*4, dimension(:, :, ), allocatable :: slab ! The 2-d array holding the data
character(len = 100), dimension(:), allocatable :: Vtable
character(len=24), dimension(:), allocatable :: hdate_hist

!-----
! Script Body
!-----

! Prompt user for map source
write(*, '(A)', ADVANCE = "NO") "Please choose data source (e.g. - ECMWF)\nEnter
here: "
read(*, *) map_source
print *, "Map source set to ", trim(map_source)

! Put list of files to be processed in 'filelist.txt'
filelist = trim(idir) // '/filelist.txt'
system_call = 'ls -l ' // trim(idir) // '*' // trim(currentYr) //'*'.nc | wc -l > ' // trim(filelist)
! Get the number of files
call system(trim(system_call))
system_call = 'ls -d -1 ' // trim(idir) // '*' // trim(currentYr) //'*'.nc >> ' // trim(filelist)
! List the file names (full path)
call system(trim(system_call))

! Read in the file list
open(unit=50,file=trim(filelist),status="old",action="read")

! Figure out how many files there are
read(50,*) nfiles
print *, "Total number of files detected: ", nfiles

! Loop over the files to retrieve data
do ff = 1,nfiles
    ! Read the next file name
    read(50,'(A)') ifile
    print *, "\n\n", trim(ifile)

    ! Reset flags
    lat_flip_flag = .FALSE.
    lon_flip_flag = .FALSE.

```

```

! Allocate & Retrieve dim arrays
if (ff.eq. 1) then
    ! Define variables for particular input data
    ! More data sources can be added this this section
    if (map_source.eq. "ECMWF") then
        lev_name = "lv_ISBL1"
        lat_name = "g0_lat_2"
        lon_name = "g0_lon_3"
        time_name = "initial_time0_hours"
        !timestamp_name = "initial_time0_encoded"
        timestamp_name = "initial_time0_double"
    else
        print *, "Input data not recognized. Exiting..."
    end if

    ! Get variable dimensions
    call get_dims_nc(ifile, tsz, latsz, ny, lonsz, nx, levsz, &
                     lev_name, lat_name, lon_name, time_name)

    ! Allocate variables with dimension infoa
    allocate(lat(1:latsz))
    allocate(lon(1:lonsz))
    allocate(pres(1:levsz))
    allocate(timestamp dbl(1:tsz))
    allocate(Vtable(1:(levsz+10)))                                ! Extra lines are to
account for header and surface fields
    Vtable(:) = ""
    allocate(hdate_hist(1:(nfiles*tsz)))
    allocate(slab(nx,ny))

    ! Get Pressure Array
    call read_1d_nc(ifile, lev_name, pres, levsz)
    if(pres(1).lt. pres(2)) then
        pres = pres(levsz:1:-1)
    endif
    if(pres(1).lt. 10000.)then
        pres = pres*100.
    endif
end if

    ! Get latitude array
    call read_1d_nc(ifile, lat_name, lat, latsz)

```

```

if(lat(1) .gt. lat(2)) then
    lat = lat(latsz:1:-1)
    lat_flip_flag = .TRUE.
endif
startlat = lat(1)
deltalat = lat(2) - lat(1)
dy = deltalat*110.
! This is an approximation.
dy is not used for equidistant cylindrical
nlats = latsz/2
!print *, "Lat array: ", lat

! Get Longitude Array
call read_1d_nc(ifile, lon_name, lon, lonsz)
if(lon(1) .gt. lon(2)) then
    lon = lon(lonsz:1:-1)
    lon_flip_flag = .TRUE.
endif
startlon = lon(1)
deltalon = lon(2) - lon(1)
dx = deltalon*110.
! This is an approximation.
dx is not used for equidistant cylindrical
!print *, "Lon array: ", lon

! Get time stamps
call get_timestamp_nc(ifile,timestamp_name,tsz,timestamp_dbl)
print *, "here"
! Loop over times
do tt = 1,tsz
    ! Create Timestamp "hdate" (for ERA-interim)
    !print *, nint(timestamp_dbl(1))
    write(tmp_str,'(I10)') nint(timestamp_dbl(tt))
    hdate = tmp_str(1:4) // '-' // tmp_str(5:6) // '-' // tmp_str(7:8) // '_' //
tmp_str(9:10) ! FORMAT: YYYY-MM-DD_HH
    hdate_hist(((ff-1)*tsz)+tt) = hdate
    print *, "\n Current Date: ", trim(hdate)

! Remove existing file and create new one, but only if this is
! the first occurrence of data at that particular time. This
! is in case the data is split up into 2+ files (e.g., surface
! and pressure fields may come in 2 separate files for the same
! time.
ofile = trim(odir) // "FILE:" // trim(hdate)
if (any(hdate_hist(:((ff-1)*tsz)+tt-1).eq.hdate)) then
    print *, " Previous file for same date detected."

```

```

else
    call check_rm_ofile(ounit, ofile)
endif

! Open the Vtable file. Important to copy whichever table to
! "Vtable" inthe directory "idir"
open(unit=20,file=trim(idir)//"Vtable",status="old",action="read")

! Reset the number of surface variables,
! although this should be consistent among
! input files
nsfc = 0

! Loop over Vtable lines
do gg=1,maxrecs

    ! Reset flags
    if (gg .eq. 1) then
        sfc_flag = .FALSE.
        pres_flag = .FALSE.
        print *, " **The format is: <Variable> Y/N"
        print *, " **Y = variable exists, N = variable does not
exist"
        Variable   | Variable   | Variable   |
        Vtable(1) = " Level | Variable   | Variable   |
        "           |
        Vtable(2) = "-----"
        -----
        "
    endif

    !Read the next line
    !print *, "Reading line #", gg
    read (20, '(A)', IOSTAT=ios) var_line

    ! Exit if end of file is reached
    if (ios /= 0) exit

    ! Blank line acts like a break before and between sections
    if (trim(var_line) .eq. " ") then
        sfc_flag = .FALSE.
        pres_flag = .FALSE.

```

```

endif

! If "var_line" is a surface field, enter this IF statement
if (sfc_flag) then

    ! Level info
    xlvl = 200100.000000
    write(xlvl_str,'(f10.2)') xlvl

    ! Get basic fields from Vtable
    VAR  = trim(var_line(1:24))           ! Get the input
    field = trim(var_line(25:40))          ! Get
    units = trim(var_line(41:56))          ! Get
    desc  = trim(var_line(57:100))         ! Get the
    !print *," Variable Name: ", VAR

    ! Get the 2D surface variable
    call read_2d_nc(ifile, VAR, slab, latsz, lonsz, tt, var_exists)

    ! Increase the counter to help build terminal output
    nsfc = nsfc + 1

    ! Determine if the variable exists in the input data
    if (var_exists) then

        ! Flip the slab if necessary
        call flip_2d(slab, nx, ny, lon_flip_flag,
lat_flip_flag)

        ! Set known fields to missing value of -1.E+30
        where (slab .eq. 1.6684628E+19 .or. slab .eq.
1.0000000E+20)
            slab = -1.E+30
            !print *, "Missing Value detected"
            elsewhere
                slab = slab

```

```

        endwhere

        ! Write the variable to unformatted binary
        call write_2d_unformatted(ounit, ofile, version,
hdate, xfcst, &
nx, ny, &
dy, &
truelat1, &
is_wind_grid_rel, &
truelat2, xlonc, nlats,
slab)

        ! Build terminal output
        if (Vtable(2 + (nsfc-1)/5) .eq. " ") then
            Vtable(2 + (nsfc-1)/5) = xlvl_str
        endif
        Vtable(2 + (nsfc-1)/5) = trim(Vtable(2 + (nsfc-
1)/5)) // " | " // field // " Y"
        else
            ! Build terminal output
            if (Vtable(2 + (nsfc-1)/5) .eq. " ") then
                Vtable(2 + (nsfc-1)/5) = xlvl_str
            endif
            Vtable(2 + (nsfc-1)/5) = trim(Vtable(2 + (nsfc-
1)/5)) // " | " // field // " N"
        end if
    end if

    ! If "var_line" is a pressure field, enter this IF statement
    if (pres_flag) then

        ! Loop over pressure levels
        do kk = 1,levsz

            ! Level Info
            xlvl = pres(kk)
            write(xlvl_str,'(f10.2)') xlvl
            !print *, "\n\nPressure Level: ", xlvl

```

```

! Get basic fields from Vtable
VAR  = trim(var_line(1:24))           ! Get
field = trim(var_line(25:40))
units = trim(var_line(41:56))
desc  = trim(var_line(57:100))          ! Get

the input (netcdf) variable name
! Get the output variable name
! Get the units
the description

! Get the 3d pressure field
call read_3d_nc(ifile, VAR, slab, latsz, lonsz, levsz,
tt, kk, var_exists)

! Determine if the variable exists in the input data
if(var_exists) then

    ! Flip the slab if necessary
    call flip_2d(slab, nx, ny, lon_flip_flag,
lat_flip_flag)

    ! Write the variable to unformatted binary
    where (slab .eq. 1.6684628e+19 .or. slab .eq.
1.0000000E+20)
        slab = -1.e+30
        !print *, "Missing Value detected"
        elsewhere
            slab = slab
        endwhere

    ! Write the variable to unformatted binary
    call write_2d_unformatted(ounit, ofile,
version, hdate, xfest, &
desc, xlvl, nx, ny, &
startlon, dx, dy, &
earth_radius, truelat1, &
is_wind_grid_rel, &
map_source, field, units,
iproj, startloc, startlat,
deltalat, deltalon,
truelat2, xlonc, nlats,

```

slab)

```
        ! Build terminal output
        if (Vtable(2 + ((nsfc-1)/5) + kk) .eq. " ")
then
        Vtable(2 + ((nsfc-1)/5) + kk) =
xlvl_str
        endif
        Vtable(2 + ((nsfc-1)/5) + kk) =
trim(Vtable(2 + ((nsfc-1)/5) + kk)) // " | " // field // " Y"
        else
            ! Build temrinal output
            if (Vtable(2 + ((nsfc-1)/5) + kk) .eq. " ")
then
            Vtable(2 + ((nsfc-1)/5) + kk) =
xlvl_str
            endif
            Vtable(2 + ((nsfc-1)/5) + kk) =
trim(Vtable(2 + ((nsfc-1)/5) + kk)) // " | " // field // " N"
            endif
        enddo
    endif

    ! Lines after "Surface Fields" denote surface variable info
    if (trim(var_line(1:14)) .eq. "Surface Fields") then
        sfc_flag = .TRUE.
    endif

    ! Lines after "Pressure Fields" denote pressure variable info
    if (trim(var_line) .eq. "Pressure Fields") then
        pres_flag = .TRUE.
    endif

    ! Print out the data source
    if (var_line(1:13) .eq. "Data Source: ") then
        print *, " ", trim(var_line)
    endif
enddo
close(20)
print *, "\n", Vtable(1:((nsfc-1)/5)+levsz)
Vtable(:) = " "
```

```

        enddo
    enddo

    ! CLEANUP and end script
    deallocate(timestamp_dbl)
    deallocate(lat)
    deallocate(lon)
    deallocate(pres)
    deallocate(slab)

    print *, " "
    print *, "*****"
    print *, "*UNPACK_NETCDF Successfully Completed!*"
    print *, "*****"

end program unpack_netcdf

subroutine get_dims_nc(FILE_NAME, tsz, latsz, ny, lonsz, nx, levsz, &
    lev_name, lat_name, lon_name, time_name)
    use netcdf
    implicit none
    integer                                     :: ncid, status, TimeDimID, LatDimID, LonDimID,
    LevDimID
    integer, intent(out)                      :: tsz, latsz, ny, lonsz, nx, levsz
    character(len = 100), intent(in)           :: FILE_NAME
    character(len = 8), intent(in)             :: lev_name, lat_name, lon_name
    character(len = 19), intent(in)            :: time_name

    !-----
    ! Open the file
    !-----
    status = nf90_open(FILE_NAME, nf90_nowrite, ncid)          ! 'nf90_noerr'
is returned if no errors with file read
    if (status /= nf90_noerr) call handle_err(status)          ! If an error was
called, display error message

    !-----
    ! Get ID of unlimited dimension
    !-----
    ! status = nf90_inquire(ncid, unlimitedDimId = RecordDimID)
    ! if (status /= nf90_noerr) call handle_err(status)
    ! What is the name of the unlimited dimension, how many records are there?
    !status = nf90_inquire_dimension(ncid, RecordDimID, &

```

```

!      name = RecordDimName, len = nRecords)
!if (status /= nf90_noerr) call handle_err(status)

!-----
! Find the time dimension
!-----
status = nf90_inq_dimid(ncid, time_name, TimeDimID)
if (status /= nf90_noerr) call handle_err(status)
! How many values of "time" are there?
status = nf90_inquire_dimension(ncid, TimeDimID, len = tsz)
if (status /= nf90_noerr) call handle_err(status)
print *, "# Times: ", tsz
!allocate(time(1:tsz))

!-----
! Find the latitude dimension
!-----
status = nf90_inq_dimid(ncid, lat_name, LatDimID)
if (status /= nf90_noerr) call handle_err(status)
! How many values of "lat" are there?
status = nf90_inquire_dimension(ncid, LatDimID, len = latsz)
if (status /= nf90_noerr) call handle_err(status)
print *, "# Latitudes: ", latsz
ny = latsz

!-----
! Find the longitude dimension
!-----
status = nf90_inq_dimid(ncid, lon_name, LonDimID)
if (status /= nf90_noerr) call handle_err(status)
! How many values of "lon" are there?
status = nf90_inquire_dimension(ncid, LonDimID, len = lonsz)
if (status /= nf90_noerr) call handle_err(status)
print *, "# Longitudes: ", lonsz
nx = lonsz

!-----
! Find the vertical dimension
!-----
status = nf90_inq_dimid(ncid, lev_name, LevDimID)
if (status /= nf90_noerr) call handle_err(status)
! How many values of "lev" are there?
status = nf90_inquire_dimension(ncid, LevDimID, len = levsz)

```

```

if (status /= nf90_noerr) call handle_err(status)
print *, " # Pres Levels: ", levsz

!-----
! Close the file
!-----
status = nf90_close(ncid)
if (status /= nf90_noerr) call handle_err(status)

end subroutine get_dims_nc

subroutine read_1d_nc(FILE_NAME, var_name, var, varsz)
use netcdf
implicit none
character(len = 100), intent(in)      :: FILE_NAME
character(len = 8), intent(in)        :: var_name
integer                           :: ncid, status, VarID
integer, intent(inout)             :: varsz
real*4, dimension (1:varsz), intent(inout) :: var

!-----
! Open the file
!-----
status = nf90_open(FILE_NAME, nf90_nowrite, ncid)           ! 'nf90_noerr'
is returned if no errors with file read
if (status /= nf90_noerr) call handle_err(status)           ! If an error was
called, display error message

!-----
! Get Latitude Variable
!-----
status = nf90_inq_varid(ncid, var_name, VarID)
if (status /= nf90_noerr) call handle_err(status)
status = nf90_get_var(ncid, VarID, var)
if (status /= nf90_noerr) call handle_err(status)

!-----
! Close the file
!-----
status = nf90_close(ncid)
if (status /= nf90_noerr) call handle_err(status)
end subroutine read_1d_nc

subroutine read_2d_nc(FILE_NAME, var_name, slab, latsz, lonsz, tt, var_exists)

```

```

use netcdf
implicit none
character(len = 100), intent(in)      :: FILE_NAME
character(len = 25), intent(in)       :: var_name
integer                           :: ncid, status, VarID
integer, intent(inout)             :: latsz, lonsz, tt
real*4, dimension (1:lonsz,1:latsz), intent(inout) :: slab
logical, intent(inout)            :: var_exists
!real*4, dimension (1:latsz,1:lonsz) :: tmp_slab

!-----
! Open the file
!-----
status = nf90_open(FILE_NAME, nf90_nowrite, ncid)           ! 'nf90_noerr'
is returned if no errors with file read
if (status /= nf90_noerr) call handle_err(status)           ! If an error was
called, display error message

!-----
! Get Latitude Variable
!-----
status = nf90_inq_varid(ncid, var_name, VarID)
if (status /= nf90_noerr) then
    !print *, " Variable does not exist!"
    var_exists = .FALSE.
    !call handle_err(status)
else
    status = nf90_get_var(ncid, VarID, slab, start=(/1,1,tt/), &
                           count=(/lonsz,latsz,1/)), map=(/lonsz,1/))
    if (status /= nf90_noerr) call handle_err(status)
    !print *, " Variable exists!"
    var_exists = .TRUE.

    !slab = transpose(tmp_slab)

    !print *, " Max: ", maxval(slab), " Min: ", minval(slab)
endif

!-----
! Close the file
!-----
status = nf90_close(ncid)
if (status /= nf90_noerr) call handle_err(status)
end subroutine read_2d_nc

```

```

subroutine read_3d_nc(FILE_NAME, var_name, slab, latsz, lonsz, levsz, tt, kk, var_exists)
  use netcdf
  implicit none
  character(len = 100), intent(in)      :: FILE_NAME
  character(len = 25), intent(in)       :: var_name
  integer                           :: ncid, status, VarID
  integer, intent(inout)             :: latsz, lonsz, levsz, tt, kk
  logical, intent(inout)            :: var_exists
  real*4, dimension (1:lonsz,1:latsz), intent(inout) :: slab
  !real*4, dimension (1:latsz,1:lonsz) :: tmp_slab

!-----
! Open the file
!-----
status = nf90_open(FILE_NAME, nf90_nowrite, ncid)           ! 'nf90_noerr'
is returned if no errors with file read
if (status /= nf90_noerr) call handle_err(status)           ! If an error was
called, display error message

!-----
! Get Latitude Variable
!-----
status = nf90_inq_varid(ncid, var_name, VarID)
if (status /= nf90_noerr) then
  !print *, "  Variable does not exist!"
  var_exists = .FALSE.
  !call handle_err(status)
else
  status = nf90_get_var(ncid, VarID, slab, start=(/1,1,levsz+1-kk,tt/), &
                      count=(/lonsz,latsz,1,1/))
  if (status /= nf90_noerr) call handle_err(status)
  !print *, "  Variable exists!"
  var_exists = .TRUE.

  !slab = transpose(tmp_slab)

  !print *, "    Max: ", maxval(slab), " Min: ", minval(slab)
endif

!-----
! Close the file
!-----
status = nf90_close(ncid)
if (status /= nf90_noerr) call handle_err(status)
end subroutine read_3d_nc

```

```

subroutine write_2d_unformatted(ounit, ofile, version, hdate, xfcst, &
                               map_source, field, units, desc, xlvl, nx, ny, &
                               iproj, startloc, startlat, startlon, dx, dy, &
                               deltalat, deltalon, earth_radius, truelat1, &
                               truelat2, xlonc, nlats, is_wind_grid_rel, &
                               slab)

implicit none
character(len=32), intent(in) :: map_source
character(len=8), intent(in) :: startloc
character(len=9), intent(in) :: field
character(len=25), intent(in) :: units
character(len=46), intent(in) :: desc
character(len=24), intent(in) :: hdate
character(len=100), intent(in) :: ofile
real*4, intent(in)          :: startlat, startlon, deltalat, deltalon, &
                               dx, dy, xlvl, xfcst, truelat1, truelat2, &
                               xlonc, earth_radius, nlats
integer , intent(in)        :: version, iproj, nx, ny, ounit
logical, intent(in)         :: is_wind_grid_rel
real*4, dimension (1:nx,1:ny), intent(in) :: slab

```

```
open (ounit, FILE=ofile, form='unformatted',access='append')
```

```
! 1) WRITE FORMAT VERSION
```

```
write(unit=ounit) version
```

```
! 2) WRITE METADATA
```

```
! Cylindrical equidistant
```

```
if (iproj == 0) then
```

```
    write(unit=ounit) hdate, xfcst, map_source, field, &
                      units, desc, xlvl, nx, ny, iproj
```

```
    write(unit=ounit) startloc, startlat, startlon, &
                      deltalat, deltalon, earth_radius
```

```
! Mercator
```

```
else if (iproj == 1) then
```

```
    write(unit=ounit) hdate, xfcst, map_source, field, &
                      units, desc, xlvl, nx, ny, iproj
```

```
    write(unit=ounit) startloc, startlat, startlon, dx, dy, &
                      truelat1, earth_radius
```

```
! Lambert conformal
```

```
else if (iproj == 3) then
```

```
    write(unit=ounit) hdate, xfcst, map_source, field, &
```

```

        units, desc, xlvl, nx, ny, iproj
    write(unit=ounit) startloc, startlat, startlon, dx, dy, &
                    xlonc, truelat1, truelat2, earth_radius

! Gaussian
else if (iproj == 4) then
    write(unit=ounit) hdate, xfcst, map_source, field, &
                    units, desc, xlvl, nx, ny, iproj
    write(unit=ounit) startloc, startlat, startlon, &
                    nlats, deltalon, earth_radius

! Polar stereographic
else if (iproj == 5) then
    write(unit=ounit) hdate, xfcst, map_source, field, &
                    units, desc, xlvl, nx, ny, iproj
    write(unit=ounit) startloc, startlat, startlon, dx, dy, &
                    xlonc, truelat1, earth_radius

end if

! 3) WRITE WIND ROTATION FLAG
write(unit=ounit) is_wind_grid_rel

! 4) WRITE 2-D ARRAY OF DATA
write(unit=ounit) slab

! 5) Close the file
close (ounit)

end subroutine write_2d_unformatted

subroutine get_timestamp_nc(FILE_NAME, timestamp_name, tsz, timestamp)
use netcdf
implicit none
integer                                     :: ncid, status, TimestampVarID
character(len = 100), intent(in)             :: FILE_NAME
character(len = 21), intent(in)              :: timestamp_name
integer, intent(in)                         :: tsz
double precision, dimension (1:tsz), intent(out) :: timestamp

!-----
! Open the file
!-----
status = nf90_open(FILE_NAME, nf90_nowrite, ncid)           ! 'nf90_noerr'

```

is returned if no errors with file read
 if (status /= nf90_noerr) call handle_err(status) ! If an error was
 called, display error message

```
!-----
! Find the time dimension
!-----
status = nf90_inq_varid(ncid, timestamp_name, TimestampVarID)
if (status /= nf90_noerr) call handle_err(status)
status = nf90_get_var(ncid, TimestampVarID, timestamp)
if (status /= nf90_noerr) call handle_err(status)
print *, "Time Stamps: ", timestamp

!-----
! Close the file
!-----
status = nf90_close(ncid)
if (status /= nf90_noerr) call handle_err(status)
```

end subroutine get_timestamp_nc

```
subroutine check_rm_ofile(ounit, ofile)
  implicit none
  character(len=100), intent(in) :: ofile
  character(len=100)           :: command
  integer                     :: status, exist
  integer, intent(in)          :: ounit

  inquire(file=ofile, exist=exist)
  if (exist) then
    open (ounit, FILE=ofile, dispose="delete")
    close(ounit)
    print *, " File successfully removed..."
  else if (.NOT. exist) then
    print *, " File does not exist..."
  end if
end subroutine check_rm_ofile
```

```
subroutine flip_2d(slab, nx, ny, lon_flip_flag, lat_flip_flag)
  implicit none
  integer, intent(in)           :: nx, ny
  logical, intent(in)          :: lon_flip_flag, lat_flip_flag
  real*4, dimension (1:nx,1:ny), intent(inout) :: slab
```

```

if(lat_flip_flag)then
    slab = slab(:,ny:1:-1)
end if

if(lon_flip_flag)then
    slab = slab(nx:1:-1,:)
end if

end subroutine flip_2d

subroutine handle_err(status)
use netcdf
implicit none
integer, intent(in) :: status

if(status /= nf90_noerr) then
    print *, nf90_strerror(status)
    stop "Stopped"
end if
end subroutine handle_err

```